Sophie A. Cottilard
Editor

Catalytic Combustion

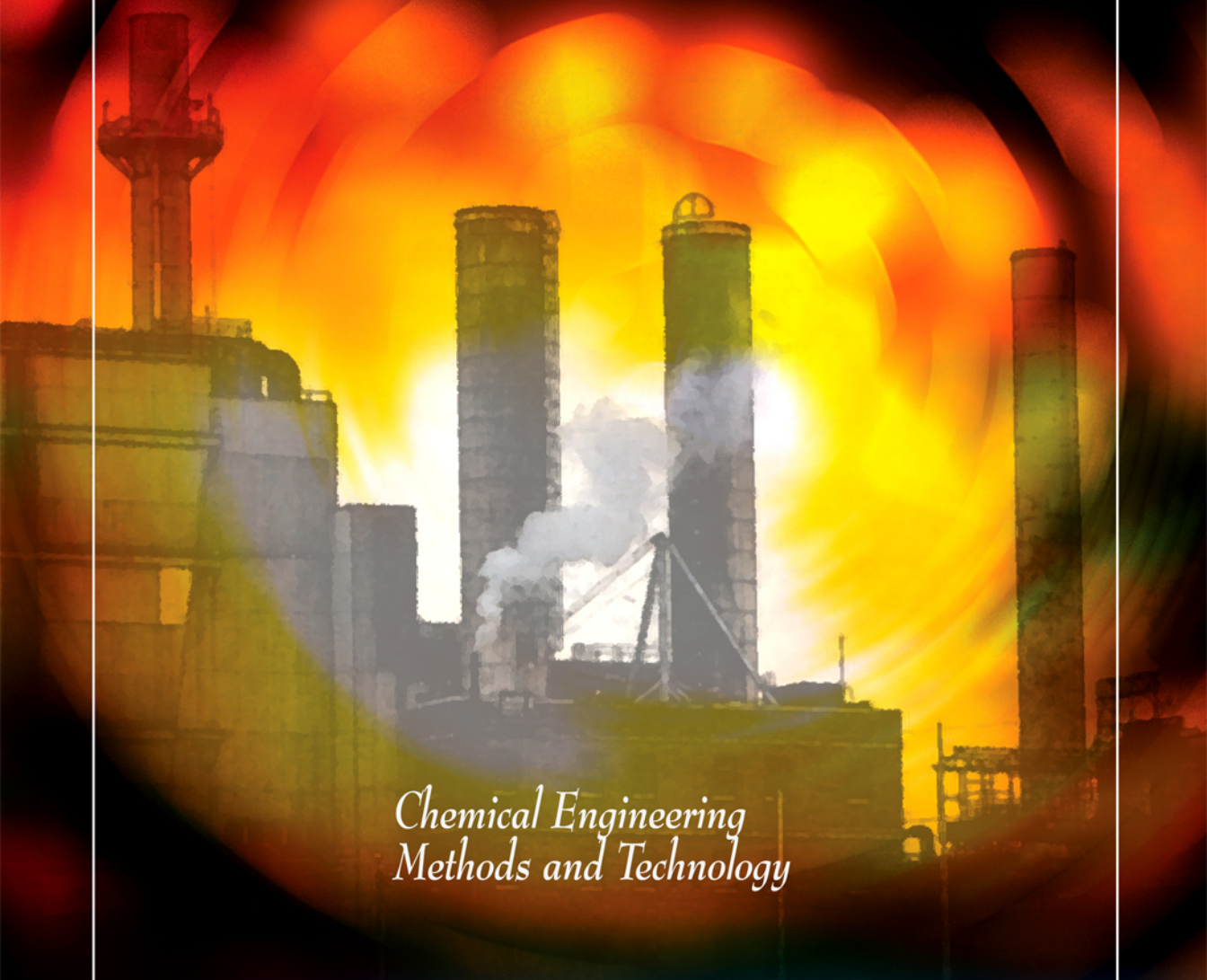

Chemical Engineering Methods and Technology

NOVA

CHEMICAL ENGINEERING METHODS AND TECHNOLOGY

CATALYTIC COMBUSTION

CHEMICAL ENGINEERING METHODS AND TECHNOLOGY

Additional books in this series can be found on Nova's website under the Series tab.

Additional E-books in this series can be found on Nova's website under the E-books tab.

CHEMICAL ENGINEERING METHODS AND TECHNOLOGY

CATALYTIC COMBUSTION

SOPHIE A. COTTILARD
EDITOR

Nova Science Publishers, Inc.
New York

Library of Congress Cataloging-in-Publication Data

Catalytic combustion / [edited by] Sophie A. Cottilard.
p. cm.
Includes index.
ISBN 978-1-62081-438-3 (eBook)
1. Combustion. 2. Catalysis. 3. Chemical reactions. I. Cottilard, Sophie A.
QD516.C38 2011
541'.361--dc22
2011010117

Published by Nova Science Publishers, Inc. †New York

CONTENTS

PREFACE

Catalytic combustion has been developed as a method of promoting efficient combustion over a wide range of air-to-fuel ratios with a minimum pollutant formation at low temperatures as compared to conventional flame combustion. In this book, the authors present current research in the study of catalytic combustion including commercial and industrial research in combustion and fluidization engineering; the catalytic combustion of soot; using metal oxides to improve catalytic efficiency; catalytic combustion in the removal of pollutants from exhaust gases and in the energy conversion field and the catalytic combustion of methane using ceria-zirconia.

Chapter 1 - Fluidization has been widely used in a number of industrial processes as an effective mean for providing good mixing and contact of the gas and solid phases, as well as good heat transfer. Applications include coal combustion, chemical, petrochemical and metallurgical processes, CO_2 capture. This attractive feature is achieved by solids circulation within the bed, in which particles are driven by gas, or bubbles, and transported around the bed. A different circulation pattern will give different heat/mass transfer rate, different mixing efficiency, different solid/gas contact and different residence time of solids and gas. Despite the extensive work carried out since 1960s, many uncertainties still remain, and the interpretations reported in literature are frequently conflict. For example, Grace and Harrison (1969) were among the first to systematically and quantitatively investigate the spatial distribution of bubbles in a two-dimensional bed by means of photography. They suggested that the bubbles with small sizes were uniformly distributed in a layer close to the distributor and then shafted inwards to the central region of the bed with the increase in the bed height, resulting in the reduction in concentration of bubbles in the region near the walls. This was used as a basis by Darton et al. for the popular model of bubble coalescence. However, different observations were reported by Werther and Molerus (1973) when they investigated the bubble spatial distribution in three-dimensional beds containing quartz sand, glass spheres and spherical copper powder under various operating conditions by using capacitance probes. In this chapter, we will report our recent funding in both bubbling fluidization and circulation fluidization by using non-invasive positron emission particle tracking (PEPT) technique. The authors will report the three flow structures that they funded in three dimensional fluidized beds, and discuss the impact of bed materials, operational parameters on the flow structure, solid gas pattern. The authors will discuss the operational conditions and flow structure on solid mixing, solid gas contact, solid and bubble residence time in both bubbling fluidized bed and circulation fluidized beds, and will discuss the distinction between the different

regimes in circulating fluidized beds. The results will benefit academic and commercial/industrial researchers in combustion and fluidization engineering worldwide.

Chapter 2 - In this paper, the background of the emission of soot particulates and the formation mechanism of soot have been briefly reviewed. The structure, chemical characteristic of soot emitted from diesel engine exhaust gases and its adverse to the people 's health have been described. Emission standards of soot particulates have been proposed and outlined to reduce remarkably the harmful emissions of diesel engines. There are several methods for reducing soot particulates. Firstly, soot particulates emissions could be reduced by improving diesel oil qualify and optimizing the fuel composition, or by using an alternative fuel. Although significant, emission reductions obtained in this way were not sufficient to fulfill the higher emission targets. Secondly, soot particulates emissions could be diminished by modifying the diesel engine. Technological advances could attain the EU-IV emission target by engine modifying alone. Finally, for the higher emission targets desired, the both above methods were not completely fulfilled. Thus, an important aftertreatment technology must be applied. The combination of traps and oxidation catalysts is one of the effective aftertreatment methods. Although this method involves many technological difficulties to be overcome (the development of efficient and thermally stable traps, the contact between catalyst and trapped soot, etc.), the active catalysts is considered to be the most important one. Several kinds of important catalysts for the catalytic combustion of soot including low-melting point catalyst, noble metal catalysts, complex oxide catalysts, and macroporous-based catalysts were detailed reviewed. In the end, the key scientific problems and development trends in soot particulates emission control will be outlined and discussed.

Chapter 3 - Currently, mankind has been facing the consequences arising from extensive fossil-fuel exploitation and their continuous use is expected to produce more harmful effects. It is an acknowledged fact that world's major energy needs are met from thermal power generation which depends mainly on the combustion of fossil fuels. On the other hand, these combustion systems have elevated much of the environmental problems. One of the emission gases of most serious concern is nitrogen oxide (NO_x), which causes acid rain, global warming and ozone depletion. To settle the global environmental and energy issues, the combustion systems need to be much more improved for high efficiency and low pollutant emissions. Catalytic combustion has been developed as a method of promoting efficient combustion over a wide range of air-to-fuel ratios with a minimum pollutant formation at low temperatures as compared to conventional flame combustion. The application of catalysts facilitates efficient combustion of hydrocarbons at relatively lower temperatures without promoting oxidation of nitrogen and also stringent control over the emission of volatile organic compounds (VOCs). Generally, effective emission control is often achieved by the use of noble metal catalysts; they are very active at low temperatures but due to the economical reasons, as well as limited availability of noble metals, motivated the investigation into the alternative materials for catalytic combustion. Metal oxides are the promising option, because they are relatively cheap, show variable valency and exhibit greater redox characteristics. Mixed metal oxides in the form of perovskites, hexa-aluminates and doped metal oxides are promising because of their thermal stability at high temperatures, low cost, and flexible composition. Among doped metal oxides, ceria-based materials are attractive in catalytic combustion apart from three-way-catalytic applications, VOC abatement, and fuel cell technologies due to their ease of redox and high thermal stability. Metal oxide catalysts exhibit good catalytic activity in narrow temperature range. However,

the catalytic combustion range is up to 1773 K for that, it is necessary to add supports to increase the thermal stability. Recently, it has been reported that ceria supported on lanthanum hexa-aluminate shows an impressive activity and stability up to 1273 K. In this chapter the authors have concentrated on the catalytic application of pure metal oxides, and mixed metal oxides such as perovskites, hexa-aluminates and ceria doped materials for catalytic combustion. They also discussed the significance of supports to metal oxides to improve the catalytic efficiency at high temperatures. Finally, the authors have provided new directions for future work on this subject.

Chapter 4 - Catalytic combustion may find application in the removal of pollutants from exhaust gases or in the energy conversion field. Proper reactor design is needed for optimised operation, *i.e.* to fully convert the fuel. When the catalytic combustion of methane is coupled with a turbogas plant, further attention should be paid to control the combustor temperature. This is needed to avoid the formation of NO_x and to preserve the catalyst from thermal deactivation. For all these reasons, a detailed knowledge of the kinetics of the process is welcome. Furthermore, some non trivial process layouts may be found for this application, such as those based on monolithic reactors. This contribution reviews some of the most typical applications of catalytic combustion, including noble metal or mixed oxide based catalysts. The discussion particularly focuses on kinetic aspects and reactor design.

Chapter 5 - The energy production by combustion of methane or natural gas in gas turbines and burners constitutes a well-developed technology. However, due to the fact that methane is a hydrocarbon molecule difficult to oxidize, the homogeneous combustion with air occurs in flames with very high temperatures. These high temperatures thermodynamically favor the formation of nitrogen oxides (NO_x), which constitutes the "photochemical smog", harmful to aquatic and terrestrial ecosystems and to human health. In recent years, global concern about the rapid increase in emissions of gaseous pollutants and greenhouse gases caused by the growth in energy demand has been growing. Under the Kyoto protocol, the reductions of hydrocarbons, carbon dioxide (CO_2) and NO_x emissions, and the increase of combustion efficiency, especially in the case of methane and natural gas, have become a central research topic. The catalytic combustion of methane emerges as a possible solution due to its advantages over the homogeneous combustion. The presence of a catalyst facilitates the total oxidation of methane and, moreover, a suitable catalyst will promote the total combustion at lower temperatures than the homogeneous reaction, leading to a reduction of NO_x emissions. The goal in this area is to develop a catalyst that promotes the total oxidation of methane at low temperatures, reducing the emission of greenhouse and harmful gases. In this review, the important aspects of the catalytic combustion of methane using ceria-zirconia catalysts are addressed. The major findings in recent years are presented.

In: Catalytic Combustion
Editor: Sophie A. Cottilard, pp. 1-73
ISBN: 978-1-61324-279-7

Chapter 1

RE-INTERPRETATION OF FLUIDIZATION

Xianfeng Fan[1,*] and Zhufang Yang[2]
[1]Institute for Material and Processes, School of Engineering,
University of Edinburgh, Edinburgh, EH9 3JL, UK
[2]Department of Mechanical, Materials and Manufacturing Engineering,
University of Nottingham, NG7 2RD, UK

ABSTRACT

Fluidization has been widely used in a number of industrial processes as an effective mean for providing good mixing and contact of the gas and solid phases, as well as good heat transfer. Applications include coal combustion, chemical, petrochemical and metallurgical processes, CO_2 capture. This attractive feature is achieved by solids circulation within the bed, in which particles are driven by gas, or bubbles, and transported around the bed. A different circulation pattern will give different heat/mass transfer rate, different mixing efficiency, different solid/gas contact and different residence time of solids and gas. Despite the extensive work carried out since 1960s, many uncertainties still remain, and the interpretations reported in literature are frequently conflict. For example, Grace and Harrison (1969) were among the first to systematically and quantitatively investigate the spatial distribution of bubbles in a two-dimensional bed by means of photography. They suggested that the bubbles with small sizes were uniformly distributed in a layer close to the distributor and then shafted inwards to the central region of the bed with the increase in the bed height, resulting in the reduction in concentration of bubbles in the region near the walls. This was used as a basis by Darton et al. for the popular model of bubble coalescence. However, different observations were reported by Werther and Molerus (1973) when they investigated the bubble spatial distribution in three-dimensional beds containing quartz sand, glass spheres and spherical copper powder under various operating conditions by using capacitance probes. In this chapter, we will report our recent funding in both bubbling fluidization and circulation fluidization by using non-invasive positron emission particle tracking (PEPT) technique. We will report the three flow structures that we funded in three dimensional fluidized beds, and discuss the impact of bed materials, operational

*E-mail: x.fan@ed.ac.uk

parameters on the flow structure, solid gas pattern. We will discuss the operational conditions and flow structure on solid mixing, solid gas contact, solid and bubble residence time in both bubbling fluidized bed and circulation fluidized beds, and will discuss the distinction between the different regimes in circulating fluidized beds. The results will benefit academic and commercial/industrial researchers in combustion and fluidization engineering worldwide.

1. INTRODUCTION

Fluidization has been widely used in a number of industrial processes as an effective mean for providing good mixing and contact of the gas and solid phases, as well as good heat transfer. Applications include coal combustion, chemical, petrochemical, metallurgical processes and CO_2 capture. This attractive feature is achieved by solids circulation within the bed, in which particles are driven by gas, or bubbles, and transported around the bed. A different circulation pattern will give *a* different heat/mass transfer rate, different mixing efficiency, different solid/gas contact and different residence time of solids and gas. When gas is introduced to a column containing solid particles through a suitable gas distributor at the base, the hydrodynamic regimes in a fluidized bed depend on the particle characteristics and the magnitude of the gas superficial velocity. A classical bubbling fluidized bed regime is formed immediately above the gas distributor when the gas velocity exceeds minimum fluidization velocity, U_{mf}, in conventional gas–solid fluidization of Geldart's Group B particles. When the gas velocity approaches the terminal velocity of a single particle, U_t, turbulent fluidization occurs which is accompanied by high particle elutriation rates. Further increasing the superficial gas velocity and recirculating solids to the bottom of the riser, fluidized beds are operated in the circulating fluidized bed (CFB) regimes (Berruti et al., 1995, Kunii and Levenspiel, 1991). Despite the extensive work carried out since 1960s, many uncertainties still remain, and the interpretations reported in literature are frequently conflict (Fan et al. 2008). For example, in the studies of bubbling fluidization, Grace and Harrison (1969) were among the first to systematically and quantitatively investigate the spatial distribution of bubbles in a two-dimensional bed by means of photography. They suggested that the bubbles with small sizes were uniformly distributed in a layer close to the distributor and then shafted inwards to the central region of the bed with the increase in the bed height, resulting in the reduction in concentration of bubbles in the region near the walls. This was used as a basis by Darton et al. (1977) for the popular model of bubble coalescence. However, different observations were reported by Werther and Molerus (1973) when they investigated the bubble spatial distribution in three-dimensional beds containing quartz sand, glass spheres and spherical copper powder under various operating conditions by using capacitance probes. Close to the distributor air bubbles preferentially formed in the vicinity of the walls, rather than being uniformly distributed in the whole cross section area. As the bubbles rose in the bed, the diameter of this annulus of bubbles decreased until a single peak formed at the centre of a bed. The packing geometry of the particle layers near the wall was altered, as in packed beds and liquid-fluidised beds, therefore leading to an increased flow through this region. In experiments recently carried out by Lim et al. (2006, 2007) in a planar fluidised bed, the bubble void fraction (BVF) was calculated by real-time vision instrumentation which accumulated images over time. The reported bubble distribution was similar to Werther and

Molerus (1973) wherein a pair of narrow bands of high bubble concentration was observed along either sides of the bed close to the walls near the distributor, which gradually migrated inwards, spreading over the centre of the bed and higher up in it (Werther, 1983). A region of bubble deprivation was observed in the bed centre near the bottom. The tapering of bubble distribution also left the regions close to the wall in the upper part of the bed deprived of bubbles. For circulating fluidization, it has been widely accepted that there are several flow regimes, such as dilute transport regime, fast fluidisation or core-annulus flow regime and dense suspension upflow regime (DSU). Controversies lie on how to distinct the regimes and the boundaries of the regimes. Some studies reported that a CFB riser can be divided into two sections, a dense bed at the riser bottom and a dilute phase or moderately dense phase (core-annulus) at the top section of the riser (Chan et al 2010; Van de Velden, et al, 2007; Li et al, 1988; Kwauk et al, 1986; Rhodes and Geldart, 1986; Rhodes and Geldart, 1989; Kato et al., 1989; Mori et al, 1992). The axial solids hold-up profile has an inflection point and is referred to as the S-profile. The depth of the bed increases with the increasing in solid flux at constant gas (Rhodes et al, 1998; Malcus et al, 2002; Karri and Knowlton, 2002; Manyele 2002). While, other studies suggest that an exponential solids hold-up profile exists with an acceleration zone but not a dense bed at the riser bottom. Controversies also lie on characteristic of other regimes such as core-annulus flow without bed, dilute transport and/or dense suspension upflow (Das et al, 2008; Arena et al, 1986; Bai et al., 1992; Brereton and Stromberg, 1986; Rhodes and Geldart 1986; Li, 1988). In experimental gas mixing studies, gas back-mixing is reported in some literature as an important character in a CFB riser, but is neglected by other researchers. This contradiction is mainly due to the lack of reliable technique to define the flow structure. The results are not specifically reported in terms of the hydrodynamic regimes, and can therefore not really be compared (Mahmoudi et al. 2010).

In this chapter, we will report our recent findings in both bubbling fluidization and circulation fluidization by using non-invasive positron emission particle tracking (PEPT) technique. We will report on the flow structures that we found in three dimensional fluidized beds, and discuss the operational conditions on flow regimes, solid mixing, solid gas contact in both bubbling fluidized bed and circulation fluidized beds.

2. MEASUREMENT TECHNIQUES

Techniques used to measure solid and gas behaviour in a fluidized bed can be classified into two categories, direct measurement and indirect measurement based on the type of signal used. In indirect measurement, particle/gas movement information is obtained through sending a signal into a fluidized bed. The variation arising from the interaction between the signal and the solid or gas flow is collected by external sensors. The solid and gas behaviour is then deducted through carefully analyzing the interaction between the imputing signal and sold/gas flow. For example, in the techniques of phase-Doppler particle anemometer, laser Doppler velocimeter, particle image velocimetry (Rix et al., 1996), X-ray computerized tomography, ultrasonic computed tomography, electrical capacitance tomography, magnetic resonance imaging, the external system provides the incident beams, such as light (Werther, 1999), laser (Berkelmann and Renz, 1991, Ibsen et al, 2004), X-ray, ultrasonic wave (Werther, 1999; Zhang et al, 2009), electrical field (Ceccio and George, 1996; Dyakowski, et

al. 2000), magnetic field (Porion, et al, 2004), to interact with the internal material in a fluidized bed and to generate informative signals (Powell, 2008). The corresponding flow field information can then be obtained via signal analysis.

In direct measurement, tracer particles are used. The tracer particles send signal from inside of the fluidized beds to a receiver located out of the fluidized bed. The signal can be phosphorescent light, gamma rays, electrical magnetic wave etc. The tracer particles are required identical with experimental bulk in their physical properties, such as size, density and shape.

The well known techniques in this category are positron emission particle tracking, positron emission tomography, phosphorescent particle technique. Recently, Particle Measurement Sensor (PMS) has been developed to sense the dynamic behaviour of solids, and temperature, pressure, and chemical components in a fluidized bed (Zhang et al, 2009, Jagtiani et al, 2006; Song, et al. 2006). In PMS technique, a micro electronic device is encapsulated into a rigid enclosure as a tracer, and sending the signal out, or record the dynamic history.

2.1. Optical Measurement Systems

Optical measurement devices have been used in fluidization engineering since 1960'. The techniques include Laser Doppler Anemometry, phase-Doppler particle anemometer and particle image velocimetry. During the measurement, the solids movement information is deduced from the reflection of light. For example, the light generated by a laser diode is firstly focused into a fiber with a small core diameter and then guided to the measuring volume by a fiber-optical beam splitter and a sensor fiber. The reflected light is received and conducted back through the same fiber, diverted at the beam splitter and finally transformed and amplified to the output voltage. The design of these techniques is fairly simple.

The optical measurement systems can yield high signal-to-noise ratios. However, the concentration of solids even in the freeboard of a bubbling fluidized bed or a dilute mode of CFB is very high. Even a laser beam will be obstructed after a short distance. The information obtained from these techniques can be only used to understand the hydrodynamics in the region adjacent to the column wall, but the gas–solid flow inside the bed cannot be characterised (Werther, 1999).

Imaging techniques suffer from the opaqueness which makes it difficult to visually observe details of the flow inside the bed. To view the flow dynamics inside of a bed, intrusive probes are normally used. Design of a suitable optical probe is still a challenge. The probes are required as small as possible to avoid interrupting the flow structure (Takeuchi and Hirama, 1991, Burschka et al., 1993, Li et al., 1991, Hartholt et al., 1994).

The operating principle of probe imaging is the illumination of particles by light through optical fibers and the detection of the light reflection by the same fibers (Sun and Burgess, 1987). The deposition of fine particles on the end face of the optical fibers is very often, and led to the formation of a thin 'ceramic' layer of extreme hardness and finally blind the probe after a couple of hours.

In addition, optical measurement system is not well suited for the measurement of the local solids concentration. It is practically impossible to realize homogeneous gas–solid suspensions over a sufficiently wide range of solids concentrations.

2.2. Tomographic Imaging

2.2.1. Capacitance Measurement Systems

Capacitance measurement systems were developed to study bubble dynamics in a fluidized bed by measuring the local dielectricity constant of the gas–solid suspension. The measured dielectricity constant is linked to the local volume fraction of solids. The bubble behaviour is then reconstructed through the two-dimensional distribution of the effective dielectric constant measured by pairs of electrodes. A capacitance measurement device developed at the University of Manchester Institute of Science and Technology (UMIST) consists of an eight-electrode capacitance sensor, a data collection system and an image reconstruction computer. The sensor is made by mounting eight metal plates on the outer surface of the insulating pipe section. The capacitances of a fluidised bed can be measured by any two of the eight electrodes in all possible combinations. The measured capacitance values are used to reconstruct a cross-sectional image of the component distribution by using a linear back-projection algorithm. Werther and Molerus (1973) used the needle-type capacitance probes to measure bubble rise velocities in a pilot-scale pressurized bubbling fluidized bed combustor by cross correlating the signals obtained with a double channel probe. Almstedt and Zakkay (1990) used a similar approach to investigate the bubble dynamics in an atmospheric bubbling fluidized bed combustor. The conventional capacitance systems are based on determining the capacitance by balancing a bridge circuit. In most cases the capacitances of probe body and cables will be larger than the sensor capacitance itself, and nearby electrically charged surfaces may produce ‘stray capacitances’ and interfere with the measurement. Miniaturization of the probes leads to capacitance values near the detection limit and finally, and resulting in an instability of the measurement (Werther 1999; Louge, 1996).

2.2.2. X-Ray Imaging

X-ray imaging has been used for studying bubble formation, the sizes, shapes and velocities of single bubbles in fluidization. In X-ray imaging, a pulse of high energy beam (50 to 180 kV) is produced from a rotating anode. The beam passes through a shuttering device that is synchronized with a video camera. The shuttering device allows one X-ray pulse pass a fluidized bed in a time interval of 0.02s. The short X-ray pulse time provides an instant-in-time representation of the internal structure of the rapid change of a fluidization system. When the X-rays pass a fluidized bed, some of them are adsorbed by solids in the bed. The X-ray absorption depends on the concentration of materials along the path. The fluidization bubbles appear as brighter areas in the picture due to the low solid concentration. The intensity of radiation is less at the periphery of the image (longer path through the bed) due to the conical shape of the X-ray between the source and the phosphor screen. This makes the corners appear dark. Determining the coordinates of the bubble outline can be determined automatically by the image analysis software. X-ray imaging has its natural limitations. The X-ray imaging likes photographing. It records all of information within the X-ray path. It is actually voidage distribution on a 2-D photo. The main disadvantage of this method is that the picture is necessarily a silhouette. Bubbles behind or partially behind another cannot be distinguished unambiguously, even though modern methods of digital image processing may help considerably. X-ray imaging is limited to beds with a few tens of centimeters thickness,

to low fluidization velocities, and to low volume concentrations of bubbles in the bed (Rowe and Yacono, 1976; Werther 1999).

2.3. PEPT Techniques

2.3.1. Detection

Optical measurement and tomographic imaging are primarily used to visualize the distribution of solids or voidage inside fluidized beds For many applications it would be interesting to have more detailed information on solids flow and large-scale circulation patterns in opaque systems. For example, in the studies of gas–solid reactions it is important to know about flow structure, flow pattern, the residence time of a particle in different regions of a reactor. Positron emission particle tracking (PEPT) technique has been developed at the University of Birmingham for this purpose. Because γ-rays can penetrate a considerable thickness of material, PEPT offers several advantages for providing an insight into flow and mixing processes inside real plant equipment without disturbing the process. Positron emission particle tracking technique (PEPT) consists of tracer labelling, a camera and algorithms for location calculation and time reconstruction at every tracking step. The camera consists of two position-sensitive detectors, each with an active area of 500×400 mm^2, mounted on either side of the field of view, and is used to detect pairs of 511 keV g-rays emitted from a tracer particle as shown in Figure 1. The two γ-rays are simultaneously detected in the two detectors and define a trajectory passing close to the source.

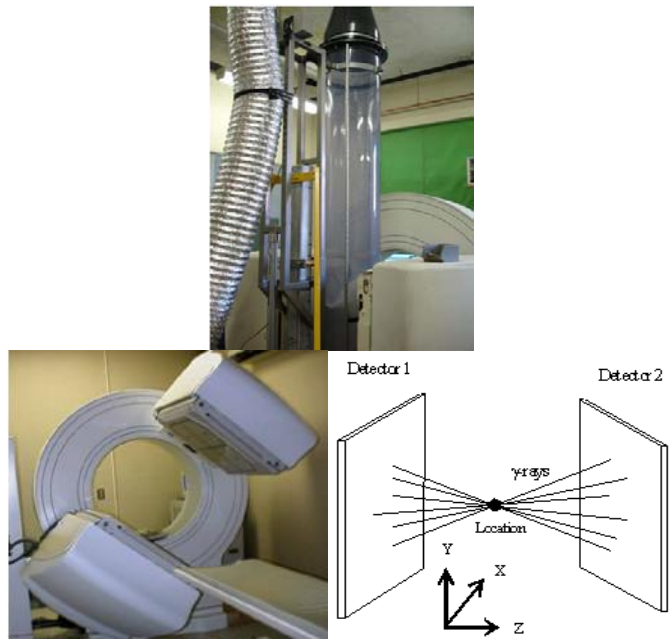

Figure 1. Positron emission particle tracking camera, (a) fluidized bed, (b) PEPT camera, (c) working principle.

When a catalyst particle, biomass or polyethylene particle is labelled using a radioisotope, such as ^{18}F, positrons annihilate with local electrons, and emit many 511 keV γ-rays from the labelled particles. These 511 keV γ-rays are in pairs and each pair emits almost back-to-back.Theoretically, all γ-ray trajectories from a labelled particle should meet at a point where the labelled particle is within the resolution of the camera. The location algorithm operates through minimizing the sum of perpendicular distances to the various trajectories of the 511 keV γ-rays. To smooth the tracking, the γ-ray events detected within one second are usually divided into many sets. For a given set of events, the point that minimizes the sum of perpendicular distances to the trajectories will be close to the tracer. The trajectories passing further away from the tracer are regarded as corrupted events and discarded. The minimum-distance point is recalculated using the remaining subset. The iteration procedure continues until the location of the tracer is calculated using just the uncorrupted events from the tracer (Parker et al, 1993, 1997, 2008, 2009; Yang et al., 2006, 2008a; Fan et al, 2006a, 2006b).

For a selected set S of sequential trajectories $L_1,\ldots,L_N$, which are recorded from a tracer moving within the camera, the sum of distances from any point (x, y, z) to the γ-ray trajectories can be stated as follows

$$D_s(x,y,z) = \sum_s \delta_i(x,y,z) \tag{1}$$

where $\delta_i(x,y,z)$ is the distance of the ith trajectory from the point (x, y, z).

The minimum solution can be obtained by

$$\frac{\partial D_s(x,y,z)}{\partial x} = 0, \quad \frac{\partial D_s(x,y,z)}{\partial y} = 0, \quad \frac{\partial D_s(x,y,z)}{\partial z} = 0 \tag{2}$$

The minimum distance point (x_0, y_0, z_0) is then obtained as the first approximation for the tracer. The mean deviation of these trajectories from the minimum distance point is given by

$$d_s(x_0,y_0,z_0) = D_s(x_0,y_0,z_0) \Big/ N(S) \tag{3}$$

where $N(S)$ is the number of events in the set S. For a given set of trajectories, the first approximation (x_0, y_0, z_0) of the tracer is located using Eqs. (1) and (2), and the corresponding distance $\delta_i(x_0, y_0, z_0)$ of the ith trajectory to the point (x_0,y_0,z_0) is calculated. If the calculated $\delta_i(x_0, y_0, z_0)$ is larger than $kd_S(x_0, y_0 ,z_0)$, the trajectory is discarded, leaving a new subset S_1, in which the number of corrupted events is smaller. An improved location (x_1, y_1, z_1) with a small mean deviation $d_{S1}(x_1, y_1, z_1)$ is then calculated from this subset S_1 of events. The algorithm proceeds by iteration in this way, selecting subsets S_2, S_3, S_4 etc. The k in $kd_S(x_0, y_0, z_0)$ is a fixed parameter and determines the rate at which trajectories are discarded. The optimum value of the k normally lies somewhere between 1 and 1.5. The final outcome is that the subset S_F of trajectories is selected from the original set, from which the location of particle, during the time interval covered by this subset, is calculated as its minimum distance point (x_F, y_F, z_F). Each event L_i has its time of measurement t_i recorded, and the location thus arrived at is considered to represent the particle's position at time

$$t = \frac{1}{N_F} \sum_{S_F} t_i \tag{4}$$

where $N_F \equiv N(S_F)$ is the number of trajectories in the final subset S_F.

Having located the particle once, the new set starts immediately from the end of the previous set. Despite being discarded as corrupt, these events actually correspond to later particle positions, and are thus involved in the subsequent set. The final data will provide the tracer locations against the time in three dimensions (x, y, z). Typically, a radioactively labelled tracer can be located 100-200 times per second. The velocity of a tracer $\boldsymbol{v}_i = (v_{x_i}, v_{y_i}, v_{z_i})$ during the time interval between locations (x_i, y_i, z_i, t_i) and $(x_{i+1}, y_{i+1}, z_{i+1}, t_{i+1})$ is given by

$$v_{x_i} = (x_{i+1} - x_i)/(t_{i+1} - t_i) \tag{5}$$

$$v_{y_i} = (y_{i+1} - y_i)/(t_{i+1} - t_i) \tag{6}$$

$$v_{z_i} = (z_{i+1} - z_i)/(t_{i+1} - t_i) \tag{7}$$

The tracer speed is given by

$v_{x_i} = (x_{i+1} - x_i)/(t_{i+1} - t_i)$, etc.

The tracer speed is given by $v = \sqrt{v_{x_i}^2 + v_{y_i}^2 + v_{z_i}^2}$ (8)

An improved technique has been developed to track up to three particles (Yang, et al, 2007a, 2008b). To track multiple particles, the tracers are labelled at different levels of radioactivity. The tracer with the highest data logging rate is found first by using the single particle tracking technique, while the trajectories from the remaining tracers are regarded as corrupt trajectories.

After the tracer with the highest data logging rate is located, trajectories passing close to the located tracer are removed from the dataset. The locations of the second and the third tracers are calculated in a similar way. The data logging rate was calculated by (Yang et al 2007b)

$$\frac{\psi(x, y.z)}{\psi_0} = [1 - 2(\frac{x}{Dx})^2][1 - 2(\frac{y}{Dy})^2][1 - 2(\frac{z}{Dz})^2] \tag{9}$$

where $\psi(x, y, z)$ is the number of trajectories passing close to the location (x, y, z), ψ_0 is the number of trajectories at the centre (x_0, y_0, z_0), and ψ_0, D_x, D_y and D_z are determined for a particular nuclide and scattering environment. The fraction of valid trajectories is calculated by

$$f(x,y,z) = \frac{number\ of\ valid\ trajectories}{sample\ size} \tag{10}$$
$$= f_0[1-0.5(\frac{x}{Dx})^2][1-0.5(\frac{y}{Dy})^2][[1-0.5(\frac{z}{Dz})^2]$$

where *Dx, Dy and Dz* are the same as mentioned above, and f_0 is the fraction of valid trajectories at the centre (x_0, y_0, z_0) of the field of view. The data logging rate changes significantly from the centre towards the edges of the detectors for the camera used. When three particles are freely moving within the camera view, the data logging rates are not always in line with tracer's radioactivity. For instance, when the weaker tracer is at the centre and the stronger tracer towards the edges of the detectors, the stronger tracer might have a lower data logging rate than the weaker tracer. The stronger tracer with a higher g-ray density does not always result in a higher data logging rate and cannot always be found first, causing loss of track. An algorithm is developed by Yang et al (2007a, 2007b) to identify the tracers by taking account of the variation of the data logging rate in the field of view of the detectors, rather than by simply comparing the numbers of valid trajectories in the located positions.

2.3.2 Tracer Labelling

Two types of tracers have been used for positron particle tracking, liquid tracers for mapping the dynamic behaviour of fluids, particle tracers for mapping both of fluids and particulate materials. The techniques used for labelling liquid tracers are similar to that used in nuclear medicine study.

2.3.2.1 Radioisotopes Used in Tracer Production

The positron sources used in PEPT work are radioisotopes which emit γ-ray mostly with 511 keV energy. When material is labelled using this γ-ray emitter, the trajectories of the back-to-back 511 keV γ-ray pairs join at the point where the tracer is. The Birmingham camera can therefore locate the tracer's position in 3D and further reconstruct the velocity and distribution of the labelled material within the experimental region. A large number of radioisotopes, having half-lives ranging from minutes to days or years can potentially meet this requirement. However, considering the experimental timescale and the application of PEPT in mixing of powder or paste, and multi-phase flows, it is not realistic to separate the radioactive materials from the bulk and recover it after a test. The half-life of the radioisotope should be necessarily short to avoid persistent radioactivity in the test object to avoid the problem of subsequent decontamination, but long enough to enable detection over the timescale of study. The radioisotopes used in Birmingham Imaging Centre are ^{68}Ga, ^{22}Na, ^{18}F, ^{124}I, ^{61}Cu and ^{64}Cu. Among them ^{18}F is the most frequently used one (Fan et al. 2006a, 2006b, 2006c). ^{18}F does not emit any γ-rays other than the 511 keV annihilation photons. Its half-life is 109 minutes and is suitable for most experimental timescales. The tracer labelled using ^{18}F gives about 74% valid events in total and a high accuracy of detected locations. ^{18}F has been produced from either purified water or solid materials via reactions ^{16}O(^{3}He, p)^{18}F and ^{16}O(^{3}He, n)^{18}Ne$\rightarrow$^{18}F under direct bombardment using a 33MeV ^{3}He beam from the Birmingham Radial Ridge Cyclotron. The ^{18}F produced from solid materials is a structural element of the solids, and chemically binds to other structural elements of the solid, such as Si-^{18}F in silicate. The ^{18}F produced from water is in freely ionic state, and can be adsorbed to organic or inorganic materials via ion-exchange or surface adsorption. The water used is

firstly distilled from tap water, then deionised. After this procedure, the purified water has a resistance of 18.2 MΩ.cm and a surface tension of 72.8 m Nm^{-1}. A specially designed target is made of titanium or silver, to hold the purified water under the beam coverage. After bombardment using a 33 MeV ^{3}He beam at a current of 10μA for 30 minutes, the specific radioactivity of the water is 15-18 mCi/ml, which is measured 20 minutes late after the bombardment to let the short lived isotopes decay (Fan et al. 2006a, 2006b).

2.3.2.2 Particle Tracer Labelling Methods

Direct Activation Method

This method is used to produce a particle tracer with a size grater than 500μm. The particles are held under the beam coverage in a target by drilling several holes on an aluminium-back plate according to particle sizes. The front of the target is sealed using aluminium foil and the back is cooled using mains water. After the bombardment using a 33MeV ^{3}He beam from a cyclotron at a currency of 10μA, the oxygen component in the particles will be converted into ^{18}F radioisotope. Meanwhile, some short-living radioisotopes are produced from other structural elements of the materials, such as ^{10}C (half-life 19.3s), ^{12}N (half-life 11 ms), ^{27}Si (half-life 1.16s), ^{29}P (half-life 4.1s) and ^{26}Al (half life 6.4s). Due to the rapid decay of the short-living isotopes, the majority of radioactivity serving for the PEPT work is from ^{18}F after 20 min "cooling". The ^{18}F in the labelled materials exists as a structural element within a layer approximately 0.3 mm deep. It is hardly replaced by the ions existing in experimental systems, and is hardly worn during the experimental environments. The radioactivity (A) achieved in a single particle via direct activation is determined by the irradiation time, the electrical current on the target and the cross-sectional area of the particle as shown in Equation 11.

$$A = f_0(I, S, t) = f(I, d^2, t) \tag{11}$$

where: *A* is the radioactivity achieved in a single particle (μCi), I is the electric current on the target (μA), *S* is cross-sectional area of the particle (mm^2), *d* is the particle diameter (mm), *t* is the irradiation time (min). Figure 2. presents the radioactivity achieved in glass beads (SiO_2) with a size range from 300 to 4000μm. The irradiation time was 60 minutes, and the electrical current in the target was 10μA.

The results indicate that, at a fixed irradiation time and a fixed electrical current on the target, the radioactivity achieved in a single particle was proportional to the square of the particle diameter. Direct activation can only be used to label materials with a size greater than 500 μm. If the tracer particle size is less than 500 μm, the radioactivity is not enough to cover most experimental timescale.

Another limitation of direct irradiation is the temperature resistance of the particles because the bombardment produces a high temperature (Fan et al. 2006a). The advantage of this method is that the tracer can be produced from materials that are identical to the bulk population in their physical and chemical properties.

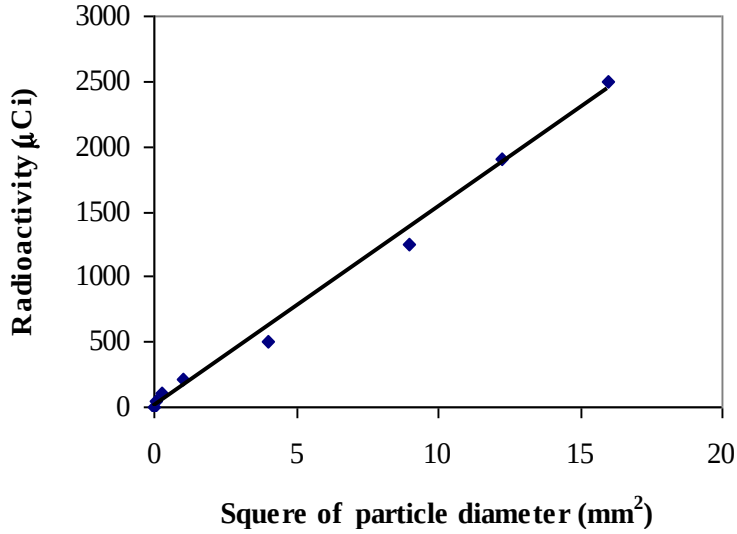

Figure 2. Effect of particle size on radioactivity achieved via direct irradiation (33MeV ^{3}He beam at a target current of 10mA for 60 minutes) (Fan et al, 2006a).

Ion-Exchange Method

To make a particle tracer with a size less than 500 μm, ion-exchange technique is employed. Two kinds of anion exchange resins, weak base anion exchange resin and strong base anion exchange resin, can be potentially used to adsorb ^{18}F ions from radioactive water (Harland, 1994).

The uptake of ^{18}F in weak base anion exchange resin is strongly controlled by the water pH. The free base amines in weak base anion exchange resins, e.g. $RCH_2N(CH_3)_2$, interact with water and form $RCH_2NH(CH_3)_2^+OH^-$, in which the OH^- performs as a counter ion. But the dissociation of the "hydroxide" form is very weak, and any significant concentration of hydroxide ions in water would immediately convert the resin back to the undissociated free base form ($RCH_2N(CH_3)_2$) as shown in Equation 3, resulting in the loss of the anion exchange capacity.

Also the affinity of ^{18}F ion to a weak base anion exchange resin is much weaker than the affinity of hydroxide ions. Therefore, the ^{18}F adsorption in the weak base anion exchange resins only can perform at a very low pH value (Fan et al. 2006a).

$$RCH_2N(CH_3)_2 + H_2O \Leftrightarrow RCH_2NH(CH_3)_2^+OH^- \text{ (Weak dissociation)} \quad (12)$$

Strong base anion exchange resins is less affected by water pH or hydroxide ions than weak base anion resins since the affinity of ^{18}F ion to a strong base anion exchange resin is stronger than the affinity of hydroxide ions.

The strong base anion exchange resins used here are quaternary ammonium derivatives and are usually provided in chloride form, such as $R\text{-}CH_2N(CH_3)_3^+Cl^-$ or $R\text{-}CH_2N(CH_3)_2(CH_2CH_2OH)^+Cl^-$, where; R is the organic backbone, $-CH_2N(CH_3)_3^+$ and $-CH_2N(CH_3)_2(CH_2CH_2OH)^+$ are functional groups and Cl^- is the counter ion. However, the resin in chloride form cannot be directly used to adsorb ^{18}F from radioactive water, because

the affinity of the ^{18}F ion to the functional groups in the resins, such as ($-CH_2N(CH_3)_3^+$ and $-CH_2N(CH_3)_2(CH_2CH_2OH)^+$), is much weaker than the affinity of the Cl^- ion as shown in the affinity subsequence below (Harland, 1994). The resin particles must be converted into fluorine form or hydroxide form before use as shown in Equations 13 and 14. Affinity subsequence of anions to a strong base anion exchange resin:

$$SO_4^{2-} > HSO_4^- > I^- > NO_3^- > Br^- > Cl^- > HCO_3^- > HSiO_3^- > F^- > OH^-$$

$$R\text{-}CH_2N(CH_3)_3^+Cl^- + OH^- \Leftrightarrow R\text{-}CH_2N(CH_3)_3^+OH^- + Cl^- \quad (13)$$

$$R\text{-}CH_2N(CH_3)_3^+Cl^- + F^- \Leftrightarrow R\text{-}CH_2N(CH_3)_3^+F^- + Cl^- \quad (14)$$

To convert a strong base anion exchange resin from chloride form to fluoride form, the resin slurry was poured into a glass column with a glass frit of porosity 80 μm, and eluted with 8-10 bed-volumes of 1 M KF solution, then was rinsed with 10 bed-volumes of deionised water. After the conversion, F^- ions acted as counter ions rather than Cl^-, and can exchange with ^{18}F ions in radioactive water under certain conditions (Fan et al. 2006a)

The radioactivity achieved in a single resin particle depends on the ion-exchange capacity of the resin material, particle size, stirring or shaking time, ^{18}F concentration and water quality.

For strong base anion exchange resin, the affinity of fluorine ion is just greater than OH^- as shown in the affinity subsequence, and any other anion can replace ^{18}F from the resin beads, resulting in the loss of the radioactivity in tracer particles. In tape water, Cl^- and HCO_3^- are unavoidable. Therefore water purification is essential. Water used in this method was distilled and then deionised. Figure 3. presents the effect of stirring time on the achieved radioactivity in resin particles (Fan et al, 2006a). The experiment was carried out in a 6-ml glass vial.

The total radioactivity in the water was 2043 μCi at the beginning of the experiment. The total amount of resin particles, in mass, was 1.2mg. The results indicate that the radioactivity achieved in resin particles not only depended on the exchange rate of ^{18}F, but also depended on the decay rate of ^{18}F.

During the first 15 minutes, the ^{18}F exchange rate was much greater than the decay rate and the total radioactivity accumulated in resin beads increased greatly with the shaking time. With increase of ^{18}F concentration in the resin particles, the ^{18}F exchange rate slowed down and was close to ^{18}F decay rate, the total radioactivity in resin particles increased very slowly. After 25 minutes, the decay rate was greater than ^{18}F exchange rate, the total radioactivity in resin particles started to decrease.

Therefore the shaking time should be properly controlled and optimised in order to achieve a maximum radioactivity in tracer particles. Table 1. presents the radioactivity achieved in a single resin bead using the ion-exchange technique.

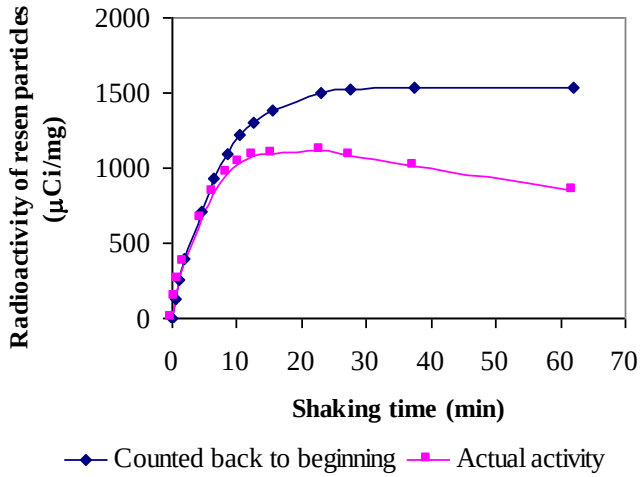

Figure 3. Effect of shaking time on the radioactivity accumulated in resin particles (Fan et al., 2006a).

Table 1. Radioactivity achieved in a single resin particle. (Fan et al, 2006a)

Particle size (μm)	600	212-250	130	60-70
Activity (μCi)	1500	800-1000	400-450	350

The advantage of the ion exchange method is that the resin particles possess a high fluorine ion exchange capacity, and tracer size can be made smaller (60μm). However, the material of the ion-exchange resin is an amine polymer. The density, shape and surface property of resin tracers may not be identical to the materials used in all PEPT experiments.

Surface Modification

Surface modification is an important method that has been used to improve the selective adsorption of chemicals onto particular surfaces in various areas. In tracer labelling, surface modification was carried out via chemical activation using metallic ions. Through this technique, the ^{18}F adsorption onto solids can be significantly improved, leading to a considerable extension in the range of materials which can be adequately labelled (Fan et al, 2006b).

In this process, metallic ions are firstly introduced to the solid surfaces as active sites, and then anions bind with the metallic ions on the solid surfaces. After the modification of solid surface chemistry, the adsorption of ^{18}F can be significantly improved as shown in Figure 4. For example, under the optimised experimental conditions, the radioactivity adsorbed in a single particle increased from 67 to 600 μCi for hydroxyapatite, from 2 to 400 μCi for quartz and from 2 to 152 μCi for polyethylene.

We do not exactly know how the metallic ions improve the adsorption of ^{18}F onto the solid surfaces. A possible explanation could be that the adsorbed metallic ions alter the surface charges of quartz and microcrystalline cellulose (MCC), or act as bridges.

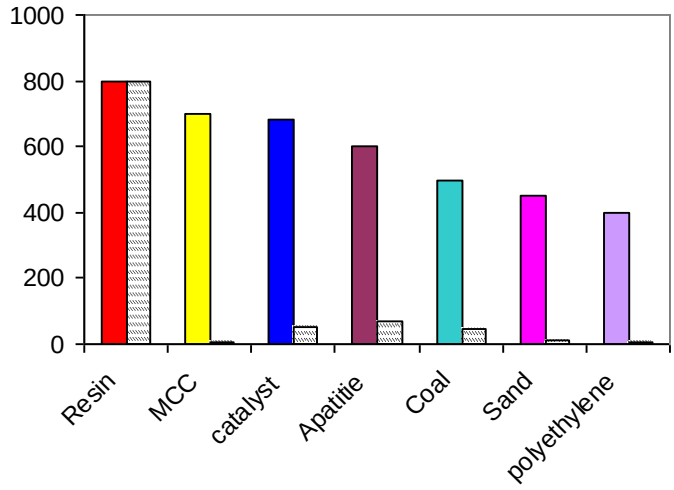

Figure 4. Radioactivity labelled in a single particle using surface modification technique (particle size: 212–250 μm). (Fan et al, 2006b).

For example, quartz interacts with water and forms a saline group in aqueous solution, therefore bearing a negative zeta potential above pH 2.6. This zeta potential decreased with increasing the pH of the aqueous solution and reached about −100mV at pH 11.5. After the modification, the metallic ions were adsorbed onto quartz surfaces, and the quartz zeta potential increased by about 30 mV over the whole pH range. The increase of quartz zeta potential could result in the impact of more $^{18}F-$ anions into the surface double layer of the solids. The adsorption of metallic ions on solid surface also enhances the adsorption of hydroxides. The adsorbed hydroxides are further replaced by ^{18}F therefore the radioactivity labelled in a single particle increase significantly.

3. BUBBLING FLUIDIZATION

Bubbling fluidization has been seen as an effective means for providing good solid mixing, solid-gas contact, and good heat transfer (Salman et al, 2007; He et al. 2004; Bokkers et al. 2004). These attractive features are achieved by injection of air to create a bubble flow via a perforated or porous surface through the solid beds. Solid particles in a fluidized bed are supported with a gas flow via a perforated or porous surface so that its weight is supported, and it exhibits some of the characteristics of a fluid-like material. The fluidisation quality of a bed is highly dependent on solid flow structure, bubble distribution and bubble physical properties in a bed. Ideally, for there to be good quality fluidisation the population of bubbles in a bed should be large, but the bubbles should be small in size, and homogeneously occupy the bed (Shibata et al, 1991; Leaper et al., 2004; Lim et al., 2006; Lim et al., 2007). High bubble population and small bubble size give a good gas-solid contact. Numerous factors within a fluidisation system can significantly affect the microscopic and macroscopic flow behaviour, such as interactions between suspended and packed particles, suspended particles and column wall, gas and particles, and gas and column wall (Seville, 2000, Kafui et al., 2002, Ding et al., 2005, Huang et al., 1999, Smolders and Baeyens, 2001).

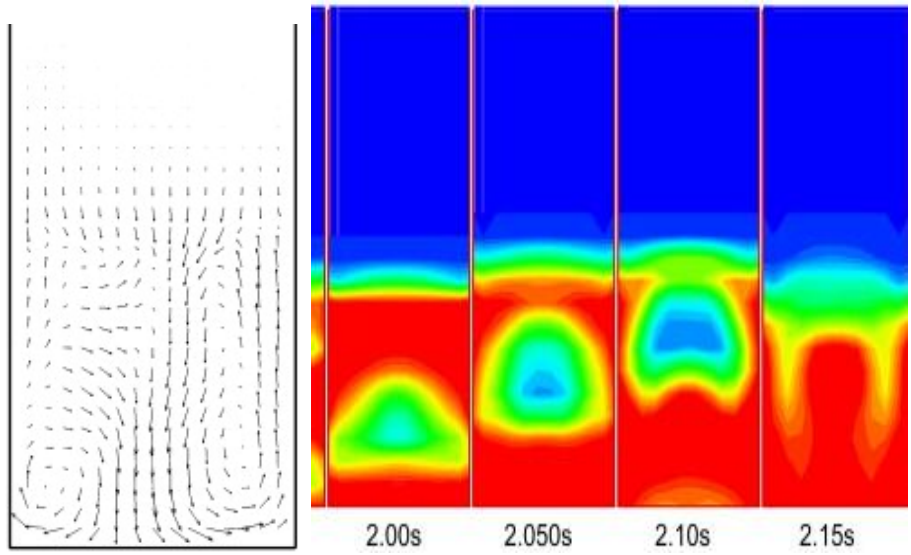

Figure 5. Typical flow structure predicted by using empirical models (Dan, et al, 2009; Wang et al, 2010).

The relative importance of these interactions further depends on the operating conditions, ratios of particle sizes to the column diameter, configuration of the flow system, and solid properties etc; therefore making fundamental theoretical analysis of the hydrodynamics difficult and in some cases almost impossible (Ding et al., 2006, Cooper and Coronella, 2005). For example, to predict solid motions and flow structures using discrete element models, the collision and friction between particles are dominated by many factors, such as: density, elasticity, surface roughness and shape of solids, static electricity, moisture, as well as the local solid concentration. Even though significant progress has been made, many uncertainties still remain, i.e. how does each of the above factors affect the solid and gas motion? How to evaluate the predicted flow patterns based on an empirical approach (Lu et al., 2006, Li and Kuipers, 2005, Baron, 1990)? The typical flow structures predicted by models are shown in Figure 5. It cannot reflect all of situations in a bubbling fluidized bed. In this section, we will introduce our newly findings on bubbling flow structure, solid, gas behaviour and solid mixing in a bubbling fluidized bed (Fan et al., 2007, 2008, 2011, Link et al. 2008).

3.1. Solid Flow Structure in a Bubbling Fluidized Bed

A literature search shows that solid flow patterns in bubbling fluidised beds vary mainly with the bed height (Kunii, Levenspiel, 1991, Duursma et al. 2001]. Solids travel upwards either along the annulus or along the central part of the bed, inducing two circulation cells within the whole bed as shown in Figure 5. However, the observation through PEPT measurements shows that solid flow pattern can vary significantly with the bed materials and gas velocity. Three types of flow patterns have been observed in our studies on glass beads,

catalysts and polyethylene fluidised beds, where the ratio of the bed height to the bed diameter is unity to 3, and the superficial gas velocity was from 0.16 m/s to 0.66m/s.

3.1.1. Effect of Gas Velocity on Flow Structure

The experiments presented here were carried out in the bubbling regime at three different superficial gas velocities, 0.30, 0.48 and 0.63 m/s. The bed materials are polyethylene particles. The particle size of the polyethylene was ranged from 500 to 1200μm, in which 87% of them were greater than 710 μm. The results indicate that the circulation pattern varied greatly with the superficial gas velocity, which can be distinguished by the circulation cells and the observed patterns of solids motion. At a lower gas velocity (0.30m/s), there was only a single large vortex observed within the whole bed, and solids circulated in the vortex from the bottom to top of the bed as shown in Figure 6.a. We named this flow structure as Pattern A. This may not be a desirable flow pattern, but reflects the effect of superficial gas velocity on the solid flow in the fluidized bed. The mean particle flow was predominantly upward on the left-hand side of the bed (Figures 6.a. and 9.a) followed by discharge into a splash zone in which the particles exhibited a fast horizontal displacement from left to right. On the right-hand side of the bed, the particle flow was predominantly downward, as a return flow. The core of the vortex was near to the bed centre where particles moved slowly in an axial direction. A similar observation has been reported by Mostoufi and Chaouki (2004). However, the interesting phenomenon observed in our investigation (Figure 6.b) is that solids moved towards the interface of upflow and downflow from all the directions in the core region. This indicates that there was a solid exchange between the portion travelling upwards and the portion travelling downwards. The solid exchange between these two groups would enhance particle mixing and heat exchange within the bed. We cannot directly observe the image of bubbles or voids in the bed through the obtained data, but from the vector maps the ascending gas channel appear to be located at the left side of the vortex where the velocity vector of particles took the same direction as y-axis as shown in Figures 3.a. and 6.a. The bulk upward bubbles moved along the left side of the bed and induced this vortex structure.

Figures 7, 8 and 9 present the time-averaged velocity vector maps for the experiments running at gas velocities of 0.48 and 0.63 m/s, respectively. The bed materials are polyethylene. We named this flow structure as Pattern C. The results indicated that the flow structure became more complex as the gas velocity increased. Macroscopically, the number of solid circulation cells in plane view increased from one to four when the superficial gas velocity increased from 0.30 to 0.48 m/s, and then further increased to five or more at a gas velocity of 0.63 m/s. At a gas velocity of 0.48 m/s, four vortices (circulation cells) can be observed in the vertical plane. Two persistent vortices of UWDC (Duursma et al. 2001) sense (upward at the wall, downward at the centre) were located just above the air distributor surface, and the others were horizontally aligned at the top of the bed (Figure 7.a).

Considering these data, the fluidised bed can be seen as three different regions. The flow near to the air distributor (0-30mm) was much more ordered and the solids moved relatively fast from bed centre towards the column wall at horizontal directions (Figures 7.a, b) and then circulated from the bed wall towards the central zone at a bed height of 40-50 mm (Figures 7.a, c). This indicates that a jet of gas at a high velocity entered the bed bottom and expanded along the wall rather than straight upwards through the centre. The air drove the solids to a bed level of 50-60 mm along the annulus as shown in Figures 7.a, b and Figures 9.b, c. At the intermediate height of 60-100mm, the upward solid flow encountered the downward flow

from the top section of the bed at the annulus. The two solid flows merged and changed the direction towards the bed centre. The solids in this region were mixed and then divided into two portions. One of them was involved in the circulations at the bed bottom as a return flow, while the other was involved in the circulations at the top region. The heat and mass exchange were achieved by three different mechanisms. Within a circulation cell, the exchange can be achieved due to the internal circulations. In the intermediate height of the bed, the encounter of upflow and downflow at the annulus caused a chaotic motion of solids with no uniform flow direction, and the solids from the top and bottom sections met, and then randomly diverged into the top or bottom sections. By this mechanism, particles from the bottom of the bed were mixed with those from the top, and then redistributed to the four vortices. The bubbles or air streams ascending from the bed bottom were split and forced to shift to the central of the bed by the solid flow returning from top region. The split gas gave opportunity for gas-solid contact. Thirdly, solids also exchanged between the neighbouring vortexes. When the gas velocity increased to 0.63m/s, the flow structure was quite similar to the pattern at a gas velocity of 0.48 m/s as shown in Figures 8. The difference is that three solid circulation cells were horizontally aligned at the bottom region in plane view.

Figure 9. shows the velocity maps (V_y) of solids within a 30 mm layer immediately above the air distributor at different gas velocities. This view enables further understanding the variation of flow structure with respect to superficial gas velocities. This high velocity peak can be used to indicate the location of the main bubble path or ascending air stream. At a gas velocity of 0.30 m/s, the air bubbles ploughed and dragged the solids upwards along the left side of the bed, therefore inducing a large solid circulation within the whole bed. When the gas superficial velocity increased to 0.48 and 0.63 m/s, the velocity map (V_y) looks like a volcanic vent. This means that the air bubbles travelled upwards along the annulus, rather than through the central region of the bed. Overall, the flow structure within the studied bed depended on the gas velocity. At a gas velocity of 0.30m/s, the solid flow returned to the bed bottom and forced the air bubbles to rise from one side of the bed. At the gas velocities of 0.48 and 0.63m/s, the solids returned to the bed bottom through the central region, therefore the emission phase forced the air bubbles to rise along the annulus.

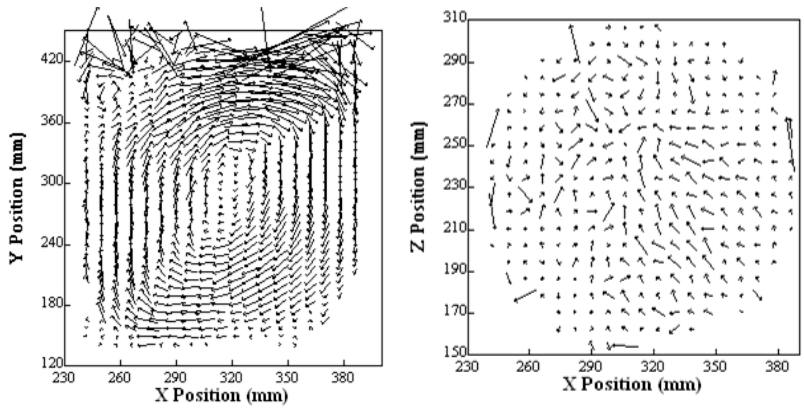

a. Vertical plane

b. Lateral plane, height: y=230-280mm

Figure 6. Time-averaged velocity vector map (pattern A) for the solid phase at Ug=0.30 m/s.

(This flow pattern is based on a data collection for two hours, but it can be observed for every 10-minute time interval)

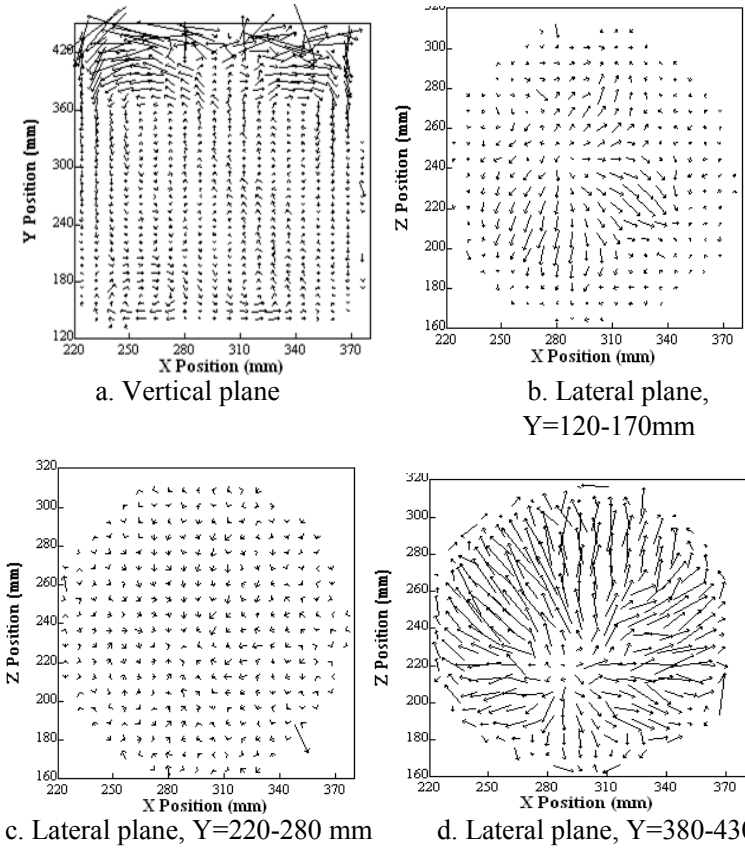

a. Vertical plane

b. Lateral plane, Y=120-170mm

c. Lateral plane, Y=220-280 mm

d. Lateral plane, Y=380-430mm

Figure 7. Time-averaged velocity vector map (pattern C) for the solid phase at U_g=0.48 m/s. (This flow pattern is based on a data collection for two hours, but can be observed for every 10-minute time interval).

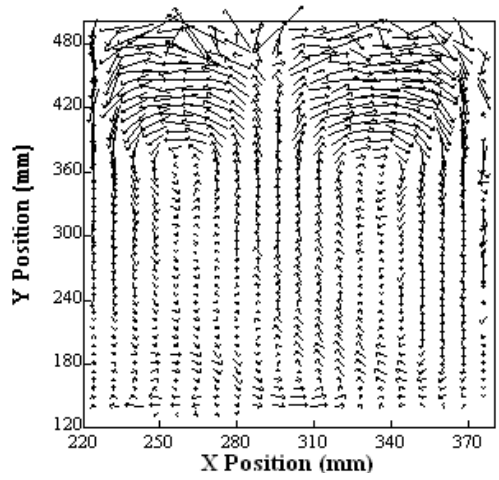

Figure 8. Time-averaged velocity vector map for the solid phase at U_g=0.63 m/s.

(This flow pattern is based on a data collection for two hours, but can be observed for every 10-minute time interval)

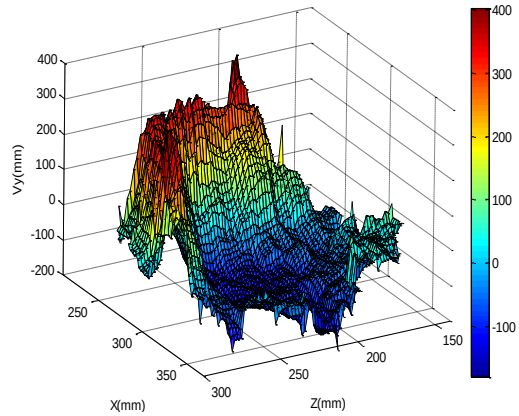

a. U_g=0.30 m/s (pattern A)

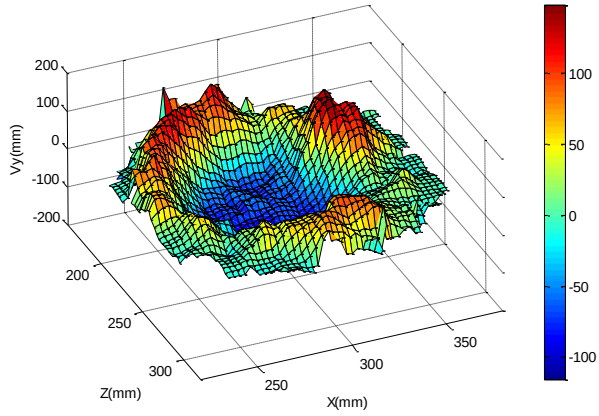

b. U_g =0.48m/s (pattern C)

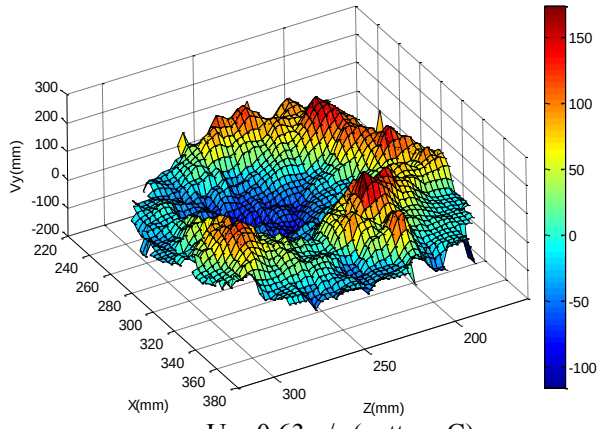

c. Ug=0.63m/s (pattern C)

Figure 9. Velocity map of solids within a layer of 30 mm immediately above the air distributor at different superficial gas velocities.

3.1.2. Effect of Particle Size on Solid Flow Structure

Figures 10-12 present the solids flow patterns for the glass beads with different size. The results show that the flow pattern varied significantly with the particle sizes. Three flow structures have been found when the bed was operated at the similar superficial gas velocity ($U-U_{mf}$ =0.4-0.42m/s).

For the glass with a size range from 700 to 1100 μm and an average size of 880μm, a large vortex can be observed within the whole bed and a small circulation cell can be observed at the top left. Solids circulated in the large vortex from the bottom to the top of the bed following the pattern as shown in Figure 10, which is similar to the flow pattern observed in a polyethylene bed operated at U_g=0.30 m/s. The mean particle flow was predominantly upward at one side of the bed followed by discharge into a splash zone in which the particles exhibited a fast horizontal displacement from right to left. On the other side of the bed, the particle flow was predominantly downward, as a return flow.

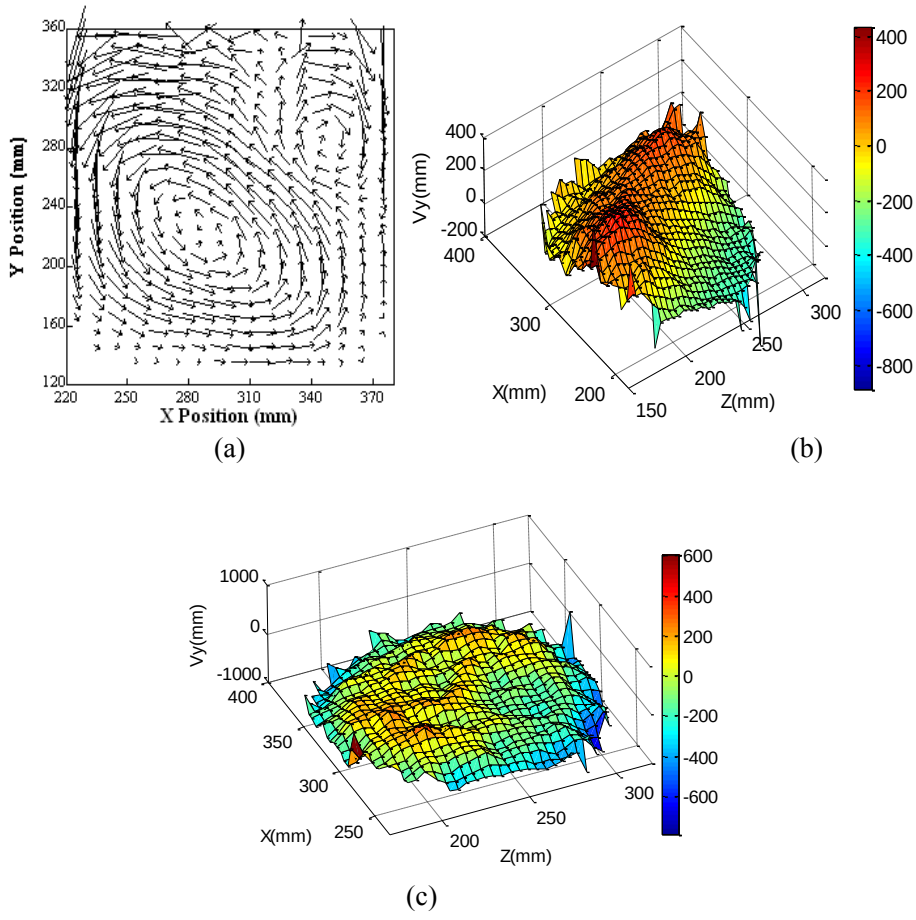

Figure 10. Flow patterns (pattern A) of glass beads with a size of 800-1000 μm. ($U-U_{mf}$= 0.40). (a) Time-averaged particle velocity vector map (b) Glass beads velocity V_y within a 10 mm layer at a height of 30 mm above the air distributor. (c) Glass beads velocity V_y within a 10 mm layer at a height of 190 mm above the air distributor (Fan, et al., 2011).

When the particle size was 250-500μm, more typical bed behaviour can be observed as shown in Figure 11. Solids moved straight upwards to the splash zone through the central region of the bed, and moved downwards along the annulus. Two circulation cells with a nearly equal size can be observed within the whole bed, and the core of the circulation cells were at a bed height from 120 to 200 mm (Fan, et al. 2011).

When the glass beads with a size range from 100 to 250 μm was operated at the similar superficial gas velocity of U-U_{mf} =0.4-0.42m/s (Figure 12), the solid flow in the bed followed the pattern C. The particles travelled upwards along the annulus and were then directed to the central region at an intermediate height of the bed by the solid flows returning from the top section of the bed. The flow pattern is similar to that observed in a polyethylene bed operated at U_g=0.48 m/s. The particles travelling in this manner induced four vortices within the bed. Two of them were located at the top region of the bed where a nearly spout bed was observed, and the others aligned just above the air distributor. In each vortex, solids experienced a local mixing. At an intermediate height of 60-100 mm, solids from all of the circulation cells merged and mixed, then redistributed to different circulation cells again (Fan, et al. 2007, 2011).

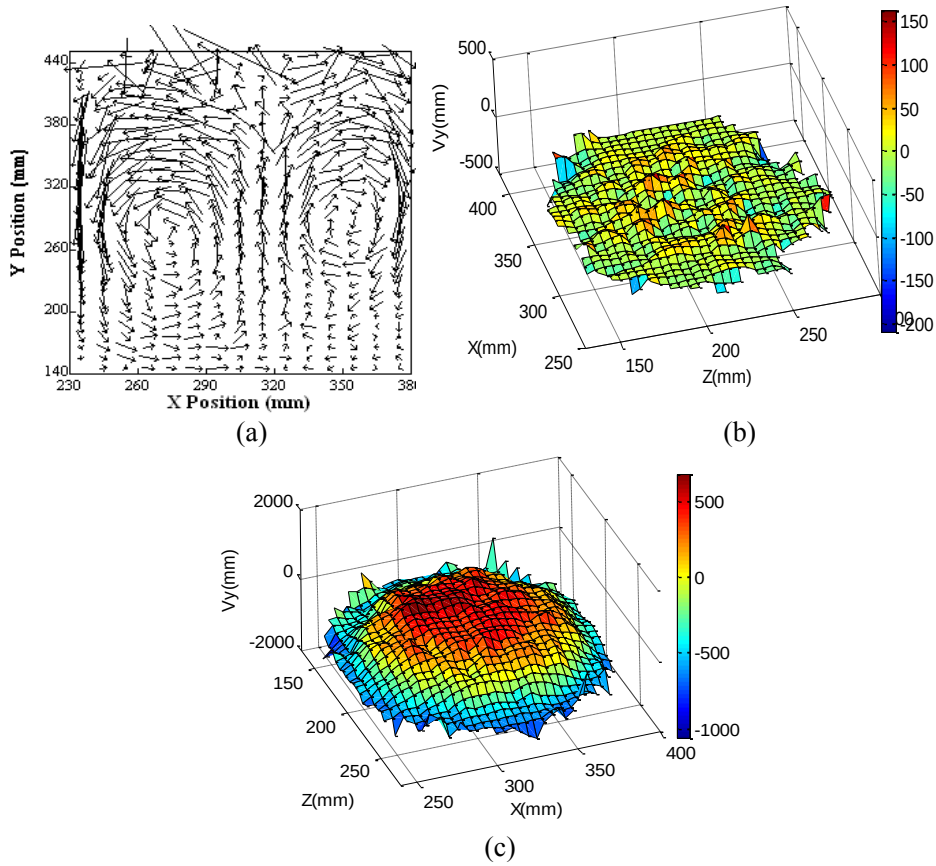

Figure 11. Flow patterns (pattern B) of glass beads with a size of 250-450 μm. (U-U_{mf}= 0.42), (a) Time-averaged particle velocity vector map (b) Glass beads velocity V_y within a 10 mm layer at a height of 30 mm above the air distributor. (c) Glass beads velocity V_y within a 10 mm layer at a height of 190 mm above the air distributor (Fan, et al., 2011).

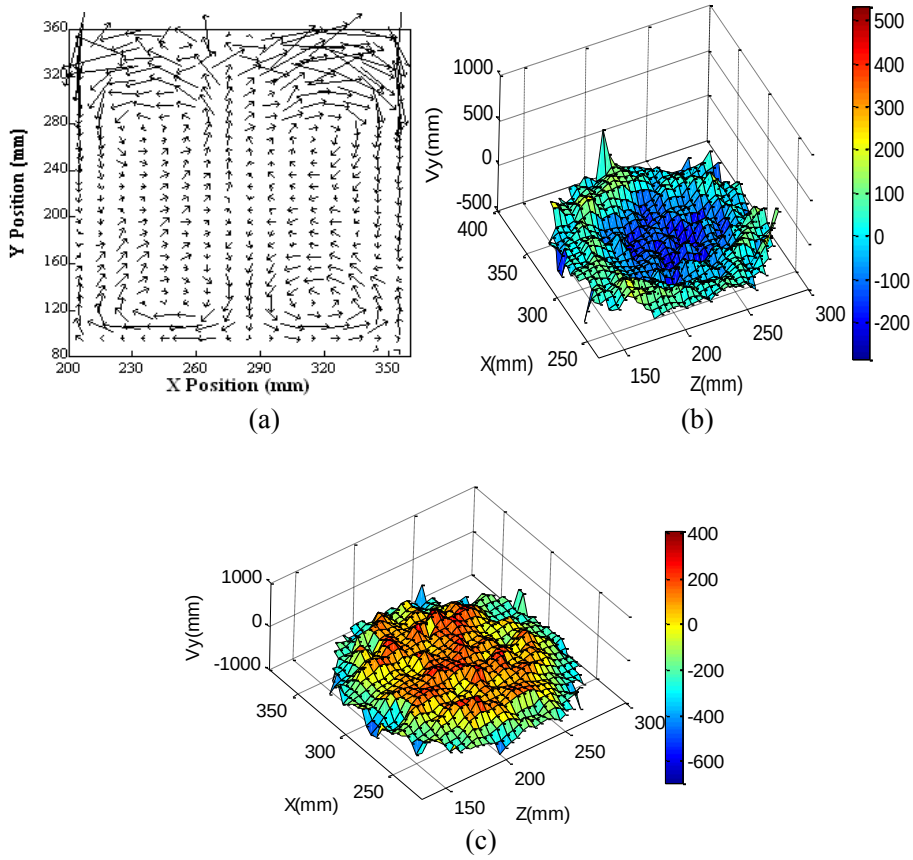

Figure 12. Flow patterns (pattern C) of glass beads with a size of 80-200 μm. ($U-U_{mf}$= 0.40), (a) Time-averaged particle velocity vector map (b) Glass beads velocity V_y within a 10 mm layer at a height of 30 mm above the air distributor. (c) Glass beads velocity V_y within a 10 mm layer at a height of 190 mm above the air distributor. (Fan et al., 2011).

3.2. Microscopic Behaviour of Solids within the Bed

Figure 13. presents typical trajectories of a labelled particle over a circulation cycle at different gas velocities. The particle motion agreed with the overall flow pattern very well. Figure 13.a. presents a recording of a tracer motion for 9 seconds for a polyethylene particle at a superficial gas velocity of 0.30 m/s (pattern A). The observation started from point A, at which the tracer was in the ascending stream. The tracer moved upwards with bubbles at the left side of the bed to the point B, and then did a circulation in the central region of the bed. The tracer trajectory was quite smooth in the central region and in the return flow, but moved in a rather tortuous manner in the ascending flow. This might be due to the difference in the solid concentration. The ascending region had a high concentration of gas and low concentration of particles. When the tracer travelled to the intermediate bed height (y=220-330mm), the air bubbles expanded and the solid concentration in the bubble wake was lower (Pallarès et al. 2006, Gao et al., 2006). Particles entrained in the bubble wake started to slip and picked up again by bubbles. The tracer trajectory from A to B is the first evidence which clearly showed the motion of an individual particle in bubble wake. The particle was dropped

and picked up by bubbles several times before it was dragged to the splash zone. This feature of solid motion in the ascending stream gives a good opportunity for particle redistribution throughout the region (Eames and Gilbertson, 2005). In the core region and the return stream, the solid concentration was higher, therefore the particles moved in block or cluster, and their trajectories were quite smooth. When the tracer particle circulated within the large vortex, the solids were not only transported in the vertical plane, but also migrated in the lateral plane (X-Z). The particle trajectory resembled a spiral. The displacement in lateral plane (X-Z) was much smaller in the main bubble path than in the core region and in the return stream. These data might give a qualitative indication of the convective lateral solids mixing. Within the main bubble path, solid mixing was mainly due to the slippery motion in the bubble wake, while the mixing achieved in the core region and return stream was mainly due to the particle drift. When the superficial gas velocity increased to 0.48 m/s for polyethylene particles, there were four circulation cells (pattern C) observed in the vertical plane, and the dynamic behaviour of a tracer particle was changed significantly as shown in Figure 13.b. These patterns were observed many times within the full data set and Figure 13.b. is just one example of the behaviour. The difference in each observation is that the tracer moved into one of the four circulation cells randomly when it was in the intermediate height of the bed, rather than always following the order as shown in Figure 13.b. This observation started from point A to point F for 13 seconds. The tracer travelled down from point A and circulated at bottom right of the bed to point B, where the ascending flow from bottom section encountered with the return flow from the circulations in the top section. The two solid flows met and particles were redistributed to different circulation cells. At point C, the tracer was picked up by the vortex at top right and circulated three times. At point D, the tracer moved into the vortex at top left, and then travelled down with a return flow from the splash zone. At point E, the particle had the same experience as at point B. The tracer was then transported to the vortex at bottom left from E to F and completed a large circulation within the whole bed. This would suggest that, the efficiency of mass and heat transfer should be much higher at this gas velocity (0.48m/s) in comparison with 0.30 m/s. At the top and bottom regions, particles experienced many circulations. In the intermediate height of the bed, the collision between the return flow and the upward flow provides a significant opportunity for reshuffle or redistribution of solid and gas.

When gas velocity increased to 0.63m/s, the solids motion became even more complex as shown in Figure 13.c, which presents a typical example of a completed cycle of the tracer moving from point A to point G. As discussed in section 4.2, there were five vortices in the plane view (Figure 8.a). Three of them were located at the bottom section of the bed, which corresponds to the particle circulations marked as B, C and D in Figure 13.c. The other two were at the top region which corresponds to the circulations marked as E and F. The tracer trajectory also agreed with the flow structure very well. At point A where the two solid flows encountered, the particles were redistributed to different circulation cells randomly.

Overall, the motion of solid particles in the fluidised bed followed specific patterns and was not “random” as might be deduced at first observation. The flow pattern and bed structure were dependent on the gas velocity and particle size. Three flow structures (Patterns A, B and C) have been observed as shown in Figures 5-13. At a lower gas velocity, for example 0.30 m/s for polyethylene particles, or at a high gas velocity but particle has a large size and density (glass beads with a size large than 600 microns), the pattern of particle motion was simple and followed a large circulation across the whole bed. In the ascending

stream, particles were slippery in the bubble wake, but underwent a smooth fluidisation in the return flow and in the core region due to the difference in solid concentrations. The major peculiarities at a higher gas velocity (0.48-0.63 m/s) or when catalyst particles have a size less than 200 microns, are that the system was highly dynamic. There were three dominant physical processes in the bulk of the bed that contributed to solid mixing. Solids circulated upwards along the annulus and downwards at the bed centre at the bottom section, while circulated upwards at the centre and downwards along the annulus at the top section. However, the time for a tracer to stay in each cell was changed randomly. In the intermediate high of the bed, the mixing was due to the collision of counter flows from bottom and top circulations. After the collision, the solids were redistributed to one of the circulation cells randomly.

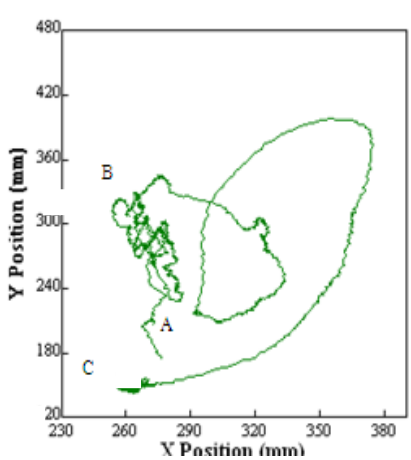

a. U_g=0.30

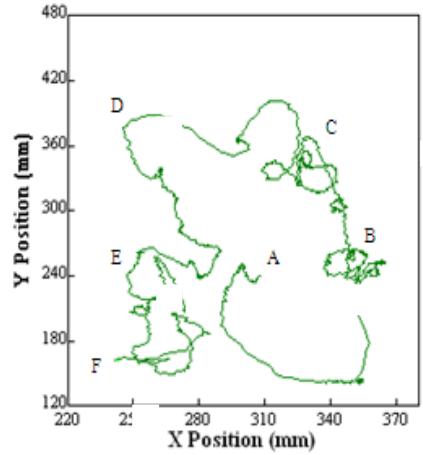

b. U_g=0.48

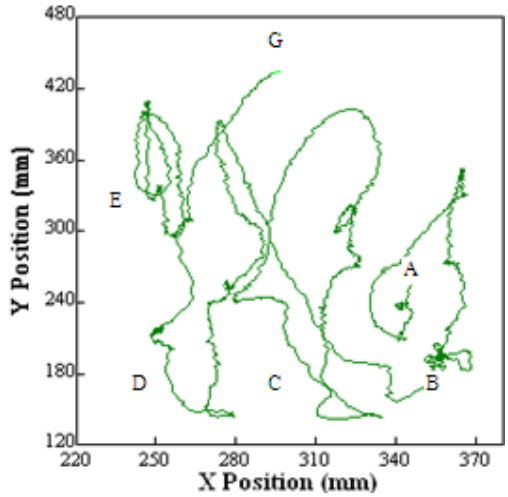

c. U_g=0.63

Figure 13. Projection of tracer trajectory over a cycle at different superficial gas velocities.

3.3. Solid Mixing

Figures 14-16. present the relative motions of two particles and their displacement profiles at different gas velocities. The results indicate that the relative motion and displacement between two labelled particles varied greatly with the flow structure, particle size and gas velocity. At a superficial gas velocity of 0.30 m/s (pattern A), the trajectories of the two labelled polyethylene particles were quite smooth and almost parallel in the descending flow, which is deduced from the variation of y values and their displacement as shown in Figure 14(a) and (b) Their trajectories in y-ordinate were mostly parallel and the displacement between the two particles changed slightly (Figure 14(b). A significant change in the displacement can be observed only when the particles ascended with air bubbles and in the splash zone. This again deduced from an increase in the y-ordinate with time (Figure 14.(a), and indicates that solids moved mainly in a block or a cluster in the return flow (or emulsion phase) at lower gas velocities. The time that the two tracers stayed in a cluster was typically 5-12 seconds. The contribution from this behaviour (cluster motion) to mass and heat transfer is often not as significant as that in the ascending flow and in the splashing zone. When the superficial gas velocity increased to 0.48 or 0.63 m/s (pattern C), the increase in circulation cells induced significant changes in tracer trajectories and the displacement between the two polyethylene tracers. From Figures 15(a) and 16.a, it can be seen that the tracers did not move in a parallel manner as had been observed at the lower velocity. The two tracers met and separated rapidly and did not stay in the same cluster or block for more than one second. Their position exchanged very frequently as shown in Figures 15(b). and 16(b) This exchange frequency could be used for directly estimating the mass and heat exchange within the bed. The fluidised bed can be divided into five regions for the flow pattern C, (comprising 4 vortices and the intermediate region of the bed). The solid motions followed specific patterns in each region. In each vortex, solids circulated and experienced a local mixing within the limited volume. The intermediate section of the bed was where solids from all of the vortices were mixed and then redistributed.

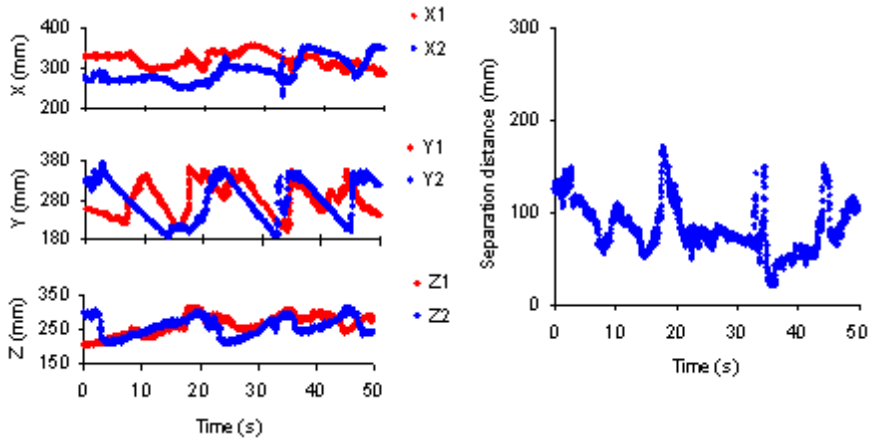

(a) Trajectories (b) Displacement between two tracers

Figure 14. Relative motion of the two moving polyethylene particles in pattern A at U_g= 0.30 m/s.

If particles, which are originally in the same region, are distributed to different regions, the particles have experienced not only a local mixing, but also a mixing with other portion of bed materials. The particles have been dispersed. The displacement between these particles can be seen as a "permanent displacement". The frequency for making this permanent displacement might be used as a direct measurement or practical estimates of mixing efficiency, and can be calculated based on the magnitude of the displacement between the two tracers using the obtained data. As shown in Figures 7.(a) and 8, the size of each region was not larger than 100 mm approximately in this study. If two particles are transported apart more than 120 mm which is 80% of the bed diameter and 50% of the bed height under a fully fluidization condition at a gas velocity of 0.30m/s, the particles have been mixed and distributed into different regions, and a permanent displacement has achieved.

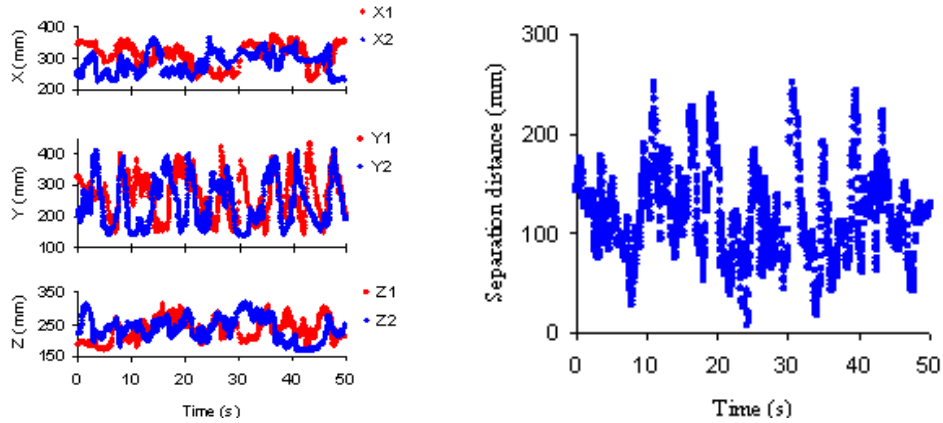

(a) Trajectories (b) Displacement between two tracers

Figure 15. Relative motion of the two moving polyethylene particles in pattern C at U_g= 0.48 m/s.

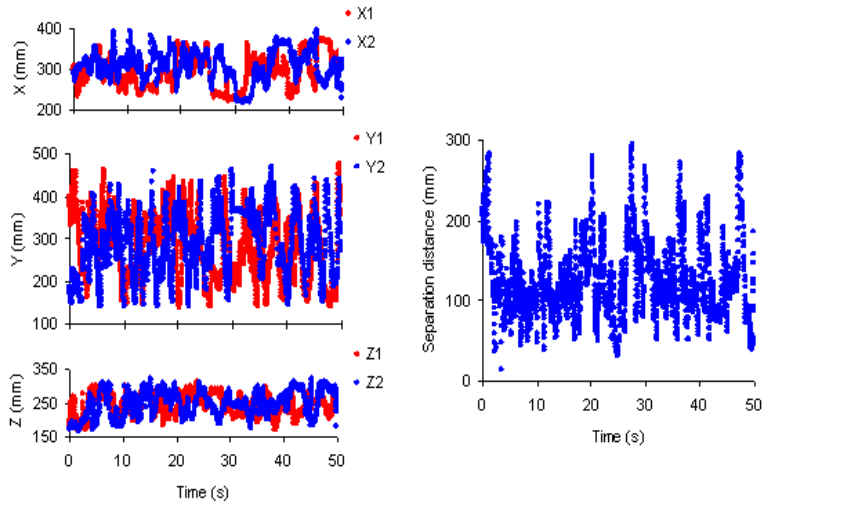

(a) Trajectories (b) Displacement between two tracers

Figure 16. Relative motion of the two moving polyethylene particles in pattern C at 0.63 m/s.

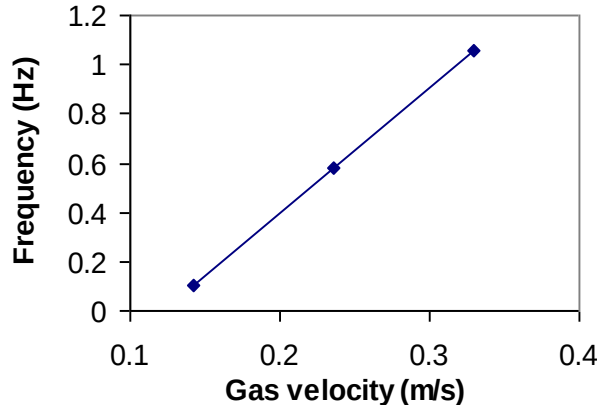

Figure 17. Frequency for making permanent displacement between two particles.

The results indicate that the maximum displacement increased from 180 mm to 300 mm and the frequency for making a permanent displacement linearly increased with superficial gas velocity as shown in Figure 17. It was increased from 0.1 to 1.1 Hz when the gas velocity increased from 0.30 to 0.63 m/s. A high frequency should be associated with a high efficiency in heat and mass transfer.

3.4. Bubble Flow Patterns

The bubble flow patterns in the studied fluidised beds can be disclosed through analysing the solid flow structure and the solid upward velocity map. As described earlier, the solids in a fluidised bed are driven upwards by air bubbles. The upward velocity (V_y) of solids is higher in the bubbles or their wakes than in the region away from the bubble path. The peaks of the V_y map of solids therefore correspond to the position of bubbles. Through plotting the V_y map at any level of the bed, the favoured ascending gas channels can be identified through the cumulative acquisition of large quantities of data during PEPT measurements.

Figures 18-20. show the solids V_y maps for the conditions under which the three solid flow patterns can be observed, where each experiment was lasted for two-hours. It can be seen that the favoured ascending gas channels vary greatly with bed materials and superficial gas velocity. Three patterns of bubble flows, corresponding to the three solid flow structures, have been observed in this study. In pattern A, the favoured channel of ascending bubbles was located at one side of the bed under the experimental conditions. As shown in Figure 18, there was not a single bubble that travelled upwards from the valley region within the two-hour experiment. The injected air was forced to one side of the bed by the returning flow of solids, inducing a large circulation cell within the whole bed. This pattern (A) was observed when the glass beads or polyethylene fluidised beds were operated at a low superficial gas velocity (U=0.40 m/s for glass beads, 0.34 m/s for polyethylene particles) (Fan et al., 2007, 2008). Pattern B of the bubble flow (Figure 19) was observed when the glass beads fluidised bed was operated at a superficial gas velocity ($U-U_{mf}$) of 0.42 m/s. The solid velocity V_y was relatively uniform within a 30mm layer immediately above the air distributor (Figure 19. a), then a peak in the V_y map was observed in the central region of the bed (Figure 19. b). This indicates that the bubbles distributed relatively uniformly in a layer close to the distributor.

The rising bubbles then moved inwards to the central region of the bed. This bubble flow pattern agrees with the observations from Grace and Harrison (1969) and Darton et al (1977), where the air bubbles are relatively uniformly distributed in a layer close to the distributor and then coalesced and shafted inwards to the central region of the bed with the increase in the bed height, resulting in the emptying of bubbles in the region near the walls (Fan et al., 2008). When the polyethylene fluidised bed was operated at superficial gas velocities ($U-U_{mf}$) of 0.25 m/s and 0.42 m/s, and catalyst with a size of 100-300 micron are fluidized at ($U-U_{mf}$) of 0.42 m/s, the bubble flow followed the pattern C. Air bubbles were favoured to form and initially travel upwards in the annulus of the bed, rather than being uniformly distributed in the whole cross section area. Figure 20.(a) shows that there was not a single air bubble that travelled upwards in the central region of the bed at the bottom section throughout the entire data collection period of two hours. The bubbles then moved inwards to the central region at an intermediate height of the bed (60-100 mm) by the solid flows returning from the top section of the bed as shown in Figures 20. (c) and (d). Above the intermediate layer, air bubbles travelled upwards from the central region of the bed and formed a peak in the V_y map as shown in Figures 20. (c) and (d). This agrees with the bubble flow pattern observed by Werther and Molerus (1973) and Lim et al (2007) in a planar fluidized bed.

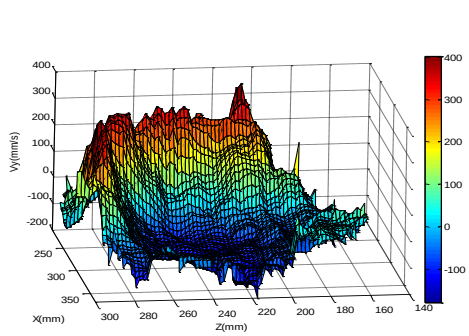

(a) bed height of 20 mm (y=160 mm)

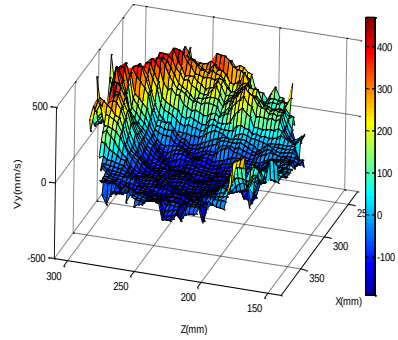

(b) bed height of 60 mm (y=200 mm)

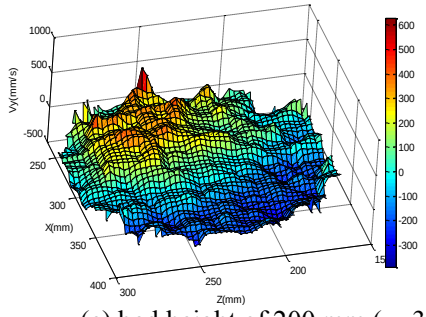

(c) bed height of 200 mm (y=340 mm)

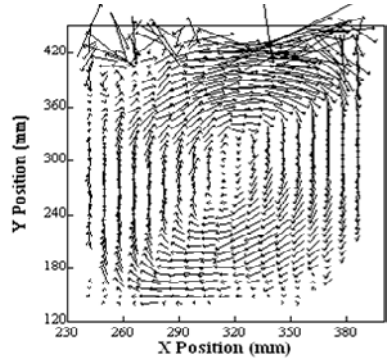

(d) Solid flow pattern

Figure 18. Bubble streams in flow pattern A. average velocity V_y within a 10 mm layer at a height of 20 mm above the air distributor. (b)average velocity V_y within a 10 mm layer at a height of 60 mm above the air distributor. (c) average velocity V_y within a 10 mm layer at a height of 200 mm above the air distributor. (d) Time-averaged particle velocity vector map.

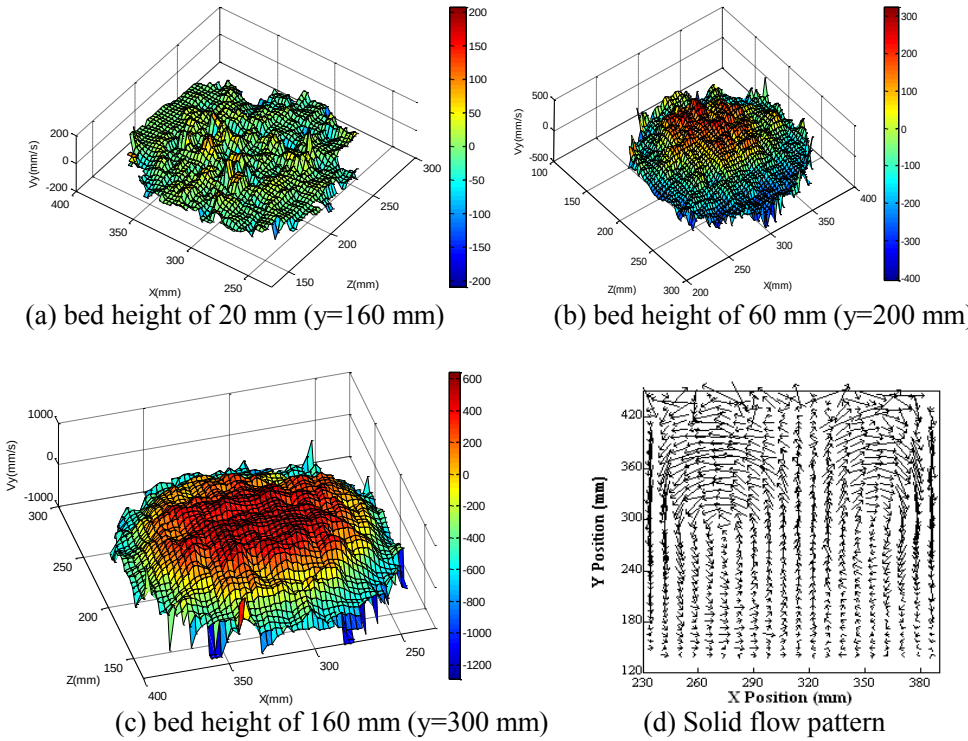

(a) bed height of 20 mm (y=160 mm) (b) bed height of 60 mm (y=200 mm)

(c) bed height of 160 mm (y=300 mm) (d) Solid flow pattern

Figure 19. Bubble streams in Flow pattern B. (a) average velocity V_y within a 10 mm layer at a height of 20 mm above the air distributor. (b)average velocity V_y within a 10 mm layer at a height of 60 mm above the air distributor. (c) average velocity V_y within a 10 mm layer at a height of 160 mm above the air distributor. (d) Time-averaged particle velocity vector map.

Overall, the favoured ascending gas channels within a bubbling fluidised bed varies not only with bed geometry and the ratio of bed height to bed diameter as described in literature (Kunii and Levenspiel 1991, Duursma et al., 2001), but also appears to vary with bed materials and superficial gas velocity. Under the similar operation conditions, different bed materials give a different gas/solid flow pattern.

3.5. Prediction of Bubble Velocity and Bubble Size

Several methods have been developed for the measurement of sizes and rise velocities of bubbles in fluidised beds. Many early measurements relied on submersible probe designs employing visible light or laser beam in 2-D beds to determine the bubbles.

X-ray and ultra-fast magnetic resonance imaging were developed later and used to study the rise velocities of bubbles non-intrusively in 3-D fluidising beds made of opaque materials (Fan, et al. 2008, Werther and Molerus 1973, Sun and Burgess 1987, Cai 1994, Burgess and Calderbank 1975).

In this section, the average rise velocities and sizes of bubbles in a fluidised bed are measured by using the data acquired by the non-intrusive PEPT technique.

3.5.1. Empirical Correlations

A number of empirical correlations have been proposed to predict the average rise velocity and the average size of bubbles in fluidised beds. Table 2. shows the correlations used most frequently for the prediction of bubble rise velocity proposed by Davies and Taylor (1950), Davison and Harrison (1963), Wallis (1969); Baeyens and Geldart (1974), Werther (1983) and Kunii (1991). Table 3. shows the correlations used most frequently for the prediction of bubble size proposed by Yasui and Johanson (1958), Whitehead and Young (1967), Rowe (1976), Darton (1977), Werther (1983), Mori and Wen (1975) and Cai (1994).

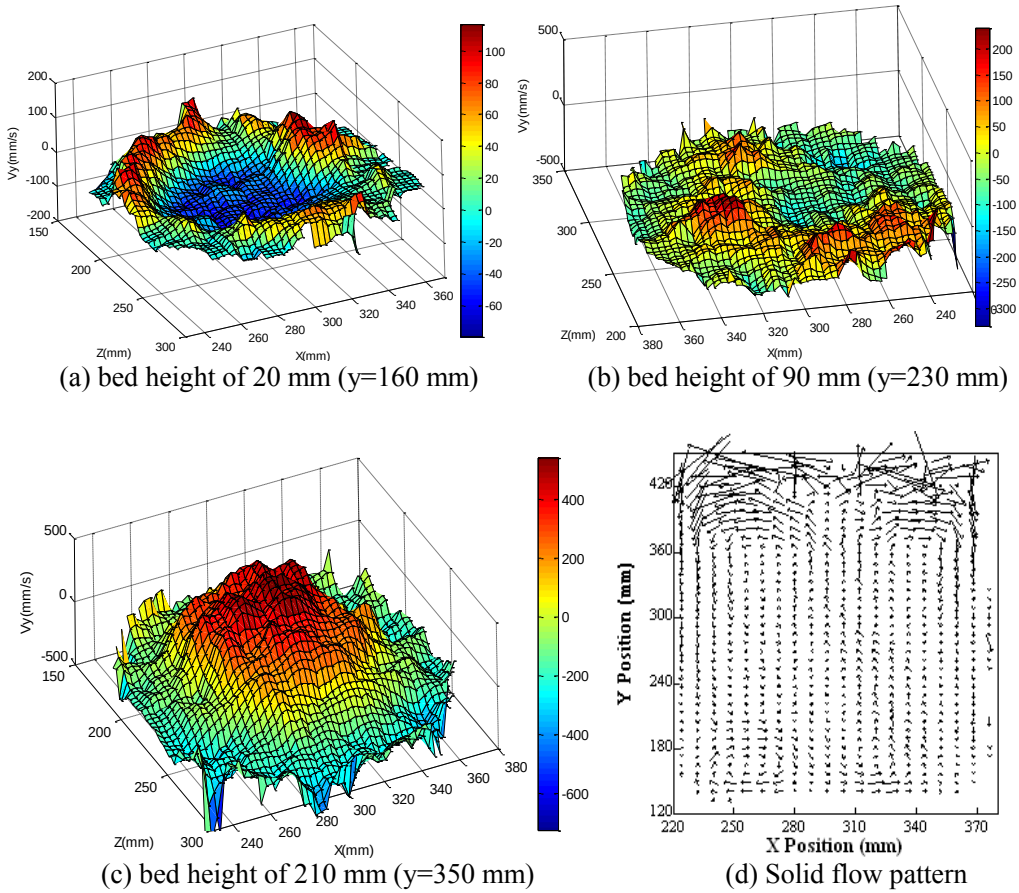

(a) bed height of 20 mm (y=160 mm)

(b) bed height of 90 mm (y=230 mm)

(c) bed height of 210 mm (y=350 mm)

(d) Solid flow pattern

Figure 20. Bubble streams in flow pattern C, (a) average velocity V_y within a 10 mm layer at a height of 20 mm above the air distributor. (b)average velocity V_y within a 10 mm layer at a height of 90 mm above the air distributor. (c) average velocity V_y within a 10 mm layer at a height of 210 mm above the air distributor. (d) Time-averaged particle velocity vector map.

Table 2. Correlations used most frequently for the prediction of bubble rise velocity (Fan et al., 2008)

Davies, Taylor	$U_B = 0.71\times\sqrt{gd_B}$	For an isolated bubble
Davison, Harrison	$U_B = U - U_{mf} + 0.711\sqrt{gd_B}$	simple two-phase theory
Werther	$U_B = (U - U_{mf}) + \phi(g \cdot d_B)^{0.5}$	For Geldart B particles, $\phi = 1.6D^{0.4}$, 0.1m < D < 1m
Wallis	$U_B = 0.71\times\sqrt{gd_B}\times 1.13\exp(-\frac{d_B}{D})$ For $0.125<\frac{d_B}{D}<0.6$	For $0.125<\frac{d_B}{D}<0.6$
Kunii	$U_B = 1.6[(U - U_{mf}) + 1.13d_b^{0.5}]D^{1.35} + 0.711(gd_b)^{0.5}$	for Geldart B solids D≤1m and $d_B/D<0.125$
Baeyens and Geldart	$U_B = \gamma(U - U_{mf}) + 0.711(gd_B)^{0.5}$ $\gamma = \frac{2.27}{A_r^{0.2}}$, $A_r = \frac{d_p^3\rho_g(\rho_p - \rho_g)g}{\mu_g^2}$	$\gamma = \frac{2.27}{A_r^{0.2}}$ $A_r = \frac{d_p^3\rho_g(\rho_p - \rho_g)g}{\mu_g^2}$

where U_B is the average velocity of a bubble rising through a bed, m/s; d_B is the spherical equivalent diameter of the bubble, m; U is the superficial gas velocity through a bed of solids, m/s; U_{mf} is the minimum fluidisation velocity, m/s; D is the diameter of a fluidised bed, m; γ is the through flow factor; A_r is the Archimedes number; ρ_g and ρ_p are the densities for air and solid particles; d_p is the average size of solids; μ_g is air viscosity[38], (1.82×10^{-5} $kgm^{-1}s^{-1}$).

3.5.2. Prediction of Bubble Rise Velocity from Particle Rise Velocity

The average bubble rise velocities and bubble sizes in a fluidised bed can be measured by using the data acquired by the non-intrusive PEPT technique (Fan et al., 2008). This is based on the fact that particle in bubble wakes or in bubbles travels upwards at an average velocity as high as the bubble.

As illustrated by a number of studies, when a bubble travels upward through a bed of particles, the particles tend to flow around the bubble in a manner somewhat like that encountered when a body moves through a fluid stream (Figures 21 and 22).

Typical bubbles are not spherical as shown in Figure 21. but have a flattish profile. The region just below the bubble is the wake region. The particles in a wake and in a bubble are carried along with the bubble as if attached to it for a certain distance (Kunii and Levenspiel, 1991, Howard, 1989).

Even though they are moving within the limited space, the average upward velocity of the particles in a wake and a bubble should be equal to the bubble rise velocity. The wake fraction, defined as the ratio of wake to the bubble by volume $f_w = V_w / V_b$, varies with bed materials, and is greater than 0.4 in most cases.

For example, the f_w is greater than 0.4 for glass spheres, and is greater than 0.6 for acrylic granules (Kunii and Levenspiel, 1991). There is also 0.2-1.0% of solids by volume in the

bubbles. In considering the total volume of bubbles in a fluidised bed, the amount of solids in the wake is significant and large enough for the calculation of bubble rise velocity.

Table 3. Correlations used most frequently for the prediction of bubble size (Fan et al., 2008)

Yasui and Johanson	$d_B = 1.6\rho_p d_p (\frac{U}{U_{mf}-1})^{0.63} h$
Whitehead and Young	$d_B = 0.34(\frac{U}{U_{mf}-1})^{0.33} h^{0.54}$
Rowe	$d_B = \frac{(U-U_{mf})^{0.5}(h-h_0)^{3/4}}{g^{0.25}}$, $h_0 = 1.61[A_0^{1.6} g^{0.2}(U-U_{mf})^{-0.4}]^{\frac{1}{3}}$
Darton	$d_B = 0.74(U-U_{mf})^{\frac{2}{5}}[h+3.94\sqrt{A_0}]^{\frac{4}{5}} / g^{\frac{1}{5}}$
Werther	$d_B = 8.53\times10^{-3}[1+27.2(U-U_{mf})]^{\frac{1}{3}} \cdot [1+6.84(h+h_0-h_y)]^{1.21}$ For Geldart B type solids $h_0 - h_y \approx 0$
Mori and Wen	$d_B = 0.652[A_t(U-U_{mf})]^{0.4} - \{0.652[A_t(U-U_{mf})]^{0.4} - 0.347[A_0(U-U_{mf}]^{0.4}\}\exp(\frac{-0.3h}{D_t})$
Cai	$d_B = 0.21h^{0.8}(U-U_{mf})^{0.42} \times \exp[-0.25(U-U_{mf})^2 - 0.1(U-U_{mf})]$

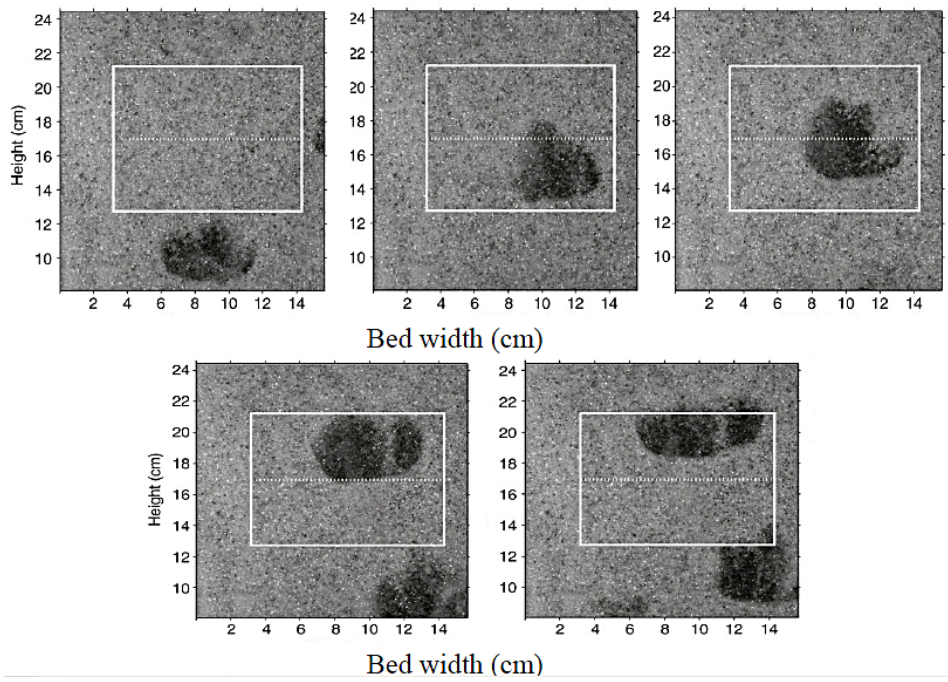

Figure 21. Bubble wakes in a fluidized bed (Sánchez-Delgado et al, 2010).

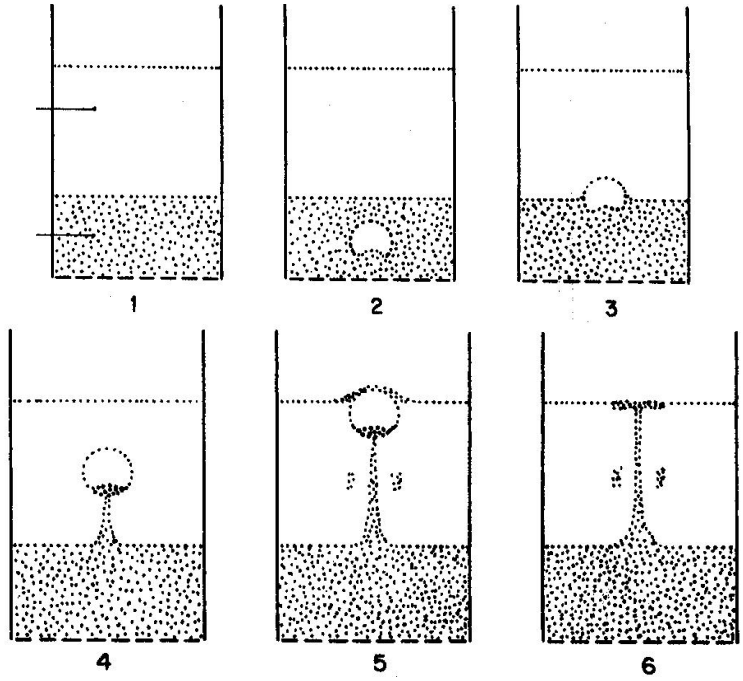

Figure 22. Illustration of displacement and mixing of solids by a rising bubble (Geldart, 1986, Cheun U, 2009).

The velocity associated with particles in a bubble wake or in a bubble in a fluidized bed can be calculated by taking a suitable top fraction from the solid upward velocity map as shown in Figures 18-20, since the upward velocities of particles in bubble wakes and in bubbles are significantly higher than those of the particles outside of the wake and the bubble (Fan et al., 2008). The size of the top fraction can be determined from Figure 23.

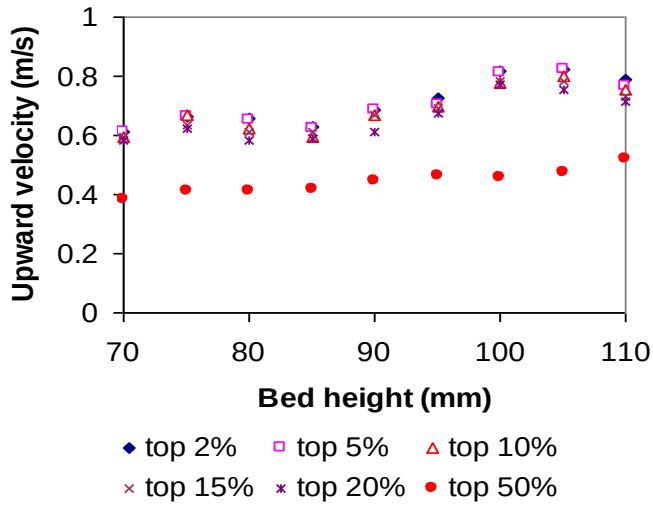

Figure 23. Average rise velocities of particles as a function of the top fraction of the upward velocity map (V_y) (Fan et al., 2008).

There is no significant difference in the rise velocity when the size of the top fraction is between 2% to 20%. This indicates that the top 10% of the upward velocity is certainly associated with the particles in the bubble and its wake.

In order to see the bubble velocity at different bed levels, the bed is divided into a number of layers, and each layer being 5 mm in height. The average upward velocity of particles within the top 10% was calculated to represent the bubble rise velocity in each layer. The bubble rise velocities calculated by using PEPT data have shown in Figures 24-26.

To calculate the bubble rise velocity by using empirical correlations, the bubble sizes are firstly calculated by using Equations listed in Table 2, respectively for the flow patterns A, B and C. The calculated bubble sizes are then put into the correlations listed in Table 1. to calculate the bubble rise velocity.

For each flow pattern, there are 7 correlations to calculate bubble sizes, and 6 correlations to calculate the bubble rise velocity. 42 calculated values can be obtained for the bubble rise velocity. Figures 24-26. present those results that have a good agreement between the PEPT measurements and empirical predictions.

For Pattern A, the PEPT measurements agree well with the rise velocities calculated from Equations 15-17 and 19-20 as shown in Figure 24-26. The equations are the combinations of Baeyens-Rowe, Baeyens-Yasui, Kunii-Rowe and Kunii-Yasui, and Werther-Darton. The rise velocities calculated from the PEPT data agree well with Equations 15-20 for the flow pattern B, where the Equation 18 is the combination of Davison and Darton.

For the flow pattern C, the bubble rise velocities calculated by using particle rise velocity in bubble wakes and in bubbles did not show a constant increase with the bed height as indicated by the empirical approaches. The bubble rise velocity firstly increased with the bed height to 0.7m/s, and then decreased to 0.35m/s at the bed height from 130mm (y=270) to 200 (y=340) mm.

Above a bed height of 200 mm, the rise velocity dramatically increased again. This data matched very well with the measured solid flow structure. The empirical correlations listed in Equations 16 and 20-23 can be used to predict the bubble rise velocity at the bottom section of the bed (h<150 mm) for the pattern C, but can not predict the bubble rise velocity at the intermediate level of the bed.

The explanation could be that the empirical correlations were deduced based on the flow patterns A or B, rather than on the pattern C. In the pattern C, the air bubbles travel upward along the annulus in the bottom section of the bed, and then shifted to the bed centre in the intermediate section of the bed due to the collision of two solid flows in the intermediate section of the bed; therefore the bubble sizes and bubble rise velocity are reduced.

After the intermediate height of the bed, the bubbles rapidly coalesce again, resulting in a fast increase in the bubble size and their rise velocity. Another reason may be due to some empirical models used in the work for bubbles are two-dimensional, and agreement with fully three dimensional measurements is difficult due to coalescence and splitting.

Combination of Baeyens-Rowe:

$$U_B = \frac{2.27}{A_r^{0.2}}(U - U_{mf}) + 0.711\sqrt{g^{0.75}(U - U_{mf})^{0.5}(h + h_0)^{0.75}} \tag{15}$$

with $h_0 = 1.61[A_D^{1.6} g^{0.2} (U - U_{mf})^{-0.4}]^{\frac{1}{3}}$

Combination of Baeyens-Yasui:

$$U_B = \frac{2.27}{A_r^{0.2}}(U - U_{mf}) + 0.711\sqrt{1.6 g \rho_P d_P (\frac{U}{U_{mf}} - 1)^{0.63} h} \quad (16)$$

Combination of Werther-Darton:

$$U_B = (U - U_{mf}) + 1.6 D^{0.4} \sqrt{0.74 g^{0.8} (U - U_{mf})^{0.4} (h + 3.94 A_0^{0.5})^{0.8}} \quad (17)$$

Combination of Davison and Darton:

$$U_B = (U - U_{mf}) + 0.611 g^{0.4} (U - U_{mf})^{0.2} (h + 3.94 A_0^{0.5})^{0.4} \quad (18)$$

Combination of Kunii-Rowe:

$$U_B = 1.6 D^{1.35} (U - U_{mf}) + (1.81 D^{1.35} + 0.711 g^{0.5}) \sqrt{\frac{(U - U_{mf})^{0.5} (h - h_0)^{0.75}}{g^{0.25}}} \quad (19)$$

Combination of Kunii-Yasui:

$$U_B = 1.6 D^{1.35} (U - U_{mf}) + (1.81 D^{1.35} + 0.711 g^{0.5}) \sqrt{1.6 \rho_p d_p (\frac{U}{U_{mf}} - 1)^{0.63} h} \quad (20)$$

Combination of Baeyens-Darton:

$$U_B = \frac{2.27}{A_r^{0.2}}(U - U_{mf}) + 0.611 g^{0.4} (U - U_{mf})^{0.2} (h + 3.94 A_0^{0.5})^{0.4} \quad (21)$$

Combination of Kunii-Darton:

$$U_B = 1.6 D^{1.35} (U - U_{mf}) + (1.81 D^{1.35} + 0.711 g^{0.5}) \frac{0.86 (U - U_{mf})^{0.2} (h + 3.94 \sqrt{A_0})^{0.4}}{g^{0.1}} \quad (22)$$

Combination of Davies-Darton:

$$U_B = 0.611 g^{0.4} (U - U_{mf})^{0.2} (h + 3.94 A_0^{0.5})^{0.4} \quad (23)$$

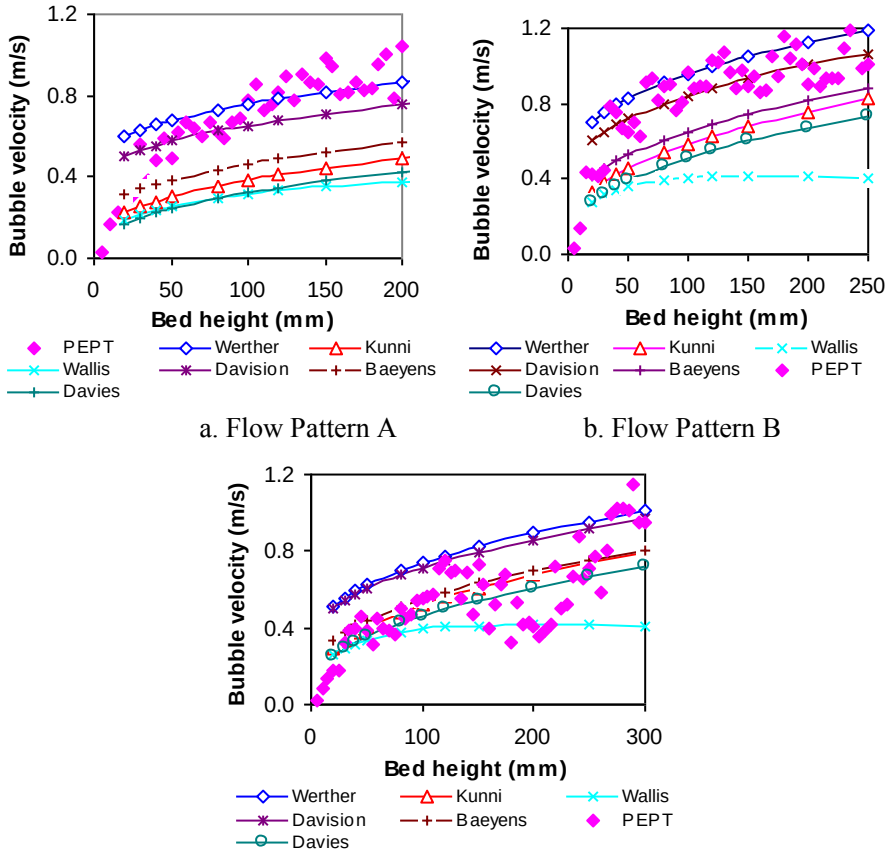

a. Flow Pattern A

b. Flow Pattern B

c. Flow Pattern C

Figure 24. Comparison of bubble velocity measured by PEPT with empirical correlations, where bubble sizes are calculated by using Darton correlations (Fan et al., 2008).

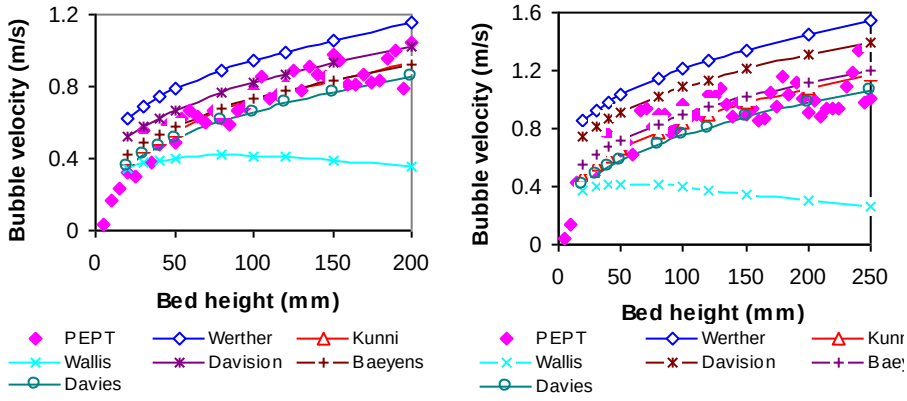

a. Flow Pattern A

b. Flow Pattern B

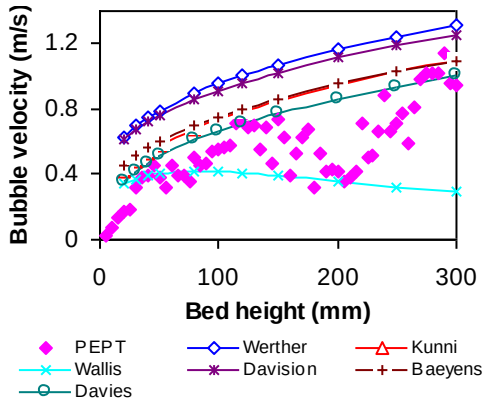

c. Flow Pattern C

Figure 25. Comparison of bubble velocity measured by PEPT with empirical correlations, where bubble sizes are calculated by using Rowe correlation (Fan et al., 2008).

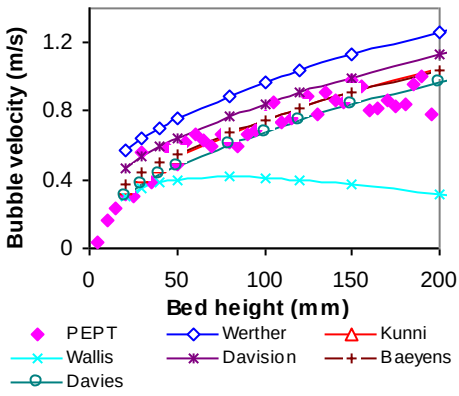

a. Flow Pattern A

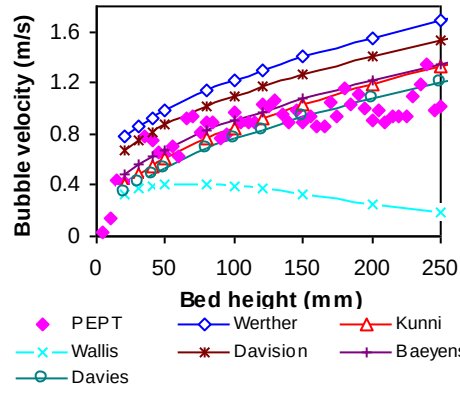

b. Flow Pattern B

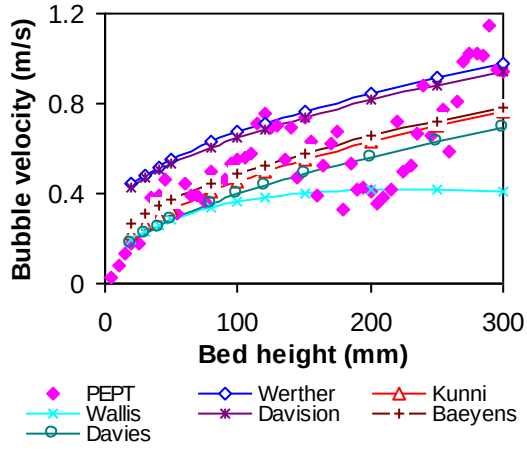

c. Flow Pattern C

Figure 26. Comparison of bubble velocity measured by PEPT with empirical correlations where bubble sizes are calculated by using Yasui correlation (Fan et al., 2008).

3.5.3. Impact of Flow Pattern on Bubble Size

Equations 24 and 25 are derived for calculating the bubble size in the studied bubbling fluidised beds by using the upward velocity of particles in bubble wakes and in bubbles. From Figure 27, it can be seen that the bubble sizes calculated from Equations 24 and 25 vary significantly with solid/bubble flow pattern. For the flow patterns A and B, the air bubbles travel straight upwards from the air distributor to the splash zone, and their sizes increased constantly when rising through the fluidised bed. The bubble sizes calculated by using the upward velocity of particles in bubbles and in their wakes agree well with the predictions from Rowe correlation and Yasui correlation. For the flow pattern C, the bubble size calculated by using the PEPT data is significantly different from the empirical prediction and the descriptions in literature. The bubble sizes firstly increase until the bed height of 150 mm (y=290) and then reduce in the middle section of the bed, rather than expanding constantly. This matches the solid/bubble flow structure detected by the PEPT technique. The bubble size in the intermediate section of the bed is much smaller than the predictions from empirical correlations. Above the bed height of 200 mm (y=340), the bubbles expand again rapidly, and the expanding rate is much higher than the predicted value.

$$d_B = \left(\frac{V_w - 1.6D^{1.35}(U - U_{mf})}{1.81D^{1.35} + 0.711g^{0.5}}\right)^2 \tag{24}$$

$$d_B = \frac{[V_w - \gamma(U - U_{mf})]^2}{0.506g} \tag{25}$$

where V_w is particle upward velocity in bubble and its wake (m/s),

$$\gamma = \frac{2.27}{A_r^{0.2}},\ A_r = \frac{d_p^3 \rho_g (\rho_p - \rho_g) g}{\mu_g^2}$$

3.6. Effect of Particle Size on Bubble Rise Velocity and Bubble Size

The bubble sizes presented in Figure 27. were calculated from equation 24 that takes the bed geometry into account. The bubble sizes presented in Figure 28. were calculated from equation 25 that takes the particle properties into account. The results indicate that the bubbling pattern is very similar for glass beads with a size of 250-450μm and of 800-1000μm. The bubble size and rising speed increase constantly with the bed height increasing (Figures 27 and 28).

However, when the particle size was 80-200μm, the bubbling pattern is completely different. Air bubbles were favoured to form and initially travel upwards in the annulus of the bed at a bed height of 20-80 mm, rather than uniformly distributed in the whole cross section area.

The bubbles were then moved inwards to the central region at an intermediate height of the bed by the solid flows returning from the top section of the bed, where the bubbles were

splitting (Figure 28), and the rise velocity slow down (Figure 27) rather than increase constantly as the description in literature.

Above the intermediate layer, air bubbles travelled faster, and their size increased significantly. This agrees with the bubble flow pattern observed by Werther and Molerus (1973) and Lim et al (2007).

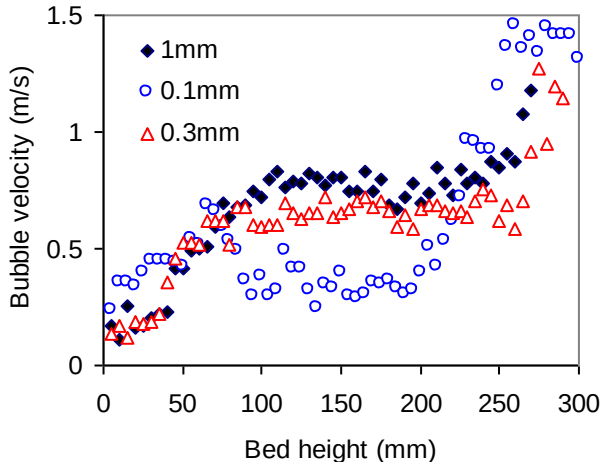

Figure 27. Impact of particle size on bubble rise velocity in a bubbling fluidized bed.

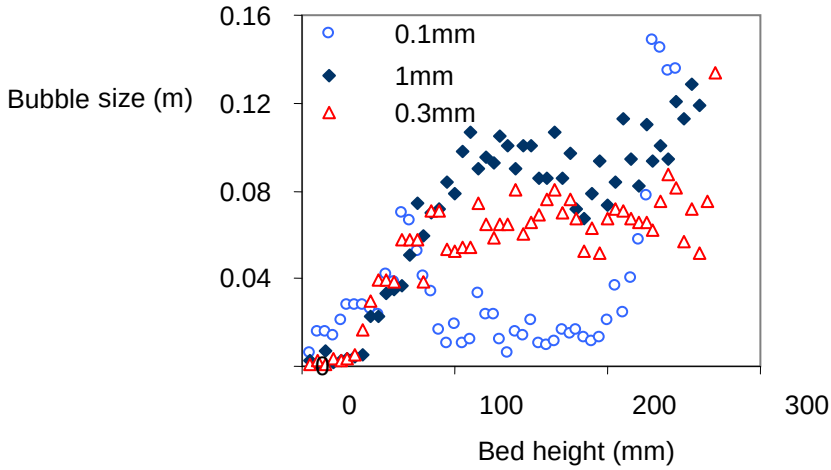

Figure 28. Impact of particle size on bubble size in a fluidized bed.

4. CIRCULATING FLUIDIZATION

Circulating fluidised beds (CFB) has been widely used in numerous industrial processes in the chemical, petrochemical and metallurgical industries, in the manufacture of fine powders and ceramics and in combustion and environmental remediation such as catalytic

cracking, combustion or gasification of biomass, coal combustion for power generation and waste incineration, pyrolysis, calcining and catalytic processes.

A CFB consists of a riser, a cyclone, a standpipe, a L-valve and other ancillary equipment, such as strippers, regenerators and external heat exchangers as shown in Figure 29. In the riser, a gas-solid suspension is transported upward, and the solid and gas are mixed and react. The gas-solid suspension density within the riser is greatly influenced by both gas superficial velocity (U) and solids mass flux (G), which therefore directly affect heat transfer, mass transfer, and chemical reaction rates. In the cyclone, the two-phase mixture is separated and solids are recycled to the bottom (Chan et al., 2008a). The standpipe and the L-valve convey solids gravitationally from the cyclone to the riser (Chan et al, 2009a).

In terms of chemical reaction, CFB processes can be classified into two categories: gas-catalytic reaction and gas -solid reaction (Van de Velden et al., 2007, 2008a). In gas-catalytic reactions, the solids serve as catalyst and heat transfer medium. The final or intermediate products are gaseous and mostly organic chemicals. Gas-catalytic reactions are fast, thus needing both a rigorous control of the gas residence time to limit side reactions (high gas velocities) and a frequent regeneration of the deactivating catalyst (high solids circulation rates).

In gas–solid reactions both phases react to yield products and/or energy. For example in coal combustion, the oxygen in the gas phase (air) reacts with the solids (coal) and its vaporized compounds to form combustion products and energy. In comparison with gas-catalytic reactions, the gas–solid reactions are generally slow, and require neither a high gas velocity, nor a high solids circulation rate. Low gas velocity operation is required because the solids are usually the key reactant/product so that the extent of gas and/or solids back mixing may not always be critical. Some gas/solid reactions, e.g. biomass pyrolysis (Van de Velden et al., 2007, 2008a) require operating conditions of gas catalytic reactions since the by-product (char) acts as cracking catalyst for the main product (bio-oil), thus considerably reducing its production yield at high residence times.

For both types of the reaction groups, a good solid mixing and good solid-gas contact are required for performing the reactions with a high efficiency. However, the different nature of the reactions requires different solid and gas residence time (Mahmoudi et al., 2010). In general, gas and solids residence times are chosen to achieve the highest product yield per unit of reactor volume.

Solids residence time is dependent on CFB design, operational mode, suspension density, and solids mass flux. Riser height is generally set to achieve sufficient pressure build-up to circulate solids at a high rate. High gas velocities and low solids hold-up are preferred in some applications to minimize compressor costs. However, for many catalytic reactions, lower gas velocities may be preferred because they give higher solids hold-up, thus maximizing specific activity per unit volume (Berruti et al. 1995).

For a given design of CFB, the residence time is a function only of the hydrodynamics of the gas/solid flow in the riser (Van de Velden, 2007). CFB process design and development therefore require a good understanding of gas and solids hydrodynamics - the effect of operating conditions, scale and particle characteristics on solids hold-up, gas and solids mixing and velocity profiles.

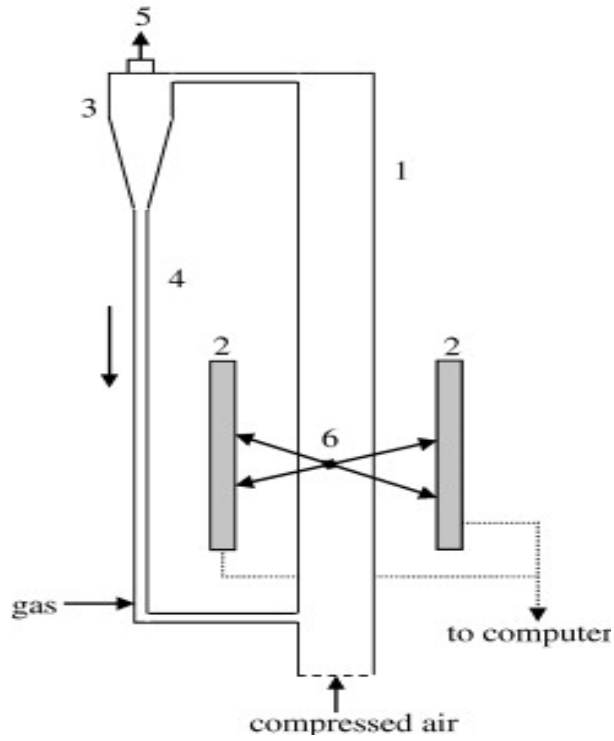

Figure 29. Schematic diagram of a circulating fluidized bed (CFB), 1) CFB-riser; 2) detectors; 3) high-efficiency cyclone; 4) downcomer and L-valve; 5) vent, to filter and atmosphere; 6) tracer (Van de Velden, et al., 2008a).

Many hydrodynamic models have been proposed to characterize the relationship between solids hold-up and gas velocity, solids mass flux, riser geometry and particle physical properties (Berruti, et al, 1995). Harris and Davidson (1994) group them into three categories: Model type I predict only axial solids suspension density; Models type II characterize both radial and axial solids hold-up and velocity profiles; and Models type III employ the fundamental equations of fluid dynamics.

Despite the intensive studies and subsequent widespread industrial application from the 1960', the hydrodynamics of a CFB are still not fully understood as far as the relationship between operating conditions and solids/gas motion are concerned. There are controversies among researchers with regards to the distinction between the different regimes of dilute transport, fast fluidisation (core-annulus flow), and dense suspension upflow (DSU) (Mahmoudi et al., 2010). For example (Chan et al., 2010):

(i) Fluidized bed contains a solid bed at the riser bottom and a dilute phase or moderately dense phase (core-annulus) at the top (Van de Velden et al., 2007, Rhodes and Geldart, 1989). The axial solids hold-up profile has an inflection point and is referred to as the S-profile. Under increasingly higher solid flux at constant gas the depth of the bed increases (Rhodes et al., 1998, Malcus et al., 2002).
(ii) Other studies indicate that an exponential solids hold-up profile exists with no dense bed but with an acceleration zone at the bottom of the riser, characteristic of other

regimes such as core-annulus flow without bed, dilute transport and/or dense suspension upflow (Li, et al., 1988, Chan, et al. 2010).

This Chapter will report our newly findings regarding the flow regimes, the hydrodynamics of solid flow in a CFB from Positron Emission Particle Tracking technique.

4.1. CFB Operating Regimes

Numerous studies on CFB riser regimes are available in the literature (Monazam et al, 2005, Li, et al, 1980, Yerushalmi and Cankurt, 1979, Bi and Grace 1995)**,** but many of them are controversy on the actual events occurring in different flow regimes and the boundary between these regimes (Smolders K., Baeyens J., 2001). Yerushalmi and Cankurt (1978) defined the CFB as a fluidized bed operating at gas velocities exceeding the minimum transport velocity. Kwauk et al. (1986) and Takeuchi et al. (1986) stated that an inflection point separating a dense phase at the bottom from a dilute phase at the top of the riser was necessary. Karri and Knowlton (1999) suggested that the fast fluidization region can be defined by two transition velocities for a given solids mass flux: the choking velocity, and the velocity corresponding to the minimum pressure drop on the *P* vs. *U***,** diagram (onset of pneumatic transport). Yang (1994) defined the incipient fast fluidization velocity as the velocity at which the solids start to reflux adjacent to the wall to form a dense phase at the bottom of the riser. Berruti et al (1995) defined a CFB as any system**,** involving solids recirculation, operating at gas velocities exceeding *U*. It may be operated under turbulent fluidization, fast fluidization or pneumatic transport regimes.

A qualitative fluidization map was initially proposed by Yerushami et al. (1978), and later refined by Yerulshalmi and Cankurt (1978). According to Yerulshalmi and Cankurt, transport velocity is defined as the velocity at which it is possible to carry all of the solids fed into the riser out again, and thus it is impossible to maintain a fluidized bed without continuous recycle of solids back into the fluid bed. This is the critical gas velocity defining the transition between turbulent and fast fluidization flow regimes. Li et al (1980) developed a regime map by plotting the voidage against superficial gas velocity. Grace (1986) proposed a unified flow regime diagram that shows the operating ranges of conventional fluidized bed, spouted beds, circulating fluidized beds and transport systems. However, the transition of different flow regimes was not clearly delineated. Bi and Grace (1995) presented a flow regime map for conventional fluidized bed and dilute phase transport. The flow regime map was lacking of transitions to dense-phase transport. Mori et al. (1992) defined the transport velocity as the velocity above which no interface exists between a dense bed and an upper dilute freeboard at any solids circulation rate. Therefore, there is lack of good understanding in the literature regarding the gas–solid flow and the actual events occurring in different flow regimes (Monazam, et al 2005).

To study the flow regimes in a CFB riser, we use Positron Emission Particle Tracking to measure the real-time particle motion in a riser to define (i) the extent of the acceleration zone, acceleration length and acceleration time; (ii) the specific operational conditions, such as superficial gas velocity U and solid reflex rate G, under which the occurrence of a bubbling/turbulent bed; (iii) the establishment of a fully developed flow and the acceleration zone; (iv) the specific combinations under which the occurrence of core-annulus flow and (v)

the disappearance of the intermediate core annulus region, where riser hydrodynamics will be either dilute or dense solid upflow at high values of U and G.

In general, a CFB riser can be divided into three zones, a dense zone at the bottom, an acceleration zone above the bottom bed and a developed zone. The riser cross section is also divided into a core region where solids rise in dilute suspension and an annular wall region with a dense phase flowing downward. Solid gas contact and the solid hydrodynamics greatly vary in different zones and vary with CFB operating regimes. They are determined mainly by the combined operating superficial gas velocity (U) and solids circulation flux (G). The transport velocity, U_{TR}, is the minimum superficial air velocity required in the riser to maintain stable CFB hydrodynamics.

4.2. Bottom Bed

The bottom part of the riser contributes to the total pressure drop and affects the solids residence time in the riser (Chan et al., 2009b). A bottom bed can be formed when the voidage of the dense bed fall in the range of 0.8 to 0.9 (Ouyong and Potter, 1993). The existence of the dense bottom bed could add an extra height not accounted for by the acceleration zone. The equation 26 proposed by Wong et al. (1992) predicts the voidage of the bubbling/turbulent bed at the bottom of the riser for Geldart Group A solids.

$$\varepsilon_b = 0.25\left(\frac{G}{\rho_P U}\right)^{-0.11} D^{-0.23}\,\mathrm{Re}_t^{0.02} \tag{26}$$

When $20 < G < 198$ kg m^{-2} s^{-1}, $4 < U < 8$ m s^{-1}.

To examine the acceleration zone and the possible occurrence of a dense bottom bed, solid motion in the bottom section of a riser was recently mapped by using PEPT technique (Chan et al 2010).

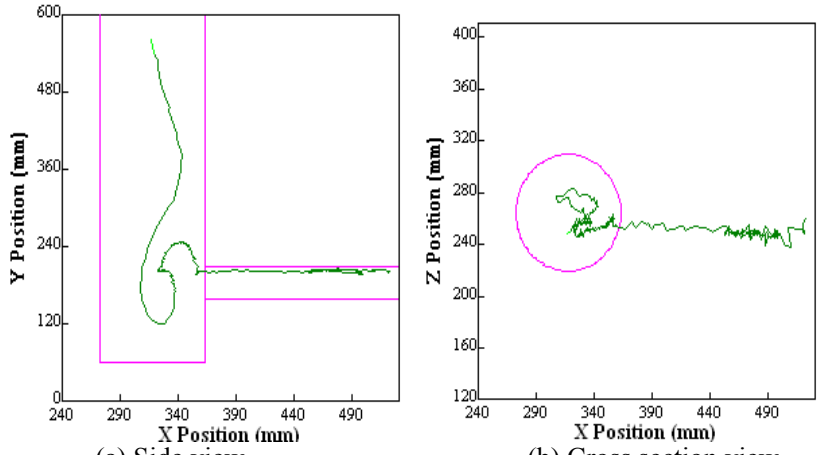

(a) Side view (b) Cross section view

Figure 30. (Continued).

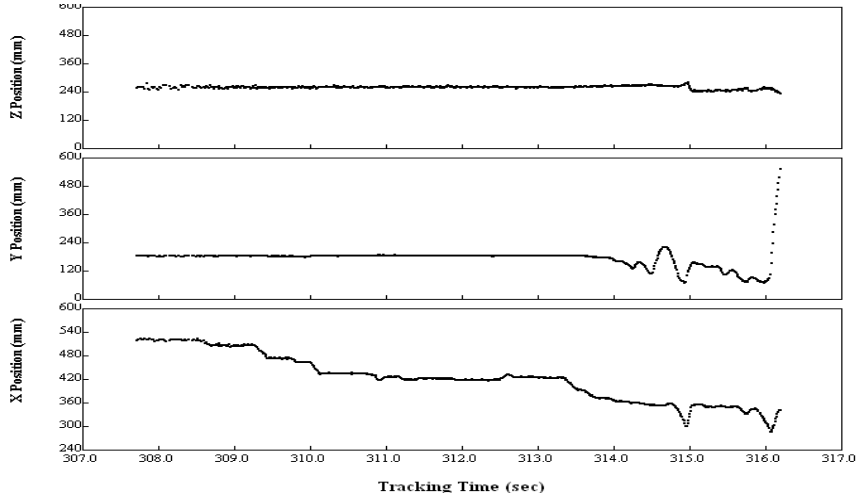

(c) Particle position in x y and z direction

Figure 30. Particle trajectory in the bottom of a riser mapped by PEPT at G = 5.5 kg m^{-2} s^{-1}, $U–U_{TR}$=2.1 m/s.

During the measurement, one particle was selected from the bed material, and was labelled by F-18 as a tracer. The tracer was introduced to the CFB together with the bed material *via* the downcomer. The air flow to the riser was set at the required superficial gas velocity. The L-valve was activated with a gas flow with a low superficial velocity to start the solids circulating. The data was recorded when the system is stabilised. The results indicate that the solids movement at the bottom section varies completely with operating regimes as shown in Figures 30-33.

When the solid flow rate G was less than 20 kg $m^{-2}s^{-1}$, there was no dense bed formed in the riser bottom due to the low G-values. The tracer particle was seen to descend below the solids entry point, and then accelerated and conveyed up the riser in a dilute flow mode. When G increased from 20 to 60 kg $m^{-2}s^{-1}$, a bubbling or a turbulent fluidized bed was formed at the riser bottom, which correspond a core-annulus flow mode that we will discuss later.

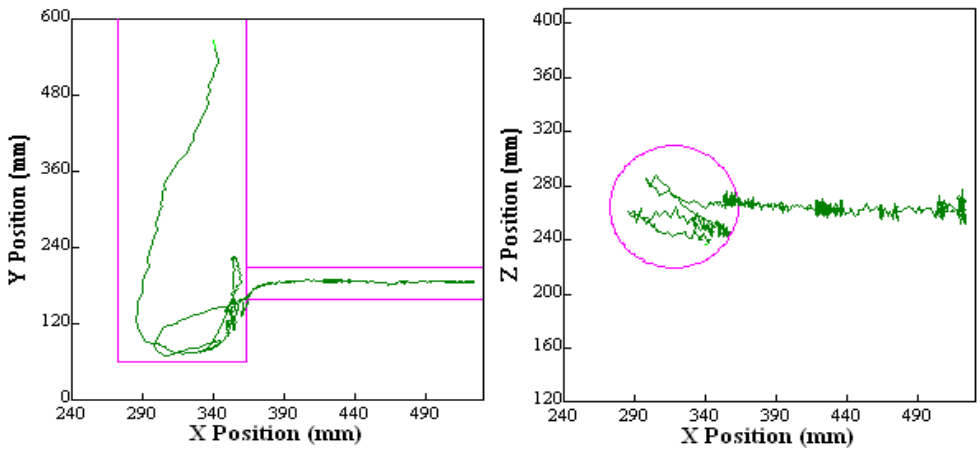

(a) Side view (b) Cross section view

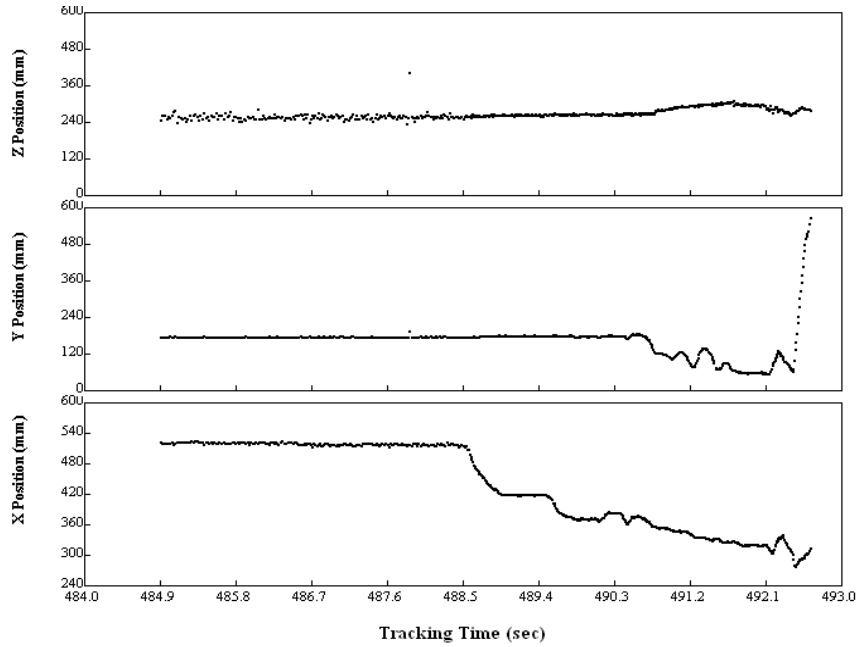

(c) Particle position in x y and z direction

Figure 31. Particle trajectory in the bottom of the riser mapped by PEPT at G = 20.1 kg m^{-2} s^{-1}, U–U_{TR}=2.1 m/s.

The tracer particles moved upwards and downwards in the bottom section. With a further increase in solid flow rate G, the dense bed disappeared. The CFB was operated in a dense suspension upflow mode.

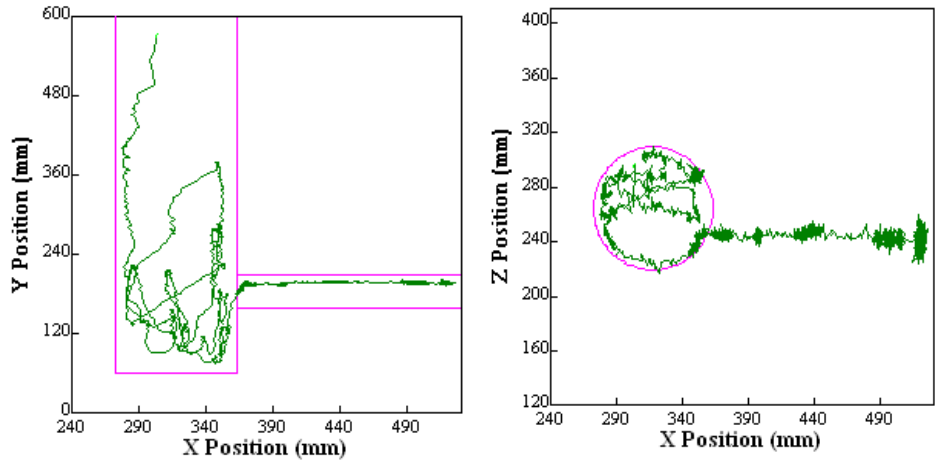

(a) Side view (b) Cross section view

Figure 32. (Continued).

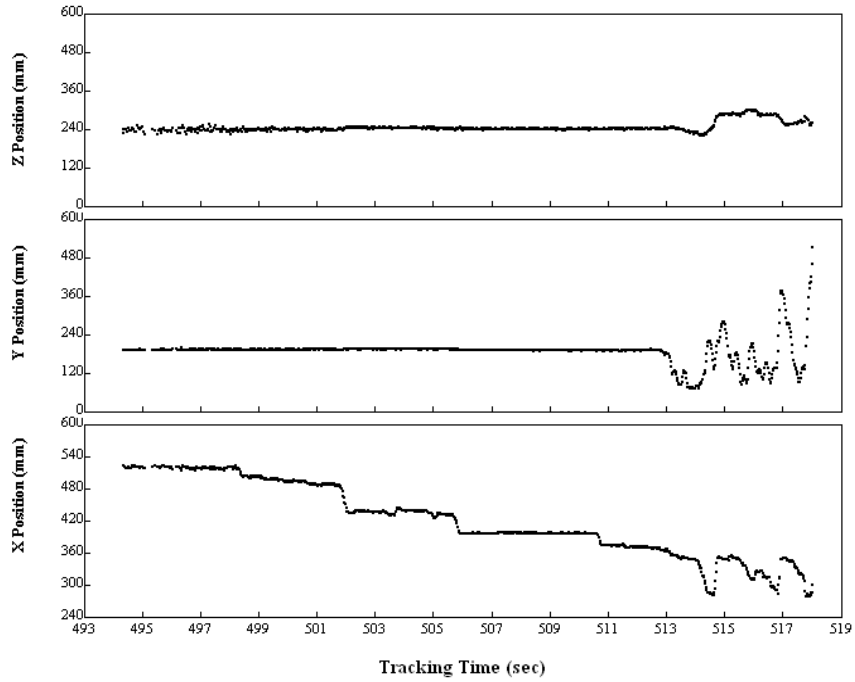

(c) Particle position in x y and z direction

Figure 32. Particle trajectory in the bottom of the riser mapped by PEPT at G = 55.5(kg m^{-2} s^{-1}, U–U_{TR}=2.1 m/s.

Tracer particles were firstly descend below the L-valve, and then accelerated and conveyed up. The existence of a bottom fluidized bed (BTFB) is limited to a specific range of U, G operating values (Chan, et al, 2008b, 2010). The occurrence of a dense bottom bed can also be seen from the voidage profile in the bed as shown in Figure 38.

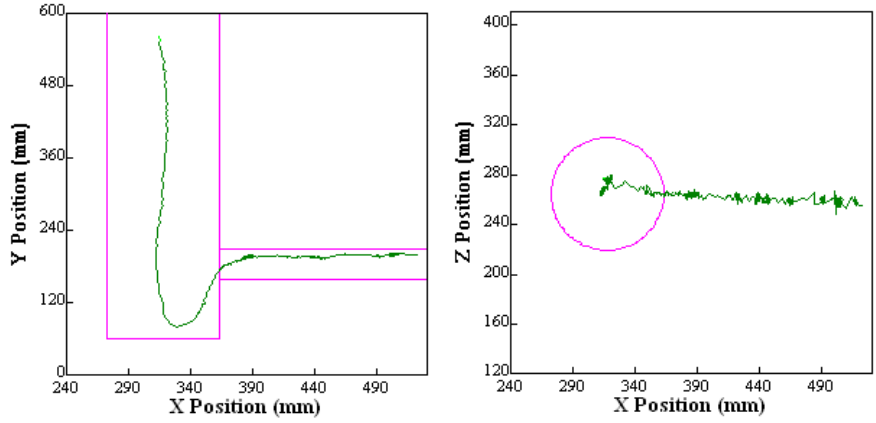

(a) Side view (b) Cross section view

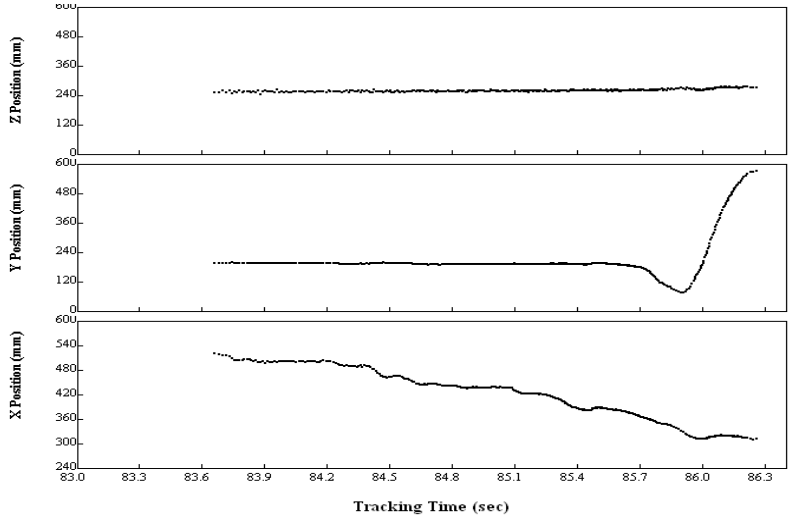

(c) Particle position in x y and z direction

Figure 33. Particle trajectory in the bottom of the riser mapped by PEPT at G = 210 kg m^{-2} s^{-1}, U–U_{TR}=2.1 m/s.

4.4. Acceleration Zone

Acceleration zone is located at bottom section of a riser or above the bottom dense bed. In an acceleration zone, particles are accelerated from zero velocity in vertical direction to a constant upwards velocity. The acceleration length and acceleration time are two important parameters. The acceleration length (L_{acc}) is the vertical distance in which a solid particle travels during the acceleration. It can be calculated by using equation 27 (Wong et al, 1992, Chan et al. 2009c). The acceleration time (t_{acc}) is the time it takes for solids to reach the constant velocity from the moment it starts accelerating. The behaviour of solids in the acceleration zone is affected by the size of the annulus region, the suspension of solids, solids friction on the wall, gas friction on the solids.

$$\frac{L_{acc}}{D} = 7.92\times10^{8}\left(\frac{D}{d_P}\right)^{-0.76}\left(\frac{\rho_P}{\rho_g}\right)^{-1.21}\left(1+\frac{G}{\rho_g U}\right)^{0.28}\mathrm{Re}^{-0.97} \qquad (27)$$

In equation 27, the acceleration length is defined from the bottom of the riser to the height where the axial voidage becomes constant; therefore including that part of the riser height where the voidage decreases less rapidly due to core-annulus flow, which can however not be considered as part of the acceleration zone (Chan et al 2009b).

The acceleration length measured by PEPT is an order of magnitude smaller than that of the value predicted by Wong et al (1992). Table 4. shows that that the experimental acceleration length is on average 0.26 m regardless of *U* and *G*. The averages of *L* and *t*, together with their respective standard deviations are given as (Chan et al, 2009c).

$$\sigma_{L_{acc}} = \sqrt{\frac{1}{N}\sum_{t=1}^{N}(L_{acc,PEPT} - \overline{L_{acc,PEPT}})^2} \tag{28}$$

where $\overline{L_{acc,PEPT}} = \dfrac{\sum_{t=1}^{N} L_{acc,PEPT}}{N}$

$$\sigma_{t_{acc}} = \sqrt{\frac{1}{N}\sum_{t=1}^{N}(t_{acc} - \overline{t_{acc}})^2} \tag{29}$$

where $\overline{t_{acc}} = \dfrac{\sum_{t=1}^{N} t_{acc}}{N}$

The standard deviation for the acceleration length, σ_L is 6 cm. In a riser with a height greater than 6 m, the L_{acc} is of insignificant consequence to the collective riser hydrodynamics. The experimental acceleration time is approximately constant at 0.21 s with standard deviation, σ_t being 0.07 s. The acceleration length can be modelled fairly accurately, using a CD-factor of approximately 3.2, which is about half the value predicted by empirical equations established for dilute transport (Chan et al, 2009c). Within the range of experimental conditions, the time spent by solids in the riser prior to acceleration is significantly longer (Figure 34) than the acceleration time itself (as seen in Figure 35). In Figure 34, prior to their acceleration the residence time of solids decreases with the increasing in U when U<5 m/s. This most probably implies the reduction in the bottom bed height. When U>5 m/s, the residence time of solids is nearly insensitive to U. This could imply that the bottom bed is virtually constant. Figure 35. shows that the time needed for acceleration is nearly constant regardless of solids circulation flux, G, taking an average of 0.21 s to completely accelerate.

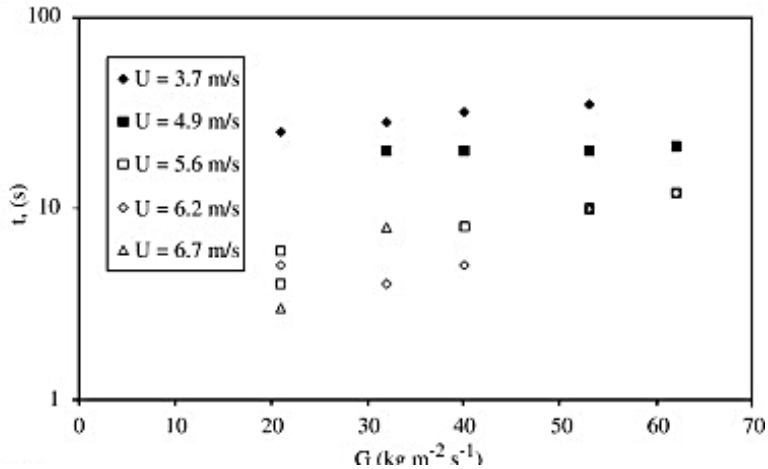

Figure 34. Residence time in a riser prior to acceleration measured by PEPT (Chan et al., 2009c).

Table 4. Acceleration length and time measured by PEPT and the predicted the emerical correlation proposed by Wong et al. (1992) (Chan et al, 2009b)

U (m s− 1)	U − UTR (m s− 1)	G (kg m−2 s− 1)	Lacc (m)	Lacc, Wong (m)	tacc (s)	tbed (s)
3.7	1.4	21	0.115	3.0	0.23	25
3.7	1.4	32	0.235	3.3	0.22	28
3.7	1.4	40	0.31	3.5	0.15	32
3.7	1.4	53	0.36	3.8	0.15	35
4.9	2.6	32	0.145	2.4	0.16	20
4.9	2.6	40	0.256	2.5	0.19	20
4.9	2.6	53	0.288	2.7	0.21	20
4.9	2.6	62	0.333	2.8	0.23	21
5.2	2.9	21	0.264	2.0	0.17	4
5.5	3.2	21	0.30	1.9	0.12	6
5.6	3.3	40	0.255	2.1	0.17	8
5.7	3.4	53	0.252	2.2	0.17	10
5.7	3.4	62	0.209	2.3	0.15	12
6.2	3.9	21	0.288	1.6	0.11	5
6.2	3.9	32	0.255	1.8	0.18	4
6.2	3.9	40	0.277	1.9	0.33	5
6.2	3.9	53	0.262	2.0	0.31	10
6.2	3.9	62	0.195	2.1	0.26	12
6.6	4.3	21	0.216	1.5	0.21	3
6.7	4.4	32	0.246	1.6	0.19	8
6.8	4.5	53	0.345	1.8	0.21	10

t_{bed} is the residence time in the bottom BTFB.

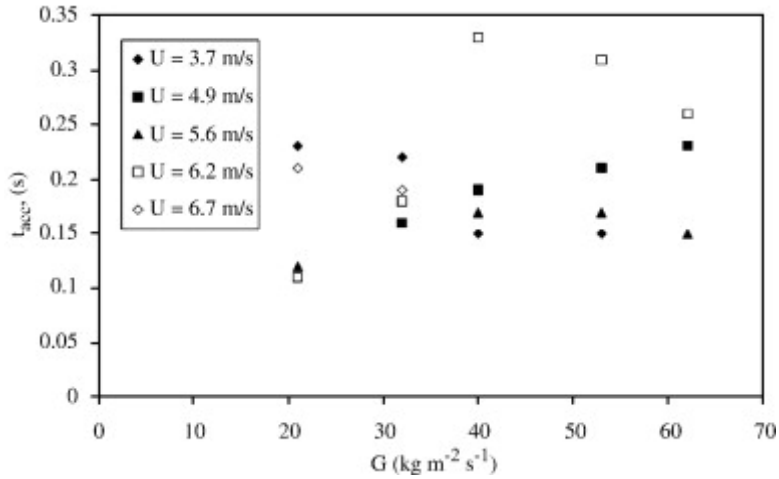

Figure 35. Acceleration time in a riser at various operating *G* values measured by PEPT (Chan et al., 2009c).

4.5. Fully Developed Zone

Above the acceleration zone is a fully developed region, where the flow characteristics are invariant from the end of the acceleration region to the riser exit when a CFB is operated in a particular mode. However, the flow characters in a fully developed zone vary with the operational mode and gas flow rate as shown in Figures 36-38. Solid particles sometimes traverse the riser in one continuous upward movement and sometimes recirculate within the riser as shown in Figure 36. The blanks between successive trajectories in Figure 36 correspond to the time interval when the tracer particle spent in the rest of the riser and in the external recycle loop. Figure 37. shows solid distribution in the cross section area of a riser in the acceleration zone, where sand with a size of 120 μm and a U_{tr} of 2.0 m/s was used as a bed material. The overall operational modes are illustrated in Figures 37-38. The operating parameters are given in Table 5. When the CFB was operated with a solid circulation rate (G) of 260 kg m^{-2}s^{-1} and a superficial gas velocity (U) of 2 m s^{-1}, it was in core/annulus mode. The solids travel upward in the whole cross sectional area, and downwards along the annular (Figure 37 (a)). The mechanisms underlying the origin and evolution of the core-annulus flow pattern have not been completely elucidated. Some researchers indicate that the core-annulus structure may result from wall effects, which slow down the gas phase, allowing particles to cluster. However some evidences show that non-ideal particle–particle collisions may result in the formation of particle agglomerates, therefore forming the core-annulus flow structure (Li and Kuipers, 2004, Helland et al. 2000).

With the increasing in the superficial gas velocity, the CFB operation shifts from core/annulus mode to core flow mode. The population of downwards particles was gradually reduced until almost them travelling upwards, and the downward particles moved towards central region. In a typical core-annulus flow mode, the downward velocity of solids in the annulus region is close to the terminal velocity (0.67 m s^{-1}) of the tracer particle, which

agrees with the data presented in literature (Chan et al., 2010, Samuelsberg and Hjertager, 1992, Yang and Gautam, 1995).

The occurrence of both core/annulus flow (up and down) and core flow (up only) is strongly dependent upon the gas superficial velocity (U) and the solids circulation rate (G) as shown in Table 4. and Figure 38. (Chan et al., 2010). When the superficial gas velocity is less than $U_{tr,}$ the minimum superficial gas velocity required in a riser to maintain stable CFB hydrodynamics, the CFB is operated in bubbling and turbulent regime. A stable CFB mode can be achieved only when the gas velocity is in excess of $U_{tr} + 1$, irrespective of the solids loading *G*. The flow regime in a riser varies with solid circulation rate, irrespective of superficial gas velocity *U,* when the CFB is operated at the gas velocity greater than $U_{tr} + 1$. A core flow mode can be achieved at a solids circulation rate in excess of 200 kg/m^2 s, and a mixed mode (core/annulus) can be achieved at solids circulation rates below 150 kg/m^2 s. Reactions requiring core flow should be carried out in a riser operated at $U > (U_{tr} + 1)$ m/s and $G \geqslant 200$ kg/m^2 s, which is higher than the values reported in literature (Figure 38). Conversely, gas/solid reactions can be operated at $U > (U_{tr} + 1)$ m/s and $G \leqslant 100$ kg/m^2 s, which is lower than the value reported in literature (Figure 38).

Equations 31-32 are the empirical correlations proposed by Bi and Fan (1991, 1992), and Kim et al (2004a) to predict the transition from dilute conveying to fast fluidization (core-annulus with or without BTFB). Equations 33-35 presents the empirical correlations proposed by Gupta and Berruti (1998), Grace (1999), Kim et al (2004b) to predict the transition from fast fluidization (core-annulus with or without BTFB) to Dense Suspension Upflow.

In a core-annulus flow CFB, the total pressure drop in a riser is the sum of pressure drop due to (Chan et al., 2009c)

i) suspension of solids,
ii) acceleration of solids,
iii) solids friction on the wall,
iv) gas friction on the solids and the wall.

The friction induced pressure drop is smaller than of the pressure drop from acceleration and suspension of solids [Pugsley and Berruti, 1996]. The acceleration length significantly contributes to the total pressure drop in the riser [Patience et al. 1992] and up to 40% although this value may include the contribution of the bottom bed (Weinstein and Li, 1989). Equation 30 is the imperial correlation proposed by Rhodes and Geldart (1989) for pressure drop calculation. For a dilute flow at low values of G, the pressure drop due to solid acceleration (ΔP_{acc}) is less than 10% of the total pressure drop in the riser. For dense upflow at high values of G and $\varepsilon \sim 0.9$, ΔP_{acc} can represent about 50% of the total pressure drop in the riser (Chan et al., 2009c).

$$\Delta P_{acc} = GU/\varepsilon \tag{30}$$

$$U_{PT} = 10.1(g \cdot d_p)^{0.345}\left(\frac{G}{\rho_g}\right)^{0.310}\left(\frac{d_p}{D}\right)^{-0.139} Ar^{-0.021} \tag{31}$$

$$\frac{U_{pT}}{U_t \cdot s} = 1160\left(\frac{G}{\rho(1-s)U_t}\right)^{-0.9} Ar^{0.2} \tag{32}$$

$$\mathrm{Re}_{DSU} = 12.55\left(\frac{G}{U_t \rho_p}\right)^{0.55} Ar^{0.36} \tag{33}$$

$$U_{DSU} = 0.0113 G^{1.192} \rho_g^{-1.064} [\mu_g g(\rho_s - \rho_g)]^{-0.064} \tag{34}$$

$$\frac{U_{DSU}}{U_t \cdot s} = 22.8\left(\frac{G}{\rho_p (1-s) U_t}\right)^{0.59} Ar^{-0.2} \tag{35}$$

Table 5. Distinction between operation modes based on PEPT measurements (Van de Velden et al., 2008a)

$U\text{-}U_{tr}$ (m/s)	G (kg/m^2s)	U_{up} (m/s)	U_{down} (m/s)	Upward moving particles (%)
0.01	220	1.22	0.68	47
0.22	270	0.98	0.60	52
0.27	462	1.55	0.81	60
0.32	296	1.36	0.72	52
0.42	622	1.68	0.69	62
1.02	251	2.08	0.52	78
1.15	305	2.17	0.13	93
1.47	316	2.73	0.39	92
1.57	263	2.73	0.47	92
2.87	210	4.04	0.02	97
3.17	260	4.33	0.03	96
3.30	347	4.52	0.03	96

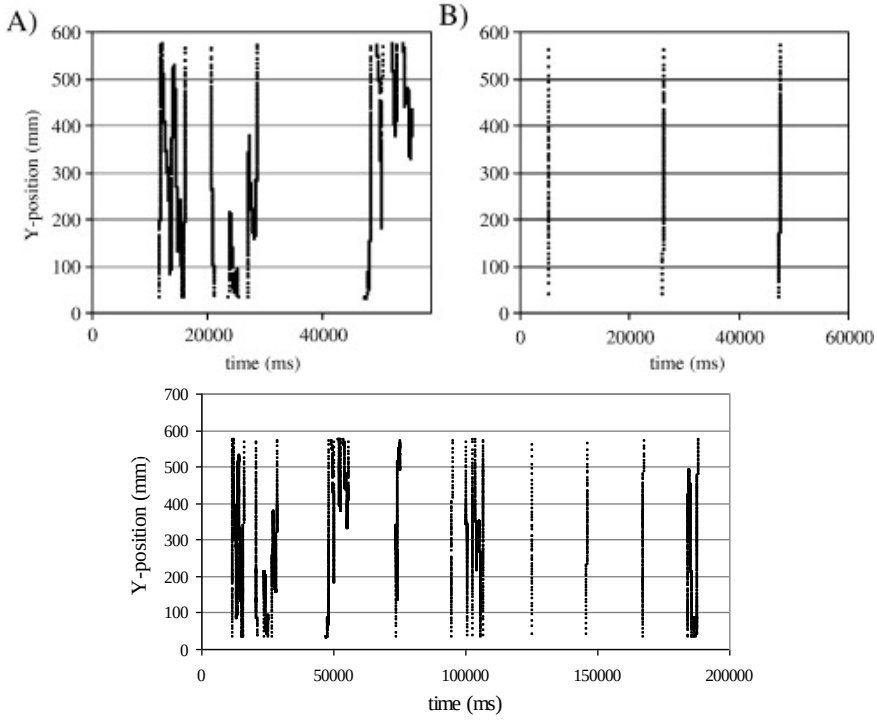

Figure 36 Motion of a solid particle at vertical direction in a riser at A) U = 2.25 m/s and B) 5.2 m/s (U_{tr} = 2 m/s) (Van de Velden et al. 2008a).

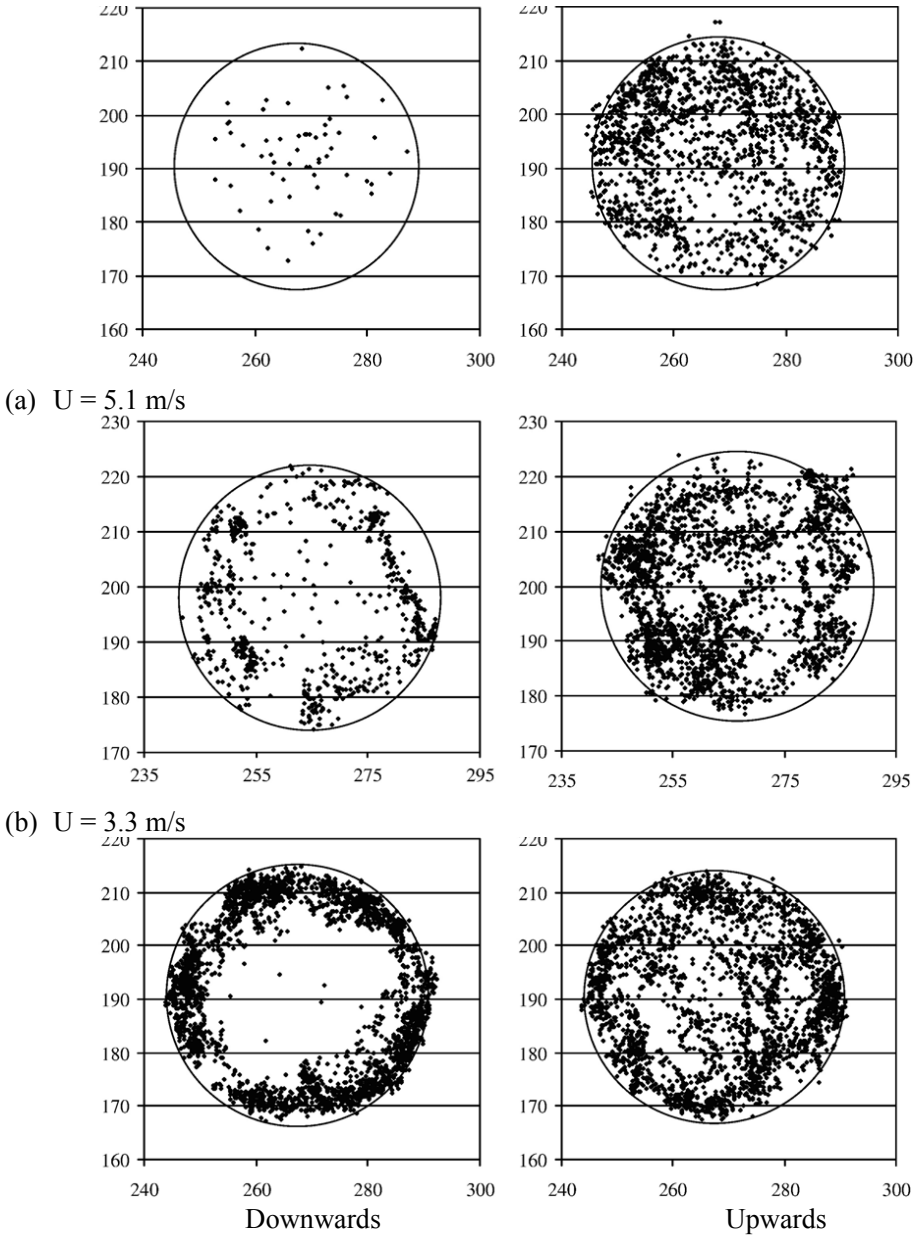

Figure 37. Particle distribution in the cross-section of a riser at G = 260 kg/m^2 s and indicated superficial gas velocity (U) (Van de Velden et al., 2008a; Chan et al. 2010).

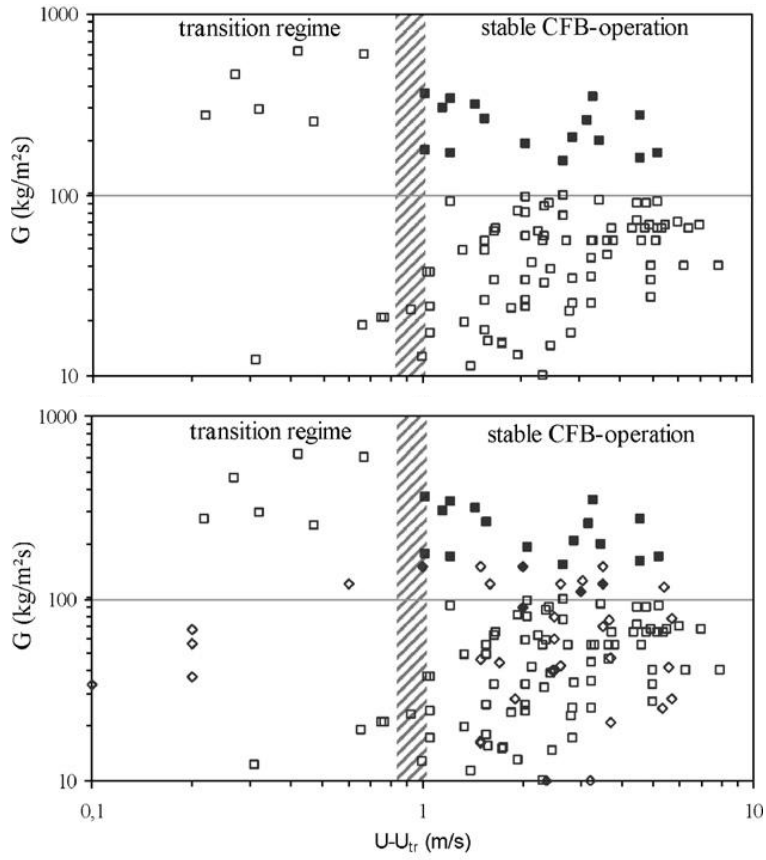

Figure 38. Core flow and core/annulus regime as a function of G and $U - U_{tr}$ (Van de Velden et al., 2008a).

Figure 39. illustrates the operating hydrodynamics over a wide operational condition, in which five distinct flow regimes in a riser as a function of gas velocity U and solid circulating rate G. Zone I is a transition regime. It is not a stable CFB mode. The bed is operated in bubbling or turbulent regime. Zone II is a dilute conveying regime. Particles with a low concentration are conveyed by the air flow, and solids are immediately accelerated upon entering the riser. The solid movement is determined by a constant particle velocity equal to $U-U_t$. Figure 36. shows a typical solid motion in the riser (Chan et al, 2009b). Zone III is a core-annulus flow regime.

The solids circulates (hence high back-mixing) in the riser rather than sprightly travel from the bottom of the riser to the top. A constant exchange of solids between the down flowing annulus and the up flowing core can be clearly seen by PEPT. When a CFB is operated in this mode, a longer solids residence time can be achieved than in dilute conveying. In zone IV, a bubbling/turbulent fluidised bed (BTFB) exists at the bottom of the riser under specific (U, G)-combinations. Solids spend considerably longer time in the BTFB than in the riser. The typical solid motion in the riser has been shown in Figure 32.

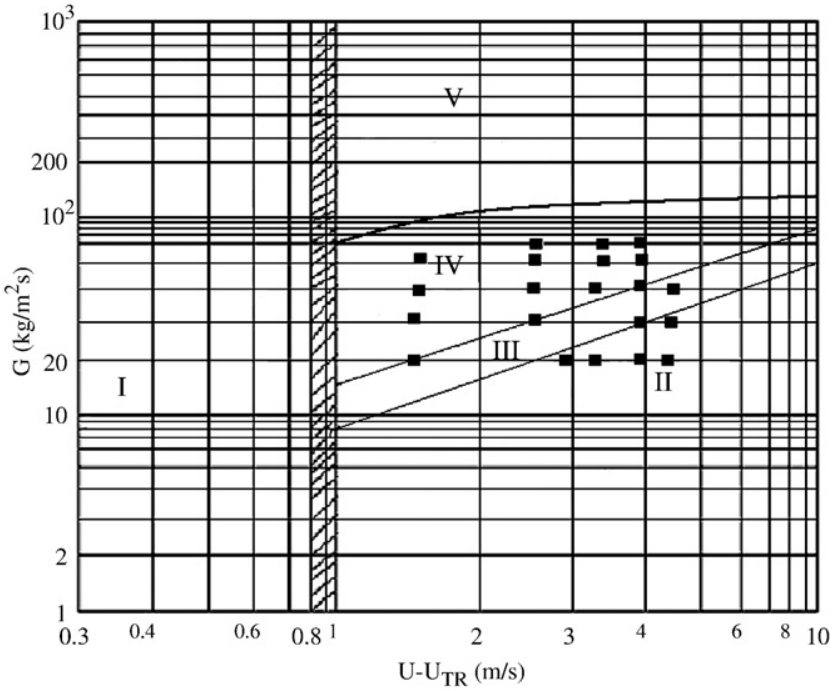

Figure 39. CFB operational modes in related with solid circulating rate and U−UTR (Chan et al., 2009b, Mahmoudi et al., 2010).

The bubbling/turbulent bed (BTFB) at the bottom of the riser is considered as Dense Suspension Zone (not to be confused with Dense Suspension Upflow) in some literature (Kim et al, 2004a; 2004b).

In zone V, a dense suspension upflow (DSU) with a high net upward solids flux and very high solids concentration is achieved at high values of U and/or G as shown in Figure 33. The Dense Suspension Zone becomes fully developed throughout the entire riser cross section (Grace et al, 1999; Gupta and Berruti, 1998; Issangya, et al. 1998; Karri and Knowlton, 1999; Van de Velden et al. 2008b). Figure 40. presents the voidage profile in different CFB regime. The voidage is determined by

$$\varepsilon = \frac{V_{air}}{V_{air} + V_{solid}} \tag{36}$$

where V_{air} is the volume of air in a riser, V_{solid} is the volume of solid in a riser. It can be calculated based on gas velocity, solid flow rate and the residence time of solid and gas in a riser.

$$\varepsilon = \frac{U \times t_a}{U \times t_a + \frac{G}{\rho_P} t_s} \tag{37}$$

where t_a is particle residence time in a riser, t_s is gas residence time in a riser, G is solid flow rate, U is gas velocity.

For dilute and dense flow systems, solids/gas residence times are nearly equal. The Equation 37 can be simplified as

$$\varepsilon = \frac{U}{U + \frac{G}{\rho_P}} \tag{38}$$

In a core-annulus flow, the flux of downward annulus solids, calculated for the cross-sectional area of the annulus region and the average $v_{p,down}$ is of the same order of magnitude as the net solids circulation rate, thus increasing the effective solids circulation flux within the riser by a factor close to 2. The voidage can be calculated by

$$\varepsilon = \frac{U}{U + 2\frac{G}{\rho_P}} \tag{39}$$

The voidage profile in Figure 40. is calculated by using equation 40 based on solid flow rate and the average particle velocity measured by PEPT technique. The calculated bed voidage varies with the height in the riser, and the operational mode.

The voidage ranges respectively from approximately 0.98 in dilute flow; 0.8–0.85 in the bottom fluidized bed, 0.95–0.98 in core-annulus mode, to ~0.9 in DSU (Chan et al., 2009b)

$$\varepsilon = 1 - \frac{G}{\overline{v_P}\rho_P} \tag{40}$$

where, $\overline{v_p}$ is average particle velocity in a riser, ρ_p is particle density.

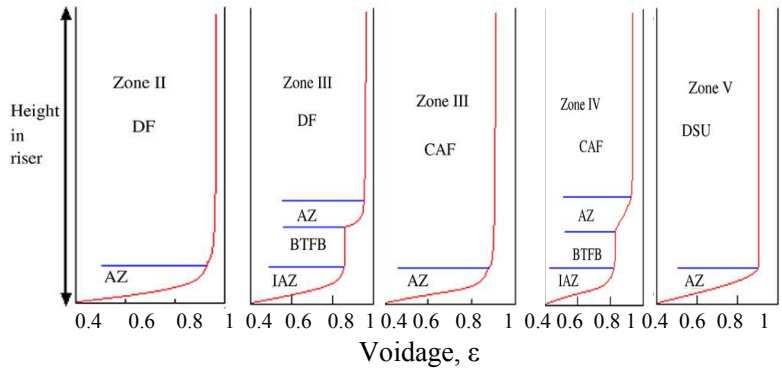

Figure 40. CFB operating regimes in terms of voidage profile (Chan et al. 2009b, 2009c).

4.6. Particle Velocities and Their Residence Time Distribution in the Riser of a CFB

The average particle velocity and the velocity distribution are essential parameters to determine the average particle residence time in the riser and the time distribution. The

average particle residence time is defined as the ratio of the riser height and the average net upward particle velocity (Chan et al., 2010).

$$\bar{t} = \frac{H}{\overline{v_p}} \tag{41}$$

where $\bar{t}$ is the average residence time of solids, [s]. H is Height of riser, [m], $\overline{v_p}$ is average net upward velocity of particle, [m s^{-1}].

In dilute flow, the particle velocity is nearly constant and close to the superficial gas velocity. However, in core-annulus flow the particle velocity is no longer equal to the superficial gas velocity. It varies with flow regimes and solid loading.

Particle velocity in Regime II

In dilute systems, the particle velocity is calculated by equation 42 (Bolton and Davidson, 1988; Yang, 1988; Geldart, 1986):

$$\overline{v_P} = \frac{U}{\varepsilon} - U_{slip} \tag{42}$$

According to Geldart (1986), the slip velocity in dilute flow is close to U_t, thus Eq. (42) gives

$$\overline{v_P} = \frac{U}{\varepsilon} - U_t \tag{43}$$

Operating in a dilute riser (ε~1) at U=5 m/s with a particle of U_t=0.8 m s−1, yields an average velocity, v_p ~4.2 m s−1.

Regime III

Within a restricted range of (U, G)-combinations, a core-annulus flow mode is observed, where particle movement is mostly upward in the core and downward in the annulus, as illustrated in Figure 36. The mechanisms underlying the origin and evolution of the core-annulus flow pattern have not been completely elucidated. There is however evidence that non-ideal particle–particle collisions cause formation of particle agglomerates which form the core-annulus flow structure (Helland et al., 2000; Li and Kuipers, 2004).

In core-annulus flow, the average velocity of the particles accounts for cluster formation: the interaction between the respective extent of downward and upward particles is expressed in a slip factor, φ, typically 2 especially for an industrial CFB (Matsen, 1976).

$$\overline{v_P} = \frac{U}{\varepsilon\varphi} \tag{44}$$

In core-annulus flow mode, with a U of 5 m s^{-1}, ε of 0.98 and φ of 2, the average particle velocity is reduced from 4.2 m s^{-1} in dilute flow to 2.6 ms−1.

Regime IV

As demonstrated in Figure 31, a turbulent fluidised bed can form at the riser bottom under certain conditions when the upper flow is of core-annulus nature. The characteristic core-annulus flow in Regime IV is similar to Regime III, and the same approach applies to this part of the riser flow. To estimate the characteristics of the bottom bed (pressure drop, height), the knowledge of the voidage is imperative. Ouyang and Potter (1993) compiled a list of voidage results and the majority of the data fall within the range of 0.8 to 0.9. Chan et al. (2010) concluded that the equation by King (1989) is the simplest and most accurate approach to predict the voidage at the bottom bed, ε_b:

$$\varepsilon_b = \frac{U+1}{U+2} \tag{45}$$

For example, the voidage of the bottom bed (ε_b) is 0.875 when the bed is operated at U=6m s−1. It is also found that the residence time of the solids in the BTFB, t_b, was between 10–20 s (Chan et al., 2009 b, 2010) as function of U and G. If the pressure drop of the bottom bed is measured (ΔP_{BTFB}), the height is defined by:

$$H_{BTFB} = \frac{\Delta\rho_{BTFB}}{\rho_P(1-\varepsilon_b)} \tag{46}$$

Residence time of solids in the BTFB can be calculated by:

$$t_b = \frac{\rho_P(1-\varepsilon_b)H_{BTFB}}{G} \tag{47}$$

For ash particles (ρ_p=2200 kg m−3) at G=65 kg m−2 s−1 and 4.5 m s−1, ε_b=0.85. At t_b of 20 s, the height of BTFB will be approximately 3.9 m for a pressure drop of 130 mbar. These values are in agreement with the recorded values of the industrial 58 MW CFB combustor of reference (Van de Velden et al., 2007).

Regime V

In a DSU flow mode, the solids velocity is determined by the solids flow rate imposed on the riser, hence

$$\overline{v_P} = \frac{G}{\rho_P(1-\varepsilon)} \tag{48}$$

Empirical equations have however linked v_p to a slip velocity, following Eq. (42), but with $U_{slip} \neq U_t$. The riser voidage will also be lower than in dilute flow as concluded by Grace (2000). For particles with density 2260 kg m−3, circulated at 200 kg m−2 s−1 at ε~0.975, the average particle velocity, v_p=3.5 m s−1 (Chan et al., 2010).

Figure 41. presents the solids velocity in a fully developed regime under dilute flow conditions, including both experimental measurement and the theoretical prediction. The experimental velocity values are slightly lower than the theoretical prediction at a low gas or

solid velocity. The larger deviation of theoretical prediction at a high U or G may be due to annulus formation, and plug behaviour with increasing back-mixing.

Under a constant gas velocity U, solid circulating flux G only marginally influences the final velocity of solids U_{pf}. The acceleration length remains approximately constant at any given *U* and *G* values and is independent of the final solids velocity as shown in Figure 42.

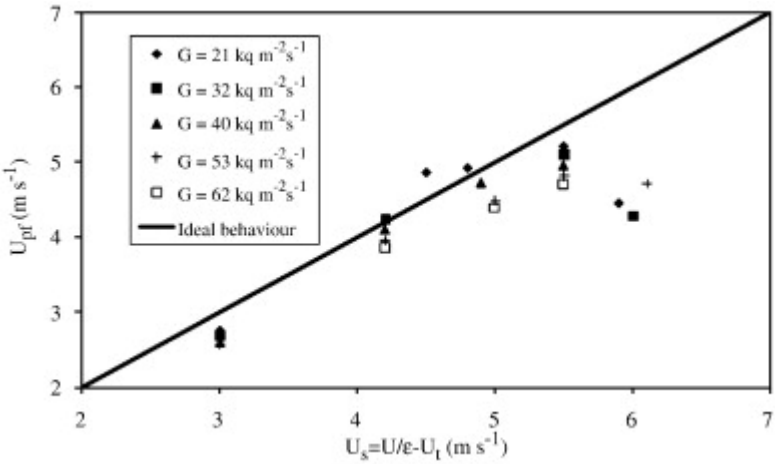

Figure 41. Comparison of theoretical (plug flow) and experimentally determined solids velocity (Chan et al., 2009b).

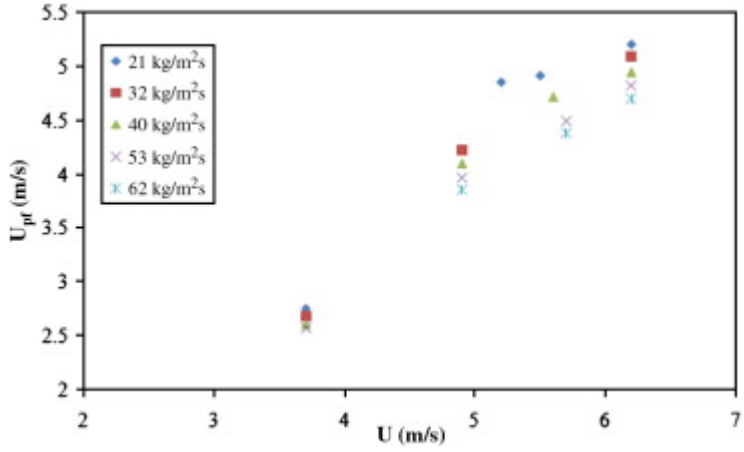

Figure 42. Solids velocity as a function of *U* under various *G* in the fully developed region (Chan et al., 2009b).

The transport velocity, U_{TR}, is the minimum superficial air velocity required in the riser to maintain stable CFB hydrodynamics. Although literature presents numerous equations to predict U_{TR} (Chan et al, 2009c; Bi and Fan, 1992), PEPT research has demonstrated that the Bi and Grace (1995) empirical equation provides a fair albeit safe prediction of the transport velocity for a wide variety of powders (Van de Velden et al., 2008a).

$$\mathrm{Re} = \frac{d_p U_{tr} \rho_g}{\mu} \tag{49}$$

$$Ar = \frac{d_p^3 (\rho_p - \rho_g) \rho_g g}{\mu^2} \tag{50}$$

$$\mathrm{Re}_{tr} = 1.53\ \mathrm{Ar}^{0.50} \tag{51}$$

4.7. Gas Mixing in CFB Risers

The literature on gas mixing in circulating fluidized bed risers is very limited. Gas mixing investigations includes either the overall behaviour or local mixing phenomena. The overall mixing behaviour has been studied through measuring the residence time distribution of a gas tracer in CFB risers, where the gas tracers are injected at the distributor level (Mahmoudi et al, 2010; Patience and Chaouki, 1993, Wang et al., 1996). A local mixing phenomena of a CFB can be obtained from studies where tracer gas is injected and measured at various locations inside the riser (Bader, et al., 1988; Dry, 1986; Li and Weinstein, 1989). The tracer gases used are He, Ar, CH_4, CO_2 etc. The injection of the tracer gas is mostly performed as a pulse (Brereton, 1988).

Three dispersion coefficients used in gas mixing studies are gas axial dispersion coefficient D_{ag} ($m^2\ s^{-1}$), gas back-mixing coefficient D_{bg} and gas radial dispersion coefficient D_{rg}. Gas back-mixing can be obtained from concentration profiles up- and downstream. The relationship among these three coefficient proposed by Schügerl (1967) as below.

$$\frac{D_{ag}}{UD} = \frac{D_{bg}}{UD} + \frac{\beta UD}{D_{rg}} \tag{52}$$

Where β is a parameter related to the nature of the velocity profile in the riser. It is ~0.005 in parabolic flow, 0.0005 in turbulent single phase flow, and 0 in uniform flow.

Gas mixing is often characterised by using a one-dimensional dispersion equation.

$$\frac{\partial C}{\partial t} = D_{ag} \frac{\partial^2 C}{\partial x^2} - \frac{U}{\varepsilon} \frac{\partial C}{\partial x} \tag{53}$$

The axial dispersion coefficient can be obtained from equation 54. It is determined by the slope of the gas tracer curve plotted vs. the distance X from the tracer injection point (Mahmoudi et al, 2010)

$$\ln\left(\frac{C}{C_o}\right) = -\frac{Pe_{ag} X}{L} \tag{54}$$

$$Pe_{ag} = \frac{UL}{D_{ag}} \tag{55}$$

where X is the distance from the tracer injection point [m], Pe_{ag} is the Axial Peclet number of gas, L is the characteristic length, which is equal to the height of the riser in some cases. For operation at high gas velocities, the axial Peclet number of the gas phase is shown to be in the range of 10 to 50 (Cankurt and Yerushalmi, 1978) and the flow of gas can hence be considered in plug flow. A lower value of P_{eag} is measured at lower gas velocities, indicating a larger degree of gas mixing (Mahmoudi et al, 2010).

The gas flow behaviour in a riser is closely linked to the solids flow patterns in a riser. As illustrated in Figures 30-38, solids move predominantly upwards in Zones II and V, where a near plug flow can be achieved. In Zones III and. IV, solids move in the core–annulus flow regime. The downwards moving particles can return some of the gas flow to lower levels in/or even to the bottom of the riser, therefore a back-mixing is possibly achieved.

Mahmoudi et al (2010) investigated the gas residence time in different flow regimes through injecting a pulse of propane to a CFB from underneath the gas distributor. The injection time was less than 0.1 s. The CFB riser consists of a Perspex 100 mm internal diameter pipe with a height of approximately 6.5 m high. The CFB loaded with 90 micron sand particles or 70 micron FCC catalyst, and was operated under a superficial gas velocity from 5.5 to 8.3 m/s, and a solid circulation flux from 40 to 170 kg/m^{2}s. The transport velocity, U_{tr} was 1.7 m/s. Figure 43. presents the propane residence time in the riser as a function of superficial gas velocity. The calculated curve in Figure 43 represents the residence time in the perfect plug flow. The residence time was determined as the ratio of the superficial gas velocity and the distance between injection and sampling point. The systematic and constant difference between the experimental measurement and the theoretical curve in Figure 43 is due to the time lag of injection and detection. It is about 0.2 s.

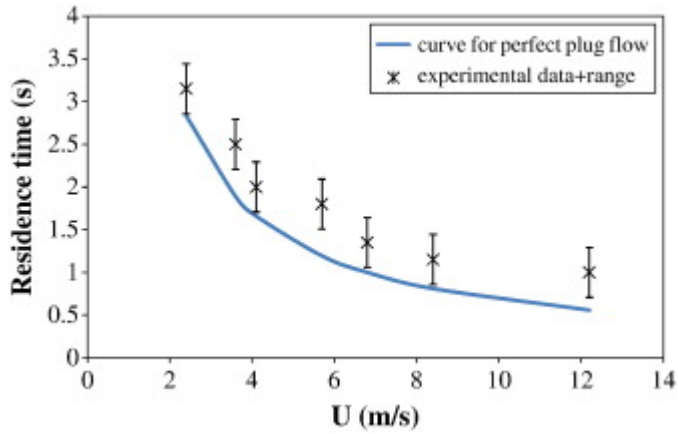

Figure 43. Residence time of propane as a function of superficial gas velocity in a riser without solids being present (Mahmoudi et al 2010).

A number of models have been reported in literature for the calculation of the residence time distribution in a CFB riser, such as the PFD- (plug flow with dispersion), the PTD- (probabilistic time delay) and the FT- (fractional tubularity) model were tested (Nauman and

Buffham, 1983. Nauman, 1987). For a perfectly mixed reactor, Equation 56 was suggested to estimate the gas residence time by Mahmoudi et al (2010).

$$E(t) = \frac{1}{\bar{t}} \exp(-\frac{t}{\bar{t}}) \tag{56}$$

For Cascade of perfectly mixed reactors, the average residence time t_i in each zone can be estimated by Equation 57.

$$E(t) = \frac{1}{(N-1)!\bar{t}_i}(\frac{t}{t_i})^{N-1} \exp(-\frac{t}{\bar{t}_i}) \tag{57}$$

For a plug flow with dispersion model (Pe > 25)

$$E(t) = \overline{t\sqrt{\frac{Pe}{4\pi\theta}} \exp(-\frac{(1-\theta)^2}{4\theta / Pe})} \tag{58}$$

With $\theta = \frac{t}{\bar{t}}$, $\bar{t}$ the mean residence time

$$Pe = \frac{L^2}{\bar{t}D_z} \tag{60}$$

D_z the axial dispersion coefficient

Fractional tubularity model combines plug flow and mixing. The "fractional tubulatirity" (t_p) indicates the contribution of plug flow in the system,

$$E(t) = 1 - \exp(\frac{t_p - t/\bar{t}}{1 - t_p}) \tag{61}$$

Probabilistic time delay model combines plug flow and intermittent mixing cells

$t < t_p$: E(t) = 0

$t > t_p$: $E(t) = \frac{\exp(-(\alpha L + (t - t_p)/t_D)}{t - t_p} \cdot \sum_{N=1}^{\infty} \frac{(\alpha L(t - t_p)/t_D)^N}{N!(N-1)!}$ (62)

where α is the chance for a particle to be retained, t_D is the time when a particle is retained (s), t_p is the residence time for pure plug flow (s). In a plug flow, behaviour of all particles is identical, velocity and residence time are the same.

$$t = t_{pf} : C(t) = C_0 \tag{63}$$

To illustrate the gas behaviour in these different regimes, Mahmoudi et al (2010) normalized cumulative residence times *F(t)* of three representative experiments as shown in Figure 44. and compared the results with model predictions. Similar results were reported for all other (U, G)-combinations (). No definite value can be attributed to Pe for operation in the core–annulus flow mode. None of the models from literature can fit the experimental data over the complete (U, G)-range, although the plug flow and PT models fit near-plug flow results. The occurrence of both mixed flow and plug flow strongly depends on the combination of gas superficial velocity and solids circulation rate. The optimum operating conditions for catalytic gas-phase reactions can be characterized by using a minimal difference between the real average residence time and the theoretical residence time according to the plug flow mode. A significant degree of back-mixing will increase solid gas contact, and might enhances secondary (unwanted) reactions.

The gas phase mixing efficiency in a riser varies with solid flow pattern and bed height. The bed height (H) at which an effective gas mixing can be achieved is determined by t_{50} and σ. The plug flow residence time for gas flow alone, $t_{pf,gas}$ is defined as H/U. Assessment of the gas-phase mixing behavior can be conducted because the F(t)-curve can be linearized between F(t) = 5% and F(t) = 95% as (Mahmoudi et al 2010):

$$F(t) = \frac{0.8}{\sigma t_{50}} t + 0.5 - \frac{0.8}{\sigma} \tag{64}$$

$$t_{50} = 3.68(U - U_{tr})^{-0.25} G^{-0.2}$$

$$\sigma = 0.87(U - U_{tr})^{1.15} G^{-0.54}$$

where: *F(t)* is cumulative residence times, t_{50} is residence time at *F(t)*=50%, , σ is Span, $(t_{90}-t_{10})/t_{50}$.

The residence time distribution function, *F(t),* is important to better assess the gas conversion in the riser, as illustrated for a simple first order reaction. The overall conversion can be calculated as: (k in 1/s)

$$X = \sum F(t)(1 - \exp(-kt_i)) \tag{65}$$

where t_i is stepwise increased from $t_{F(t)} = 0$ *to* $t_{F(t)} = 1$.

The gas flow regime in a CFB riser is closely linked to the solids flow. A nearplug flow can be achieved in Zones II and V, where solids move predominantly upwards. A possible back-mixing can be achieved in the regime of core–annulus flow (Zones III and IV), where some of the gas flow is returned to lower levels in/or even to the bottom of the riser by downwards moving particles. The presence of a turbulent fluidized bed at the bottom of a riser will lead to a different gas flow profile. Gas residence times are short in dilute and DSU operating modes, moderate in core-annulus mode and long for the operation of core-annulus mode with BTFB present.

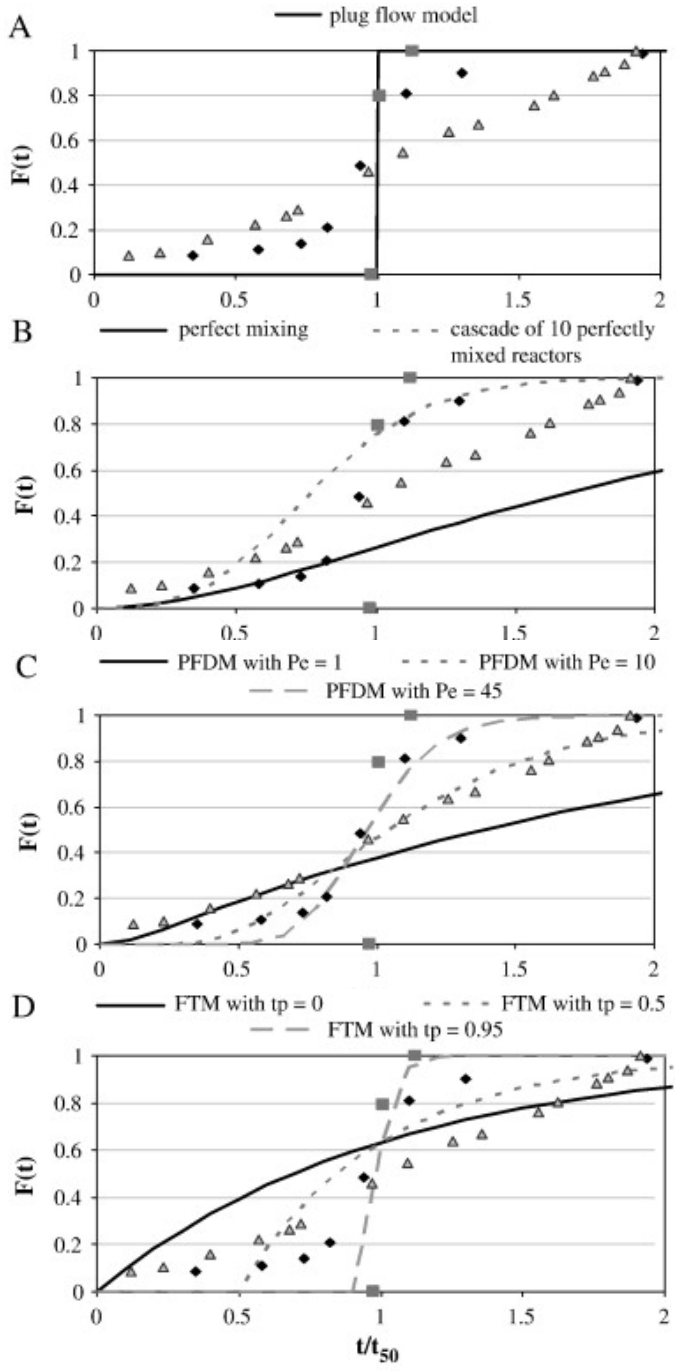

Δ G = 40 kg/m^{2}s, U = 6.0 m/s ■ G = 122 kg/m^{2}s, U = 6.4 m/s
♦ G = 168 kg/m^{2}s, U = 6.4 m/s

Figure 44. Cumulative residence time for A) plug flow model, B) perfect mixed tank reactor and cascade of perfectly mixed tanks, C) PFDM, and D) FTM (Mahmoudi et al 2010).

ACKNOWLEDGMENTS

This chapter is mainly based on our recent PEPT work and publications by Fan, Yang, Baeyens, Chan, Van de Velden and Seville. The authors gratefully acknowledge the work of a number of colleagues and industrial collaborators, particularly Professor David Parker and Mr Mike Smith at Birmingham Positron Imaging Center.

REFERENCES

Agba D., Salman, A.D., Hounslow, M.J. (2007). Fluidized Bed Applications. *Chemical Engineering Science*, 62(1-2), 1.

Almstedt, A.E., Zakkay, V. (1990). An investigation of fluidized bed scaling-capacitance probe measurements in a pressurized fluidized bed combustor and a cold model. *Chemical Engineering Science*, 45, 1071–1078.

Arena, U., Cammarota, A., Pistone, L. (1986). High velocity fluidization behavior of solids in a laboratory scale circulating fluidized bed, in: P. Basu (Ed.), *Circulating Fluidized Bed Technology I*, Pergamon Press, Toronto, 119–125.

Bader, R., Findlay, J., Knowlton, T.M. (1988). Gas/solids flow patterns in a 30.5 cm diameter circulating fluidized bed, in: P. Basu, J.F. Large (Eds.), *Circulating Fluidized Bed Technology II*, Pergamon Press,133–137.

Bai, D.R., Jin, Y., Yu, Z.Q., Zhu, J., (1992). The axial distribution of the cross-sectional averaged voidage in fast fluidized beds. *Powder Technology*, 71, 51–58.

Baron, T., Briens, C. L., Galtier, P., Bergougnou, M. A. (1990). Verification of models and correlations for bubble properties in fluidized beds. *Chemical Engineering Science*. 45(8), 2227-2233.

Baeyens, J., Geldart, D. (1974). An investigation into slugging fluidized beds. *Chemical Engineering Science* 29(1), 255-265.

Berkelmann, K.G., Renz, U. (1991). Gas and solid flow in the freeboard of a fluidized bed combustor. *Powder Technology* 68, 271–280.

Berruti, F., Chaouki, J., Godfroy, L., Pugsley, T.S.; Patience, G.S. (1995). Hydrodynamics of circulating fluidized bed risers: a review, *Canadian Journal of Chemical Engineering* 73, 579–602.

Bi, H.T., Grace, J.R. (1995). Flow Regime Diagrams for Gas-solid Fluidization and upward Transport, *International Journal of Multiphase Flow*, 21, 1229.

Bi, H., Fan, L.S. (1992). Existence of Turbulent Regime in Gas–solid Fluidization, *AIChE Journal.* 38, 297–301.

Bi, H.T., Fan, L.S. (1991). Regime transitions in gas–solid circulating fluidized beds, *AIChE Annual Meeting*, AIChE, Los Angeles, 17–22.

Bokkers G.A., van Sint Annaland, M., Kuipers J.A.M. (2004). Mixing and segregation in a bidisperse gas–solid fluidised bed: a numerical and experimental study. *Powder Technology,* 140, 176– 186.

Bolton, L.W., Davidson, J.F. (1988). Recirculation of Particles in Fast Fluidized Risers, in: P. Basu, J.F. Large (Eds.), *Circulating Fluidized Bed Technology II*, Pergamon, Oxford, 139.

Brereton, C.M.H., Stromberg, L. (1986). Some aspects of the fluid behavior of fast fluidized beds, in: P. Basu (Ed.), *Circulating Fluidized Bed Technology I*, Pergamon Press, Toronto, 133–143.

Brereton, C.M.H., Grace, J.R., Yu, J. (1988). End effects in circulating fluidized bed hydrodynamics, in: P. Basu, J.F. Large (Eds.), *Circulating Fluidized Bed Technology II*, Pergamon Press, 123–127.

Burgess, J.M., Calderbank, P.H. (1975). The measurement of bubble parameters in two-phase dispersions—II: The structure of sieve tray froths. *Chemical Engineering Science*, 30, 1107-1121.

Burschka, A.C. (1993). Wandnahe Partikelbewegung und Wärmeübergang in Gas-Feststoffwirbelschichten, Dr.-Ing. thesis, University Erlangen-Nürnberg.

Cai, P., Schiavetti, M., De Michele, G., Grazzini, G.C., Miccio, M. (1994). Quantitative estimation of bubble size in PFBC. *Powder Techology*, 80, 99-109.

Cankurt, N.T., Yerushalmi, J. (1978). Gas backmixing in high velocity fluidized beds, in: J.F. Davidson, D.L. Kearns (Eds.), *Fluidization*, Cambridge University Press, Cambridge, 387.

Ceccio, S. L., George, D. L. (1996). A review of electrical impedance techniques for the measurement of multiphase flows. *Journal of Fluids Engineering-Transactions of the ASME,* 118(2), 391–399.

Chan, C.W., Seville, J., Fan, X., Baeyens, J. (2008a). Particle Motion in CFB cyclones as observed by Positron Emission Particle Tracking. *Industrial and Engineering Chemistry Research*, 48, 253–261.

Chan, C.W., Seville, J., Fan, X., Dewil, R., Baeyens, J. (2008b). CFB cyclones: pressure drop and particle motion, viewed by positron emission particle tracking, *Proceedings of Circulating Fluidized Bed IX*, Hamburg, Germany, 2008, pp. 981–986.

Chan, C.W., Seville, J., Fan, X., Baeyens, J. (2009a). Particle motion in L-valve as observed by positron emission particle tracking. *Powder Technology*, 193, 137–149.

Chan, C.W., Seville, J., Yang , Z., Baeyens, J. (2009b). Particle motion in the CFB riser with special emphasis on PEPT-imaging of the bottom section. *Powder Technology*, 196, 318–325.

Chan, C.W., Seville, J., Fan, X., Baeyens, J. (2009c). Solid particle motion in a standpipe as observed by Positron Emission Particle tracking. *Powder Technology*, 194, 58–66.

Chan, C.W., Seville, J., Parker, D.J., Baeyens, J. (2010). Particle velocities and their residence time distribution in the riser of a CFB. *Powder Technology*, 203, 187–197.

Cheun U, Y. V, 2009, *Solids Motion in Fluidised Beds of Fine Particles*, PhD thesis, the University of Birmingham.

Cooper S., Coronella C.J. (2005). CFD simulations of particle mixing in a binary fluidized bed. *Powder Technology* 151, 27-36.

Dana S., Shuyan W., Huilin L., Zhiheng S., Xianga L, Shuai W., Yunhua Z., Lixin W. (2009). A second-order moment method of dense gas–solid flow for bubbling fluidization, *Chemical Engineering Science* 64, 5013 -- 5027

Darton, R.C., LaNauze, R.D., Davidson, J.F., Harrison, D. (1977). Bubble growth due to coalescence in fluidised beds. *Transactions of the Institution Chemical Engineering*, 55, 274.

Das, M., Bandyopadhyay, A., Meikap, B.C., Saha, R.K. (2008).Axial voidage profiles and identification of flow regimes in the riser of a circulating fluidized bed. *Chemical Engineering Journal*, 145, 249–258.

Davies, R,M., Taylor, G.I. (1950). The mechanics of large bubbles rising through extended liquids and through liquids in tubes. In: *Proceedings of the Royal Society of London, Series A*, Mathematical and Physical Sciences 200, 375–390.

Ding Y, Wang Z, Wen D, Ghadiri M, Fan X, Parker D. 2005. Solids behaviour in a gas–solid two-phase mixture flowing through a packed particle bed. *Chemical Engineering Science* 60, 5231-5239.

Ding, Y.L., Wang, Z.L., Wen, D.S., Ghadiri, M., Fan, X., Parker; D. (2006). Solids Behaviour in A Dilute Gas-solid Two-phase Mixture Flowing through Monolith Channels, *Chemical Engineering Science,* 61(5), 1561-1570, 2006.

Dry, R.J. (1986). Radial concentration profiles in a fast fluidized bed, *Powder Technology*, 49, 37–44.

Duursma, G.R., Glass, D.H., Rix, S.J.L. (2001). Yorquez-Ramirez MI. PIV investigations of flow structures in the fluidised bed freeboard region. *Powder Technology* 120, 2–11.

Dyakowski, T., Jeanmeure, L. F. C., and Jaworski, A. J. (2000). Applications of electrical tomography for gas–solids and liquid–solids flows—A review. *Powder Technology*, *122*(3), 174–192.

Eames, I., Gilbertson, M.A. (2005). Mixing and drift in gas-fluidised beds. *Powder Technology*, 154, 185 – 193.

Fan, X., Parker, D.J., Smith, M.D. (2006a). Labelling a single particle for positron emission particle tracking using direct activation and ion-exchange techniques. *Nuclear Instrument and Methods A* 562, 345-350.

Fan, X., Parker, D.J., Smith, M.D., (2006b). Enhancing ^{18}F Uptake in A Single Particle for Positron Emission Particle Tracking through Modification of Solid Surface Chemistry, *Nuclear Instrument and Methods in Physics research*, A, 558(2) 542-546.

Fan, X., Parker, D.J., Smith, M.D., Yang, Z., Seville, J.P.K. (2006c). A Simple and Selective Method for Separation of Trace ^{61}Cu from Nickel Solutions, *Nuclear Medicine and Biology*, 33, 939-944.

Fan, X., Yang, Z., Parker, D.J., Seville, J.P.K., Baeyens, J. (2007). The effect of bed materials on the solid/bubble motion in a fluidised bed. *Chemical Engineering Science*, 63, 943 – 950.

Fan, X., Yang, Z., Parker, D.J., Armstrong, B. (2008). Prediction of bubble behaviour in fluidised beds based on solid motion and flow structure. *Chemical Engineering Journal*, 140, 358–369.

Fan, X., Yang, Z., Parker, D.J. (2011). Impact of Solid Sizes on Flow Structure and Particle Motions in Bubbling Fluidization. *Powder Technology*, 206, 132-138.

Gao, K., Wu, J., Wang, Y., Zhang, D. (2006). Bubble dynamics and its effect on the performance of a jet fluidised bed gasifier simulated using CFD. *Fuel*, 85, 1221-1231.

Geldart, D. (1986). Particle Entrainment and Carry-Over, in: D. Geldart (Ed.), *Gas Fluidization Technology*, New York, Wiley, 123–153.

Grace, J.R., Harrison D. (1969). The distribution of bubbles within a gas-fluidized bed. *Institute of Chemical Engineering Symposium Series*, 30, 105–125.

Grace, J.R. (1986). Contacting modes and behaviour classification of gas—solid and other two-phase suspensions, *Canadian Journal of Chemical Engineering*, 64, 353.

Grace, J.R., Issangya, A.S. Bai, D., Bi, H. (1999). Situating the high density circulating fluidized bed, *AIChE* 45, 2108–2116.

Grace, J.R. (2000). Reflections on turbulent fluidization and dense suspension upflow, *Powder Technology*, 113, 242–248.

Gupta, S.K., Berruti, F. (1998). Modeling considerations for large scale high density risers, in: L.S. Fan, T.M. Knowlton (Eds.), *Fluidization IX,* Engineering Foundation, New York, 189–194.

Harland, C.E., (1994). Ion Exchange—Theory and Practice, The Royal Socity of Chemistry, UK.

Hartholt, G.P., Hoffmann, A.C., Janssen, L.P.B.M. (1994). Visual observation of individual particles in fluidized beds, *First Int. Particle Technology Forum*, preprints, Denver, USA.

He Y., Lu H., Sun Q., Yang L., Zhao Y., Gidaspow D., Bouillard J. (2004). Hydrodynamics of gas–solid flow around immersed tubes in bubbling fluidized beds. *Powder Technology* 145, 88– 105.

Helland, E., Occelli, R., Tadrist, L. (2000). Numerical study of cluster formation in a gas-particle circulating fluidized bed, *Powder Technology*, 110, 210–221.

Howard J.R. (1989). *Fluidized bed technology: Principle and applications*. Adam Higer, Bristol and New York, 8-12.

Huang S., Wang Z., Jin Y. (1999). Studies on gas–solid–solid circulating fluidised-bed reactors. *Chemical Engineering Science* 54, 2067–2075.

Ibsen, C.H., Helland, E., Hjertager, B.H., Solberg, T., Tadrist, L., Occelli, R. (2004). Comparison of multifluid and discrete particle modelling in numerical predictions of gas particle flow in circulating fluidised beds. *Powder Technology*, 149, 29-41.

Issangya, A.S., Bai, D., Grace, J.R., Zhu, J. (1998). Solids flux profiles in a high density circulating fluidized bed riser, in: L.S. Fam, T.M. Knowlton (Eds.), *Fluidization IX*, Engineering Foundation, New York, 197–204.

Jagtiani, A. V., Sawant, R., and Zhe, J. (2006). A label-free high throughput resistivepulse sensor for simultaneous differentiation and measurement of multiple particle-laden analytes. *Journal of Micromechanics and Microengineering*, *16*(8), 1530–1539.

Kafui, K.D., Thornton, C., Adams, M.J. (2002). Discrete particle-continuum fluid modelling of gas–solid fluidised beds. *Chemical Engineering Science* 57, 2395 – 2410.

Karri, S.B.R., Knowlton, T.M. (2002) Wall solids upflow and downflow regimes in risers for Group A solids, in: J.R. Grace, J. Zhu, H. de Lasa (Eds.), Circulating Fluidized Bed Technology VII, *CSChE*, Ottawa, Canada, 310–316.

Karri, S.B.R., Knowlton, T.M. (1999). A comparison of annulus solids flow direction and radial solids mass flux profiles at low and high mass fluxes in a riser, in: J. Werther (Ed.), *Circulating Fluidized Bed Technology* VI, DECHEMA, Germany, 71–76.

Kato, K.H., Shibasaki, H., Tamura, K., Arita, S., Wang, C., Takarada, T. (1989). Particle hold-up in a fast fluidized bed. *Journal of Chemical Engineering Japan*, 22, 130–136.

Kim, S.W., Kirbas, G., Bi, H., Lim, C.J., Grace, J.R. (2004a). Flow structure and thickness of annular downflow layer in a circulating fluidised bed, *Powder Technology* 142, 48–58.

Kim, S.W., Kirbas, G., Bi, H., Lim, C.J., Grace, J.R. (2004b). Flow behaviour and regime transition in a high-density circulating fluidized bed riser. *Chemical Engineering Science*, 59, 3955–3963.

King, D. (1989). Estimation of Dense Bed Voidage in Fast and Slow Fludized Beds of FCC Catalyst, in: J.R. Grace, M.A. Bergougnou (Eds.), Fluidization VI, *Engineering Foundation*, New York, 1–8.

Kwauk, M., Wang, N., Li, Y., Chan, B., Shen, Z. (1986). Fast fluidization at ICM, in: P. Basu (Ed.), *CFB Technology* I, Pergamon Press, 33–62.

Kunii, D., Levenspiel, O. (1991). *Fluidization Engineering* (2nd edition). Boston: Butterworth-Heinemann.

Leaper, M.C., Seville, J.P.K., Hilal, N., Kingman, S.W., Burbidge, A.S. (2004). Investigating the dynamics of segregation of high jetsam binary batch fluidised bed systems. *Chemical Engineering Proc.* 43, 187-192.

Li, J., Kuipers, J.A.M. (2005). On the origin of heterogeneous structure in dense gas–solid flows. *Chemical Engineering Science* 60(5), 1251-1265.

Li, J., Kuipers, J.A.M. (2004). Flow structure formation and evolution in circulating gas fluidized beds, *China Particuology*, 2, 1–12.

Li, J., Weinstein, H. (1989). An experimental comparison of gas backmixing in fluidized beds across the regime spectrum, *Chemical Engineering Science*, 44, 1697–1705.

Li, H., Xia, Y., Tung, Y., Kwauk, M. (1991). Micro-visualization of two-phase structure in a fast fluidized bed, in: P. Basu, M. Horio, M. Hasatani (Eds.), *Circulating Fluidized Bed Technology III*, Pergamon, Oxford, 193.

Li, J., Tung, Y., Kwauk, M. (1988). Axial voidage profile of fluidized beds in different operating regions, in: P. Basu, J.F. Large (Eds.), *Circulating Fluidized Bed Technology II*, Pergamon Press, Oxford, 537–544.

Li, Y., Kwauk, M. (1980). In: J.R. Grace and J.M. Matsen, Editors, *Fluidization*, Plenum, New York, 537.

Lim C.N., Gilbertson M.A., Harrison A.J.L. (2006). Measurement and simulation of bubbling fluidised beds. *Powder Technology* 170, 67-177.

Lim C.N., Gilbertson M.A., Harrison A.J.L. (2007). Bubble distribution and behaviour in bubbling fluidised beds. Chemical Engineering Science 62, 56-69.

Link, J.M., Deen, N.G., Kuipers, J.A.M., Fan, X., Ingram, A., Parker, D.J., Wood, J., Seville, J.P.K. (2008). Comparison of PEPT Measurements and Discrete Particle Simulations in a Rectangular 3D Spout-fluid Bed, *AIChE Journal*, 54(5) 1189-1202.

Louge, M. (1996). Experimental techniques, in: J. Grace, T. Knowlton, A.A. Avidan Eds.., Circulating Fluidized Beds, Chap. 9, *Chapman and Hall*, London, 1530–1539.

Lu H., Shen Z., Ding, J., Li, X., Liu, H. (2006). Numerical simulation of bubble and particles motions in a bubbling fluidized bed using direct simulation Monte-Carlo method. *Powder Technology,* 169(3), 159-171.

Mahmoudi, S., Seville, J.P.K., Baeyens, J. (2010). The residence time distribution and mixing of the gas phase in the riser of a circulating fluidized bed, *Powder Technology*, 203, 322–330.

Malcus, S. Cruz, E., Rowe, C., Pugsley, T.S. (2002). Radial solid mass profiles in a highsuspension density circulating fluidized bed. *Powder Technology*, 125, 5–9.

Manyele, S.V., Khayat, R.E., Zhu, J. (2002). Investigation of the hydrodynamics of a high-flux CFB riser using chaos analysis of pressure fluctuations. *Chemical Engineering and Technology*, 25, 801–810.

Matsen, J.M. (1976). Some Characteristics of Large Solids Circulation Systems, in: D.L. Keairns (Ed.), *Fluidization Technology*, *Hemisphere*, 2, 135.

Monazam, E.R., Shadle, L.J., Mei, J.S., Spenik, J. (2005). Identification and characteristics of different flow regimes in a circulating fluidized bed, *Powder Technology*, 155, Issue 1, 17-25.

Mori, S., Kato, K., Kobayashi, E., Liu, D., Hasatani, M., Matsuda, M., Hattori, T., Hirama, T., Takeuchi, H. (1992). Effect of apparatus design on hydrodynamics of CFB, *AIChE*, Symposium Series 289, 17–25.

Mori, C., Wen, C.Y. (1975). Estimation of bubble diameter in gaseous fluidized beds. *AIChE Journal*, 21, 109-115.

Mostoufi, N., Chaouki, J. (2004). Flow structure of the solids in gas–solid fluidized beds. *Chemical Engineering Science*, 59, 4217 – 4227.

Nauman, E.B., Buffham, B.A., (1983). *Mixing in Continuous Flow Systems*, John Wiley and Sons, New York

Nauman, E.B. (1987). *Chemical Reactor Design*, John Wiley and Sons, New York.

Ouyong, S., Potter, O.E. (1993). Consistency of circulating fluidized bed experimental data. *Industrial and Engineering Chemistry Research*, 32, 1041–1045.

Pallarès, D., Filip Johnsson F. (2006). A novel technique for particle tracking in cold 2-dimensional fluidized beds—simulating fuel dispersion. *Chemical Engineering Science*, 61, 2710- 2720.

Parker D.J., Broadbent C.J., Fowles P., Hawkesworth M.R., Mcneil P. (1993). Positron Emission Particle Tracking – a technique for studying flow within engineering equipment, *Nuclear Instruments and Methods A*. 326, 592-607.

Parker, D.J., Allen, D.A., Benton, D.M., Fowles, P., McNeil, P.A., Tan, M., Beynon, T.D., (1997). Developments in particle tracking using the Birmingham Positron Camera. *Nuclear Instruments and Methods in Physical Research A* 292 (1997) 421–426.

Parker, D.J., Fan, X. (2008). *Positron emission particle tracking—Application and labelling techniques. Particuology*, 6, 16-23.

Parker, D.J., Leadbeater, T.W., Fan, X., Hausard, M.N., Ingram, A., Yang, Z., (2009). Positron emission particle tracking using a modular positron camera, *Nuclear Instruments and Methods in Physics Research Section A: Accelerators, Spectrometers, Detectors and Associated Equipment*, *604, 339-342.*

Patience, G.S., Chaouki, J., Berruti, F., Wong, R. (1992). Scaling considerations for circulating fluidized bed risers, *Powder Technology*, 72, 31–37.

Patience, G.S., Chaouki, J. (1993). Gas phase hydrodynamics in the riser of a circulating fluidized bed. *Chemical Engineering Science*, 48, 3195–3205.

Porion, P., Sommier, N., Faugere, A. M., and Evesque, P. (2004). Dynamics of size segregation and mixing of granular materials in a 3D-blender by NMR imaging investigation. *Powder Technology*, *141*(1/2), 55–68.

Powell, R. L. (2008). Experimental techniques formultiphase flows. *Physics of Fluids*, *20*(4) (Art. No. 040605).

Pugsley, T.S., Berruti, F.A. (1996). Predictive model for circulating fluidized bed risers. *Powder Technology*, 89 (1996) 57–69.

Rhodes, M.J. Geldart, D., (1989). The upward flow of gas/solid suspensions, part I: A model for the CFB incorporating dual level entry into the riser, *Chemical Engineering Research and Design*, 67, 20–29.

Rhodes, M.J. Geldart, D. (1986). The hydrodynamics of circulating fluidized beds, in: P. Basu (Ed.), *Circulating Fluidized Bed Technology I*, Pergamon Press, Toronto, 193–206.

Rhodes, M.J., Sollaart, M., Wang, X.S. (1998). Flow structure in a fast fluid bed, *Powder Technology*, 99, 194–200.

Rix, S.J.L., Glass, D.H., Greated, C.A. (1996). Preliminary studies of elutriation from gas-fluidised beds using particle image velocimetry. *Chemical Engineering Science* 51, 3479-3489.

Rowe, P.N., Yacono, C.X.R. (1976). *Chmical Eneinrcrhs Science*, 31, 1179-1192. Pergamon Press. Printed in hat Britain.

Rowe, PN. (1976). Prediction of bubble size in a gas fluidised bed. *Chemical Engineering Science*, 31, 285-288.

Samuelsberg, A., Hjertager, B.H. (1992). An experimental and numerical study of flow patterns in a circulating fluidized bed reactor fluidized bed risers. *Powder Technology*, 72, 31–37.

Sánchez-Delgado, S., Marugán-Cruz, C., Acosta-Iborra, A., Santana, D. (2010). Dense-phase velocity fluctuation in a 2-D fluidized bed. *Powder Technology*, 200, 37–45.

Salman, A.D., Hounslow, M,J. (2007). Fluidized Bed Applications. *Chemical Engineering Science*, 62(1-2).

Schügerl, K. (1967). Experimental comparison of mixing processes in two- and three-phase fluidized beds, in: A.A.H. Drinkenburg (Ed.), *Proceedings of the International Symposium on Fluid*ization, Netherlands University Press, Amsterdam, 782–794.

Seville, JPK, Willett, C.D., Knight, P.C. (2000). Interparticle forces in fluidisation: a review. *Powder Technology*, 113 261-268.

Shibata K., Shimizu M., Inaba S., Takahashi R., Yagi J. (1991). Pressure loss and hold-up powders for gas-powder two-phase flow in packed beds. *ISIJ International* 31, 34–439.

Smolders K., Baeyens J. (2001). Gas fluidized beds operating at high velocities: a critical review of occurring regimes. *Powder Technology*, 119, 269-291.

Song, G. M., Yuan, H. Y., Tang, Y., Song, Q. J., and Ge, Y. J. (2006). A novel three-axis force sensor for advanced training of shot-put athletes. *Sensors and Actuators A-Physical*, *128*(1), 60–65.

Sun, D., Wang, S., Lu, H., Shen, Z., Li, X., Wang, S., Zhao, Y., Wei, L. (2009). Second-order moment method of dense gas–solid flow for bubbling fluidization. *Chemical Engineering Science*, 64, 5013-5027.

Sun, J.S., Burgess, J.M. (1987). A laser-based method for bubble parameter measurement in two dimensional fluidised beds. *Powder Technology,* 49, 165-175.

Takeuchi, H., Hirama, T. (1991). Flow visualization in the riser of a circulating fluidized bed, in: P. Basu, M. Horio, M. Hasatani (Eds.), *Circulating Fluidized Bed Technology III,* Pergamon, Oxford, 177–182.

Takeuchi, H., Hirama, T., Chiba, T., Biswas, J., hung, L.S. (1986). A Quatitative Definition and Flow Regime Diagram and for Fast Fluidization. *Powder Technology*, 47, 195-199.

Van de Velden, M., Baeyens, J., Seville, J.P.K., Fan, X. (2008a). The solids flow in the riser of a CFB viewed by positron emission particle tracking (PEPT), *Powder Technology*, 183, 290–296.

Van de Velden, M., Baeyens, J., Boukis, I. (2008b). Modelling CFB biomass pyrolysis reactors. *Biomass and Bioenergy*, 32, 128–139.

Van de Velden, M., Baeyens, J., Dougan, B., McMurdo, A. (2007). Investigation of operational parameters for an industrial CFB combustor of coal, biomass and sludge. *China Particuology*, 5, 247–254.

Wallis, G.B. (1969). *One-dimensional Two-Phase Flow*, McGraw-Hill, New York.

Wang, Q. Zhou, J., Tu, J., Luo, Z., Li, X., Fang, M., Cheng, L., Ni, M., Cen, K.(1996). Residence time in circulating fluidised bed, in: M. Kwauk, J. Li (Eds.), *Circulating Fluidised Bed Technology* V, Science Press, Beijing, 128–133.

Wang, J., van der Hoef, M.A., Kuipers, J.A.M. (2010). Coarse grid simulation of bed expansion characteristics of industrial-scale gas–solid bubbling fluidized beds. *Chemical Engineering Science*, 65(6), 2125-213.

Weinstein, H., Li, J. (1989). An evaluation of the actual density in the acceleration section of vertical risers. *Powder Technology*, 57, 77–79.

Werther J., Molerus O. (1973). The local structure of gas fluidized beds-I. A statistically based measuring system. *International Journal of Multiphase Flow* 1, 103–122.

Werther, J. (1983). Hydrodynamics and mass transfer between the bubble and emulsion phases in fluidized beds of sand and cracking catalyst, in Fluidization, Eds. D.Kunii and R.Toei, Engineering Foundation, New York, 93.

Werther, J. (1999). Measurement techniques in fluidized beds. *Powder Technology*, *102*(1), 15–36.

Whitehead, A.B., Young, A.D. (1967). In: *Proc. Intern. Symp. on Fluidisation*, Eindhoven, U.P., Amsterdam, 284 Netherlands .

Wong, R., Pugsley, T., Berruti, F. (1992). Modelling the axial voidage profile and flow structure in risers of circulating fluidized beds. *Chemical Engineering Science*, 47, 2301–2306.

Yang, H., Gautam, M. (1995). Experimental study on the surface of core-annulus flow in the riser of a circulating fluidized bed. *Powder Technology*, 85, 57–64.

Yang, W.C. (1994). "Incipient Fast Fluidization Bouniary and Operational Maps for Circulating Fluidized Bed Systems", in "Circulating Fluidized Bed Technology IV", A. A. Avidan, Ed., *American Institute of Chemical Engineers*, New York, 62-69.

Yang, W.C. (1988). A Model for the Dynamics of a Circulating Fluidized Bed Loop, in: P. Basu, J.F. Large (Eds.), *Circulating Fluidized Bed Technology II*, Pergamon, Oxford, 181.

Yang, Z., Parker, D.J., Fryer, P.J., Bakalis, S., Fan, X. (2006). Multiple-particle tracking – an improvement for positron particle tracking, *Nuclear Instrument and Methods A* 564, 332-338.

Yang, Z., Fan, X., Bakalis, S., Parker, D.J., Fryer, P.J. (2007a). Multiple-positron emission particle tracking - a technique for studying flows within engineering equipment. *AIChE Journal*, 53, 1941-1951.

Yang, Z., Bakalis, S., Fan, X., Parker, D.J., Fryer, P.J. (2007b). An Improved Algorithm for Tracking multiple, Freely Moving Particles in A Positron Emission Particle Tracking System. *Nuclear Instruments and Methods in Physics Research Section A*, 577, 585-594.

Yang, Z., Fan, X., Bakalis, S., Parker, D.J., Fryer, P.J. (2008a). A method for characterising solids translational and rotational motions using Multiple-Positron Emission Particle Tracking (Multiple-PEPT). *International Journal of Multiphase Flow*, 34(12), 1152-1160.

Yang, Z., Fan, X., Bakalis, S., Parker, D.J., Fryer, P.J. (2008b). Impact of solids fraction and fluid viscosity on solids flow in rotating cans. *Food Research International*, 41(6), 658-66.

Yasui, G., Johanson, L.N. (1958). Characteristics of Gas Pockets in Fluidized Beds, *AIChE Journal*, 4(4), 445-452.

Yerushalmi, J., Cankurt, N. T., Geldart, D., Liss, B., (1978). "Flow Regimes in Vertical Gas-Solids Contact Systems", *AICHE Symp. Ser*. 74, No. 176, 1.

Yerushalmi, J., Cankurt, N.T. (1979) Further Studies of the Regimes of Fluidization. *Powder Technology*, 24, 187.

Zhang, Q., Huang, C., Jiang, D., Wei, X., Qian, Z., Wei, F. (2009). Particle Measurement Sensor for in situ determination of phase structure of fluidized bed. *Particuology*, 7175–182.

In: Catalytic Combustion
Editor: Sophie A. Cottilard, pp. 75-104
ISBN: 978-1-61324-279-7

Chapter 2

THE CATALYTIC COMBUSTION OF SOOT

Jian Liu, Zhen Zhao* and Chunming Xu*
State Key Laboratory of Heavy Oil, College of Science,
China University of Petroleum
Beijing, 102249, P.R. China

ABSTRACT

In this paper, the background of the emission of soot particulates and the formation mechanism of soot have been briefly reviewed. The structure, chemical characteristic of soot emitted from diesel engine exhaust gases and its adverse to the people 's health have been described. Emission standards of soot particulates have been proposed and outlined to reduce remarkably the harmful emissions of diesel engines. There are several methods for reducing soot particulates.

Firstly, soot particulates emissions could be reduced by improving diesel oil qualify and optimizing the fuel composition, or by using an alternative fuel. Although significant, emission reductions obtained in this way were not sufficient to fulfill the higher emission targets.

Secondly, soot particulates emissions could be diminished by modifying the diesel engine. Technological advances could attain the EU-IV emission target by engine modifying alone.

Finally, for the higher emission targets desired, the both above methods were not completely fulfilled. Thus, an important aftertreatment technology must be applied.

The combination of traps and oxidation catalysts is one of the effective aftertreatment methods. Although this method involves many technological difficulties to be overcome (the development of efficient and thermally stable traps, the contact between catalyst and trapped soot, etc.), the active catalysts is considered to be the most important one.

Several kinds of important catalysts for the catalytic combustion of soot including low-melting point catalyst, noble metal catalysts, complex oxide catalysts, and macroporous-based catalysts were detailed reviewed. In the end, the key scientific problems and development trends in soot particulates emission control will be outlined and discussed.

*Corresponding author: e-mail: zhenzhao@cup.edu.cn; xcm@cup.edu.cn

1. THE ORIGINATION AND FORMATION MECHANISM OF SOOT

Soot is produced by incomplete combustion of fossil fuels and biomass. Soot is mainly originated from diesel engine emission, and also small part of soot is produced from lean-burned gasoline engine emission and municipal waste combustion. Therefore, the main strategy of controlling soot emissions is to reduce and remove the diesel soot. Here, it is noteworthy that the different concept should be distinguished between soot and diesel particulates. Diesel particulates are defined by the US Environmental Protection Agency (EPA) as "all compound collected on a pre-condition filter in diluted diesel exhaust gases at a maximum temperature of 50 °C". These particulates consist of soot nuclei including inorganic material, adsorbed hydrocarbons (often referred to as SOF: soluble organic fraction), SO_3 (or sulphuric acid) and some water. However, the term soot is given to the particulates formed during combustion of carbonaceous fuels under substoichiometric conditions, either by design e.g. for the production of carbon black, or in poor mixing conditions (e.g. diesel soot). Soot forms during incomplete combustion of fuels and typically contains 80-95% carbon atoms. Soot is mainly comprised of aggregates of spherical primary particles. The primary particles from petroleum fuel combustion have a diameter of 10 nm - 1 μm with highly disordered graphitic structures. In addition to the spherical graphitic bodies, soot contains varying quantities of native organic material. The relative abundance of soot carbon and organic material highly depends on the fuel type and the combustion conditions, and the reported experimental values also depend on the quantification methods. The fraction of carbon that has been removed by volatilization and/or oxidation up to the threshold temperature is defined as organic carbon (OC). The remaining resistant fraction of carbon is termed elemental carbon (EC) or black carbon (BC). EC refers to the results of thermal-optical analysis (TOA), while BC refers to material measured optically [1, 2].

Soot formation occurs in the high temperature, fuel-rich reaction zone around individual fuel droplets, where fuel hydrocarbons are oxidized under substoichiometric oxygen conditions. This reaction is limited by the oxygen concentration. Oxygen transport occurs by diffusion through the flame front, and this type of reaction zone is therefore called a diffusion flame. Another flame type which occurs in combustion processes is the premixed flame, i.e. the combustion of a premixed amount of fuel and air. Temperatures in premixed flames are higher than in diffusion flames. As studies on soot formation in diesel engine cylinders pose practical problems, many studies have been performed under model conditions. Diffusion flames in burner are often studied. Soot formation processes in burner diffusion flames do not fundamentally differ from those in diesel engines. With solid fuels, e.g. coal, soot is formed by the pyrolysis of tarry materials ejected by particles undergoing devolatilisation. The droplets dehydrogenate and/or partially oxidize into chains of soot spherules.

The soot from various sources, i.e. from different fuels and combustion conditions tend to be similar in size and composition, which indicates that the same formation and growth processes. It is universally accepted that a number of elemental steps including pyrolysis, nucleation, surface growth and coagulation, aggregation and oxidation take place in the formation processes of soot [2, 3]. These processes take place on different time scales, ranging from a few microseconds (initial nucleation processes) to some milliseconds (completion of soot formation, oxidation, and cooling by cylinder expansion).

Pyrolysis is the process in which gas-phase molecules from soot precursor molecules by free radical mechanisms. Two different types of pyrolysis can be distinguished: pyrolysis in oxygen-free reaction zones (often called “pure pyrolysis”) and pyrolysis in oxygen-containing reaction zones. Diffusion flame studies in burner at atmospheric pressure and relatively low temperatures indicate that pyrolysis is an order of magnitude faster in the presence of small amounts of oxygen (as O_2, O^- or OH) than in oxygen-free diffusion flame, and references therein). This accelerating effect decreases with increasing temperature and with decreasing air–to-fuel ratio. In both types of pyrolysis it is generally accepted that both alophatic and aromatic fuel molecules will first break down into olefins and then form acetylene. This molecules is generally thought to be a major soot precursor. An additional route involves the reactions of biomass pyrolysis fragments. A representative species is eugenol which undergoes side-chain cracking, followed by conventional phenol decomposition reactions, and also decomposition and reaction via cyclopentadiene.

Nucleation is the process in which soot precursor molecules grown into small soot nuclei. Nucleation is, in fact, a misleading term, as soot nuclei can be regarded as larger PAH molecules. Inception would therefore be a more appropriate name for this process, however, “nucleation” remains the commonly used term. The oxidation of pyrolysed diesel fuel molecules take place at high temperatures and at high concentrations of reactive compounds such as ions and radicals of hydrocarbons, O* and *OH. Under these conditions, the decomposition rate of some nuclei is lower than their rate of reaction with other unsaturated, charged or radical hydrocarbons, resulting in a net growth of the soot nuclei.

Surface growth is the process in which the precursor molecules grow from some 1-2 nm to 10-30 nm. The most important reaction is thought to be the fast addition of acetylene or polyacetylene molecules by mechanisms similar to nucleation. The H/C ration of the soot decreased during this process This is the result of the addition of polyacetylene, which has a much lower H/C ratio than the original nuclei, and of dehydrogenation reactions. The rate of soot formation during growth was reported to depend only upon the number of nuclei present. Surface growth accounts for most of the soot formed (mass base). It occurs a few μs to 0.05 ms after the formation of nuclei. Simultaneously, another process takes place, coagulation. Small soot particulates collide and coalesce , forming larger, still more or less spherical particles. Although this process contributes to the growth is still assumed to be the major growth process during this stage of soot formation.

Aggregation or chain-forming coagulation, which starts at 0.02-0.07 ms after nucleation, accounts for the formation of the well-known fractal structure of soot. The process occurs outside the cylinder and no chain-like structures are found by cylinder sampling. The soot spheres, now of the order of 20 nm, collide at a rate proportional to the square number of spheres, and form chain-like structures with final dimensions of some hundreds of nanometers. For this part of the mechanism, there is no difference between soot from hydrocarbon fuels and from biomass.

Oxidation of soot takes place lowering the soot tail-pipe emission. Soot oxidation is thought to take place both inside and outside the cylinder. In diesel engine, the soot formation mainly takes place at the beginning of the diffusive combustion phase. At that time, the fuel spray has been separated by entrainment air flow, and the fuel drop is surrounded by high-temperature production left by premixed combustion. Meanwhile, the higher temperature air and later mixing disturbance will accelerate the oxidization of soot, and the agglomerate time of carbon particles can be shortened. During surface growth and coagulation, oxidation

reactions do not seem to play an important role. However, the soot formed in the later combustion phase is difficult to oxidize for two reasons. First, it is close to the end of the combustion period, and second, the temperature decreases rapidly in expansion stroke. In the same manner, the soot produced during the main combustion phase will not be oxidized easily for the lower temperature in-cylinder. It is well known that the soot oxidization can be carried through only in combustion and expansion strokes, because all the oxidization reactions have to stop if the temperature in-cylinder decreases dramatically when the exhaust valve opens. A certain amount of fuel inducted in the later combustion phase enhances the disturbance of fuel/air mixture in-cylinder. Their burning again raises the temperature in-cylinder additionally, which promotes the oxidization of the incomplete combustion production [4]. The main oxidizing species are reported to be *OH, O*, and O_2, although CO_2 and H_2O may also oxidize soot to some extent. In the exhaust tail-pipe of diesel engine, exhaust gases cool down. Hydrocarbons of relatively low vapor pressure, sulphates and sulphuric acid bound water will condense on the soot. The resulting conglomerates are called particulates.

2. THE ADVERSE AND EMISSION REGULATIONS OF SOOT

Soot particles have been arguably concerned on the widest range of potential environmental impacts, including health effects, climate change, ecological effects, and visibility. Freshly emitted soot particles are typically hydrophobic and unlikely to act as cloud condensation nuclei. However, chemical and physical aging during atmospheric transport considerably alters hygroscopicity, morphology, and composition of soot particles, resulting in stronger direct and indirect effects of soot on climate [5]. Different chemical composition in soot particles should have different influence for environment. Sulfate aerosols reflect sunlight, but elemental carbon (EC) particles absorb light, with opposite influences on climate change [6,7].

Numerous epidemiological studies reveal a small yet persistent association between ambient soot particulates levels and a variety of primarily cardio-pulmonary adverse health effects [8,9]. Soot particles are emitted as complex aggregates, and their structure is directly related to their atmospheric fate and deposition efficiency in the human respiratory system [5]. Diesel particulates are so small that they can penetrate the respiratory tract of the human or animal lung and are lung and are deposited in the pulmonary region of the lung, where they may cause adverse health effects. In outdoor air, diesel particulates contribute to the total concentration of so-called total suspended particulates (TSP). A fraction of this TSP, denoted PM-10 (roughly, the particulates smaller than 10 μm), enters the human lung. All diesel particulates can be classifies as PM-10. It has been found difficult to correlate causes of death to exposure to diesel engine gases or PM-10 during a person's life. It has been made plausible that a statistical relationship exists between exposure to diesel exhaust gases and particulates and a tendency towards lung disorders and a higher daily mortality. Moreover, high concentrations of other poorly soluble respirable particles (quartz, coal dust, titanium oxide, etc.) also cause increased incidence of lung tumour, which has been attributed to stress of the lungs. The stress of the lungs may be a caused by the very high particle concentrations and the chemical genotoxity of soot particulates-related compounds [2]. In addition to a possible

effect on lung cancer, diesel particulates are also suspected of increasing bladder cancer. Maudetrly reviews the epidemiological studies performed on bladder cancer increase, and comes to a conclusion similar to that found for lung cancer: ”there appears to be a small positive risk for bladder cancer among ling-term workers in occupations with high presumed exposures to diesel exhaust” [10]. It is noteworthy that PM emission reductions are not equally translated into ecotoxicity reductions, according to the research results by Elias Vouitsis et al. [11].

Besides having adverse effects on atmospheric environment and human health, diesel exhaust gases have other undesired properties. Diesel particulates contributing significantly to the soiling of buildings, as the “blackness” (light absorption properties) of diesel particulates, which in environmental studies are often denoted as “black smoke”, is much higher than the blackness of other fine particulates. Soiling is mainly an aesthetic problem, which cannot easily be quantified. This effect, however, is largely recognized by the general public. In addition, this soiling can cause substantial damage to the materials exposed, which is due to a combination of chemical and polluting effects. Finally, diesel particulates reduce visibility and diesel exhaust gases have an unpleasant smell, presumably caused by aldehydes present in the gases.

The awareness of the detrimental effects of soot emissions to the environment and human health has brought about deep concern and strict regulation by many state government. In the early 1970s, automotive exhaust emission regulations were introduced in both Europe and the United States of America. These first standards applied to light-duty vehicles, a general term for passenger cars. These standards, expressed in grams of regulated compound per mile, were so lenient that passenger cars could easily fulfill them. In the following years the regulations have been increasing tightly, leading to the development of the three-way catalyst. Particulate standards were introduced in 1982 only for light-duty vehicles and not until 1990 for heavy-duty engines. The rapid changes in government air quality and emission regulations take place over the present decade. In Europe, the starting emission standards operative in 1993 and 1994 are denoted as “Euro-I” standards, and the limits to be implemented in 2008 are referred to as “Euro-V” standards. “Euro-VI” standards are still under discussion and will become effective in 2012. In the United States of America, the 49 States have implemented the emission standards. Because of greater air pollution problems, California itself has the most stringent standards in the world. Many other countries have diesel emission standards, which are often derived from the emission standards for the EU, USA or Japan. In general, they are less stringent from than the USA federal emission standards. The EPA Tier II and 2007 heavy duty diesel (HDD) regulations limit PM emissions to 10 mg/mi and 10 mg/hp^{-h}, respectively, for light-duty and heavy-duty vehicles. Europe’s Euro-V standard is now being implemented and this Euro V rules requires for light-weight motor vehicles (i.e. with a weight up to 2500 kg) a fivefold decrease of soot emissions if compared to the previous Euro IV regulations, from 0.025 g/km (Euro IV) to 0.005 g/km (Euro V). An even more drastic reduction is expected for soot with the coming Euro VI rules. And Japan has limited soot emissions to 5 mg/km beginning in 2009. Additional regulations apply to non-road applications. In 2004 the EPA promulgated its Clean Air Nonroad Diesel—Tier 4 Final Rule (US EPA, 2004). These regulations mandate emission reductions of greater than 90% for construction, agricultural and industrial diesel-powered equipment, consistent with the measures applied to motor vehicles. These standards can be also online consulted from www.diesel.net.com.

3. The Structure and Chemical Characterization of Soot

The chemical properties of soot particulate matter (PM) in diesel vehicle exhaust were different when emission regulations, diesel technology development, and particle characterization techniques are all undergoing rapid change. Particle composition is of central interest to the practical issues of health effects, climate change, source apportionment, and aerosol modeling.

As regulations drive down the allowed tailpipe emission levels, advances in engine and aftertreatment technology have made it possible to substantially reduce PM emissions. Besides the reduction in level, new technologies such as diesel particulate filters (DPFs) and selective catalytic reduction (SCR) can also affect the physical and chemical properties of PM.

Soot particulates consists of two types of particles: (a) fractal-like agglomerates of primary particles 15–30 nm in diameter, composed of carbon and traces of metallic ash, and coated with condensed heavier end organic compounds and sulfate; (b) nucleation particles composed of condensed hydrocarbons and sulfate. The Raman spectrum analysis demonstrates a more homogeneous structure with a lower content of molecular carbon for EURO VI and EURO IV soot than for spark discharge carbon, and a higher degree of disorder and a higher amount of molecular carbon for untreated spark discharge carbon samples than for untreated EURO VI and EURO IV soot [12]. The sulphur is apparently present as compounds adsorbed onto the surface (as sulphates), whereas the oxygen is strongly bonded. FTIR analysis reveals the presence of -C-C-, -C=C-, -C=O-, C–O–C and C–OH bonds, and some aromatic structures. Apart from carbon, hydrogen, nitrogen, and oxygen, also sulphur, iron, and silicon have been found to be the major inorganic components of diesel particulates.

The surface of soot diesel particulates contains the highest oxygen concentrations in the form of partly oxygenated absorbed hydrocarbons, sulphate and water, and surface oxygen complexes on the carbon core of the particulates, as phenol, carbonyl and carboxyl groups. A schematic representation of soot particulates has already been shown in Figure 1 [13].

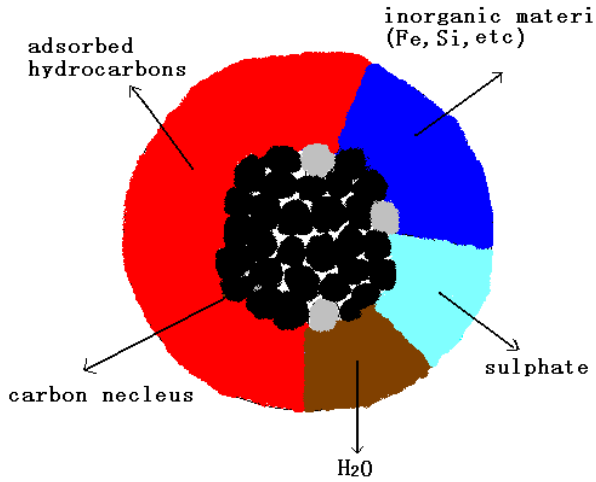

Figure 1. The scheme for the composition of diesel particulates.

The standard approach to studying the composition of soot particulates is by off-line chemical analysis. This generally proceeds in the following steps: (1) preparation of collection substrates, (2) sampling exhaust from the vehicle, (3) extraction of PM from the substrates, and (4) chemical analysis of the recovered material. The main chemical analysis used in PM studies include: (1) elemental analysis, (2) inorganic ions, (3) hydrocarbons, and (4) polar organic compounds. Elemental analysis is usually accomplished using X-ray fluorescence (XRF), X-ray photon electron spectroscopy (XPS), or inductively coupled plasma mass spectrometry (ICP-MS). XPS is a surface technique, and thus it is applicable to the surface rather than the bulk of diesel particulates. XRF is quite sensitive technique, and is good for quantitative analysis of concentrations. The PM is collected by Teflon filters that are preleached using HCl or HNO_3 and then flushed with water. Kellog and Winberry describe the application of XRF to analysis of ambient PM for 44 chemical elements lying in the second or lower rows of the periodic table [14]. The detection limits vary by element, but are typically in the range of mg/cm^2 when using Teflo filters. ICP-MS has superior sensitivity for many trace metals and is well suited for metal speciation, but the samples must first be processed by microwave-assisted acid digestion, as described in the roadway tunnel measurements of [15]. Inorganic ions, especially SO_4^{-2}, are important constituents of motor vehicle PM and they have also analyzed by many technology such as ion chromatography and IR [9,13].

The organic chemical speciation of PM should be cleaned by extraction with high purity solvents (examples include dichloromethane, hexane, methanol, and acetone) before use. After testing, but prior to extraction, they are spiked with a mixture of deuterated internal standards (e.g., *n*-decane-d12, *n*-hexanoic acid-d11, benzaldehyde-d6, naphthalene-d8, biphenyl-d10, pyrene-d12, etc.), which are used to gauge the efficiency at which material can be reclaimed for analysis from the collection substrates. There are a variety of methods available for extraction, including Soxhlet, ultrasonic, and microwave-assisted. These methods were compared for the extraction of PAH and their variability both with respect to standard reference materials and ambient samples [16]. The extracted organic material is usually identified using gas chromatography/mass spectrometry (GC/MS). Individual species are distinguished by their retention times, identified by the mass spectrum, and quantified by the total ion count relative to those from reference standards.

Motivated by potential health benefits, an important application for the chemical analysis of PM has been to evaluate “environmentally friendly” fuels. Important fuel parameters are found to be density, 90% distillation point, final boiling point, specific energy, total aromatics, di-aromatics, tri-aromatics, and PAH contents. A multivariate statistical analysis supports a relationship between the PAH contents of the diesel fuel and their emissions in the exhaust [17]. Ultra-low sulfur (also Fischer–Tropsch) fuel in combination with the DPF result in ~95% reductions in PM mass emissions, and lower levels of 2, 3, and 4+ ring PAHs than emitted by the CNG fueled vehicles. Nitro-PAH emissions are close to detection limits [18].

4. DPF AND OXIDATION CATALYST

Nowadays, soot particles emitted by diesel engines are reduced by physically trapping the particles with on-board diesel particulate filters (DPF). The key technology is filtration

materials and regeneration of filter. At present, the study on the filtration material technologies has great breakthrough. Silicon carbide wall-flow filters have already widely used at home and abroad. The particles capture is carried out in wall-flow monoliths and the progressive soot loading in the filter generates an increasing pressure drop. Regeneration is then promoted through the post-injection of hydrocarbons (burned in a specific upstream catalytic converter to heat up the trap) in order to ignite the filtered soot. Characteristic pressure drop evolutions across DPF show that the filtration process can be divided into two subsequent phases: [19] (1) In the first phase, called depth filtration, the soot nanoparticles are collected inside the filter porosities. This step is characterized by a non linear increase of the pressure drop, due to the modification of the porosity and the permeability of the porous media. (2) When the maximum particle packing density is reached inside the porous media, the filter becomes locally "impermeable" to the particles, and a soot layer on the filter channels surface is built up. This phase is called cake formation. At that time the pressure drop starts increasing linearly with time, according to the thickening of the soot layer deposited on the filter channels surface [20]. The filter durability is closely entailed by the successful control of periodic regeneration by combustion of the deposited particulate. In order to promote soot combustion at lower temperatures compared to a standard trap, the surface of the filter channels can be coated with a tailored oxidation catalyst [21]. DPF are generally recognized as the most viable solution to soot emissions. Frequent regeneration prevents undesired backpressure buildup related to the soot particulates accumulated in the filter.

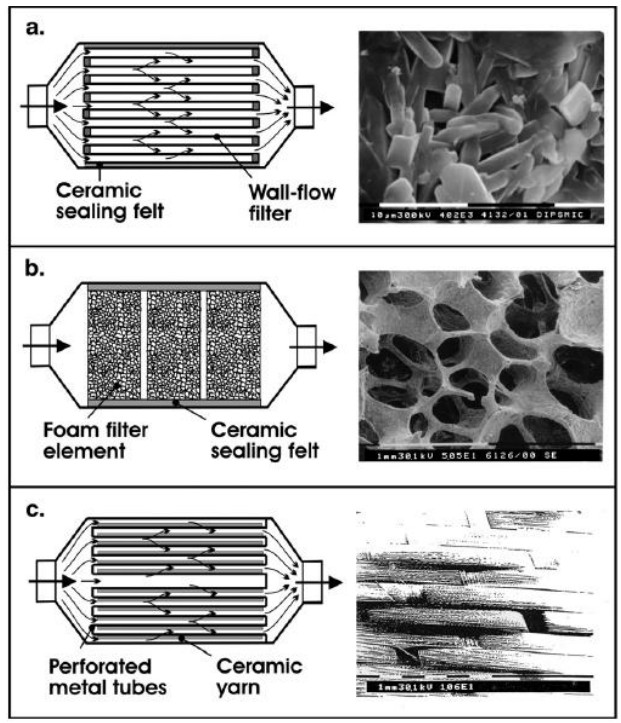

Figure 2. Sketch and SEM pictures of the major trap types: a. wall-flow monolith made of cordierite (coring); b. SiC-ceramic foam traps (saint Cobain); c. alumina-ceramic fiber filter (3M).

Figure 2. shows the three major trap types available in the market [22,23]. Wall-flow filters (Figure 2.a.; materials: partially sintered SiC or cordierite grains, pore size: 10 μm) are very efficient (90%) since they are based on a shallow-bed filtration mechanism, whereas foam (Figure 2.b; materials: zirconia-toughened-alumina or -mullite, SiC, pore size: 100‑400 μm) and fibre filters (Figure 2.c; materials: doped-alumina; fibre size: 10 μm) are somehow less efficient as a consequence of the deep filtration mechanism they enable. Wall-flow filters act as "cake filters", while foams and fibre yarns as deep bed filters. If an excess of soot is collected on the filter, the traps located in the under-floor exhaust line get laden by particulates and increase their pressure drop. Thus, once the particulates are collected, it is necessary to burn it off. This is accomplished by burning the trapped particulates off, an operation which can be assisted by the use of catalysts.

Among all the generation technology, catalytic regeneration has become core technology. Through controlling the diesel combustion, we can make the particulate matter in filter burn with catalysts at low temperature, so as to shorten generation time and improve degree of regeneration, which has broad application foreground. The impact of oxidation catalyst depends on many factors such as the fuel composition. On one hand it removes hydrocarbons that could otherwise condense on soot particles or nucleate as the exhaust subsequently cools. But on the other hand, it oxidizes SO_2 to SO_3.

In the presence of water vapor this yields sulfuric acid, which can promote nucleation or condense on soot. The result is a synergistic effect between the catalyst and fuel sulfur level that alters the chemical makeup of diesel engine PM, and affects the particle size distribution. Light duty diesel vehicles that have an oxidation catalyst or are operated with conventional diesel fuel (350 ppm sulfur), but not both, typically exhibit a single lognormal accumulation mode of particle emissions. The addition of a DPF increases the complexity in the engine/aftertreatment system. The DPF substantially lowers PM mass emissions, but its effect on particle number is ambiguous. This is because the mass is dominated by the soot accumulation mode, which is efficiently trapped, but the number can be dominated by nucleation particles formed downstream of the DPF, a process that is very sensitive to engine operating conditions.

A further complication is that particle traps need to be regenerated periodically to avoid excessive back pressure on the engine. This introduces a new set of circumstances for particle formation that needs to be examined. Again, there are possible interactions with fuel structure, where high sulfur fuel can yield substantial numbers of nucleation particles during regeneration [9,24].

5. Catalysts of the Catalytic Combustion of Soot

The ignition temperature of diesel soot particulate is in the range of 550–600 °C in air. Since the temperature of the exhaust gases of modern diesel engines is relatively low (180–400 °C), for oxidizing the soot at that temperature, it is necessary to have active oxidation catalysts within this temperature range. Studies with a large number of catalysts for soot oxidation have been reported during the last few years. Several catalytic systems lowering down the ignition temperature of diesel soot has been proposed: noble metal catalyst system [25-29], alkali based metal oxides [30-32], chlorides of transition metals [33,34], transitional

metal mixed oxides [35-39], or complex oxide [40-46]. Among the catalytic systems reported for soot oxidation, Pt based catalyst system exhibit the best activity, however they are very expensive.

Many other attempts have been made to develop catalyst for diesel soot combustion on the basis of simple metal oxides and mixed oxides. As we consider the results of this study, two challenges remain for future research, i.e., to design appropriate catalytic materials that possess strong redox ability and to design new systems that improve the contact between soot and catalyst. On the one hand, The catalysis nature of soot oxidation is a deep redox process. Therefore, the redox property of the catalyst determines its' intrinsic activity. Some ideas should be considered to get high redox property. One is to select the transition metal elements, whose ions have several oxidation states and possess good redox properties such as, Mn, Co, Fe etc. The other one is to tune the redox property of complex oxides with the alkali metal or alkali earth metal ions.

On the other hand, the reactions of soot oxidation is three-phase catalyzing reactions. The reaction supposedly takes place at the three-phase boundary among a solid catalyst, a solid reactant (soot) and gaseous reactants (O_2, NO). The efficiency of a catalyst is strongly influenced by the contact between soot and catalyst. Though by using many other mechanical methods, such as ball milling, mechanic mixing, part of the catalyst particles may be contacted with soot materials, this method gave only tight contact condition between soot and catalyst.

The condition cannot be easily obtained under the real exhaust gases emitted from diesel engine. Therefore, the catalytic effect is weakened in the real application. Some strategies have been proposed for getting the good contact between the catalyst and soot:

a) To seek the oxides or mixed oxides with low melting points or low eutectic melting points. Molten salt catalysts evaluated under realistic conditions gave promising results. However, in this case, the catalyst design is restricted to compounds that melt at the temperature in which the soot combustion is going to be carried out. It means that the catalyst formulation is carried out first looking for materials that form an eutectic point around 300°C or lower and then choosing according to the catalytic performance among these materials. Thus, something that is important in the catalyst formulation is to include active components with high mobility. In some studies, chlorine-containing compounds have been found by Neeft et al. [47] and used for the above objective. But these catalysts were easy to vaporize and cause new pollution for environment.
b) To synthesize nano-particle oxide catalyst. It is because the surface particle sizes of nanoparticle catalyst are small. Surface atoms on surface of nanoparticle catalysts have extra and high surface energies and they are good at mobility. In order to intensify the catalytic effect, nano-particle catalysts may be used. Since the nano-particle catalysts have higher fraction of surface atoms than the conventional catalysts with large particle size, the catalyst is in close proximity with soot particle and more catalyst surface is exposed to reaction atmosphere. A decrease in particle size from 1 μm to 10 nm will increase the probability of contact each other by 100 times. For a given catalyst, the more the surface of catalyst is exposed to soot, the stronger the catalytic effect. Therefore, the catalytic effect of nano-particle catalyst will be stronger than that of the big particles when the same amount of catalysts is

used. And lower amounts of catalysts are needed when the catalyst is in nano-particles compared to the big catalyst particles for the same level of catalytic effect. Using smaller amounts of catalysts in relatively short time can also effectively combust soot particle and decrease the total cost of the materials.

c) Similarly to noble metal Pt catalysts, to search the efficient oxide catalysts for catalyzing the NO to NO_2. In a previous work, a strategy successfully developed by Johnson Matthey for their DPF is to use the oxidizing properties of NO_2 to combust the PM, i.e. the famous CRT technology (continuous regeneration traps). In the CRT system the removal of PM by oxidation with NO_2 is achieved by placing an Pt-based oxidation catalyst upstream of the trap in order to convert NO in the exhaust into NO_2. The oxidizing ability of NO_2 is much stronger than that of O_2 and it can directly oxidize the soot particle to CO_2 [48]. If the cheap metal oxide catalysts might oxidize NO to NO_2 like Pt catalyst they could subtly change solid (soot) -solid (catalyst) contact into solid (soot) - gas (NO_2) - solid (catalyst) contact. Then, the catalyst should have good activity for oxidizing soot to CO_2 and CO under loose contact conditions.

d) It is noted that the pore size of catalyst would affect the catalytic combustion of soot. The size of soot particle is about 10 nm ~ 1 μm. It depends on the type of diesel engine and burning conditions, etc.. The pore sizes of normal catalysts are less than 10 nm, therefore, soot particles are difficult to enter inner pores of the general catalysts. Thus, the contact area and the exposed active site amounts are limited and only the outer surface area is the valid reactive surface area for the title reactions. And then the catalytic performances of catalysts would be largely affected. Three-dimensionally ordered macroporous (3DOM) materials with big pore size (>50 nm) can permit solid reactant to enter the inner pores of materials and to easily transport and diffuse. Therefore, the tangible active points between reactant and catalysts will be increased dramatically. It is a new approach to synthesize the oxide catalysts with macroporous pores or macroporous carrier-supported catalysts for the diesel soot oxidation.

In the end, the catalysts to be the used in the combustion of diesel soot must be stable both at high temperatures and in the presence of other combustion products and contaminants such as H_2O and SO_2. The activity should be high enough at temperatures as low as 200 °C for low charge diesel engines, unless an external heating power is supplied to the catalytic filter. In any case, the catalyst stability is a key factor in determining its applicability in a commercial scale.

Another key factors to be taken into account is the presence of other gaseous products that may affect the catalytic behavior. In the case of diesel exhaust, the presence of CO_2, NO_2, and water is unavoidable, and in the majority of cases, SO_2 is also important.

According to the above points, the review is to give an overview of relevant catalyst research progress for the catalytic combustion of soot, and a short summary and future outlook will be also outlined for the catalyst investigation about soot emission reduction techniques.

5.1. Low-Melting Point Catalyst

Low-melting point salt catalyst is regarded as a promising catalyst stuff, which includes Cs_2O、V_2O_5、MoO_3、Cs_2SO_4 and mixture of them. Neeft et al. [49,50] described TGA experiments to examine a number (~30) of simple single-component oxides as candidate oxidation catalysts for soot combustion. One result noted by Neeft et al. was that the nature of the contact between the catalyst and the soot affects the apparent effectiveness of the catalyst in promoting soot oxidation [49]. For example, a comparison of Fe_2O_3 and MoO_3 revealed that Fe_2O_3 is an active catalyst in "tight" contact mode, but shows hardly any activity in "loose" contact. On the contrary, MoO_3 exhibits activity in loose contact mode that is only slightly less than what is observed in tight contact mode. Loose contact mode always shows lower activity than tight contact mode for all compositions, but the degree of degradation varies from different type compounds. A weak but significant correlation exists between loose contact oxidation temperature and melting point and partial pressure of the catalytic material. Most metals or metal oxides and all alkali salts with high loose contact activities have low melting points and high volatilities: Sb_2O_4, MoO_3, PbO, KNO_3 etc.. And the other mixed metal chlorate such as Cu/K/Mo/Cl or Cu/K/V/Cl etc. have also thought to be high volatile. Most metal oxides with a high melting temperature and relatively low partial pressure such as Co_3O_4, Fe_2O_3, and CaO etc. are hardly or not active in loose contact. The mobility of low melting point or high volatility catalysts is good, and thus these molten catalyst particles are still in a rather good contact with soot by wetting of the soot under loose contact condition. Only mobile catalysts are active for soot oxidation when the contact is loose. However, catalyst mobility by a high catalyst volatility is not a desirable catalyst property under diesel exhaust gas conditions when the catalyst is used as a coating and catalyst stability is concerned. For high volatility catalysts, the loss of catalyst material is unavoidable in the high space velocity during diesel engine emission, thus, low-melting point salt may be more suitable for catalytic filter. In general, the high activity of low melting point catalysts may be due to the following reasons [51]: 1) melting at high temperature, be capable of wetting the particles, thus tightly contact with the particles. 2) stable distribution of liquid state catalyst can be achieved via choosing suitable supporters. 3) unwanted reactions between catalyst and supporter can be effectively depressed via selecting proper foam ceramic filter. The schematic diagram for action mechanism of the low-melting point salt catalyst was shown in Figure 3.

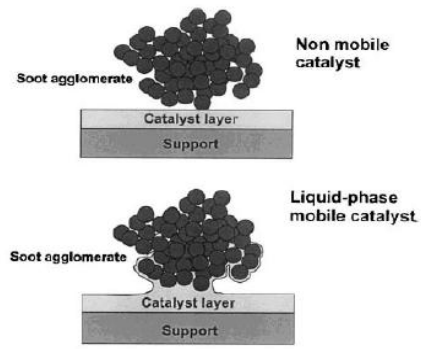

Figure 3. schematic diagram for action mechanism of the low-melting point salt catalyst.

Table 1 The catalytic activity of low melting point catalysts for soot combustion [52-56]

Catalyst	If existed NO_x/Yes or No	O_2/%	contact	Combustion temperature of soot T_{10}/**°C**	Temperature rising rate/ **°C**·min^{-1}
$CsVO_3$	N	10	Tight	359	5
$CsVO_3$+KCl	N	10	Tight	343	5
$Cs_4V_2O_7$	N	10	Tight	255	5
$Cs_4V_2O_7$/Ag/Cs/Cl	N	10	Tight	252	5
$CsVO_3$	N	10	Loose	360	5
Cs_2SO_4-V_2O_5	N	10	Loose	320	5
Au/V/TiO_2	N	10	Loose	361	5
MoO_3/SiO_2	Y	10	Loose	289	10
V_2O_5/SiO_2	Y	10	Loose	278	10
K/Cu/V/Al_2O_3	Y	10	Tight	267	5
K/Ce/V/Al_2O_3	Y	10	Tight	320	5
K/Zn/V/Al_2O_3	Y	10	Tight	284	5
Cu/V/K/Cl/Ti	Y	10	Loose	330	10
Cu/V/K/Cl	Y	10	Loose	277	10
V_4/TiO_2	Y	5	Tight	337	2
V_4/ZrO_2	Y	5	Tight	346	2
Li_4V_4/TiO_2	Y	5	Tight	299	2
K_4V_4/ZrO_2	Y	5	Tight	309	2

Vanadium-based composite catalyst exhibit good activity, studies have been carried out by researchers [52-56]. Performance parameters of such catalyst are listed in Table 1. Compared with other type catalyst, the contact mode has little influence on the activity of low-melting point salt catalyst. $CsVO_3$ exhibit remarkable activity in loose contact mode, even better than noble metals in the absence of NOx in the reactant gases. $Cs_2V_2O_7$ has a reaction peak temperature ca.100 K lower than $CsVO_3$, which possess higher activity than it. When AgCl is added to the $Cs_2V_2O_7$ system, the activity of the catalyst can be improved slightly, and the ignition temperature reduces to 252 °C. Another type of low-melting point salt catalyst is mixed-type compounds represented by Cu/K/M（M=V、Mo）catalyst. Early study shows that Cu/K/M system possess good activity, the activity data of some catalyst of such type can be referred in Table 1. Neeft et al. [47,57] have investigated the reaction mechanism of particle stuff oxidation, the result indicates that the mobility of catalyst is key factor that impacts on the activity when catalyst particles distributed on the soot surface either in loose contact mode or tight contact mode. Based on this, Badini et al. [58,59] found that the mobility of catalyst depends on the formation of liquid alloy, such alloy melts in the range of reaction temperature and wets the soot particles, thus the gas-solid-solid reaction transfers to gas-liquid-solid reaction, which greatly enhanced the contact of catalyst and the soot particles. Experimental data shows that the activity of catalyst depends on the "synergistic effect' between vanadates and chlorides. Ciambelli et al. [60-63] investigated Cu/K/V/Cl type catalyst deeply with the consideration influences of NO presence on the soot oxidation. Being similar with noble metal catalyst, Cu/K/V/Cl catalyst follow the mechanism of two reactions (with the presence of NO): Large amount of NO is oxidized to NO_2 in the range of 200 ~ 400

°C, then soot react with NO_2 and produce NO, CO, CO_2. NO_2 then is reduced to NO, and a oxidation-reduction circle is formed. Thus the whole reaction process is insistently carried out. Meanwhile, Small amount of water and SO_2 in the emission can promoting the oxidation of NO. Cu/K/V/Cl supported on the foam ceramic filter has also been studied in abundance, this emission control system is capable of reducing the particle concentration effectively and regenerating: when the outlet temperature is above 250°C, the pressure drop of the filter begins to reduce. However, when the outlet temperature is stabilized at 623 K, the pressure drop can be stabilized in a relatively low level.

Alkali metal oxides and salts, such as K, Cs and etc, can enhance the contact between soot particles and catalysts, due to the remarkable mobility. It has been tested for soot combustion catalysis of diesel engine emission, and exhibit a good performance. With the presence of alkali metal on the soot particle surface, C_8K and C_8Cs species generate, which promote the deeply distribution of catalyst on the soot particle surface, thus enhance the activity and accelerate the reactions. K and Cs possess strong capability of adsorbing oxygen (O), bond with the O in NO*x* and form cyclic oxygen compounds, thus weaken the C-C bond and promote the oxidation of soot particles In addition, alkali metal can form the surface phenate-C-O-K, this type of functional group can also weaken the C-C bonding. Pisarello et al. [64] established the three area theory of soot particle oxidation by alkali metals, take potassium as an example, as shown in Figure 4. The square in Figure 4 represents the K catalyst supported on the soot particle surface, which may forms the K*x*O*y* species. While the smaller square represents the inner layer of the catalyst. The so-called three area include surface layer that contact with soot particles, interfacial area between the catalyst surface and soot particles, and surface layer contact with the air, which are denoted as A, B, C. In K*x*O*y,* the valence of K is not saturated, and can capture a oxygen atom easily under low temperature condition, and form K_xO_{y+1} species. In the range of 0 ~ 50°C, K*x*O*y* adsorb the oxygen in NO*x*, and form K_xO_{y+1} in C area. As the temperature increases, the peak value of adsorption is achieved at 250°C, and K_xO_{y+1} oxides are formed in the whole catalyst. When the temperature is above 250°C, oxygen atoms in area A. B will transport to soot particle surface and produce CO_2, meanwhile, the oxygen adsorbed in area C will transport to area A through area B, and then react with the soot. Thus a channel is established for transportation of oxygen from gas species to soot particles, and the goal of soot removal is achieved.

Alkali metals supported on different supporters exhibit different activity, and different alkali metal types have also shown different catalytic performances. Castoldi et al. [65] systematically investigated on the role of alkali metal oxides in the combustion of soot. They found that the combustion of soot is greatly enhanced by the presence of alkaline or alkali earth metal oxides under full contact conditions, with the overall activity ranking (Cs $\geqslant$ K > Ba > Na > Ca >> Mg) which follows the electropositivity order of the investigated elements. The correlation between electropositivity and activity in the soot combustion is however not apparent under the loose contact condition between the catalytic elements and the soot. Under these conditions the catalytic activity is governed by other factors, and particularly by the mobility of the surface species which favors the soot – catalyst contact and hence the reactivity. Due to the high mobility of alkali metals, the difference of ignition temperature between loose contact and tight contact condition is small.

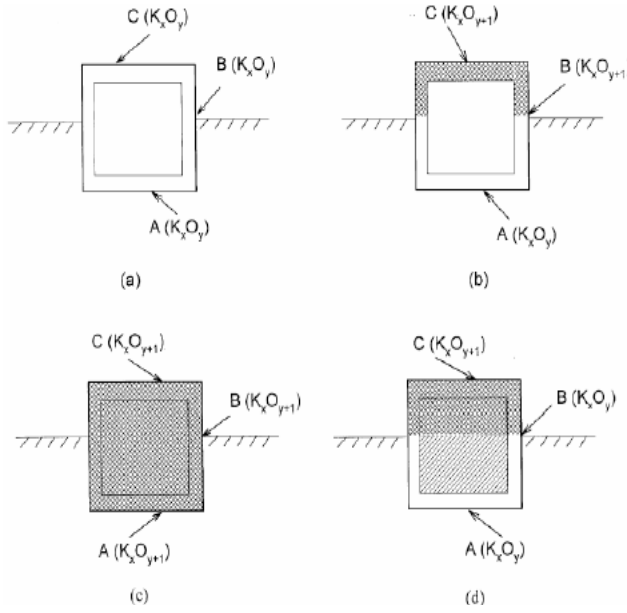

Figure 4. Three area reaction diagram of K-catalyst.

Because alkali oxides have lower melting point, and variable valence transition metal oxides have better redox property, it is another hot topic that catalytic soot particle combustion reaction with transition metal oxides modified by alkali metal. Zhang et al. [66] investigated the catalytic activity of complex oxide catalyst loading KNO_3 and K_2CO_3 to Mg-Al hydrotalcite for the reaction of soot particle combustion with air in tight contact. The results showed that K, which exists in Mg-Al hydrotalcite, can promote activity of soot combustion. Wang et al. [67] reported the property of hydrotalcite oxide (MAlO, M=Ni^{2+}, Co^{2+},Cu^{2+}) and hydrotalcite oxide modified by K catalysts, which are applied to soot combustion. They found that adding K can improve the surface mobility of catalyst, so as to improve the activity of soot combustion.

Low-melting point salt possess lower oxidation activity compared with noble metals, thus can not oxidize the particle species effectively with the utilization of NOx. In fact, with the presence of NOx, the reaction peak temperature of particle species oxidation for noble metal catalyst is ca. 80°C lower than such low-melting point salt catalyst [53]. Moreover, Cu/K/V/Cl catalyst may release toxic chloride of copper when utilized under high temperature conditions, in addition, oxychlorides may generated during the process, it is harmful to the catalyst and will leads to the formation of oxychloride hydrocarbons, which is source of secondary pollution. Hence, many researches have switched to finding the alternatives of Cu and chlorides. Low melting points of metal oxides or other salts are, however, often accompanied by high vapor pressure, which causes that such catalysts are not readily available. An ideal soot oxidation catalyst is thought to consist of a compound with a high intrinsic catalytic activity, and a low melting point, a relatively low vapor pressure above the molten catalyst.

5.2. Noble Metal Catalysts

Recently, most of studies are focused on the development of novel catalytic systems avoiding the use of expensive noble metals, and the catalysts have also exhibited well catalytic performance for diesel soot combustion, for example, transition metal (Fe, Cu, Co-based etc.) oxides, alkaline metal (Li, K, Cs-based) oxides, perovskite-like type oxides and rare earths ceria-based oxides. However, most of non-noble metal oxide catalysts are much less active than noble metals, especially the ignition temperatures are much higher than those on the noble metals. Moreover, only the noble metals are currently commercialized under practical conditions. For example, the famous technology of continuously regenerating particles trap (CRT) still used Pt-based catalysts which have the best catalytic performance and are applied in most of commercial heavy-duty diesel vehicles for diesel soot combustion, and none of bare cheap metal catalyst system seems to be used in the practical application due to their relatively low intrinsic activity. Therefore, there are still many researches on noble metal catalysts for the catalytic combustion of soot emitted form diesel engines.

Transition metal oxide catalysts modified by alkali metal and supported noble metal catalysts are high activity catalytic system under the condition of loose contact .At present, the best activity catalyst reported in literature is supported precious metal Pt catalyst developed by Hinot et al. [68], Jeguirim et al. [69] and Oi-Uchisawa et al. [70-72]. In this study, firstly NO, which is a main pollutant in diesel exhaust, is oxidized to NO_2, and then PM is oxidized by NO_2 to CO and CO_2, which has very strong oxidizing ability. So, NO_2 is used as intermediate to facilitate an indirect contact between the platinum catalyst and soot. This mechanism subtly changed solid(soot) – solid(catalyst) contact into solid(soot) – gas(NO_2) – solid(catalyst) contact. Thus, PM and catalysts can contact non-directly and reaction rate of PM catalytic combustion is improved, and the platinum catalyst system obtained the best results so far reported for soot combustion under loose contact conditions. The high oxidation rate of soot is due to the strong oxidizing ability of NO_2. Oi-Uchisawa et al. [73] has investigated soot catalytic oxidation activity, using a heat-resistant ceramic cloth as catalyst support and using low melting point metal oxide loaded by Pt as catalyst. Under actual diesel exhaust conditions, the cloth loaded with V_2O_5+Pt showed a filtration rate of 59% with a balance point temperature of 553 °C. The mobility of the catalyst over the cloth surface and easiness of reduction and oxidation of the catalyst are important for promotion of soot oxidation.

An interesting observation was reported by many researcher, which might explain the high activity of platinum found in some studies. They measured high soot oxidation activities over a platinum catalyst, and showed that this was caused by oxidation of NO to NO_2, followed by a subsequent reaction of soot with NO_2

$$O_2 + 2NO \rightarrow 2NO_2 \quad (1)$$

$$2NO_2 + C \rightarrow 2NO + CO_2 \quad (2)$$

$$NO_2 + C \rightarrow NO + CO \quad (3)$$

By placing a platinum catalyst upstream of the particulate trap. Copper and Thoss [74,75] showed that contact between soot and catalyst is not a prerequisite in the case of platinum catalyzed soot oxidation. The orders of reaction with respect to the NO inlet concentration and to soot weight were found equal to 1. The benefit of the presence of water in the feed gas for emissions soot oxidation was noted.

An important drawback of platinum catalysts is their high activity for SO_2 oxidation. Pt catalyst is tend to poisoning because of carbon deposition, Corro et al. [76] added Sn on soot combustion catalyst 1% Pt/γ-Al_2O_3, preventing polymerized carbonaceous residues generated during soot oxidation. XPS determinations showed that the presence of high amounts of Sn species over the catalyst surface that many prevent polymerized hydrocarbon residues to reach the interface between platinum and the support. Cooper and Thoss [74,75] found the SO_2 conversion to SO_3 to be of the same order of magnitude as the conversion of NO to NO_2. This high SO_2 oxidation in conjunction with NO oxidation is not surprising, as it is known that in one of the oldest chemical processes (the so-called "lead chamber process") SO_2 is oxidized catalytically by NO_2 (formed continuously by oxidation of NO). Later, platinum was used in sulphuric acid production. Xue and coworker [77-79] also studied NO and SO_2 oxidation over Pt on SiO_2. They concluded that the oxidation of SO_2 to SO_3 is more highly favoured than the oxidation of NO to NO_2. These studies report very slow pressure drop increases over particulate traps at low temperatures. This NO/NO_2 mechanism might also explain the sometimes rather high activity of noble metal catalysts at low temperatures.

The addition of noble metal into perovskite oxides promotes the catalytic performances of catalysts for soot combustion. Cauda et al. [80] developed an innovative multifunctional catalyst ($La_{0.9}K_{0.1}Cr_{0.9}O_{3-\delta}$ +1 wt% Pt) for diesel soot combustion combining direct and indirect (NO – NO_2 – NO cycle) oxidation mechanisms. As far as the comparative analysis of the activity of the catalysts towards soot combustion is concerned, the programmed-temperature reaction curves show that the perovskite catalyst doped by noble metal Pt significantly shift the combustion temperature range towards temperature values lower than those typical of the catalytic combustion no Pt. The good catalytic activity shown by the K-substituted chromite catalyst ($La_{0.9}K_{0.1}Cr_{0.9}O_{3-\delta}$) is a consequence of its superior chemisorbed α-oxygen amount. Pt can add some oxidative activity to the basic perovskite catalysts. Conversely, as above anticipated, the superior activity of the $La_{0.9}K_{0.1}Cr_{0.9}O_{3-\delta}$ +1 wt% Pt in the presence of NO is attributed to its capability of promoting soot oxidation indirectly, by promoting the $NO\text{-}NO_2$ oxidation. This reaction is thermodynamically limited at high temperature but can be significant in the temperature range 150-450 °C, the temperature range of interest for the diesel engine exhaust. Since Au or Pd is much cheaper than Pt, thus to replace Pt-based catalyst by Au-based or Pd-based catalysts are industrially preferred from an economical viewpoint. Of course, the thermal stability of Au-based catalysts should be further improved. Therefore, the use of gold or palladium as component of the catalyst for soot combustion is very significant. The 2 wt% Au-$LaNiO_3$ shows a good catalytic performance with a peak carbon combustion temperature of 335 °C and a half CO conversion of 162 °C [81]. And Craenenbroeck et al. [82] studied the catalytic oxidation of diesel soot over Au–VOx/TiO_2 and Au – VOx/ZrO_2 of catalytic systems with different vanadia loadings. They found a synergistic effect between Au nanoparticles and vanadia when VOx presents as a monolayer on the support. Catalysts with higher V loadings show a higher activity but no synergistic effects between Au and V could be observed. The addition of Au produces two

effects. Au particles promote the oxygen transfer which increases the activity in the combustion of soot particles. This effect is clear at low V loadings when no V_2O_5 is present. Au particles also provide very active sites able to ignite the soot within the desired temperature range but retard the oxidation process at high V loadings because of the diminished contact. Moreover, other supported noble metal catalysts such as Ir, Ru, Pd, Ag also exhibited very high catalytic activity for soot combustion [83-87]. Especially, palladium has been suggested to (partially) replace platinum, to suppress sulphate formation at higher temperatures [87-90]. Soot oxidation and SOF conversion curves are shifted slightly towards higher temperatures for palladium catalysts compared with platinum catalysts. In addition, the sulphur oxidation behaviour is shifted to much higher temperatures. Besides, palladium or combined platinum/palladium catalyst are cheaper than platinum catalysts.

5.3. Complex Oxide Catalysts

Recent years, researchers are devoted to study on non-noble metal catalytic system, for the lack of precious metal materials. And they got some exciting results. An important group of cheap catalysts studied in diesel soot combustion is complex oxides catalysts including Ce-Zr mixed oxides, perovskite, spinel or hydrotalcite oxides etc. Because CeO_2 plays an important role in gasoline engine exhaust three-way catalyst and its excellent oxygen storage-release and oxidation-reduction function, there are many researches on cerium base oxide catalyst for carbon particle of diesel engine exhaust. Zhu et al. [91] prepared a series of Ce-Zr oxide support loading KNO_3 catalyst. When the catalyst and soot particulates contacted in loose style, soot combustion peak temperature kept below 400 °C. Wu et al. [92-94] prepared Ce-Zr composite oxide catalyst doping Cu, which has high catalytic activity on soot combustion. Atribak et al. [95] studied on structured morphology of CeO_2, TiO_2 and ZrO_2, and investigated these three oxides catalytic properties for soot particulate combustion. They found TiO_2 exists in the form of rutile and anatase crystal, and ZrO_2 is in the form of monocline or square crystalloid. The difference between the two crystalline structure square crystalloid, is no effect on soot combustion. CeO_2 exists mainly in the form of cubic fluorite structure. Among these three oxides, CeO_2 has the best oxidation activity for soot combustion. This is because, compared to the other two oxides, CeO_2 has the function of making NO to NO_2. In addition, CeO_2 can make CO oxidized to CO_2, which has high selectivity of CO_2. Krishna et al. [96] studied on soot oxide catalytic properties under a loose contact with the catalyst of rare-earth modified CeO_2, with feed gas containing NO and O_2. The results showed that the samples combustion activity modified by Pr and La is higher than the samples non-modified. While the samples modified by Sm and Y showed a contrary result. Liu et al. [97] prepared a series of Ce-Zr-Pr oxides by a new synthesis approach combining rotating evaporation with auto-combustion techniques. These as-prepared nanometric Ce-Zr-Pr mixed oxides had good catalytic activities for soot combustion. They decreased the temperature of soot combustion by more than 200 °C compared to that of uncatalytic combustion of soot. In the past years, perovskite-type oxides (ABO_3) and perovskite-like oxides (A_2BO_4) oxides have been investigated extensively and intensively for the total oxidation of soot and carbon. The good catalytic activities of these materials are due to the presence of a large number of structural defects such as cationic and anionic vacancies,

among which excessive- or deficient-oxygen stoichiometry is the most common case. Another reason for the good catalytic performance is the strong redox ability derived from the coexistence of at least two kinds of oxidation states of the transition metal ion. Therefore, the amount of nonstoichiometric oxygen and the ability of redox determine the catalytic property of the perovskite. By partial substitution of ions in site A and/or site B, one can regulate the amount of oxygen nonstoichiometry and the valence distribution of the B-site ion. The controllable physicochemical properties of these catalytic materials make them useful models for the study of specific reactions. Perovskite-type mixed oxides possess general formula ABO_3. Perovskite-type complex metal oxides ABO_3, where A and B represent 12-coordinated and 6-coordinated metal cations, respectively, are good candidate catalysts for diesel soot combustion. The rare earths A-position based perovskites are mainly studied in the processes of soot particulates removal. The ignition temperature with rare earth perovskite oxides also decreases by more than 200 °C as compared to carbon particulates alone. In the ABO_3 perovskites, partial substitution of alkali and alkaline-earth metals at the A-site enhances the catalytic activity in the combustion of soot particulates. Fino et al. [98-100] reported that activity in soot combustion decreases in the following order of La based perovskites $LaCrO_3$ > $LaFeO_3$ > $LaMnO_3$, and the catalytic activity is further improved for lanthanum partially substituted by alkali metals in $LaCrO_3$. In the several containing chromite perovskite catalysts ($LaCrO_3$, $La_{0.9}CrO_3$, $La_{0.8}CrO_3$, $La_{0.9}Rb_{0.1}CrO_3$, $La_{0.9}K_{0.1}CrO_3$, $La_{0.9}Na_{0.1}CrO_3$, $La_{0.9}Li_{0.1}CrO_3$) prepared by combustion synthesis, the Li-substituted chromite catalyst ($La_{0.9}Li_{0.1}CrO_3$) exhibits the highest activity as a consequence of its greater amount of weakly chemisorbed O^- species (α -oxygen) which are pointed out as the key player in the soot oxidation state. The progressive increase in the Li content of the catalysts induces an increase in the catalytic activity owing to the enhancement of the amount of weakly chemisorbed oxygen O^- species (even exceeding 1200 mmol/g), key players in the soot oxidation mechanism. However, beyond 20% Cr substitution with Li, part of this latter metal got segregated as $LiCrO_2$. The best single-phase catalyst ($La_{0.8}Cr_{0.8}Li_{0.2}O_3$) was already active well below 352 °C. La substoichiometry and the addition of Li at the Cr site were found to lead to a very active catalyst, i.e., $La_{0.8}Cr_{0.9}Li_{0.1}O_3$. As outlined in earlier papers, the substitution of part of lanthanum with a lower valence alkali metal brings about formation of high valence B site ions to maintain electro-neutrality and possibly to obtain more active or more concentrated oxygen species over the catalyst surface. The activation energies of carbon oxidation over all catalysts are indeed significantly lower than that of noncatalytic combustion. Furthermore, the activation energies for the catalytic reactions are not very different from one another. This might suggest that all perovskites deliver to the carbon particulates oxygen species of a similar reactivity, which differ from one sample to another, just for their surface concentration. The various nano-structured bulk Li-substituted La–Cr perovskites ($La_{0.8}Cr_{0.9}Li_{0.1}O_3$, $La_{0.8}Cr_{0.8}Li_{0.2}O_3$, $La_{0.8}Cr_{0.7}Li_{0.3}O_3$) are prepared and characterized. Their catalytic performances are improved contrary to the reference $LaCrO_3$. [100-102] Wang et al.[103-105] prepared a series of $La_{1-x}M_xMnO_3$ and $La_{1-x}M_xCoO_3$ (M=Li, Na, K, Rb, x=0~ 0.25) perovskite-type oxide samples by the method of citric acid-ligated. They obtained a highly catalytic activity for soot combustion on la-K-Mn-O_3 catalysts under loose contact conditions between catalysts and soot. The combustion temperatures of soot particle are between 558 and 703 K, as shown in Figure 5. The catalytic activities of these cheap materials for the combustion of soot particle are as good as supported Pt catalysts,

which is the best catalyst system so far reported for soot combustion. [103-105] Fino et al. [101] carried out Compositional and structural optimal design of a nanostructured diesel-soot combustion catalyst for a fast-regenerating trap. They investigate the soot conversion by coupling the effects of catalytic activity of $PrCrO_3$ perovskite and CeO_2 oxide on the practical wall-flow traps for diesel particulate removal. A promising result is fully confirmed at a prototype trap level where the presence of the catalyst in the tested wall-flow traps enabled, compared to a non catalytic trap, a significant reduction of post-injected fuel for the regeneration (10% against 24% additional fuel consumption) and a much more complete trap regeneration.

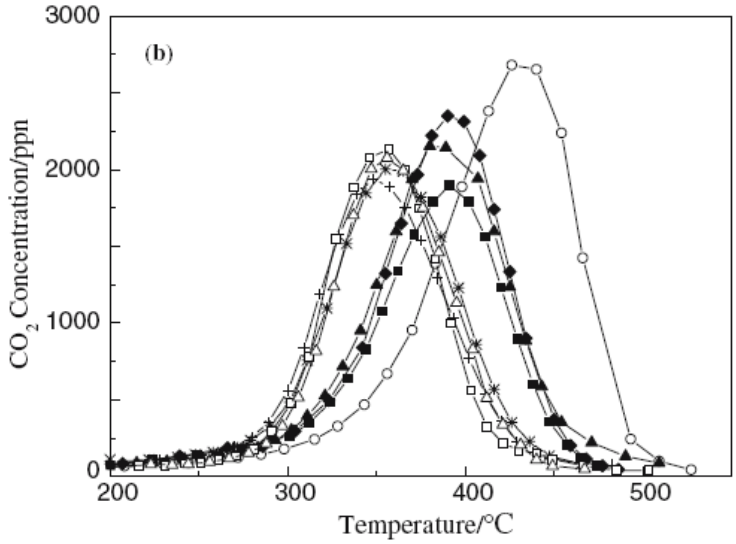

Figure 5. Programmed-temperature reaction profiles of carbon oxidation over $La_{1-x}K_xMnO_3$ catalysts under loose contact conditions. Reactant gas: 2000 ppm NO+5% O_2/He (x = 0~0.35).

In a kinetic study, Shuangguan et al. [106,107] obtained a half-order kinetics in the partial pressure of oxygen using a $CuFe_2O_4$ spinel catalyst and proposed that the formation of a reactive oxygenated intermediate on the soot surface is the rate-determining step. Liu et al. [108] prepared $Mn_{1-x}(Li,Ti)_xCo_2O_4$ spinel-type complex oxides by the method of citric acid-ligand combustion. The $Mn_{1-x}(Li,Ti)_xCo_2O_4$ still retain intact spinel-type structure after Li or Ti were doped into $MnCo_2O_4$. $Mn_{1-x}(Li,Ti)_xCo_2O_4$ spinel-type complex oxides are good candidate catalysts for the catalytic combustion of diesel soot particulates. The optimal substitution amount of Li or Ti x is equal to 0.05. T_{ig} is 397 °C under the loose contact conditions between soot and the catalyst.

5.4. Macroporous-Based Catalysts

The catalytic combustion of soot is very difficult. It's mainly because that the pore sizes of common catalysts are much smaller than these large particles' diameters. Therefore, large soot particles can’t enter the inner pores of catalysts, and only the external surface supplies the available active surface area, which leads to lower activity. Three-dimensionally ordered

macroporous (3DOM) materials with big pore size (>50 nm) could be used to solve this problem because of their uniform big pores and well-defined periodic structure Firstly, the pore is big enough to permit large particles to enter their inner pores. Moreover, the uniform macroporous network allows easy mass transfer and less diffusion resistance when the large size particles go through the catalyst structure. So far, various kinds of 3DOM metal oxides have been prepared by the colloidal crystal template (CCT) method through alkoxide-based sol-gel processes [109-112]. Three-dimensionally ordered macroporous materials can permit solid reactant to enter the inner pores and to easily transport and diffuse. Therefore, the tangible active points between reactant and catalyst will be increased dramatically. Recently, 3DOM oxides show good catalytic activity for diesel soot oxidation. Ueda et al. [113,114] successfully obtained 3DOM alumina, iron oxide, chromium oxide, manganese oxide, and their mixed-metal oxides using the EG in situ nitrate oxidation method which could ensure the desired metal ratio throughout the whole preparation procedure. The preparation process can be described as Figure 6. Zhang et al. [115] prepared the microstructure with open, interconnected macropores of 3DOM $Ce_{1-x}Zr_xO_2$ using PMMA colloidal crystal as template and cerium nitrate and zirconium oxide chloride as raw materials. And these 3DOM) oxide catalysts show higher activity than the corresponding particle or disordered macroporous catalyst.

Unfortunately, 3DOM materials with other metal (Cu, Ni, Zn, Co, Mg, Ca, La, Ce) oxides could not be obtained, because their nitrate oxidation temperature are higher than the glass transition temperature which can't maintain the 3DOM framework. Orilall et al. [116] synthesized the simple oxide Nb_2O_5 using a combined assembly by soft and hard (CASH) chemistries method with the carboxyl-modified PS spheres as template. In this method, the carboxyl groups that has sp2-hybridized carbon atoms is converted to a sturdy amorphous carbon material, when heat treated under an inert environment, supporting the 3DOM framework without structural collapse. Zhang et al. [117,118] presented a facile procedure to produce macroporous perovskite-type complex oxides of $La_{1-x}K_xCo_{1-y}Fe_yO_3$ (x=0, 0.1, y=0, 0.1) by using the combined method of organic ligation and solution combustion. The formation of complex could ensure the desired metal ion ratio throughout the whole preparation procedure. The obtained catalysts had a lot of honeycomb-like macropores with average diameters of more than 50 nm. Such macroporous structure could improve the soot-catalyst contact effectiveness. Therefore, the macroporous perovskite oxides showed higher catalytic activity than that of corresponding nanometric catalysts for soot combustion. However, the regularity of these macroporous structures is poor. Furthermore, Xu et al. [118] prepared 3DOM $La_{1-x}K_xCoO_3$ catalysts with uniform big pores and well-defined periodic structure by a new CMCCT method using the nonionic-surfactant as coverlayer and carbon source. In this method, the nonionic-surfactant of ethanol solution was permeated the voids between the close-packed spheres firstly, followed by removing the ethanol upon drying. Then the EG and metal nitrate hydrates re-impregnated the impregnated CCT.

There are several advantages as the introduction of the nonionic-surfactant. Firstly, the nonionic-surfactant could be added between the carboxyl-modified microspheres and the metal precursor solution to prevent the action. Secondly, it also could offer the carbon framework as well as carboxyl group to support the 3DOM structure while heat treated under an inert environment. Thirdly, lots of mesopores and micropores could be kept in the macropore wall after calcination, which can increase the active surface area. These catalysts

which have not any noble metal exhibit super catalytic performances as good as supported Pt catalysts under loose contact condition for soot combustion.

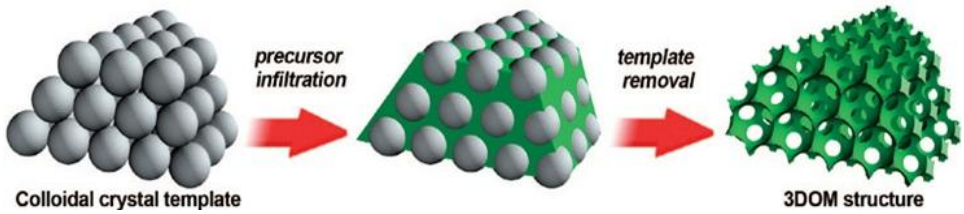

Figure 6. The scheme of 3DOM materials prepared by colloidal crystal template method.

5.5. The Simultaneous Removal of Soot and NO_x under Rich Oxygen Condition

Diesel-powered vehicles, because of their high thermal efficiency, emit less CO and unburned hydrocarbons than gasoline-fueled vehicles, but the emission of soot particulates and NO_x are still high. Since diesel exhausts, especially nitrogen oxides (NO,) and soot particulate have been causing serious problems on human health and global environment, the process to be able to reduce these emissions should be developed. However, the reduction of both soot and NO_x emissions to the regulated level cannot be accomplished by engine modifications alone due to the trade-off effect, therefore, after–treatment techniques for the simultaneous reduction of their emissions from diesel exhaust should be developed [119-121]. Under the rich oxygen condition, the removal of NO_x becomes very difficult in the exhaust emitted from diesel engines. As one possible process, Okajima et al. proposed the simultaneously catalytic conversion of soot and NO_x into CO_2 and N_2 in an oxidizing atmosphere by using catalyzed soot traps [122]. Although this method involves many technological difficulties to be overcome (the development of efficient and thermally stable traps, the contact between catalyst and trapped soot, etc.), the active catalysts are considered to be the most important one, and the perovskite and spinel oxides are the most mainly catalysts for the simultaneous removal of soot and NO_x [123].

Teraoka et al. and other researchers have done many explorative and pioneering works using rare earth perovskite oxides for the simultaneous removal reaction of soot and NO_x, [122-126]. In addition, the substitutional incorporation of alkali metal into A-sites of perovskite-type (ABO_3) oxides was quite effective in enhancing the activity and selectivity for the NO_x-O_2-soot reaction. For example, Teraoka et al. found that La-K-Mn-O perovskite-type oxides were good candidate catalysts for diesel soot combustion and the reduction of NO_x. On the other hand, the catalytically intrinsic performance of B site ion has affected on the catalytic activity of perovskite oxides. For different B site ions of perovskite related oxide, the ignition temperature of carbon particulate slightly decreases in the order Co > Mn > Fe > Cu. The catalytic activity for gas-phase oxidation reactions of Co- and Mn-based perovskite-type oxides is known to be higher than that of Fe-based and Cu-based perovskites [127-131]. Furthermore, the mutual substitution of B site ions can also improve their catalytic activities. Higher catalytic activity is exhibited by such substituted compounds because of their structural defects and the effect of valence alternation. Fino et al. reported that $La_{2-x}K_xCu_{1-}$

$_yV_yO_4$ layered oxides had good catalytic performances for the combined removal of diesel particulates and NO_x [131], and Peng et al. found the partial substitution of Mn by Cu in the $La_{1.8}K_{0.2}Cu_xMn_{1-x}O_3$ compound leads to the ignition temperature of soot combustion decreases 15 °C [127]. Judging from ignition temperature, this activity order with respect to the B-site cations is also true in the present soot–NO–oxygen reaction. This ignition temperature, however, is not significantly changed in comparison to substitution of A-site of $LaCoO_3$ catalyst. The NO conversion shows almost same values over all the catalyst, but the curve moves to high temperature range on the Fe-based perovskite. In consistent with previous reviews, the substitution of monovalent alkali metal ion for trivalent La^{3+} brings about the formation of oxide ion vacancy site or the oxidation of B-site cations. In addition, from the simple geometric consideration, unit cells should expand by the substitution of large alkali metal ion for smaller lanthanum. As far as the $LaCoO_3$ catalyst which possessed the optimal activity in different B-site ion pervoskite oxides is concerned, the alkali ion substitution of $LaCoO_3$ increases the activity of carbon oxidation. Accordingly the substitution of Cs gives rise to easy reduction of oxides and forms oxide ion vacancies of surface and then increases the adsorption rate of active oxygen at catalyst surface. The partial substitution of Cs into A-site enhances the catalytic activity in the combustion of soot particulate and NO reduction. In $La_{1-x}Cs_xCoO_3$ catalysts, the ignition temperature of carbon particulate decreases with increasing x values and shows almost constant values at substitution of $x > 0.2$ and NO conversion also shows the similar tendency [128]. In the Cs-substituted different perovskite oxide, the ignition temperature of carbon particulate slightly decreased in the order Co > Mn > Fe of B-site metal cation but NO conversion showed almost similar values. With increasing NO concentration, NO conversion decreased but the ignition temperature moved to high temperature when the NO concentration was higher than 1000 ppm. The carbon particulate played an important role on the reduction of NO, but NO had little effect on the oxidation of carbon particulate. On the contrary, NO retards the oxidation of carbon particulate at high concentration of NO. Anyway, the formation of carbon dioxide is controlled not by NO concentration but by oxygen concentration, because NO is introduced into reactants in a very small amount compared to oxygen.

The above reports exhibited the relevant catalytic activities under tight contact conditions between catalysts and soot particles. But it is a loose contact between catalyst on the surface of filter and soot particles under practical conditions [131-133]. Thus, it is rather significant to study and design the active catalysts for soot particulate oxidation under loose contact conditions. Zhao et al. investigated the simultaneous removal of soot-NO_x on the Cu-based perovskite-liked catalysts under loose contact conditions between the catalysts and soot. [130,134] They thought that the simultaneous removal reaction of soot-NO_x takes place at the three-phase boundary of a solid catalyst, a solid reactant (soot) and gaseous reactants (NO and O_2). The simultaneous removal of carbon particulate and NO_x has been studied over perovskite-type oxides whose sizes are in the range of nanometer. These catalysts were prepared by citric acid auto-combustion method. Because of the experimental difficulty to supply the solid soot continuously to the reaction system, the reaction have been exclusively investigated by the temperature programmed reaction (TPR) technique in which a mixture of a catalyst and a soot is heated in gaseous reactants. With increasing temperature, the charged soot, which is one of the reactants, is progressively consumed and eventually exhausted. This makes it difficult to study the reaction kinetically as compared with the usual catalytic reaction of gaseous reactants over a solid catalyst. Around the onset of the TPR of the

simultaneous removal of soot-NO_x where the substantial amount of soot remains in the soot-catalyst mixture, good linear Arrhenius-type relations were obtained for the formation rates of products. In this region, the effective contact area between the catalyst and the soot can be regarded as constant and thus the reaction rate is independent of, or in the zero order in the amount of soot.

Some new technologies are used to promote the reaction of the simultaneous removal of soot and NO_x. The typical one is nonthermal plasma (NTP) technology. NTP produced by electronic discharge has been broadly studied as a potential candidate for diesel exhaust post treatment since the 1990s. The plasma process is effective for low-temperature oxidation of soot in lean ambience without catalysts because the O radicals formed in the plasma zone oxidize the soot at a near-gas-kinetic rate within a wide temperatures range. The ionic wind induced by plasma enhances the quantity of the nitrogen oxides (NO_x) adsorbed onto the catalyst surface, and therefore promotes the redox reactions between diesel soot and NO_x.

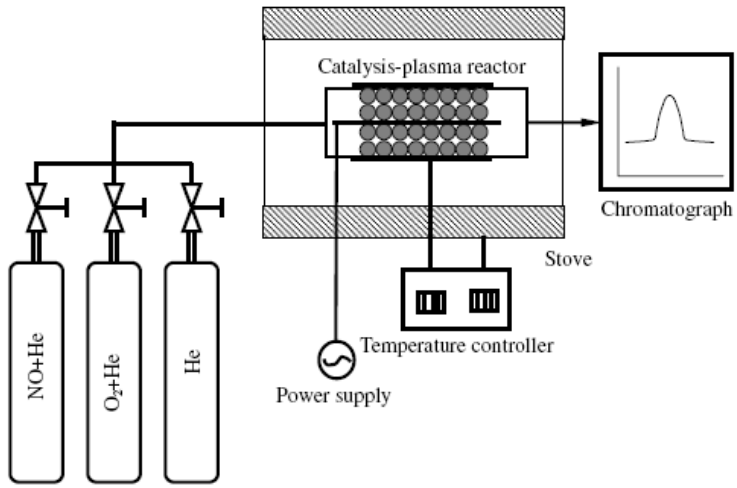

Figure 7. The scheme of the nonthermal plasma experimental system.

Furthermore, the plasma process improves soot oxidation by enhancing the NO_2 amount, which is an important intermediate in soot oxidation and NO_x reduction. A NTP experimental setup is as shown in Figure 6.

As the power supply is turned on, periodic current pulses varying with the voltage waveforms are seen a digital oscilloscope, which suggests that the gases between the discharge electrode and the dielectrics are ionized and that millisecond micro-discharges take place in the gaps. Lin et al. [135] uses NTP technology to promote the reaction of the simultaneous removal of soot and NO_x over a perovskite type of $La_{0.8}K_{0.2}MnO_3$ catalyst, as shown in Figure 7. It is found that the O radicals originating from the decomposition of O_2 advance PM oxidation, and the ignition temperatures of soot can be reduced efficiently by the plasma process.

The reactions between PM and NO_x, as well as the decomposition of nitrogen monoxide in plasma, will create N_2, and the N_2/NO rate (conversion rate of NO into N_2) can be promoted markedly by the plasma process. They found a low ignition temperature for soot combustion (about 388°C) by the method of hybrid catalysis-plasma. However, the selectivity

of the catalyst in reducing NO_x to N_2 is still low and ought to be further enhanced. In addition, the redox micro-mechanism between soot and NO_x should be thoroughly understood and the obstacle to NO_x reduction should be explored.

CONCLUSIONS AND PROSPECTS

Recent advances in diesel particulate control fitment of suitable particulate filters with highly efficient oxidation catalyst has been shown to effectively eliminate the larger coarse and accumulation modes of PM from the exhaust gas of diesel engines. At present, there are still many researches on diesel engine exhaust purification catalysts and catalytic post-processing technology.

Although every technology has its own advantages, there are no completely effective methods to satisfy the increasingly strict control requirement of exhaust emissions of diesel engine. Considering all the research progress for the removal of soot particulates, there are many problems unsolved on the catalysts of purification of diesel engine.

(1) The chemical reactions involved in the field of diesel exhaust are very complicated, which include the oxidation of soot, CO and hydrocarbon and the reduction of NO_X, and also include steam reforming reaction and water-gas shift reaction with a little of SO_2. It isn't clear that the mutual competition and promotion of these reactions on diesel exhaust catalytic converter, which would hamper us from understanding the interaction and coupling law of chemical reaction.
(2) The color of soot is deep-black, which lead to the deficiency of effective characterization technology by means of in situ and dynamic research for soot catalytic reaction. There is some debate about chemical essence of soot combustion reaction, such as the activation of adsorbed molecules on the surface of catalyst, the interaction between activation adsorption oxygen and intermediate species, the desorption, readsorption and further transformation of product molecule etc. At present, it is unclear that the reaction mechanism and influencing factors about the elimination of soot and NO_X in diesel exhaust, which would affect us to understand the essence of catalytic process and to design and develop the catalyst with high activity. Researchers need pay more attention to fundamental investigation and deepen the understanding of chemical nature of diesel exhaust catalytic purification.
(3) There are little reports on engineering of catalyst for the catalytic combustion of soot particulates, which plays an important role for practical catalyst of diesel exhaust purification. Engineering of catalyst involves the combination mode of catalyst bed, different reactor design, different goal reaction, and engineering knowledge such as mass transfer and heat transfer.

It is impossible to use one kind of catalyst to complete purifying the diesel exhaust gases. The catalytic systems for diesel exhaust purification include scientific law and technology of catalyst preparation, catalyst properties and characterization, catalyst system construction and catalyst reaction coupling etc. It's beneficial for people's health to solve the problems of diesel engine emission pollution (especially soot emission) with the development of catalytic

science and technology. The application of the catalytic combustion technology of soot will depend on many factor: emission laws accelerating soot particulates reduction, catalytic technological itself improvements, automotive interest to implement this technology, economy, and especially important people concern to their health possible adverse caused by soot emission.

ACKNOWLEDGMENT

This work was supported by the Program for New Century Excellent Talents in University of China (NCET), the National Natural Science Foundation of China (No. 20803093, 20833011), the 863 Program of China (No. 2009AA06Z313), CNPC Innovation Foundation (2010D-5006-0402), the Doctor Select Foundation for the University of State Education Ministry (No. 200804251016), and the Beijing Outstanding Ph. D Thesis Foundation (No. YB 20091141401).

REFERENCES

[1] Subramanian R., Winijkul E., Bond T.C., Thiansathit W., Nguyen T., Ittipol P., Duleep K.G., *Environ. Sci. Technol*., 2009, 43: 4213–4218.
[2] Neeft J.P.A., Makkee M., Moulijn J.A., *Fuel Process. Tech*., 1996, 47: 1-69.
[3] Stanmore B.R., Brilhac J.F., Gilot P., *Carbon*, 2001, 39: 2247-2268.
[4] Shi X., Qiao X., Zheng Y., *Energy and Fuels*, 2009, 23: 2413–2419.
[5] Xue H., Khalizov A. F., Wang L., Zheng J., Zhang R., *Sci. Technol*. 2009, 43: 2787–2792.
[6] Jacobson M.Z., *Nature*, 2001, 409: 695–697.
[7] Penner J.E., Chuang C.C., Grant K., *Climate Dynamics*, 1998, 14: 839–851.
[8] Pope C.A., Burnett R.T., Thurston G.D., Thun M.J., Calle E.E., Krewski D., Godleski J.J., *Circulation*, 2004, 109: 71–77.
[9] Maricq M.M., *J. Aerosol Sci*., 2007, 38: 1079-1118.
[10] Mauderly J.L., *Human Exposures and Their Health Effects*, 1992: 119-162.
[11] Vouitsis E., Ntziachristos L., Pistikopoulos P., Samaras Z., Chrysikou L., Samara C., Papadimitriou C., Samaras P., Sakellaropoulos G., *Environ. Pollution*, 2009, 157: 2320-2327.
[12] Knauer M., Schuster M.E., Su D., Schlogl R., Niessner R., Ivleva N., *J. Phys. Chem. A,* 2009, 113: 13871–13880.
[13] Liu J., Zhao Z., Xu C., Duan A., Jiang G., *Energy Fuels*, 2010, 24: 3778–3783.
[14] Kellog R., Winberry Jr.W. EPA compendium method IO-3.3 U.S. *Environmental Protection Agency*. 1999.
[15] Lough G.C., Schauer J.J., Park J.S., Shafer M.M., Deminter J.T., Weinstein J.P., *Environ. Sci. Technol*., 2005, 39: 826–836.
[16] Pineiro-Iglesias M., Lopez-Mahia P., Vazquez-Blanco E., Muniategui-Lorenzo S., Prada-Rodriquez D., *Polycyclic Aromatic Compounds*, 2002, 22: 129–146.
[17] Westerholm R., Li H., *Environ. Sci. Technol*., 1994, 28: 965–972.

[18] Lev-On M., Zielinska B., *SAE Paper*, 2004-01-1991.
[19] Villata G., Tarabocchia A., Bozzolini V., Caroca J., Russo N., Fino D., Saracco G., Specchia V., *SAE Paper*, 2009-01-0278.
[20] Bensaid S., Marchisio D.L., Fino D., *Chem. Eng. Sci*., 2010, 65: 357-363.
[21] Cauda E., Fino D., Saracco G., Specchia V., *Chem. Eng. Sci*., 2007, 62: 5182-5185.
[22] Fino D., Specchia V., *Powder Technol*., 2008, 180: 64-73.
[23] Saracco G., Fino D., *Pollution Control Mater.,* 2001, 1: 273.
[24] Guo G., Xu N., Laing P., Hammerle R.H., Maricq M.M. *SAE Paper* 2003-01-0047.
[25] Sánchez B.S., Querini C.A., Miró E.E., *Appl. Catal. A*, 2009, 366: 166-175.
[26] Hawker P., Myers N., Huthwohl G., Vogel H. T., Bates B., Magnusson L., Bronnehberg P., *SAE Paper* 970182.
[27] Kenneth V., Walter V., Duoduo L., Gustaaf V. T., Johan A. M., *Environ. Sci. Technol.,* 2006, 40: 2727-2733.
[28] Zhu R., Guo M., Ouyang F., *Catal. Today*, 2008, 139: 146-151.
[29] Wei Y., Liu J., Zhao Z, Xu C., Duan A., Jiang G., He H., *Angew. Chem. Int. Ed.*, 2011, 50: 2326-2329.
[30] Zhao Z., Liu J., Xu C., Duan A., Kobayashi K., Wachs I. E., *Top. Catal.* 2006, 38: 309-325.
[31] Sui L., Yu L., Zhang Y., *Energy Fuels*, 2006, 20: 1392-1397.
[32] Matarrese R., Castoldi L., Lietti L., Forzatti P., *Catal. Today*, 2008, 136: 11-17.
[33] Milt V.G., Querini C.A., Miro E.E., Ulla M.A., *J. Catal*., 2003, 220: 424-435.
[34] Mul G., Kapteijn F., Moulijn J.A., *Appl. Catal. B*, 1997, 12: 33-47.
[35] Liu J., Zhao Z., Wang J., Xu C., Duan A., Jiang G., Yang Q., *Appl. Catal. B,* 2008, 84: 185-195.
[36] Liang Q., Wu X., Weng D., Xu H., *Catal. Today*, 2008, 139: 113-118.
[37] Banús E.D., Milt V.G., Miró E.E., Ulla M.A., *Appl. Catal. A*, 2009, 362: 129-138.
[38] Chin P., Grant C.S., Ollis D.F., *Appl. Catal. B*, 2009, 87: 220-229.
[39] Masato M., Yuichiro M., Kouji K., Zhang D., Keita I., *Chem. Mater*., 2008, 20: 4489-4494.
[40] Atribak I., Bueno-López A., García-García A., Navarro P., Frías D., Montes M., *Appl. Catal. B*, *2010*, *93*: 267-273.
[41] Li S., Kato R., Wang Q., Toshiro Y., Tatsuya T., Wataru U., *Appl. Catal. B*, 2010, 93: 383-386.
[42] Liu J., Zhao Z., Lan J., Xu C., Duan A., Jiang G., Wang X., He H., *J. Phys. Chem.* C, 2009**,** *113*: 17114–17123.
[43] Liu J., Zhao Z., Xu C., Duan A., *Appl. Catal. B*, 2008, 78: 61-72.
[44] Russo N., Furfori S., Fino D., Saracco G., Specchia V., *Appl. Catal. B*, 2008, 83: 85-95.
[45] Shangguan W. F., Teraoka Y., Kagawa S., *Appl. Catal. B,* 1998, 16: 149-154.
[46] Liu J., Zhao Z., Xu C., Duan A., Meng T., Bao X., *Catal. Today*, 2007, 119: 267-272.
[47] Neeft J. P. A., Schipper W., Mul G., Makkee M., Moulijn J. A., *Appl. Catal. B,* 1997, 11: 365-382.
[48] Burch R., *Catal. Rev*., 2004, 46: 271-333.
[49] Neeft J.P.A., Makkee M., Moulijn J.A.. *Appl. Catal. B*, 1996, 8: 57-78.
[50] Neeft J.P.A., Makkee M., Moulijn J.A., *J. Chem. Eng*., 1996, 64: 295-302.
[51] Setten B.A.A.L., Gulijk C., Makkee M., Moulijn J.A., *Top. Catal*., 2001, 16: 275-278.
[52] Fino D., Fino P., Saracco G., Specchia V., *Chem. Eng. Sci*., 2003, 58: 951-958.

[53] Setiabudi A., Setten B.A.A.L., Makkee M., *Appl. Catal. B*, 2002, 35: 159-166.
[54] Setten B.A.A.L., Dijk R., Jelles S.J., Makkee M., Moulijn J.A., *Appl. Catal. B*, 1999, 21: 51-61.
[55] Liu J., Zhao Z., Xu C., Duan A., Zhu L., Wang X., *Catal. Today*, 2006, 118: 315-322.
[56] Liu J., Zhao Z., Xu C., Duan A., Zhu L., Wang X., *Appl. Catal. B*, 2005, 61: 36-46.
[57] Mul G., Neeft J.P.A., Kapteijn F., Makkee M., Moulijn J.A., *Appl. Catal. B*, 1995, 6: 339-352.
[58] Badini C., Saracco G., Serra V., *Appl. Catal. B: Environ*, 1997, 11: 307-328.
[59] Serra V., Saracco G., Badini C., Specchia V., *Appl. Catal. B*, 1997, 11: 329-346.
[60] Ciambelli P., Palma V., Russo P., *Catal. Today*, 2002, 75: 471-478.
[61] Ciambelli P., Palma V., Russo P., Vaccaro S., *Catal. Today*, 2000, 60: 43-49.
[62] Ciambelli P., Palma V., Russo P., Vaccaro S., *J. Mol. Catal. A: Chem*., 2003, 204: 673-681.
[63] Ciambelli P., Palma V., Russo P., Vaccaro S., *Ind. Eng. Chem. Res*., 2000, 39: 4914-4919.
[64] Pisarello M.L., Saux C., Miro E.E., Querini C.A., *Stud. Surf. Sci. Catal.,* 2001, 139: 141-148.
[65] Castoldi L., Matarrese R., Lietti L., Forzatti P., *Appl. Catal. B*, 2009, 90: 278-285.
[66] Zhang Z., Mou Z., Yu P., Zhang Y., Ni X., *Catal. Commun*., 2007 , 8: 1621-1624.
[67] Wang Z., Shangguan W.F., Su J., Jiang Z.. *Catal. Lett*., 2006 , 112: 149-154.
[68] Hinot K., Burtscher H., Weber A.P., Kasper G., *Appl. Catal. B*, 2007, 71: 271-276.
[69] Jeguirim M., Tschamber V., Ehrburger P., *Appl. Catal. B*, 2007, 76: 235-243.
[70] Oi-Uchisawa J., Obuchi A., Zhao Z., Kushiyama S., *Appl. Catal. B,* 1998, 18: L183-187.
[71] Oi-Uchisawa J., Obuchi A., Wang S. D., Nanba T., Ohi A., *Appl. Catal. B*, 2003, 43: 117-129.
[72] Oi-Uchisawa J., Wang S. D., Nanba T., Ohi A., Obuchi A., *Appl. Catal. B,* 2003, 44: 207-215.
[73] Oi-Uchisawa J., Obuchi A., Ohi A., Nanba T., Nakayama N., *Powder Technol*., 2008, 180: 39-44.
[74] Cooper B.J., Thoss J.E., *SAE paper* 890404.
[75] Cooper B.J., Radnor H.J., Jung W., Thoss J.E., *US patent*, 904487, 1990.
[76] Corro G., Fierro J.L.G., Romero F.B., *Catal. Commun*., 2006, 7: 867-874.
[77] Xue E., Seshan K., Ross J.R.H., *Appl. Catal. B*, 1996, 11: 65-79.
[78] Xue E., Seshan K., Ommen J.G., Ross J.R.H., *Stud. Surf. Sci. Catal*., 1993, 75: 2665-2668.
[79] Xue E., Seshan K., Ommen J.G., Ross J.R.H., *Appl. Catal. B*, 1993, 2: 183-197.
[80] Cauda E., Fino D., Saracco G., Specchia V., *Top. Catal*., 2004, 30: 299-308.
[81] Russo N., Fino D., Saracco G., Specchia V., *Catal. Today*, 2008, 137: 306-311.
[82] Craenenbroeck J.V., Andreeva D., Tabakova T., Werde K.V., Mullens J., Verpoort F., *J. Catal*. 2002, 209: 515-527.
[83] Zhu R., Guo M., Ci X., Ouyang F., *Catal. Commun*., 2008, 9: 1184-1188.
[84] Villani K., Kirschhock C.E.A., Liang D., Tendeloo G.V., Martens J.A., Angew. *Chem. Int.* Ed., 2006, 45: 3106-3109.
[85] Aouad S., Abi-Aad E., Aboukaïs A., *Appl. Catal. B,* 2009, 88: 249-256.

[86] Aneggi E., Llorca J., Leitenburg C., Dolcetti G., Trovarelli A., *Appl. Catal. B*, 2009, 91: 489-498.
[87] Wyatt M., Manning W.A., Roth S.A., DAniello M.J.Jr., Andersson E.S., Fredholm, S.C.G., *SAE paper* 930130.
[88] Ball D.J., Stack R.G., *SAE paper* 902110.
[89] Heak M.G., Williamson W.B., Silver R.G., *SAE paper* 920368.
[90] Engler B.H., Lox E.S., Ostgathe K., Cartellieri W., Zelenka P., *SAE paper* 910607.
[91] Zhu L., Wang X.Z., Yu J.J., Hao Z.P., *Acta Phys. Chim. Sin*, 2005, 21: 840-845.
[92] Weng D., Li J., Wu X.D., Lin F., *Catal. Commun*., 2008, 9: 1898-1901.
[93] Wu X.D., Liang Q., Weng D., Lu Z. X., *Catal. Commun*., 2007, 8: 2110-2114.
[94] Liang Q., Wu X.D., Weng D., L Zh. X., *Catal. Commun*., 2008, 9: 202-206.
[95] Atribak I., SuchBasáÌez I., BuenoLópez A., García A., J., *Catal*., 2007, 250: 75-84.
[96] Krishna K., Bueno López A , Makkee M , Moulijn J.A., *Appl. Catal B*, 2007, 75: 201-209.
[97] Liu J., Zhao Z., Xu C., Duan A., Wang L., Zhang S., *Catal. Commun*., 2007, 8: 220-224.
[98] Biamino S., Fino P., Fino D., Russo N., Badini C., *Appl. Catal*. B, 2005, 61: 297-305.
[99] Russo N., Fino D., Saracco G., Specchia V., *J. Catal.*, 2005, 229: 459-469.
[100] Fino D., Russo N., Cauda E., Saracco G., Speccia V., *Catal. Today*, 2006, 114: 31-39.
[101] Fino D., Specchia V., Chem. Eng. Sci., 2004, 59: 4825-4832.
[102] Fino D., Russo N., Saracco G., Speccia V., *J. Catal*., 2003, 217: 367375.
[103] Wang H., Zhao Z., Xu C., Liu J., *Catal. Lett*., 2005, 102: 251-256.
[104] Wang H., Zhao Z., Xu C., Liu J., Lu Z., *Chin. Sci. Bull*., 2005, 50: 1440-1444.
[105] Wang H., Zhao Z., Liang P., Xu C., Duan A., Jiang G., Xu J., Liu J., *Catal. Lett*., 2008, 124: 91-99.
[106] Liu G., Huang Z., Shangguan W.F., *Chin. Sci. Bull*., 2002, 47: 1620-1624.
[107] Shangguan W.F., Teraoka Y., Kagawa S., *Appl. Catal. B,* 1996, 8: 217-227.
[108] Liu J., Zhao Z., Xu C., Wang H., Duan A., Chin. *J. Jnorg. Chem*., 2005, 21: 1306-1311.
[109] Velev O.D., Lenhoff A.M., *Current Opinions in colloid and Interface Science*, 2000, 5: 56-63.
[110] Chi E.O., Kim Y.N., Kim J.C., Hur N.H., *Chem. Mater*., 2003, 15: 1929-1931
[111] Velev O.D., Jede T.A., Lobo R.F., Lenhoff A.M., *Nature*, 1997, 389: 447-448.
[112] Sun K., Xia H., Hensen E., Santen R., Li C., *J. Catal*., 2006, 238: 186-197.
[113] Sadakane M., Asanuma T., Kubo J., Ueda W., *Chem. Mater*., 2005, 17: 3546-3551.
[114] Sadakane M., Asanuma T., Kato N., Takahashi C., Ueda W., *Chem. Mater*., 2007, 19: 5779-5788.
[115] Zhang G., Zhao Z., Liu J., Duan A., Jiang G., Zheng J., Chen S., Zhou R., *Chem. Commun*., 2010, 46: 457-459.
[116] Orilall M.C., Abrams N.M., Wiesner U., *J. Am. Chem. Soc.* 2008, 130: 8882-8883
[117] Zhang G., Zhao Z., Liu J., Xu J., Jing Y., Duan A., Jiang G., *J. Rare Eartrhs*, 2009, 27: 955-960.
[118] Xu J., Liu J., Zhao Z., Zheng J., Zhang G., Duan A., Jiang G., *Catal. Today,* 2010, 153: 136-142.
[119] Liu Z.P., Jenkins S.J., King D.A., *J. Am. Chem. Soc*., 2004, 126: 10746-10747.
[120] Peng X., Lin H., Shangguan W.F., Huang Z., *Catal. Commun*., 2007, 8: 157-164.
[121] Okajima S., Kumagai S., *Symposium on Combustion*., 1991, 23: 275-279.

[122] Teraoka Y., Nakano K., Kagawa S., Shangguan W.F., *Appl. Catal. B*, 1995, 5: 181-185.
[123] Teraoka Y., Nakano K., Shangguan, W.F. Kagawa S., *Catal. Today*, 1996, 27: 107-113.
[124] Shangguan W.F., Teraoka Y., Kagawa S., *Appl. Catal. B*, 1998, 16: 149-154.
[125] Teraoka Y., Kanada K., Kagawa S., *Appl. Catal. B*, 2001,34: 73-78.
[126] Shangguan W.F., Teraoka Y., Kagawa S., *Appl. Catal. B*, 1996, 8: 217-227.
[127] Peng X., Lin H., Shangguan W., Huang Z. *Ind. Eng. Chem. Res*., 2006, 45: 8822-8829.
[128] Hong S.S., Lee G.D., *Catal. Today*, 2000, 63: 397-404.
[129] Zhu L., Wang X., Liang C., *J. Rare Earths*, 2008, 26: 254-257.
[130] Liu J., Zhao Z., Xu C., Duan A., Jiang G., *Ind. Eng. Chem. Res*., 2010, 49: 3112-3119.
[131] Fino D., Fino P., Saracco G., Specchia V., *Appl. Catal*. *B*, 2003, 43: 243-259.
[132] Zhao Z., Obuchi A., Oi-Uchisawa J., Ogata A., Kushiyama S., *Chem. Lett*., 1998, 4: 367-368.
[133] Wang Z., Jiang Z., Shangguan W., Catal. Commun. 2007, 8: 1659-1664.
[134] Liu J., Zhao Z., Xu C., Duan A., Jiang G., *J. Phys. Chem.* C, 2008, 112: 5930-5941.
[135] Lin H., Huang Z., Shangguan W., Peng X., *Proceed. Comb. Institute*, 2007, 31: 3335-3342.

In: Catalytic Combustion
Editor: Sophie A. Cottilard, pp. 105-140
ISBN: 978-1-61324-279-7

Chapter 3

CATALYTIC COMBUSTION OVER CHEAPER METAL OXIDES

Thallada Vinodkumar **and** ***Benjaram M. Reddy****
Inorganic and Physical Chemistry Division, Indian Institute of Chemical Technology, Uppal Road, Hyderabad – 500 607, India

ABSTRACT

Currently, mankind has been facing the consequences arising from extensive fossil-fuel exploitation and their continuous use is expected to produce more harmful effects. It is an acknowledged fact that world's major energy needs are met from thermal power generation which depends mainly on the combustion of fossil fuels. On the other hand, these combustion systems have elevated much of the environmental problems. One of the emission gases of most serious concern is nitrogen oxide (NO_x), which causes acid rain, global warming and ozone depletion. To settle the global environmental and energy issues, the combustion systems need to be much more improved for high efficiency and low pollutant emissions. Catalytic combustion has been developed as a method of promoting efficient combustion over a wide range of air-to-fuel ratios with a minimum pollutant formation at low temperatures as compared to conventional flame combustion. The application of catalysts facilitates efficient combustion of hydrocarbons at relatively lower temperatures without promoting oxidation of nitrogen and also stringent control over the emission of volatile organic compounds (VOCs). Generally, effective emission control is often achieved by the use of noble metal catalysts; they are very active at low temperatures but due to the economical reasons, as well as limited availability of noble metals, motivated the investigation into the alternative materials for catalytic combustion. Metal oxides are the promising option, because they are relatively cheap, show variable valency and exhibit greater redox characteristics. Mixed metal oxides in the form of perovskites, hexa-aluminates and doped metal oxides are promising because of their thermal stability at high temperatures, low cost, and flexible composition. Among doped metal oxides, ceria-based materials are attractive in catalytic combustion apart from three-way-catalytic applications, VOC abatement, and fuel cell technologies due to their ease of redox and high thermal stability. Metal oxide catalysts exhibit good catalytic

*E-mail: bmreddy@iict.res.in; mreddyb@yahoo.com

activity in narrow temperature range. However, the catalytic combustion range is up to 1773 K for that, it is necessary to add supports to increase the thermal stability. Recently, it has been reported that ceria supported on lanthanum hexa-aluminate shows an impressive activity and stability up to 1273 K. In this chapter we have concentrated on the catalytic application of pure metal oxides, and mixed metal oxides such as perovskites, hexa-aluminates and ceria doped materials for catalytic combustion. We also discussed the significance of supports to metal oxides to improve the catalytic efficiency at high temperatures. Finally, we have provided new directions for future work on this subject.

1. GENERAL INTRODUCTION

Scotsman James Watt improved the steam engine in the second half of the 18th century making it possible for the first time to convert thermal energy of the fuel into useful work which was earlier done by using the hydropower. Steam engine became a truly viable piece of machinery that helped the start of Industrial Revolution that shaped the world what we see today [1]. During the last part of the 19th and the early part of the 20th century several other engines were developed, e.g., the Otto engine, the diesel engine, the steam turbine, and the gas turbine. All of which were based on thermal combustion of fuels. During the 20th century apprehension over the availability of energy sources and the impact of combustion processes on the global environment have attracted more and more attention. Although the power sources such as nuclear power, solar power, wind power, etc., have been developed during this period; the main contribution to the world's power demand still comes from combustion of fossil fuels [2]. Currently, mankind has been facing the consequences arising from extensive fossil-fuel exploitation, and their continuous use is expected to produce more harmful effects [3]. During the combustion process it emits huge amount of pollutants which are fatal to the environment. There are two types of combustion processes: (i) incomplete combustion and (ii) complete combustion. In the incomplete combustion process, carbon monoxide (CO), unburned hydrocarbons (UHC), soot, dioxins, etc., are normally emitted. However, even if it undergoes complete combustion, some of the emissions are still formed such as nitrogen oxides (NO_x), sulfur oxides (SO_x), carbon dioxide (CO_2), etc. NO_x can be formed directly from the nitrogen and oxygen in the air if the temperature is high enough, i.e., above 1773 K. So, introducing a catalytically active surface at which the fuel can react with the air makes it possible to move the combustion over a wide range of air-to-fuel ratios. By using a much higher air-to-fuel ratio, the adiabatic flame temperature could be lowered below the threshold temperature for NO_x formation, at the same time keeping the combustion stable, i.e. yielding very low emissions of NO_x as well as CO, UHC, etc [2].

1.1. Conventional Combustion

Combustion is defined as the burning of a fuel and oxidant to produce heat. It starts with mixing of fuel and oxidant, and sometimes in the presence of other species or catalysts. The fuel can be gaseous, liquid, or solid and the mixture may be ignited with a heat source. When ignited, chemical reactions of fuel and oxidant take place and the heat release from the reaction creates a self-sustained process. The typical combustion products include heat,

chemical species, and pollutants [4]. It is the major energy release mechanism in the Earth and key to mankind's existence. Still today more than 90% of the world's energy production comes from combustion sources. When a fuel is burnt using a conventional combustion a flame is generally visible. If we consider fuel and air mixture, it is seen that flames can only occur within a certain composition range, known as flammability limits which depends on the type of fuel. For example, methane in air the flammability limits are between 5 and 16% methane by volume, and therefore flames can only occur between these flammability limits. Temperatures within the flame often exceed the maximum desired temperature range [5]. The mechanism involved in the combustion processes is a complex one which involves large number of radicals and other short lived species. For fuels like diesel or gasoline hundreds of reactions take place at high temperatures involved in the combustion process. The high temperatures and the complex chemistry involved in the combustion processes yield emissions of reaction products ranging from small molecules like carbon monoxide and nitrogen oxides up to large particles of soot built up of thousands of polyaromatic hydrocarbons [2]. The technology of combustion finds applications in the equipment for heating, for power production, and for propulsion, as well as in the techniques for creating explosions, for destruction of toxic wastes, and for mitigating fire hazards [6]. The application of combustion is not without problems. During the combustion fuels require high temperature to oxidize completely. At high temperatures thermal NO_x is formed since the nitrogen molecule is very stable. The energy of the N≡N bond is 954 kj mol^{-1}. Generally, the chemical reactions are controlled by temperature, pressure, concentration, and residence time. However, fuel is normally burnt at atmospheric pressure for this reason, pressure condition do not effect the nitric oxide formation in the combustion processes. The typical conditions of NO_x formation are: (i) high atomic oxygen concentration, (ii) high combustion zone temperature, and (iii) long residence time in high-temperature zone. In fact, thermal NO_x formation is mainly controlled by peak temperature in the reaction zone, atomic oxygen concentration, and residence time of combustion products in the high temperature zone [7].

1.2. Impact of Nitrogen Oxides

The nitrogen oxides emitted by combustion sources are predominantly in the form of nitric oxide (NO) with the residual, usually less than 5%**,** in the form of nitrogen dioxide (NO_2) [8]. The nitrogen oxides are dangerous for humans if inhaled in as low concentrations as 0.05 ppm [9]. They are formed during various combustion processes and have been identified as the cause of various environmental and health-related issues [10]. While carbon dioxide remains inert within the atmospheric reservoir, the other components participate in many chemical reactions assisted by various factors such as solar radiation. Volatile organic compounds in combination with NO_x cause atmospheric ozone and smog formation. The presence of large amounts of ozone in the troposphere has negative effects illustrated by the formation of nitrogen pentoxide that in reaction with water droplets causes the formation of nitric acid, resulting in the so-called acid rain. Acid rain has a strong impact on the human health as well as on the environment, causing forest depletion, acidification of lakes, and water ways. Strong evidence indicated that the major culprit in NO_x production was the automobile. However, as automobile emission standards were enforced, attention has been directed towards power plants that utilize fossil fuels [11].

1.3. Paths of NO_x Formation

Nitrogen oxides are formed during combustion via three different routes namely, (i) thermal NO_x, (ii) prompt NO_x, and (iii) fuel NO_x. The first two involve the nitrogen in the combustion air, while the last one involves nitrogen bound in the fuel. Thermal nitrogen oxides are formed by the radical chain mechanism proposed by Zeldovich [12] and Kotler [13] as shown in the equations (1−3).

$$O_2 + M \underset{}{\overset{k_1}{\rightleftharpoons}} 2O + M \quad (1)$$

$$N_2 + O \underset{}{\overset{k_2}{\rightleftharpoons}} NO + N \quad (2)$$

$$O_2 + N \underset{}{\overset{k_3}{\rightleftharpoons}} NO + O \quad (3)$$

M can be any molecule that can act as an energy transfer agent. Where, $k_1 = 2.5 \times 10^{11} T^{1/2} \exp(-E/RT)\ cm^3\ mol^{-1}\ s^{-1}$; E = 118 kcal/mol; $k_2 = 10^{13.8} \exp(-75/RT)\ cm^3\ mol^{-1}\ s^{-1}$; $k_3 = 10^{13.5} \exp(-7.9/RT)\ cm^3\ mol^{-1}\ s^{-1}$. Reaction (3) is much faster than (2); therefore, the rate of NO formation is given in the equation (4)

$$\frac{d[NO]}{dt} = 2k_2[O][N_2] = k_{eff}.k^{1/2}[O_2]^{1/2}\ [N_2] \quad (4)$$

in which k_{eff} is the effective rate constant. The concentration of thermal NO_x depends on the temperature exponentially; large amounts of NO_x may be formed even at 1600 K which is shown in Figure 1.

Regarding prompt NO_x, Fenimore [15] discovered that some NO_x was formed in the flame zone before the residence time was sufficient for the formation of NO_x through the thermal mechanism.

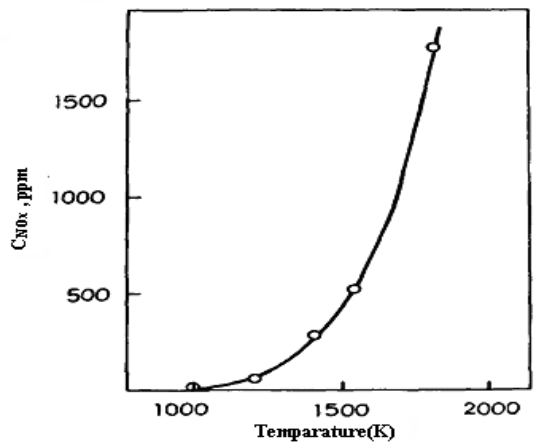

Figure 1. The formation of thermal NO_x verses temperature [Ref. 14].

Due to the fast reaction it was named prompt NO_x [16]. It is formed from reactions between hydrocarbon radicals and nitrogen molecules forming hydrogen cyanide, which is further oxidized into NO.

The formation of prompt NO_x takes place in hydrocarbon-containing flames. Most of it is formed in rich flames. Prompt NOx formation may occur at much lower temperatures than the formation of thermal NOx. The prominent reaction for forming prompt NOx is shown in the equation (5). The N radical can then react further as shown in the equation (6).

$$HC + N_2 \rightarrow HCN + N \quad (5)$$

$$N + OH \rightarrow H + NO \quad (6)$$

The prompt NOx formation cannot be avoided by lowering the combustion temperature, which is the case for the thermal NOx. As the formation temperature is much lower than for the thermal NOx, hence the only way to circumvent its formation is by lowering the amounts of hydrocarbon radicals formed.

The other important source for NOx production is from nitrogen-bearing fuels such as certain coals and oil. As the fuel is being burnt the nitrogen-containing molecules will thermally decompose into low molecular weight compounds and radicals. These radicals will then be oxidized into NOx. The nitrogen contents will almost inevitably be oxidized to nitrogen oxide, as the oxidation process of the nitrogen-containing molecules is very fast. Effect of temperature on the formation of prompt NO_x and fuel NO_x upon coal combustion is shown in Figure 2.

To clear up these global environment and energy issues, the combustion systems need to be much improved for high efficiency and low pollutant emissions. Schematic representation of combustion processes is shown in Figure 3.

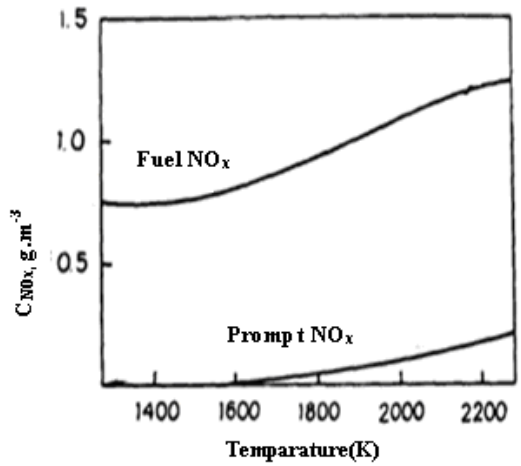

Figure 2. Effect of the temperature on the formation of prompt NO_x and fuel NO_x upon coal combustion [Ref. 17].

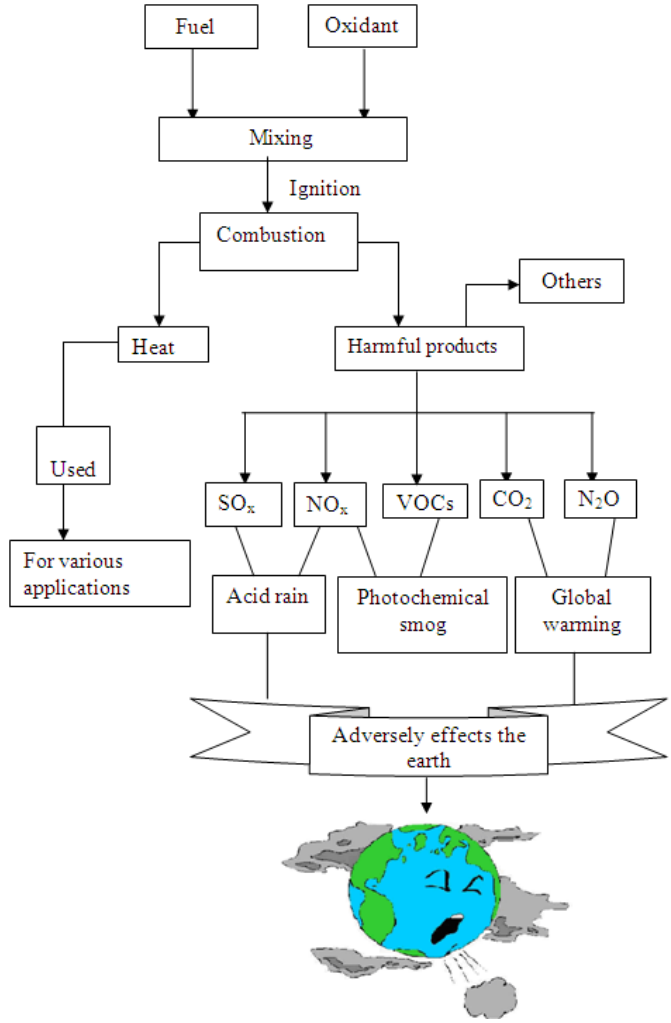

Figure 3. Schematic representation of the combustion processes [Ref. 18].

2. IMPORTANT NO_x CONTROLLING TECHNOLOGIES

The important NO_x controlling technologies include (i) lean premixed combustion, (ii) catalytic combustion, (iii) water or steam injection, and (iv) selective catalytic reduction. Among various technologies catalytic combustion is the best controlling technology [19].

2.1. Catalytic Combustion

Interestingly, the first use of catalysts to promote combustion was discovered at the beginning of the 19th century when Sir Humphrey Davy observed that the coal gas could be combusted in air without a flame over a platinum surface [20]. Davy's observation was that catalytic combustion reactions not only take place "without flame" but also with high

radiative fluxes from the hot catalyst wall, which led to the development of numerous radiative heater devices and thus the first practical use of catalysts.

The devices of Weiss [21] and Milligan [22] are some other examples. The discovery resulted in the invention of the miner's safety lamp, which could be used in mines without risking mine gas explosions.

Different applications of catalytic combustion have been introduced since then, for example, abatement of volatile organic compounds, small-scale heaters, and ultra low NO_x emissions etc. William Pfefferle was the first to propose catalytic combustion for gas turbines in the early seventies [23]. Since then, an increasing number of publications have been appeared in this field [23−32]. Catalytic combustion differs from homogeneous combustion in that the main part of the combustion occurs on a catalytically active surface. This facilitates the reaction mechanism to follow another route with lower activation energy. Thus the temperature for complete combustion can be lowered, as the amount of heat generated remains the same [16]. Contrast to conventional combustion, catalytic combustion occurs over a wide range of air-to-fuel ratios. It does not require the presence of flame, nor ignition source like a spark or pilot flame. There is however, minimum inlet gas temperature required to have a sufficiently high catalyst activity to achieve complete combustion.

During the last 40 years, two powerful pressures have combined and forced the scientific community to pay more and more attention to this grand old process. The first pressure was the increased awareness of the problems caused by air pollution. This forced to look up and develop combustion techniques which reduce pollutant emissions from anything we burn. The second pressure was the energy crisis from 1973 onwards, leading to enhance continuously the combustion efficiency of any fuel that we burn. These two pressures led to the development of catalytic combustion. Use of catalysts facilitates efficient combustion of hydrocarbons at relatively low temperatures without promoting oxidation of nitrogen. The reaction of atmospheric nitrogen with oxygen is slow at temperatures below 1773 K. The major applications of catalytic combustion are twofold: at low temperatures to eliminate VOCs and at high temperatures greater than 1273 K to reduce NO_x emission from gas turbines, jet motors, etc [33,34]. Apart from these the commercial applications of catalytic combustion are (i) radiant heaters, (ii) house hold appliances, (iii) sensors, (iv) domestic burners, (v) chemical reactor heaters etc. Conventional combustion verses catalytic combustion upon fuel combustion is shown in Figure 4.

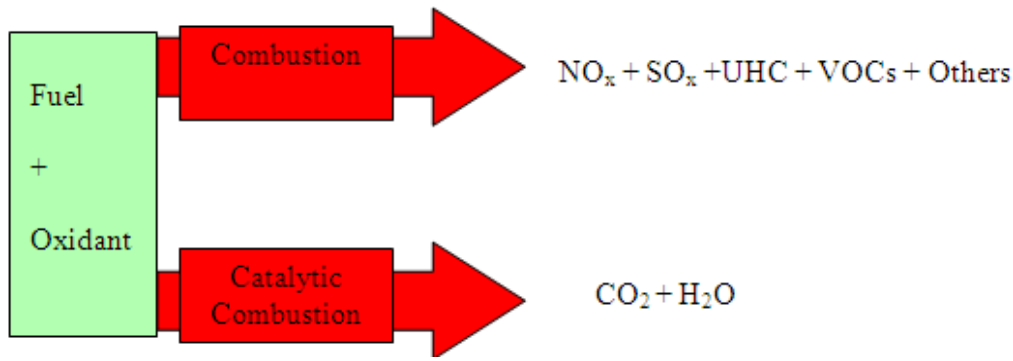

Figure 4. Conventional combustion verses catalytic combustion.

2.2. Characteristics of Catalytic Combustion

In its simplest form, a catalytic combustor consists of a catalyst bed through which a pre-mixed fuel/air mixture is passed. Three distinct regions in the combustion system are shown in the following Figure 5.

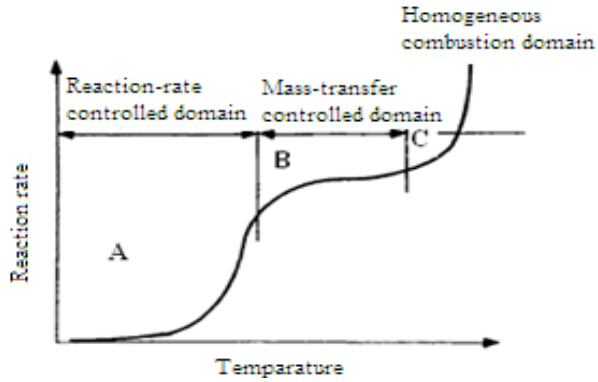

Figure 5. Reaction rate verses temperature for a combustion catalyst [Ref. 34].

In the first part of the catalyst bed that is at region A the reaction is kinetically controlled at low temperatures. The intrinsic surface kinetics controls the overall process. Here the reaction rate increases exponentially with temperature. With more active catalysts, or at higher temperatures, or at higher fuel concentrations, the overall reaction can be controlled by mass transport to the catalyst surface (region B). Here the reaction becomes quite insensitive to the changes in the temperature, also insensitive to the precise nature or activity of the catalyst. Here the heterogeneous catalytic kinetics plays a secondary role in determining the reaction rate. As the exothermic reaction continuous further, the temperature increases. Finally, at some point in the bed, the bulk gas temperature becomes so high that the homogeneous gas-phase reactions occur simultaneously with the catalytic reactions on the surface. Then the combustion goes to completion i.e., 100% conversion (region C). This shows that in a catalytic combustor, the combustion process is initiated and stabilized by the catalyst. The formation of NO_x with temperature in various combustion processes is shown in Figure 6.

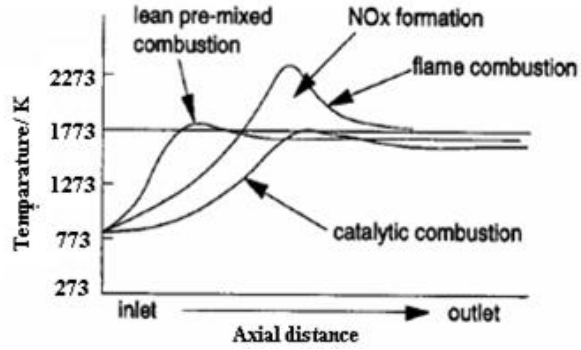

Figure 6. Schematic profiles of temperature and NO_x emission in conventional combustion, catalytic combustion, and in lean premixed combustion [Ref. 35].

3. CATALYTIC COMBUSTION APPLICATIONS

Depending upon the temperature range, catalytic combustion can be broadly divided into two categories, low-temperature catalytic combustion (LTCC) and high-temperature catalytic combustion (HTCC). The LTCC is used to eliminate traces of VOCs in air, and the HTCC is most commonly used to produce heat either for direct use or for transformation into electricity, for example, in a gas turbine. In this chapter a brief overview of the VOCs and gas turbines are presented. To understand the application of catalytic combustion in gas turbines and abatement of VOCs, it is very important to have some basic knowledge of VOCs and gas turbines and the conditions prevailing in both.

3.1. Volatile Organic Compounds (VOCs)

VOCs are present at everywhere, for example, they are present at (i) homes, (ii) food precursors, (iii) petroleum refineries, (iv) automobile service stations, (v) electronics and chemical plants, (vi) paint shops, etc [36]. VOCs are the chemicals that evaporate easily at room temperature that includes hydrocarbons, olefins, aromatics, and various nitrogen-, oxygen-, sulfur- and halogen containing molecules. There are thousands of different VOCs produced and used in our daily lives. Some common examples include: acetone, benzene, ethylene glycol, formaldehyde, methylene chloride, perchloroethylene, toluene, xylene, 1,3-butadiene, etc [37]. The US Environmental Protection Agency (EPA) gave the following definition for VOCs. VOC means any compound of carbon, with out including carbon monoxide, carbon dioxide, carbonic acid, metallic carbides or carbonates, and ammonium carbonate, which participates in atmospheric photochemical reactions. These compounds contribute to air pollution by their vapour [38]. Most VOC emissions result from man-made sources. They are emitted from many industrial processes and transportation activities, and are considered to be an important class of air pollutants [37]. Approximately 235 million tonnes of VOCs are released per year into the atmosphere by man-made sources. The three major sources of VOCs as shown in Figure 7. are: (i) power generation (20%), (ii) vehicle emissions (40%), (iii) solvents (27%), (iv) and others (13%) [39].

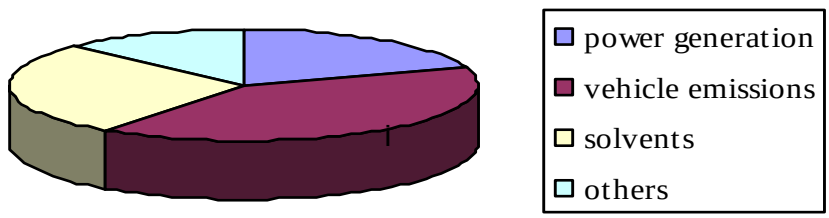

Figure 7. Representation of VOC sources using pie diagram.

VOCs are dangerous for humans, fauna, and vegetation. Firstly, these compounds have been proved to cause a variety of adverse health effects. VOCs generally refer to a group of chemicals. Each chemical has its own toxicity and potential for causing different health

effects [40]. The ground level or "bad" ozone is a key component of urban smog which is created by a chemical reaction between oxides of nitrogen (NO_x) and VOCs in the presence of sunlight. Repeated exposure to ozone pollution may cause a variety of health problems [41]. Ozone also reduces the growth rate of trees and agricultural production. VOCs participate in the greenhouse effect, acid rain, and stratospheric or "good" ozone depletion, which are serious environmental problems [42,43].

3.1.1. VOC Abatement Technologies

The progressive increase of VOCs emissions, as well as of the information about their harmful effects, and determined environmental legislation of the worldwide were led to introduce more stringent regulations to control their release [41]. The Clean Air Act Amendments of 1990 calls for a 90% reduction in emissions of 189 toxic chemicals, 70% of them are VOCs, over the next years. For that call, US EPA has been working for a cleaner and healthier environment for the American people for 30 years, and states and cities implemented programs to further reduce emissions from stationary and mobile sources. Some of the solutions include green technologies, cleaner car and fuel gas station using special nozzles at the pumps to recapture vapour, vehicle inspection programs, etc. At the beginning of 1997 there were over 6000 systems operating throughout the world controlling VOC emissions [44].

Various strategies exist to control VOCs release which includes condensation, adsorption, scrubbing, thermal oxidation, flaring, biological treatment, odor modification, air dilution, membrane separation, ultraviolet treatment, and catalytic oxidation/combustion [45−52]. They use either the capture of the pollutants or/and their destruction. When products recovery is desired capture techniques like condensation, absorption and adsorption are required. Scrubbing and adsorption cause other problems of separation and solid waste disposal. The use of these methods depends on the nature of the VOCs, the concentration levels and the conditions (temp, pressure, and flow rates) [36]. Among the technologies mentioned above for VOCs abatement the most widely implemented is the incineration (oxidation). Destruction efficiency of this method can achieve more than 99% depending on the type of the system employed [53]. There are two forms of oxidation: thermal oxidation and catalytic oxidation.

3.1.2. Catalytic Oxidation versus Thermal Oxidation

Oxidation, the most often used method, destroys VOCs by burning them at temperatures higher than 1273 K. These high temperature processes generate the formation of undesirable by-products such as nitrogen oxides, dibenzofurans, dioxins etc. This is a thermal oxidation and it occurs in a thermal oxidizer as shown in Figure 8. This reaction is an exothermic one, so the resulted heat could be used to preheat the incoming exhaust. Thus, the input energy required is less and fuel costs are reduced. This can be used for almost any VOC compound. Thermal oxidizers are rarely used on gas streams having VOC concentrations exceeding approximately 25% of the *lower explosive limit (LEL)***.** This limit is imposed by safety constraints due to the possibility that a short-term concentration spike would exceed the LEL, and the gas stream would explode. The 25% LEL depends on the actual gas constituents and usually is in the 10,000 to 20,000 ppm range.

In the presence of catalyst the same reaction occurs in a catalyst bed. This is the catalytic oxidation which occurs in a catalytic oxidizer as shown in Figure 9. The activation energy barrier is lower for this method, so the temperature required is significantly lower, typically

starting at 478 to 533 K [54]. In addition, the catalyst facilitates a faster reaction in smaller volume equipment.

Exhaust air from the process is ducted to the catalytic oxidizer system, passing through a primary heat exchanger and then into the auxiliary burner chamber where the air is heated to the specific VOC catalyst reaction temperatures. The heated exhaust then passes through a catalyst bed where a rapid chemical oxidation reaction occurs. The air leaving the catalyst carries the additional heat released, due to this oxidation process and this leaving energy is used for heat recovery.

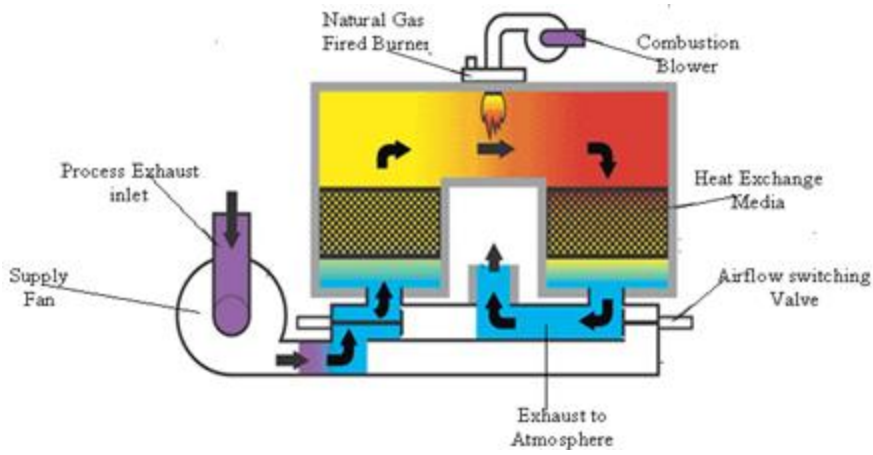

Figure 8. Typical thermal oxidizer.

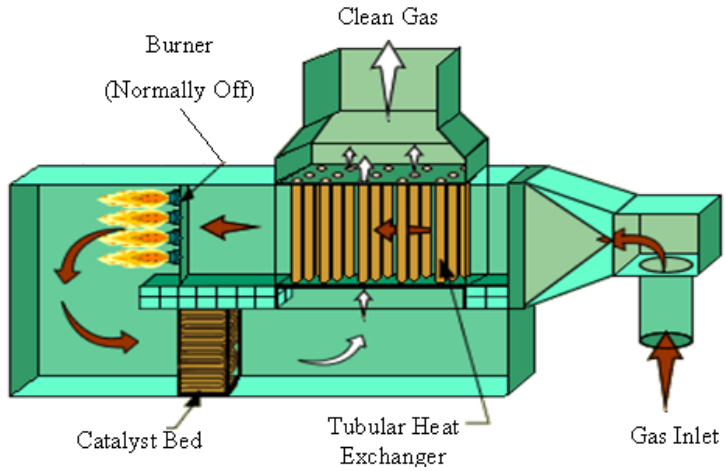

Figure 9. Typical catalytic oxidizer.

Catalytic oxidation typically has environmental applications for VOCs concentrations from a few hundred to a few thousand parts per million but, is the preferred technology for relatively low VOCs concentrations (~10 ppm). Destruction efficiencies up to 99% can be achieved [55]. The major benefit of the catalytic combustion is that it can treat very dilute

pollutants less than 1% efficiently which cannot be thermally combusted without additional fuel. It is more energy efficient, and therefore, has a distinct economic advantage [56,57].

3.2. Gas Turbines

The gas turbine is one of the most important inventions in the 20th century and it changed the life style of society in many ways. Gas turbine development started just before the Second World War with the electric power applications in the mind. Early gas turbines for power generation applications were of low power, and thermal efficiency was too low. By the end of 20th century, however, gas turbines are capable of outputs up to 300 MW with the thermal efficiencies of 40% and the gas turbine became widely used in power generation [58]. The first patent for a combustion turbine was issued in 1791 to John Barber. Since then, gas turbines have been used for a great number of applications. However, with the use of gas turbines large amounts of pollutants were released into the atmosphere. The pollutants released from gas turbines were mainly NO_x , CO etc. The effects of these pollutants were first noticed in the 1950's, because these are the precursors to the formation of smog and acid rain which became prominent. The attentiveness of these effects has resulted in numerous regulations concerning the allowed pollution levels.

As the electricity demand is increasing and thereby the amounts of pollution, the regulations become more stringent every year. Therefore, it has become an important issue for the gas turbine manufacturers to improve combustion efficiency in order to reduce fuel consumption and emissions. They work by mixing fuel with compressed and heated air, which burns and generates energy to run the turbines. A typical gas turbine in its simplest form consists of three main components, i.e., a compressor, a combustion chamber, and a turbine. They are connected as illustrated in Figure 10.

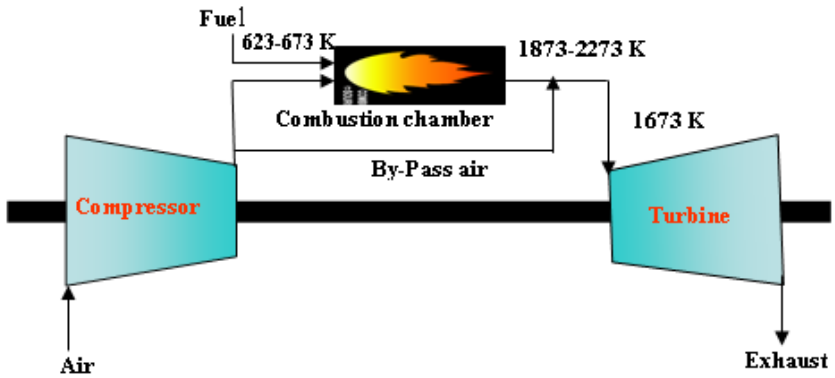

Figure 10. Flow diagram of simple gas turbine.

The first component in a gas turbine is a compressor, which increases the pressure of air from atmospheric to 5-30 bars, depending on the type of gas turbine. When air is compressed, the temperature is simultaneously increased. The compressor discharge temperature is

dependent on the pressure ratio over the compressor, and may therefore vary between 623 and 723 K. This temperature is in some cases increased further by exchanging the heat from the turbine's warm exhaust gas. If the compressed air is expanded directly in the turbine, and if there are no losses in any of the components the power developed by the gas turbine would equal to the power supplied to the compressor. Consequently, there would not be any net power produced in the gas turbine. If the temperature of the air is extensively increased prior to expansion, the power development is on the other hand significantly improved. The second component in a gas turbine is a combustion chamber, also called a combustor. The compressed air is fed into the combustion chamber, where it is mixed with fuel. The conventional way of combusting the fuel is homogeneously in the gas phase by means of a flame. The combustion generates heat, which is taken up by the gas, which is shown in Figure 10. The temperature is raised from 623–723 K before the combustion chamber to above 1673 K at the exit. This high temperature arises due to the combustion having to occur within the flammability limits of the fuel. However, the temperature may vary with the type of gas turbine. Since the outlet temperature from the combustion chamber often is too high for the turbine materials, the gas has to be cooled prior entering the turbine. The hot gas is therefore mixed with air, which has bypassed the combustion chamber. The turbine itself consists of blades connected to a shaft, which are cooled by complex systems. The gas, which has reached the desirable pressure and temperature, is expanded through the turbine. Electricity may be extracted from the turbine via a generator. Thereafter, the gas is led either directly out to the atmosphere or via a heat exchanger in order to heat the air before entering the combustion chamber. The levels of pressure and temperature mainly influence the efficiency of the gas turbine. Therefore, the gas turbine manufacturers aim for as high values of these two parameters as possible. Nevertheless, due to material restrictions these levels are limited. Many different types of gas turbines may be found on the market, with a large variety of temperatures and pressures. Unfortunately, nitrogen oxide gases, which contribute to global warming, are emitted during this process. Pfefferle developed a process that uses a catalyst to allow combustion without the significant formation of nitrogen oxides and carbon monoxide [59]. The difference between the two techniques is that no by-pass air is necessary in the catalytic process for reducing the temperature prior to entering the turbine, as illustrated in Figure 10. Not only the kinetics affects the combustion rate over a catalyst, but other mechanisms such as the diffusion inside the catalyst pores and mass transport of reactants to the surface and/or products from the surface may affect the overall combustion rate. Catalytic combustion is one of few combustion techniques meeting the low emission limits stated by legislation e.g. in the US and Japan. The basic principle of catalytic gas turbine combustors is to let the combustion reaction take place heterogeneously on or near the catalyst surface instead in a flame, which is shown in Figure 11. Flame-based combustion, on the other hand, occurs homogeneously in the gas phase via a range of radical reactions at higher temperatures. Despite the different combustion routes, the reaction products are the same. However, both of these reaction mechanisms are very complex and are not yet fully understood. Other major advantages of this technology include a stable combustion of the fuel outside the flammability limits and less noisy operation. This combustion technology has been developed during last decades and has been commercialized [32].

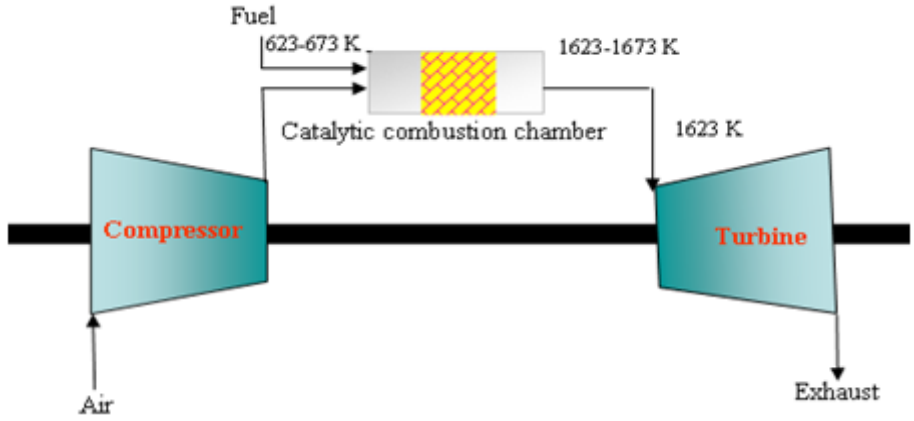

Figure 11. Flow diagram of catalytic gas turbine.

4. CATALYTIC MATERIALS FOR COMBUSTION APPLICATIONS

Materials for high-temperature combustion of hydrocarbons like methane and natural gas need exceptionally high chemical and morphological stability at temperatures of the order of 1773 K. Less strict requirements are needed for VOC abatement technologies operating at lower temperatures [60,61]. In either case, catalytic materials should be stable enough to sintering and surface area loss as well as to volatilization of the active phase. The activity of the catalytic materials depends on the type of preparation method adopted apart from other parameters. The preparation method is of fundamental importance to determine both activity and durability of the catalyst. Generally, catalytic materials are divided into two categories: (i) noble metals based and (ii) and non-noble metals based. Generally, effective emission control is often achieved by the use of noble metal catalysts. They are very active at low temperatures. In spite of their high activities, because of the cost, sensitivity to high temperature, poisoning, and scarcity, researchers have been provoked to try the substitution for noble metals. Various materials that were tried as catalysts for combustion applications include metal oxides, mixed metal oxides, and supported metal oxides, because they are relatively cheap, show variable valancy and exhibit greater redox properties. The catalytic activity of metal oxides for the oxidation of hydrocarbons by oxygen has been studied by a number of research groups [62−64].

In general, high oxidation activity requires metal ions that can assume more than one valence state and can participate in the reduction-oxidation (redox) reactions. Among the metal oxides only the oxides which are refractory and can maintain their activity at high temperatures have potential combustion applications. Metal oxide catalysts typically have lower catalytic activity and higher light off temperatures than noble metal catalysts. However, under typical catalytic combustor operating conditions; their activities are comparable to those of the noble metals [65]. The mechanisms involved in the oxidation over both noble metal and metal oxide catalysts differ greatly. Also, different oxides may allow different reaction paths. The kinetics and mechanism of catalytic oxidation of hydrocarbons have been studied extensively. According to Trimm [66] there is a correlation between the rate of hydrocarbon oxidation and metal-oxygen bond strength.

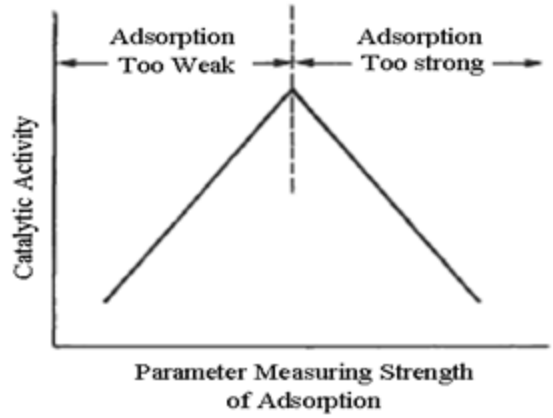

Figure 12. Catalytic activity verses adsorption strength [Ref. 72].

This point of view is supported by a number of researchers [67−71]. Generally, this correlation can be presented as a so-called volcano plot which is shown in Figure 12. This plot represents that there is some optimum level of metal-oxygen interaction in an oxide catalyst. This is because the catalytic activity of a metal oxide catalyst is inversely related to the strength of chemisorptions of the VOC and oxygen, provided that adsorption is sufficiently strong for the reactants to achieve a high surface coverage [72]. If the chemisorptions are too strong, the catalyst will be quickly deactivated. If chemisorptions are too weak, only a small fraction of the surface is covered and the catalytic activity is very low. It is interesting to examine the quantities used for the abscissa of Figure 12 [72,73].

5. CATALYTIC MATERIALS FOR VOC OXIDATION

5.1. Metal Oxides

Metal oxides are alternative options to noble metals as catalysts for VOCs oxidation. At high temperature the catalytic activity of metal oxides are similar to noble metals. The most frequently used ones are the oxides of V, Cr, Mn, Fe, Co, Cu, Ce, Zr, etc. They have been found to be very active, both in complete and selective oxidation of hydrocarbons [74]. The choice of catalyst is always dependant upon several factors such as (a) types of VOC (b) concentration of VOC, and (c) inlet temperature constraints etc [75]. Oxygen can be activated by interacting with oxide surfaces. Coordination, dissociation, and incorporation into the oxide lattice may be the steps involved in the activation process. Two possible states of activated oxygen can be recognized: (i) highly reactive, surface states of adsorbed oxygen and (ii) less active, lattice-incorporated oxygen species. Clearly, the lattice-incorporated species are more strongly bound than the adsorbed species. The lattice form is generally believed to participate in selective partial oxidations. The surface oxygen is usually considered to be the important species involved in complete oxidation reactions. However, Arai et al and others [76,77] proved the participation of both types of oxygen species in complete oxidation of methane. At higher temperatures, the activity of lattice oxygen can no longer be neglected, with the increasing of temperature the participation of lattice oxygen increases.

Table 1. Melting points of metal oxides [Refs. 8,79]

S. No.	Oxide	Melting Point (K)
1	Al_2O_3	2345
2	MgO	3125
3	CaO	2837
4	Cr_2O_3	2539
5	MnO_2	808
6	Fe_2O_3	1867
7	Co_3O_4	1163-1213
8	NiO	2257
9	Y_2O_3	2683
10	CeO_2	2873
11	ZrO_2	2973

Although metal oxides have high melting points, severe sintering may occur at temperatures as low as two thirds of the melting temperature [78] which is shown in Table 1 [8,79]. Considerable improvements can be obtained by exploitation of complex oxides which is supported by the data given in Table 2 showing the melting temperatures of a number of perovskites [8].

5.1.1. Chromium Oxide

Chromium oxide containing catalysts (typically 12-25 wt.% chromia calculated as Cr_2O_3) seem to have been used broadly and successfully on halogenated compounds. They are claimed to be one of the most active catalysts in the destruction of these compounds. The performance of some chromia based catalysts seems to be superior to noble metals containing catalysts.

But, at elevated temperatures highly toxic volatile chromium oxychloride (CrO_2Cl_2) is formed. This is one of the reasons to restrict the application of Cr-based catalysts to low operation temperatures only. High toxicity of chromium causes serious environmental catalyst disposal problems. It was reported that the presence of water can inhibit this unwanted process. It improves the catalyst stability and loss of Cr from the reactor [80−83].

5.1.2. Manganese Oxides

Mn-oxides such as β-MnO_2, γ-MnO_2, α-Mn_2O_3, γ-Mn_2O_3, and α-Mn_3O_4 are optimal surface redox catalysts. Among the above mentioned different types of manganese-based metal oxides, it is reported that γ form of MnO_2 is more active for VOCs oxidation and in many respects superior to conventional catalysts based on noble metals. Their catalytic application is due to their high efficiency in the reduction/oxidation cycles. Redox capabilities are strongly improved when combined with other elements.

Manganese oxides are considered to be environmentally friendly materials. According to some authors, to have Mn-based catalysts very active for oxidation, it is needed to have tetravalent Mn. But, Mn (IV) compounds are usually unstable at high temperatures and decompose to oxygen and less oxidized Mn compounds. Thus, there were some efforts to stabilize this cation [84,85].

Table 2. Melting points of $LnAO_3$ Perovskites (A = Al, Co, Cr and Sc) [Ref. 8]

Ln^{3+}	A^{3+} T(K)			
	Al	Co	Cr	Sc
La	2110	1740	2500	2390
Pr	2080	_	_	_
Nd	2090	1420	2415	2240
Sm	2040	1340	2380	2160
Gd	2000	1380	2370	2150
Dy	1940	1270	2340	2100
Er	_	1220	2330	_
Yb	_	1180	2330	_

5.1.3. Copper Oxide and Cobalt Oxide

Copper oxide is a well-known component of oxidation catalysts and exhibited high activity in VOCs emission control applications. CuO/TiO_2 was found to be more active than oxides of Fe, Co and Mn in toluene oxidation. CuO has the tolerance to sulfur. Due to its high activity, tolerance to sulfur and refractory nature, CuO-based catalysts have been considered as substitutes for noble metal catalysts in the VOCs control [86]. CoO_x is an efficient catalyst for total oxidation reactions. In addition, it was found that the oxides of cobalt can sorb sulfur, and $CoAlO_4$ is stable towards SO_2 [87,88].

5.1.4. Cerium Oxide

There have been a number of reports on catalytic oxidation of VOCs on various metal oxides. According to the literature, ceria-based catalysts are very active in VOCs oxidation and many other non-selective oxidations because of the unique features of their oxygen storage capacity [89-93]. The mechanism involved in VOC oxidation reactions over ceria is generally considered to be a redox type mechanism, in which the important steps are the supply of oxygen by the readily reducible oxide and its re-oxidation by oxygen. However, the catalyst is not thermally stable, undergoes rapid sintering under high temperature applications, thereby loosing oxygen buffer capacity. Therefore, there are several attempts in the literature to conquer this problem [85]. Some disadvantages with the single metal oxides are presented in Table 3.

Among the various types of VOCs, aromatics are the major source of air pollution and they endanger human health severely. Therefore, in this study, the main aim was to find a base metal oxide catalyst that is inexpensive and yet has high activity for the catalytic incineration of aromatics. Table 4 shows the temperature required for 50% conversion (T_{50}) and 90% conversion (T_{90}) of toluene with each of the metal oxide catalysts. The lowest temperatures of T_{50} and T_{90} were recorded with CeO_2, i.e., CeO_2 was the most active catalyst. Wang and Lin found that there is no regular relationship between catalyst activity and surface area (BET surface areas also shown in Table 4) [94].

Generally, with increasing surface area catalytic activity increases. Therefore, one can conclude from Table 4 that it is not the surface area but the redox property that leads to the different activity values observed for different metal oxides. Among all the metal oxides, ceria exhibited good catalytic activity due to its high redox property [94,95]. Interestingly, mixed metal oxides often exhibit greater activity and stability than the single oxides.

Table 3. Some disadvantages with single metal oxides

S. No.	Metal Oxides	Disadvantages
1	Chromium oxide	Disposal problems
2	Mn(IV) oxide	At high temperatures decomposes to less oxygenated compounds
3	Vanadia	Corrosive nature
4	γ-alumina	At high temperatures changes to α-alumina
5	Ceria	Not thermally stable
6	Zirconia	Not thermally stable

Table 4. BET surface area and activity of metal oxide catalysts for toluene oxidation. [a] The reaction temperature (T_{50}) for 50% conversion of toluene, [b] The reaction temperature (T_{90}) for 90% conversion of toluene [Ref. 94]

Catalyst	BET surface area (m^2g^{-1})	T_{50}[a] (K)	T_{90}[b] (K)
CeO_2	79	485	497
CuO	8	305	615
Fe_2O_3	10	593	618
V_2O_5	3	623	664
ZrO_2	5	654	683
γ-Al_2O_3	135	671	705
TiO_2 (rutile)	43	688	>713

5.2. Mixed Metal Oxides

Among the mixed metal oxides, (i) doped metal oxides and (ii) perovskites are most prominent.

5.2.1. Doped Metal Oxides

Generally, for improving the catalytic efficiency of a single metal oxide one can dope with the other metal oxide and the resulting mixed metal oxide will offer better activity due to the changes in the surface area, electronic properties, etc. With the doping, the crystal structure of metal oxide changes which is responsible for the increase in the catalytic activity. Thus mixed metal oxides are more active than the single ones. Copper and manganese-containing catalysts proved also as highly active in the combustion of VOCs [96]. The incorporation of small amounts of copper in MnO_x catalyst reduced the crystalline structure of manganese oxide, and thus increased the number of oxygen vacancies [97]. Similarly, Mn–Zr mixed oxides with 40 mol% manganese content have been found to be effective catalysts for the combustion of chlorinated VOCs. The enhanced catalytic activity of Mn–Zr mixed oxides was attributed to increased surface acidity and availability of accessible active oxygen species. Li et al. reported a series of manganese oxides mixed with Zr, Fe, Co, and Cu oxides, prepared by a reverse micro emulsion method, for catalytic combustion of toluene [98]. The results are summarized in Table 5. These manganese oxide containing mixed oxides showed very good activity for the catalytic combustion of toluene, indicating that the reverse microemulsion method is an effective method to incorporate highly active species into the

combustion catalyst and hence emphasize some potential active species for catalytic combustion. For the complete combustion of diluted methane, transition metal (viz. Mn, Co, Cr, Fe and Ni) doped ZrO_2 (cubic) showed high catalytic activity. The combustion activity of the Mn- and Co-doped ZrO_2 catalysts was found to be comparable to that of alumina supported Pd and Pt catalysts. For this reason, it was interesting to study the activity of the transition metal-doped ZrO_2 (cubic) catalysts in the combustion of VOCs, such as toluene. The catalytic combustion of toluene over various transition metal doped zirconia catalysts has the following order for their performance (based on both the catalytic ignition temperature and combustion activity) in the toluene combustion: Co-doped ZrO_2 > Mn-doped ZrO_2 > Cr-doped ZrO_2 > Fe-doped ZrO_2 > Ni-doped ZrO_2 (Table 6). Up to 596 K, the undoped ZrO_2 showed no catalytic activity in the combustion of toluene. Among various transition metals doped zirconia, the Co-doped ZrO_2 catalyst exhibited high catalytic activity in the combustion of toluene. However, the combustion activity of the Co-doped ZrO_2 catalyst for toluene mainly depends on the Co/Zr ratio which is given in Table 7 [100]. As can be noted from the table, the optimum Co/Zr ratio for toluene combustion is 0.25, which is to be most active. For higher and lower Co/Zr ratios (0.67 and 0.11, respectively), the Co-doped ZrO_2 catalysts contained monoclinic phase along with the cubic phase. However, for Co/Zr ratio of 0.25, the catalyst contained only cubic phase. This may be the reason for the catalyst with Co/Zr ratio of 0.25 to be the most active. The previous studies on the combustion of dilute propane over the Co-doped ZrO_2 also showed the involvement of lattice oxygen, and hence the redox mechanism in the hydrocarbon combustion over these catalysts was proposed [99,100].

Table 5. The activity results of doped manganese oxide. [a] The temperature where the toluene conversion reaches around 3%, [b] The temperature where the toluene conversion reaches around 98% [Ref. 98].

Catalyst	Molar ratio	T_3[a] (K)	T_{98}[b] (K)
$Mn_{0.4}Zr_{0.6}$	Mn/Zr = 2:3	528	553
Mn_2O_3	-	533	553
$Mn_{0.4}Fe_{0.6}$	Mn/Fe = 2:3	553	573
$Mn_{0.4}Co_{0.6}$	Mn/Co = 2:3	523	543
$Mn_{0.4}Cu_{0.6}$	Mn/Cu = 2:3	503	513
$Mn_{0.4}Cu_{0.33}$	Mn/Cu = 2:1	483	493

Table 6. The activity results of doped zirconium oxide. [a] Temperature of catalytic ignition corresponding to 10% combustion of toluene, [b] Temperature required for half the combustion of toluene [Ref. 100].

Catalyst	T_i [a](K)	$T_{1/2}$ [b](K)
Mn-doped ZrO_2	545	580
Cr-doped ZrO_2	567	608
Co-doped ZrO_2	541	576
Fe-doped ZrO_2	587	632
Ni-doped ZrO_2	626	677

Table 7. Co/Zr ratio of Co-doped ZrO_2 catalyst: [a] Temperature of catalytic ignition corresponding to 10% combustion of toluene, [b] Temperature required for half the combustion of toluene [Ref. 100].

Co/Zr ratio	T_i[a] (K)	$T_{1/2}$[b] (K)
0.11	551	588
0.25	536	578
0.43	554	602
0.67	559	604

5.2.2. Perovskites

The ideal perovskite-type structure is cubic.The unit formula of perovskite-type oxide is ABX_3, in that A is the larger cation and B is the smaller cation. In this structure, the B cation is 6-fold coordinated and the A cation is 12-fold coordinated with the oxygen anions. Figure 13 depicts the corner sharing octahedra that form the skeleton of the structure, in which the center position is occupied by the A cation. Alternatively, this structure can be viewed with the B cation placed in the center of the octahedron and the A cation is in the center of the cube [101]. The use of perovskites has been advocated especially in applications involving high temperatures, oxygen rich and steam rich atmospheres, where their significant thermal stability comes into play.This was identified since the early 1970s. Under suitable circumstances; the activity of perovskites can be very considerable, even comparable to that of noble metal catalysts [102]. Perovskite type structures received a constant attention since early 1970s due to their potential use as total oxidation catalysts [103]. The catalytic activity of perovskites mainly depends on the cations A and B which are responsible for catalytic activity in different ways, due to their physicochemical and catalytic properties such as ionic conductivity, oxygen mobility within their lattice, oxygen sorption properties, greater stability at high temperatures, and stabilization of unusual cation oxidation states in the structure. Therefore, they were proposed as an attractive alternative to the very active noble metal based oxidation catalysts [104−107]. They are less expensive and thermally more stable than noble metals. Some compositions were reported to possess similar or higher activity than Pt-supported catalysts [108,109].

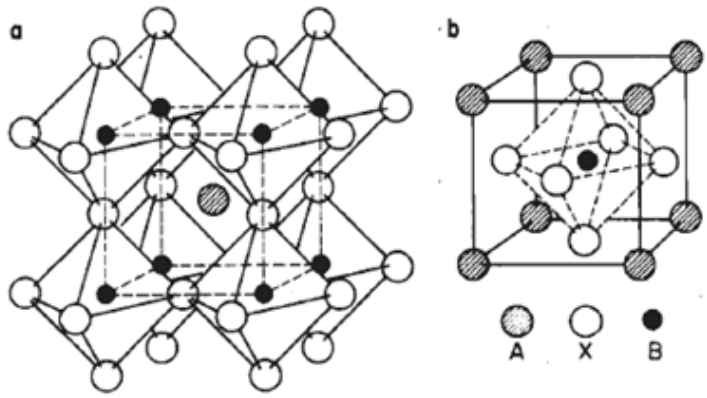

Figure 13. ABX_3 ideal perovskite structure: (a) cation A, or (b) cation B, at the center of the unit cell (X= oxygen atom) [Ref. 101].

Table 8. Catalytic activity of $La_{0.8}Sr_{0.2}CoO_3$ and $LaCoO_3$ perovskites: [a] The temperature where the toluene conversion reaches 50%, [b] The temperature where the toluene conversion reaches 99% [Ref. 115]

Catalyst	$T_{50\%}$[a](K)	$T_{99\%}$[b](K)
$LaCoO_3$	436	673
$La_{0.8}Sr_{0.2}CoO_3$	< 433	573

Among the various transition metal perovskites, $LaMO_3$ (M = Mn, Co) are known to be very good oxidation catalysts [110,111], and much cheaper than noble metal supported catalysts. The redox properties of the M cation, the presence of lattice defects and the availability of weakly bonded oxygen at the surface, have been often claimed to be responsible for their better catalytic activity [112−114]. The presence of oxygen surface species, easily available and sufficiently mobile, is a fundamental requisite for a high catalytic activity, as found in $LaMnO_3$. By partial replacement of La^{3+} with Sr^{2+} one can observe an increase in the combustion activity. The important challenge in developing perovskite catalysts is to obtain their structures while preserving sufficiently high surface areas. The preparation of a perovskite oxide involves a solid-state reaction of its precursor oxide to form the characteristic ABX_3 structure. The catalyzed reactivity relates to the energy needed to break the weakest C–H bond and C–C bond. Partial substitution of strontium for lanthanum at the A-sites of $LaCoO_3$ modified the surface structure of the catalyst by greatly enhances the oxygen vacancies in the surface region, which increases the catalytic activity of $La_{0.8}Sr_{0.2}CoO_3$ material being higher than that of $LaCoO_3$ which is shown in Table 8 [115]. Strontium influences the properties of the catalyst. The Sr-containing perovskites are less crystalline, can be reduced at lower temperatures, and possess a higher surface area [116]. To improve the catalyst life and specific surface area, stable supports must be introduced.

5.3. Supports for VOCs Oxidation

The catalyst support serves three important functions in the whole catalyst system: (i) it increases the surface area of the active metal or metal oxide by providing a matrix that enables their dispersion as very small particles, (ii) it can reduce sintering of the active catalyst material and improve its thermal stability, and (iii) it could increase the activity of the catalyst material. The active oxide can be deposited on a support to increase its dispersion. Further, the specific activity can be increased due to a reaction or interaction with the support [56]. Most commonly used supports are Al_2O_3, SiO_2, TiO_2, CeO_2, ZrO_2, CeO_2-ZrO_2, hexa-aluminates, etc. The hexa-aluminates may be used as supports for high temperature combustion which are discussed in the following section.

Depending on the type of active component and method of preparation, various supports could be chosen. The most commonly used support for the active phases for VOCs destruction is γ-Al_2O_3. γ-Aluminas may have a surface area of 100-200 m^2/g, but at high temperatures its crystal structure changes to most thermodynamically stable phase which is α-Al_2O_3 with a surface area of 1-5 m^2/g. One of its drawbacks is its poor resistance to hydrogen chloride and chlorine [117]. This is a major reason to search for new carriers. Other metal oxides such as CeO_2 and ZrO_2 are receiving increasing interest in the field of heterogeneous

catalysis as active phases or supports/promoters because of their thermal stability, chemical stability, coupled with acid-base properties and oxygen storage capacity [118]. The catalytic activity of ceria support can be increased by introduction of zirconia in the ceria lattice which is responsible for higher mobility of surface and bulk lattice oxygen species [119].

As mentioned earlier, perovskites exhibit good catalytic activity towards total oxidation (100% selectivity to CO_2 for hydrocarbons). However, the use of perovskites is generally limited owing to their low specific surface area. One of the most common approaches to increase the activity of the perovskites is through deposition on supports. In this respect, up to date, deposition of perovskites on thermally stable oxides seems to be an apparent solution. Unfortunately, the most commonly and largely used supports are Al_2O_3 and SiO_2 which are reactive towards the elements contained in the perovskites, resulting in catalytically inert compounds such as spinnels [120]. This is mainly observed in the case of Co-containing perovskites, Co easily diffuses into alumina network yielding $CoAl_2O_4$, but when coming to both Ce and Zr they are static towards the components of the perovskite. Moreover, the presence of Ce might be helpful for Co-based perovskites.

The increase of $LaCoO_3$ activity after impregnation on ceria-zirconia supports can be explained by larger surface area exposed by the deposited phases. However, the role and the chemical nature of the support cannot be neglected. The amount of zirconia introduced into the ceria lattice influences the oxidative properties of catalysts like oxygen mobility [103]. Supported copper catalysts were reported as promising catalysts for complete oxidation of benzene and other contaminants. Among the transition metals, Cu/Al_2O_3 was found to be the most active catalyst for the complete oxidation of benzene, toluene and xylene [121]. CuO/CeO_2 catalyst was observed to show better catalytic performance for the complete oxidation of benzene, toluene and p-xylene than that of CuO/Al_2O_3 catalyst [122,123].

A systematic analysis of the catalytic activity of different formulations of transition metal oxides (CrO_x, MnO_x, VO_x, SnO_x, WO_x, NbO_x, TaO_x, MoO_x, ZrO_x and BiO_x) supported on TiO_2, Al_2O_3, and SiO_2 for the total oxidation of benzene showed that for almost all active phases, the conversion increases when the support is changed from SiO_2 to Al_2O_3 and TiO_2 [124]. This is evident by the XPS and XRD techniques which demonstrate a better spreading of active phase as a monolayer at the surface of titania than on Al_2O_3 and SiO_2. The latter induces a heterogeneous dispersion of almost all the active phases as crystallites. The variation of spreading of the active phase on different supports is governed by the difference in surface free energy and is fully explained by the ‘‘solid–solid wetting’’ concept [125]. However, some studies were made on VOCs oxidation over various metal oxides and perovskites that are listed in the Table 9 and 10.

6. CATALYTIC MATERIALS FOR GAS TURBINE APPLICATIONS

The temperatures used for different types of gas turbines are in the range of 623-1773 K Unfortunately, it seems to be a law of nature that catalysts with high activity are not stable at high temperatures. Therefore, in order to operate in the whole temperature range the catalyst is generally divided into at least two segments. The first segment, termed the ignition segment (active component), is characterized by high activity. The second segment, termed the high-temperature segment, is characterized by high thermal stability. The temperature ranges of

ignition and high-temperature segments are approximately 623-972 K and 1173-1273 K, respectively, above this temperature homogeneous combustion zone is used.

A combustion catalyst for gas turbine applications consists of three key components: (i) the active component (ignition segment) that facilitates the heterogeneous combustion reaction, (ii) the (substrate) monolith, increases the mechanical strength and stability, and (iii) the wash coat that brings a high surface area.

Table 9. An overview of some studies made on VOCs oxidation over various metal oxides

VOCs		Catalysts	References
Aliphatic Hydrocarbons	Methane	MnO_x/CeO_2-ZrO_2 MnO_x/WO_3-TiO_2	[126]
	Ethane Propane Butane Iso-butane	Cu and Mn Doped Ceria-Zirconia	[127]
Aromatic Hydrocarbons	Benzene	Co_xMg_{3-x} /Al Composite Oxides Mn-Zr and Mn-Ti Supported Oxide	[128] [129]
	Toluene	V_2O_5/Nb_2O_5 CuO/γ-Al_2O_3	[130] [131]
	Phenanthrene	Mn-Zr Mixed Oxides	[132]
O-VOC_S	Ethyl acetate Formaldehde Acetone n-Butyl acetate	CuO/CeO_2-ZrO_2-TiO_2 MnO_x-CeO_2 $Mn_2O_3/Al_2O_3(SiO_2)$ V_2O_5/TiO_2	[133] [134] [135] [136]
C-VOCs	Trichloro-ethylene	Mn-Zr Mixed Oxides	[137]
	Dichloroethane	Ce/Zr Mixed Oxides in Different Ratios	[138]

6.1. Active Component

The chemical stability and sintering resistance of catalytically active phases is a key technical problem that must be solved for the development of commercially viable combustion catalysts. Due to high temperature in the catalytic combustor, great care has to be taken in the selection of active materials. Volatilization, sintering and solid-state reactions with the support are three of the most common deactivation mechanisms that need to be considered [150]. Most single metal oxides are not enough active to be used as active components for ignition segment [77]. Therefore, mixed metal oxides are often used as active components. For example, the activity of ceria has been investigated in several studies. It has been shown that ceria has a significant activity in itself, which can be further improved by doping with Zr and La. Doping with the trivalent La ions has been shown to be especially

effective, due to the formation of extrinsic oxygen vacancies. Furthermore, doping with Zr and La has also been shown to stabilize the surface area of ceria at high temperatures. Just as perovskites, ceria has a strong tendency to sinter. Even if ceria is stabilized with Zr, severe sintering after calcination for a few hours at 1273 K has been reported [151−154]. This suggests that ceria should be supported when used for high-temperature applications. The typical materials used in the ignition segment are discussed in the previous section.

Table 10. An overview of some studies made on VOCs oxidation over perovskite catalysts

VOCs		Catalysts	References
Aliphatic Hydrocarbons	Methane	$La_{2-x}Sr_xNiO_{4-\lambda}$	[139]
	Hexane	$LaMO_3$ (M = Mn, Co, Fe)	[140]
	Propene	Zirconium Doped $LnMnO_3$	[141]
Chlorinated compounds	Chlorinated- Methanes	$LaCo_3$, $LaCo_{3+\delta}$	[142,143]
	Chlorobenzene	$LaCo_3$, $LaCo_{3+\delta}$	[142]
	1,2 Dichlorobenzene	ABO_3 (A = La, Nd, Gd, or Y B = Fe, Mn, Co or Cr)	[144]
	Toluene	$La_{1-x}Sr_xCo_{1-y}Fe_yO_3$	[145]
		$LaZn_xFe_{1-x}O_3$	[146]
		$La_{1-x}Sr_xMnO_{3-\lambda}$	[147]
O-VOCs	Acetone	$Cu_xCe_{1-x}O_y$	[148]
	Methyl Ethyl Ketone	$LaBO_3$ (B = Cr, Co, Ni, Mn) and $La_{0.9}K_{0.1}MnO_{3+\delta}$	[149]

6.2. Substrate

The substrate should have a (i) large geometric surface area, (ii) low pressure drop, (iii) good thermal shock resistance, and (iv) it should allow high working temperature. High velocities are used in gas turbines so that no packed catalyst bed is used. Many types of substrates exist; the most common substrates are pellet, wire mesh, and monolith. Among them monolithic honeycomb structures are preferred for gas turbine applications due to the low pressure drop and reasonable surface area. To minimize the pressure drop over the catalysts, the catalyst material is supported on a monolith. The monolith consists of a number of parallel channels through which the gas easily passes with only a small loss in pressure. The catalyst material itself is coated onto the channel walls, in order to enable contact with the reacting gas. A common design is the passive channel structure, where only every second channel is coated with active material and the uncoated channels work as heat exchangers and cool the walls of the monolith. In this way, the temperature over the catalyst may be more

easily controlled and temperature run-away is suppressed [32]. In principle, the monoliths can be metallic or ceramic. The important properties of ceramic and metallic monoliths have been summarized in the following Table 11 [Ref. 11].

Table 11. The typical properties of the ceramic and metallic monoliths

Material Property	Ceramic	Metallic
Maximum operating temperature (K)	1673	1553-1648
Maximum continuous temperature (K)	1473	1173-1423
Thermal expansion coefficient (10^{-7} K^{-1})	7	150-200
Thermal conductivity ($W \cdot K^{-1} \cdot cm^{-1}$)	2-3	15-25
Geometric surface area (cm^2)	26.5	36.5

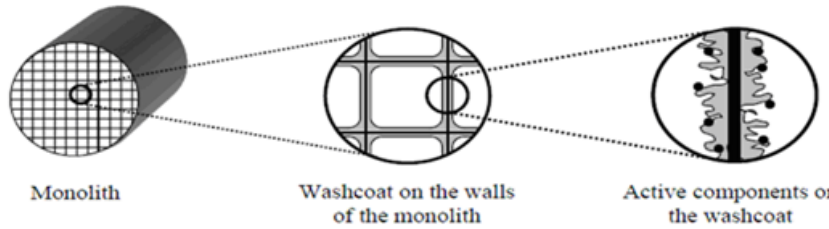

Figure 14. Schematic representation of honeycomb monolith [Ref. 32].

Ceramic monoliths are made by extrusion; their disadvantages are breaking or cracking under thermal shocks and poor heat conductivity. Metallic monoliths are made from alternating thin metal sheets of corrugated and plane types, by rolling them. The great advantages of metallic monoliths are their mechanical strength and high thermal conductivity, avoiding hot spots and resulting in a more uniform bed temperature. In addition, the use of metallic monolith allows the manufacturing of monolithic catalysts with passive channels that appear to be one of the most promising designs for circumventing the need for high temperature resistant catalytic material [11]. If the wash coat acts as a support, it helps disperse the active components and increases the exposure of active components to reactants. Schematic representation of honeycomb monolith is shown in Figure 14.

6.3. Wash Coat or Support

The monolith material is often a low surface area material, which makes it unsuitable for direct application in the combustion chamber. Therefore, a high surface area material, commonly known as the wash coat or support, is attached onto the monolith walls. The wash coat may be active in itself, which often is the case for more temperature-stable catalysts, or act as support for another active component, as often is the case for the ignition catalysts [32]. The support is a primary objective to disperse the active component on a large surface area, the support could also increase the activity and stability of the active components by interaction between the two. When choosing support material, the first thing to consider is whether the material is stable at the operating temperature, i.e., if the surface area can be

retained If not, activity will be lost due to loss of surface area and possibly encapsulation of active components. The commonly used supports are alumina, zirconia, and hexa-aluminates.

6.3.1. Alumina

Due to its relatively low cost, high surface area and thermal stability alumina is the most commonly used material as a support. The high surface area is highly beneficial for achieving a low ignition temperature, since it makes a high dispersion possible. Alumina has several crystal phases, the most commonly used phase is γ-alumina which has high surface area and obtained at low temperatures. If γ-alumina is subjected to high temperatures (1123-1373 K) it will go through phase-transitions to the θ-and δ-phases and eventually to the α-phase, which has a very low surface area and is not suitable as a support. The phase transformations are shown in figure 15.

In order to avoid formation of the α-phase, small amounts (a few wt.%) of additives, such as lanthanum or barium etc are often used [155]. The addition of BaO, La_2O_3, SiO_2, Li_2O or K_2O is effective in retaining large surface areas of alumina because the additive cations occupy the surface sites or bulk sites to prevent atomic diffusion (surface diffusion and bulk diffusion). Some of these additives show a remarkably large retarding effect on the phase transformation. According to Burtin et al [156], In^{3+}, Ga^{3+} and Mg^{2+} accelerate the transition to α-alumina, whereas Zr^{4+}, Ca^{2+}, Th^{4+} and La^{3+} inhibit it. However, systematic understanding of the effect of additives has not been established yet. Effect of additives on γ-alumina is shown in Table 12. A drawback with using alumina as support is that solid state reactions with transition metals such as Co and Ni easily occur, thereby forming less active species with spinel structure [162].

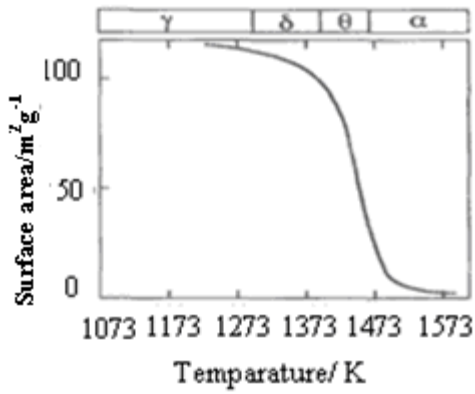

Figure 15. Phase transformation and specific surface area of alumina [Ref. 155].

6.3.2. Zirconia

Generally zirconia has a lower specific surface area than alumina, due to both higher density and its tendency to sinter. In order to stabilize the surface area of zirconia, it is often doped with different elements. Cerium is frequently used, which also increases the oxygen mobility and oxygen storage capacity of the support [163]. Cerium also offers some

combustion activity, especially when combined with zirconium. Yttrium and lanthanum are two other elements worth mentioning as stabilizers for zirconia [16].

Table 12. Effect of additives on γ-alumina

Catalyst	Temperature (K)	Surface Area (m^2g^{-1})	References
Ba-added γ-alumina	1473	_	[157]
La-added γ-alumina	1273	120	[158,159]
Si-added γ-alumina	1473	_	[157]
La-added γ-alumina	1173	92	[160]
SiO_2-Al_2O_3	1573	46	[161]
Lanthanide (La, Pr, Nd)-added γ-alumina	1423	63	[160]

6.3.3. Crystal Structure and Sintering Behavior of Hexa-aluminate

Hexa-aluminate compounds including β-alumina, magnetoplumbite, or their derivatives have been studied extensively in various fields of application such as electrical ceramics, matrices for permanent immobilization of radioactive elements and refractory cement, and concrete. Their excellent thermal stability against sintering and/or grain growth above 1473 K has made the group frequently studied for high-temperature catalytic combustion. The existence of a hexaaluminate was first reported in 1916 by Rankin and Merwin [164]. The different structures of the hexa-aluminates were first discussed and summarized in 1976 [165]. Hexa-aluminates are hexagonal aluminates with a layered structure with β-alumina or magnetoplumbite structure which is schematically shown in Figure 16.

β-Alumina and magnetoplumbite (MP) consist of "spinel blocks" and "conduction layers," which are stacked alternately to form a sort of layer structure. Spinel blocks are composed only of $A1^{3+}$ and O^{2-} ions, having the same rigid structure as spinel. Large cations such as Na^+, K^+, Sr^{2+}, and La^{3+} are usually accommodated in the spacious conduction layer which has a mirror symmetry plane.

The major difference between β-alumina and MP is in the contents and arrangement of the ions within the conduction layer [166,167]. The layered structure of the hexa-aluminates can be represented by the general formula $AB_xAl_{12-x}O_{19}$, where A represents a large metal ion usually from the alkaline, alkaline earth or rare earth metal groups. These large ions are located in the mirror planes, which are separated by alumina spinel blocks as shown in Figure 16. The crystal structures of the hexa-aluminates are determined by the size and charge of the large cation.

The B, in the above formula represents a transition metal ion of similar size and charge as aluminium. The stability of the hexa-aluminate is generally governed by the large cation in the mirror planes, whereas the activity is mainly determined by the transition metal substituting Al. By substituting a few Al ions with another cation with similar radii and charge in the hexa-aluminate crystal lattice, a substantial increase of the oxidation activity can be obtained, with only minor influence on the sintering resistance. The high sintering resistance of hexa-aluminates has been connected to their layered crystal structure.

It has been shown that anisotropic oxygen diffusion occurs in the structure, due to inhibition of the oxygen diffusion along the c-axis. When the rate of the solid-state sintering

process is limited by oxygen diffusion, as reported for similar structures, preferential grain growth will occur along the mirror planes in two directions. This leads to the formation of plate-shaped particles with high aspect ratios. The formation of particles with high aspect ratios is suppressed due to increased surface energy of the particles, therefore, sinter very slowly. The sintering resistance of the hexa-aluminates has also been connected to the preferential exposure of the mirror planes, which hinders crystal coalescence [168−171].

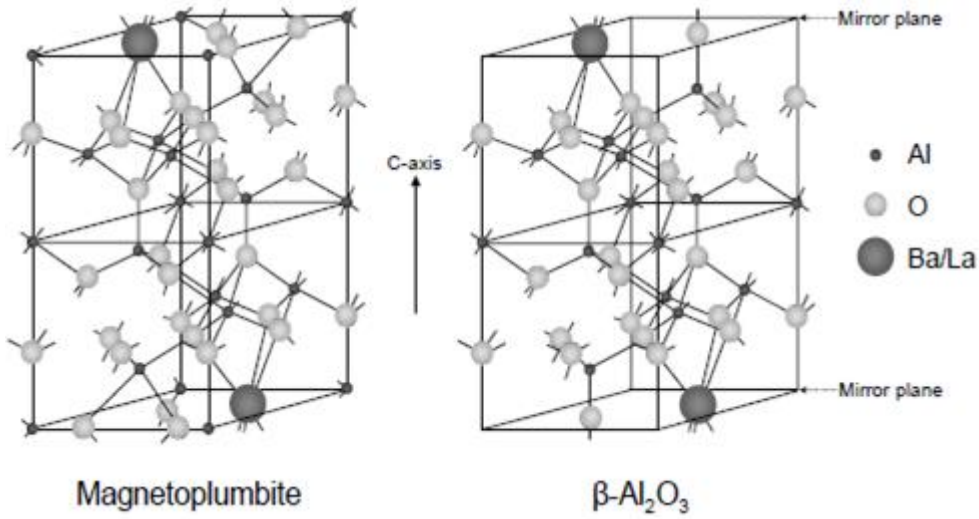

Figure 16. Schematic illustration of the locations of the ions in the two structures of hexa-aluminate: magnetoplumbite and β-alumina [Ref. 16].

6.4. The Commonly Used Hexa-Aluminate Materials

6.4.1. Barium Hexa-aluminate (BHA)

Barium hexa-aluminate (BHA) has, since 1987 when it was first proposed for high-temperature catalytic combustion by Machida et al. [172], been frequently studied due to its extreme sintering resistance. This is evident by the fact that the surface area as high as 11 m^2/g after calcination at 1873 K has been reported. BHA has a general formula of $BaAl_{12}O_{19}$ ($BaO{\cdot}6Al_2O_3$), forming a β-alumina type structure. BHA has been reported to actually consist of two different crystal phases, a barium-rich ($BaAl_{9.15}O_{14.73}$) and a barium-poor ($BaAl_{14.66}O_{23}$), $BaAl_{12}O_{19}$ which consists of a 1:1 mixture of these phases, has shown superior sintering properties compared to both the individual phases. The non-substituted BHA has poor activity for high temperature combustion, which makes it only suitable for use as support for active materials.

The activity of the material has been shown to be greatly enhanced by substitution of aluminium by transition metals. If one aluminium ion is substituted, the activity has been shown to decrease in the order of Mn ≈ Cu > Fe ≈ Co ≈ Cr ≈ Ni. More than one aluminium ion per unit cell of BHA can in many cases be substituted, while retaining the crystal structure. This is dependent on the solubility limit of the respective transition metal ion in the BHA crystal lattice. The solubility limit should not be exceeded, since sintering will be

induced due to phase segregation. If more transition metal is added, an increase of activity is generally observed since the number of active sites increases. For Mn, a solubility limit of approximately three ions per unit cell has been observed, whereas the limit for Cu is around one. For Fe, the solubility limit is around two in the β-alumina lattice. However, if the amount of Fe is further increased, a hexa-aluminate with magnetoplumbite structure is formed in which complete substitution of Al by Fe is possible. The sintering resistances of these materials with high Fe content are however poor [173−177].

6.4.2. Lanthanum Hexa-Aluminate (LHA)

Lanthanum hexa-aluminate (LHA) is another frequently studied hexa-aluminate. Compared to BHA, the LHA has been shown to be less susceptible to sulfur poisoning since it forms less stable sulfates. Furthermore, LHA has stability comparable to that of BHA; LHA with transition metal substitution has been shown to be slightly more active than its BHA counterpart. LHA has the general formula $LaAl_{11}O_{18}$, forming a highly distorted magnetoplumbite structure. The phase consisting of $LaAl_{11}O_{18}$ has been reported to exist only in a certain temperature range that is 1873-2123 K. Just as for BHA, the non-substituted LHA has poor activity for high temperature combustion, which is greatly enhanced by substitution of aluminum with transition metals (preferably Mn). Partial substitution of La by Sr in the mirror plane, according to the formula $La_xSr_{1-x}MnAl_{11}O_{19}$ has been shown to increase both the surface area and the activity of the hexa-aluminate. An optimum was found for x = 0.2, which also was the composition chosen for industrial scale-up. However, later reported that x = 1 gave the most active catalyst, which also has been confirmed by others. The activity of the Mn-substituted LHA has been shown to be further enhanced by partial substitution of Mn by Mg according to the formula $LaMg_xMn_{1-x}Al_{11}O_{19}$. An optimum was found for x = 0.3 [178−184,16].

CONCLUSION

Catalysts play very significant role in the combustion processes, besides many practical applications. In this chapter we discussed about the VOCs abatement for pollution control and gas turbines for power generation. Low temperature is desired for destruction of VOCs and High temperature is required for gas turbine applications, for both the selection of materials is very important. Catalytic activity and thermal stability of catalyst play very significant role in the low temperature and high temperature combustion applications. Number of studies has revealed that the activity of catalytic materials is dependent upon several factors such as oxidation state, nature of the support, particle size, and morphology. Although the noble metal catalysts exhibit higher activity than metal-oxide catalysts, they suffer from disadvantages, such as higher volatility and limited availability. As an alternative, metal-oxide catalysts have received constant attention. Mostly, perovskite type metal oxides, doped metal oxides have been extensively employed as combustion catalysts. The catalytic properties of these materials are easily tuned up by partial substitution in the lattice structure. The major problems connected with these catalysts for operation under the high temperature conditions required for power generation in natural gas-turbines are as follows: (i) structure collapse, i.e. reduction in surface area, (ii) solid state reactions between the active

components amongst themselves or with the support, and (iii) evaporation of catalytically active components. Presently, the substituted hexa-aluminates seem to be the most important candidates for high temperature combustion. However, they suffer from much lower activity and higher light-off temperatures. As of today the effects of water, catalyst supports, and coke formation continue to create practical challenges for VOC catalytic combustion and should be investigated further. However, harsh conditions in the combustor together with long operating time are putting high demands on the performance of the catalysts, both in terms of activity and stability. Further research in materials design is definitely desired for the successful operation of the high temperature gas-turbines employing catalytic combustion.

ACKNOWLEDGMENTS

We wish to specially acknowledge all the researchers whose work is described in this chapter for their valuable contributions. T.V. is the recipient of junior research fellowship of CSIR, New Delhi. Financial support was received from Department of Science and Technology, New Delhi, under SERC Scheme (SR/S1/PC-63/2008).

REFERENCES

[1] http://americanhistory.about.com/od/industrialrev/p/steamengine.htm.
[2] Anders, E. *Materials for High-Temperature Catalytic Combustion*, PhD thesis, 2003, Kungl Tekniska Högskolan, Stockholm.
[3] Nicola, A.; Vincenzo, B. *Angew. Chem. Int. Ed*. 2007, 46, 52–66.
[4] http://en.wikipedia.org/wiki/Combustion.
[5] Hayes, R.E.; Kolaczkowski, S.T. *Introduction to Catalytic Combustion*, Amsterdam, Gordan and Breach Science, 1997, 1−681.
[6] Williams, F.A. University of California, San Diego, Combustion.
[7] Michael, F.; Christian, P. B.; Hans, K. *Chem. Eng. Technol.* 1988, 11, 104−112.
[8] Armor, J.N. *Appl. Catal. A: General*. 2000, 194–195, 3–11.
[9] Fritz, A.; Pitchon, V. *Appl. Catal. B: Environ*. 1997, 13, 1−25.
[10] Degobert, P. *Automobiles and Pollution*, Society of Automotive Engineers, Inc., Warrendale, PA 1995.
[11] Philippe, T. *Catalytic Combustion of Methane*, PhD thesis, 2002, Kungl Tekniska Högskolan, Stockholm.
[12] Zeldovich, Ya. B. *Acta Physicochem*. 1946, (USSR), 21, 557.
[13] Kotler, V. R. *Nitrogen Oxides in Flue Gases* (in Russian), Energoatomizdat, Moscow, 1987, p. 19.
[14] Ismagilov, Z.R.; Kerzhentsev, M.A. *Catal. Rev. Sci. Eng*. 1990, 32, 51−103.
[15] Fenimore, C.P. *Formation of Nitric Oxide in Premixed Hydrocarbon Fuels*. In 13th Symposium (International) on Combustion, the Combustion Institute, Pittsburgh, 1970, 373–380.
[16] Svensson, E.E. *Nanotemplated High-Temperature Materials for Catalytic Combustion*, PhD thesis, 2008, Kungl Tekniska Högskolan, Stockholm.

[17] Sigal, I.Y. *The Development and Aims of Investigation to Study the Conditions of Formation of Nitrogen Oxides in Furnace Processes* (in Russian), *Teploenergetika,* 1983, 9, 5.
[18] Beer, J.M. *Prog. Energy Combust. Sci.* 2000, 26, 301–327.
[19] http://www1.eere.energy.gov/industry/distributedenergy/pdfs/gas_turbines_nox_cost_analysis.pdf.
[20] Hunt, L. B.; Johnson Matthey. *Platinum Metals Rev*. 1979, 23, (l), 29−31
[21] Weiss, G. *Radiant Gas Burner*, U.S. Pat. 3,191,659, 1958.
[22] Milligan, W.C. *Catalytically Active Radiant Tile*, U.S. Pat.3,302,689**,** 1965.
[23] Pfefferle, W.C. *J. Energy,* 1978, 2, 142–146.
[24] Choudhary, T.V.; Banerjee, S.; Choudhary, V.R. *Appl. Catal. A: Gen*. 2002, 234, 1–23.
[25] Zheng, M.; Asad, U.; Reader, G T.; Tan, Y.; Wang, M. *Int. J. Energy Res*. 2009, 33, 8–28.
[26] Pfefferle, L.D.; Pfefferle, W.C. *Catal. Rev. Sci. Eng*. 1987, 29, 219−267.
[27] Lee, J.H.; Trimm, D.L. *Fuel Process. Technol.* 1995, 42, 339−359.
[28] Carroni, R.; Schmidt, V.; Griffin, T. *Catal. Today*, 2002, 75, 287–295.
[29] Akhmedova, V.M.; Al-Khowaitera, S.H. *Catal. Rev. Sci. Eng*. 2002, 44, 455–498.
[30] Forzatti, P.; Groppi, G. *Catal. Today*, 1999, 54, 165–180.
[31] Ciuparu, D.; Lyubovsky, M.R.; Altman, E.; Pfefferle, L.D.; Datye, A. *Catal. Rev. Sci. Eng.* 2002, 44, 593−649.
[32] Persson, K. *Bimetallic Palladium Catalysts for Methane Combustion in Gas Turbines*, PhD thesis, 2006, Kungl Tekniska Högskolan, Stockholm.
[33] Arai, H.; Fukuzawa, H. *Catal. Today,* 1995, 26, 217−221.
[34] Menon, P.G.; Zwinkels, M.F.M.; Järås, S.G. *Stud. Surf. Sci. Catal*. 1998, 113, 97−109.
[35] Eguchi, K.; Arai, H. *Catal. Today*, 1996, 29, 379−386.
[36] Rusu, A.O.; Dumitriu, E. *Environ. Eng. Manage. J*. 2003, 2, 273−302.
[37] Anand, S.S.; Mehendale, H.M. *Encyclopedia of Toxicology*, 2005, 450–455.
[38] Ron Joseph and Associates, (2000), *VOC definition in: Regulations, Violations*, *Permits*, VOC, HAP and Such, on line at: http://www.ronjoseph.com/QandA/permits_q20.htm.
[39] O'Malley, A.; Hodnett, B.K. *Catal. Today*, 1999, 54, 31–38.
[40] On line at: http://www.health.state.mn.us/divs/eh/indoorair/voc.
[41] Clean Air Counts, (2003), Low-VOC Paints, on line at: http://www.cleanaircounts.org.
[42] Avila, P.; Bahamonde, A.; Blanco, J.; Sánchez, B.; Cardona, A.I.; Romero, M. *Appl. Catal. B: Environ*. 1998, 17, 75−88.
[43] Tsou, J.; Magnoux, P.; Guisnet, M.; Órfão, J.J.M.; Figueiredo, J.L. *Appl. Catal. B: Environ*. 2005, 57, 117−123.
[44] *Anguil Environmental Systems Inc*., on line at: http://www.anguil.com.
[45] Gupta, V.K.; Verma, N. *Chem. Eng. Sci*. 2002, 57 (14), 2679–2696.
[46] Carratala-Abril, J.; Lillo-Rodenas, M. A.; Linares-Solano, A.; Cazorla-Amoros, D. *Ind. Eng. Chem. Res*. 2009, 48 (4), 2066–2075.
[47] Davis, R.J.; Zeiss, R.F. *Environ. Prog.* 2002, 21, 111−115.
[48] Kastner, J.R.; Das, K.C. *J. Air Waste Manage. Assoc*. 2002, 52(4), 459−469.
[49] Bertinchamps, F.; Attianese, A.; Mestdagh, M.M.; Gaigneaux, E.M. *Catal. Today*, 2006, 112, 459−469.
[50] Reddy, B. M.; Khan, A. *Catal. Rev. Sci. Eng*. 2005, 47, 257−296.

[51] Hermia, J.; Vigneron, S. *Catal. Today*. 1993, 17, 349−358.
[52] McGrath, M. *Appl. Catal. B: Environ.*1995, 5, N25.
[53] GlobalSpec Inc., (2003), *Instrumentation and Equipment Used to Control the Properties and Degree of Purity of Air*, on line at: http://processequipment.globalspec.com/ProductFinder/Manufacturing_Process_Equipment/Air_Quality
[54] Cooley, R (2002), Burning Questions – Catalytic Oxidation Q and A, *Environmental Protection*, on line at: www.alzeta.com/CATALYTIC_OXIDATION_COOLEY.pdf.
[55] http://www.marketplacelists.com/remediation/thermal_remediation_services.htm.
[56] Hong, S.S.; Lee, G.H.; Lee, G.D. *Korean J. Chem. Eng*. 2003, 20(3), 440−444.
[57] Armor, J.N. *Appl. Catal. B: Environ.* 1992, 1, 221−256.
[58] Saravanamutto, H.I.H.; Cohen, H.; Roger, G.F.C. *Gas Turbine Theory* , Fifth edition, India, Dorling Kindersley,2001,1−491.
[59] http://en.wikipedia.org/wiki/William_C._Pfefferle.
[60] Zwinkels, M.F.M.; Jaras, S.G.; Menon, P.G.; Griffin, T.A. *Catal. Rev. Sci. Eng*. 1993, 35, 319−358.
[61] Busca, G.; Daturi, M.; Finocchio, E.; Lorenzelli, V.; Ramis, G.; Willey, R. J. *Catal. Today*, 1997, 33, 239−249.
[62] Finocchio, E.; Willey, R.J.; Ramis, G.; Busca, G.; Lorenzelli, V. *Stud. Surf. Sci. Catal*. 1996, 101, 483−492.
[63] Dadyburjor, D.B.; Jewur, S.S.; Ruckenstein, E. *Catal. Rev. Sci. Eng.* 1979, 19, 293−350.
[64] Morooka, Y.; Ozaki, A. *J. Catal*. 1966, 5, 116−124.
[65] Prasad, R.; Kennedy, L.A.; Ruckenstein, E. *Catal. Rev. Sci. Eng.* 1984, 26, 1−58.
[66] Trimm, D.L. *Appl. Catal*. 1983, 7, 249−282.
[67] Briot, P.; Auroux, A.; Jones, D.; Primet, M. *Appl. Catal*. 1990, 59, 141−152.
[68] Briot, P.; Primet, M. *Appl. Cata*. 1991, 68, 301−314.
[69] Hicks, R.F.; Qi, H.; Young, M.L.; Lee, R.G. *J. Catal*. 1990, 122, 280−294.
[70] Hicks, R.F.; Qi, H.; Young, M.L.; Lee, R.G. *J. Catal*. 1990, 122, 295−306.
[71] McCarty, J.G.; Wise, H. *Catal. Today*, 1990, 8, 231−248.
[72] Bond, G.C. *Heterogeneous Catalysis: Principles and Applications*; Oxford University Press: Oxford, UK, 1974, 1−120.
[73] Spivey, J.J. *Ind. Eng. Chem. Res.* 1987, 26, 2165−2180.
[74] Andersson, S.L.T. *J. Catal.* 1986, 98, 138–149.
[75] Noordally, E.; Richmond, J.R.; Tahir, S.F. *Catal. Today*, 1993, 17, 359−366.
[76] Arakawa, T.; Tsuchi-Ya, S.; Shiokawa, J. *J. Catal*.1982, 74, 317−322.
[77] Arai, H.; Yamada, T.; Eguchi, K.; Seiyama, T. *Appl. Catal*. 1986, 26, 265−276.
[78] Wachs, I.E. *Catal. Today,* 2005, 100, 79–94.
[79] McCarty, J.G.; Gusman, M.; Lowe, D.M.; Hildenbrand, D.L.; Lau, K.N. *Catal. Today*, 1999, 47, 5−17.
[80] Lester, G.R. *Catal. Today*, 1999, 53, 407–418.
[81] Petrosius, S.C.; Drago, R.S.; Young, V.; Grunewald, G.C. *J. Am. Chem. Soc*. 1993, 115, 6131−6137.
[82] Manon, M.R.; Jeurissen, F.; Jorna, J.J.; Nieuwenhuys, B.E.; Sinquin, G.; Petit, C.; Hindermann, J.P. *Catal. Today*, 1999, 54, 65−79.
[83] Kulażyński, M.; Van Ommen, J.G.; Trwezynski, J.; Walendziewski, *J. Appl. Catal.B: Environ.* 2002, 36, 239−247.

[84] Kim, S.C.; Shim, W.G. *Appl. Catal.B: Environ*. 2010, 98, 180–185.
[85] Li, W.B.; Wang, J.X.; Gong, H. *Catal. Today*, 2009, 148, 81−87.
[86] Larsson, P.O.; Andersson, A.; Wallenberg, L.R.; Svensson, B. *J. Catal*. 1996, 163, 279−293.
[87] Ji, L.; Lin, J.; Zeng, H.C. *J. Phys. Chem. B*. 2000, 104, 1783−1790.
[88] Everaert, K.; Baeyens, J. *J. Hazard. Mater.* 2004, 109, 113−139.
[89] Reddy, B.M.; Rao, K.N.; Reddy, G.K.; Khan, A.; Park, S.-E. *J. Phys. Chem. C*, 2007, 111, 18751 – 18758.
[90] Reddy, B.M.; Saikia, P.; Bharali, P. *Catal. Surv. Asia*, 2008, 12, 214 – 228.
[91] Reddy, B.M.; Thrimurthulu, G.; Katta, L.; Yamada, Y.; Park, S.-E. *J. Phys. Chem. C*, 2009, 113, 15882 – 15890.
[92] Reddy, B.M.; Saikia, P.; Bharali, P.; Park, S.-E.; Muhler, M.; Grünert, G. *J. Phys. Chem. C*, 2009, 113, 2452 – 2462.
[93] Reddy, B.M.; Lakshmi, K.; Thrimurthulu, G. *Chem. Mater.* 2010, 22, 467 – 475.
[94] Wang, C.H.; Lin, S.S. *Appl. Catal. A: Gen*. 2004, 268, 227–233.
[95] Prasad, R.; Kennedy, L.A.; Ruckenstein, E. *Combust. Sci. Technol*. 1980, 22, 271−280.
[96] Zimowska, M.; Michalik-Zym, A.; Janik, R.; Machej, T.; Gurgul, J.; Socha, R.P.; Podobinski, J.; Serwicka, E.M. *Catal. Today*, 2007, 119, 321–326.
[97] Morales, M.R.; Barbero, B.P.; Cadus, L.E. *Fuel*, 2008, 87, 1177−1186.
[98] Li, W.B.; Chu, W.B.; Zhuang, M.; Hua, *J. Catal. Today*, 2004, 93–95, 205−209.
[99] Choudhary, V.R.; Banerjee, S.; Pataskar, S.G. *Appl. Catal. A: Gen*. 2003, 253, 65−74.
[100] Choudhary, V.R.; Deshmukh, G.M.; Pataskar, S.G. *Catal. Commun*. 2004, 5, 115–119.
[101] Tejuca, L.G.; Fierro, J.L.G.; Tascón, J.M.D. *Adv. Catal.* 1989, 36, 237−328.
[102] Libby, W.F. *Science*, 1971, 171, 499−500.
[103] Alifanti, M.; Florea, M.; Somacescu, S.; Parvulescu, V.I. *Appl. Catal. B: Environ*. 2005, 60, 33–39.
[104] Islam, M.S.; Cherry, M.; Catlow, C.R.A. *J. Solid State Chem.* 1996, 124, 230−237.
[105] Leanza, R.; Rossetti, I.; Fabbrini, L.; Oliva, C.; Forn, L. *Appl. Catal. B: Environ*. 2000, 28, 55−64.
[106] Pena, M.A.; Fierro, J.L.G. *Chem. Rev.* 2001, 101, 1981−2017.
[107] Forni, L.; Rossetti, I. *Appl. Catal. B: Environ*. 2002, 38, 29–37.
[108] Anderson, R.B.; Stein, K.C.; Feenan, J.J.; Hofer, L.J.E. *Ind. Eng. Chem.* 1961, 53, 809−812.
[109] Klvana, D.; Kirchnerova, J.; Chaouki, J.; Delval, J.; Yaici, W. *Catal. Today*, 1999, 47, 115−121.
[110] Yamazoe, N.; Teraoka, Y. *Catal. Today*, 1990, 8, 175−199.
[111] Zhang, H.M.; Shimizu, Y.; Teraoka, Y.; Miura, N.; Yamazoe, N. *J. Catal*. 1990, 121, 432−440.
[112] Yu, Z.; Gao, L.; Yuan, S.; Wu, Y. *J. Chem. Soc., Faraday Trans*. 1992, 88,3245−3249.
[113] O'Connell, M.; Norman, A.K.; Hutterman, C.F.; Morris, M.A. *Catal. Today*, 1999, 47, 123−132.
[114] Spinicci, R.; Faticanti, M.; Marini, P.; De Rossi, S.; Porta. P. *J. Mol. Catal. A: Chem.* 2003, 197, 147−155.
[115] Huang, H.; Liu, Y.; Tang, W.; Chen. Y. *Catal. Commun*. 2008, 9, 55−59.
[116] Irusta, S.; Pina, M.P.; Menéndez, M.; Santamaría, J. *J. Catal*. 1998, 179, 400–412.

[117] Müller, H.; Deller, K.; Despeyroux, B.; Peldszus E.; Kammerhofer P.; Kuhn W.; Spielmannleitner, R.; Stoger, M. *Catal. Today*, 1993, 17, 383−390.
[118] Reddy, B.M.; Patil, M.K. *Chem. Rev*. 2009, 109, 2185 – 2208.
[119] Bozo, C.; Garbowski, E.; Guilhaume, N.; Primet, M. *Stud. Surf. Sci. Catal*. 2000, 130, 581−586.
[120] Peter, S.D.; Garbowski, E.; Perrichon, V.; Primet, M. *Catal. Lett*. 2000, 70, 27−33.
[121] Kim, S.C. *J. Hazard. Mater*. 2001, 91, 285–299.
[122] Wang, C.; Lin, S.; Chen, C.; Weng, H. *Chemosphere,* 2006, 64, 503–509.
[123] Tanga, X.; Xua, Y.; Shen, W. *Chem. Eng. J*. 2008, 144, 175–180.
[124] Vu, V.H.; Belkouch, J.; Ould-Dris, A.; Taouk, B. *AIChE Journal,* 2008, 54, 1585−1591.
[125] Bertinchamps, F.; Grégoire, C.; Gaigneaux, E.M. *Appl. Catal. B: Environ*. 2006, 66, 1–9.
[126] Kantzer, E.; Döbber, D.; Kießling, D.; Wendt, G.; *Stud. Surf. Sci. Catal*. 2000, 143, 489−497.
[127] Terribile, D.; Trovarelli, A.; Leitenburg, C.D.; Primavera, A.; Dolcetti, G.; *Catal. Today,* 1999, 47, 133−140.
[128] Jiang, Z.; Yu, J.; Cheng, J.; Xiao, T.; Jones, M. O.; Hao, Z; Edwards, P. P. *Fuel Process Technol*. 2010, 91, 97−102.
[129] Raciulete, M.; Afanasiev, P. *Appl. Catal. A: Gen*. 2009, 368, 79–86.
[130] Huuhtanen J.; Andersson S.L.T. *Appl. Catal. A: Gen*. 1993, 98, 159−171.
[131] Wang, C. H. *Chemosphere,* 2004, 55, 11−17.
[132] López, E.F.; Escribano, V.S.; Resini, C.; Amores, J.M.G.; Busca, G. *Appl. Catal. B: Environ.* 2001, 29, 251−261.
[133] Yang, Y.; Xu, X.; Sun, K. *J. Hazard. Mater*. 2007, 139, 140−145.
[134] Tang, X.; Li, Y.; Huang, X.; Xu, Y.; Zhu, H.; Wang, J.; Shen, W. *Appl. Catal. B: Environ.* 2006, 62, 265−273.
[135] Gandía, L.M.; Gil, A.; Korili, S.A. *Appl. Catal. B: Environ*. 2001, 33, 1−8.
[136] Parus, W.J.; Paterkowski, W. *Pol. J. Chem. Tech*. 2009, 11, 30−37.
[137] Gutiérrez-Ortiz, J.I.; Beatriz de, R.; López-Fonseca, R.; Martín, S.; González-Velasco, J.R. *Chemosphere,* 2007, 68, 1004−1012.
[138] Beatriz de, R.; López-Fonseca, R.; Sampedro, C.; Gutiérrez-Ortiz, J. I. *Appl. Catal. B: Environl*. 2009, 90, 545−555.
[139] Athanasios, K.; Ladavos, P.J. *J. Chem. Soc., Faraday Trans*. 1992, 88, 2557−2562.
[140] Spinicci, R.; Tofanari, A.; Faticanti, M.; Pettiti, I.; Porta, P. *J. Mol. Catal. A: Chem.*2001, 176, 247−252.
[141] Roche, V. ; Mazri, L.; Boréave, A.; Ta, M.H.; Retailleau-Mevel, L.; Giroir-Fendler, A.; Vernoux, P.; Deloume, J.P. *Appl. Catal. A: Gen*. 2010, 385, 163−169.
[142] Sinquin, G.; Hindermann, J. P.; Petit, C.; Kiennemann, A. *Catal. Today*, 1999, 54 107−118.
[143] Sinquin, G.; Petit, C.; Libs, S.; Hindermann, J.P.; Kiennemann, A. *Appl. Catal. B: Environ.* 2000, 27, 105−115.
[144] Poplawski, K.; Lichtenberger, J.; Keil, F.J.; Schnitzlein, K.; Amiridis, M.D. *Catal. Today*, 2000, 62, 329−336.
[145] Lia, N.; Boréavea, A.; Deloumea, J.; Gaillard, F. *Solid State Ionics*, 2008, 179, 1396−1400.

[146] Hosseini, S.A.; Sadeghi, M.T.; Almei, A.; Niaei, A.; Salari, D.; Kafi-Ahmadi, L. *Chin. J. Catal*. 2010, 31, 747−750.
[147] Denga, J.; Zhanga, L.; Daia, H.; Hea, H.; Aub, C.T. *J. Mol. Catal. A: Chem*. 2009, 299, 60–67.
[148] Hu, C.; Zhu, Q.; Jiang, Z.; Chen, L.; Wu, R. *Chem. Eng. J*. 2009, 152, 583−590.
[149] Álvarez-Galván, M.C.; de la Peña O'Shea, V.A.; Arzamendi, G.; Pawelec, B.; Gandía, L.M.; Fierro, J.L.G. *Appl. Catal. B: Environ*. 2009, 92, 445−453.
[150] Thevenin, P.O.; Ersson, A.G.; Kuar, H.M.J.; Menon, P.G.; Järås, S.G. *Appl. Catal. A: Gen*. 2001, 212, 189–197.
[151] Bozo, C.; Guilhaume, N.; Garbowski, E.; Primet. M. *Catal. Today*, 2000, 59, 33–45.
[152] Kundakovic, L.; Flytzani-Stephanopoulos, M. *J. Catal*. 1998, 179, 203–221.
[153] Kaspar, J.; Fornasiero, P.; Balducci, G.; Di Monte, R.; Hickey, N.; Sergo, V. *Inorg. Chim. Acta,* 2003, 349, 217-226.
[154] Zarur, A.J.; Ying. J.Y. *Nature*, 2000, 403, 65–67.
[155] Arai, H.; Machida, M. *Appl. Catal. A: Gen*. 1996, 138, 161–176.
[156] Burtin, P.; Brunelle, J.P.; Pijolat, M.; Soustelle, M. *Appl. Catal*. 1987, 34, 239−254.
[157] Amato, I.; Martorama, D.; Silengo, D. *Mater. Sci. Res*. 1975, 10, 187−197.
[158] Schaper, H.; Doesburg, E.B.M.; De Korte, P.H.M.; Van Reijen, L.L. *Solid State Ionics*, 1985, 16, 261−265.
[159] Schaper, H.; Amesz, D.J.; Doesburg, E.B.M.; Van Reijen, L.L. *Appl. Catal*. 1984, 9, 129−132.
[160] Oudet, F.; Courtine, P.; Vejux, A. *J. Catal*. 1988, 114, 112−120.
[161] Horiuchi, T.; Sugiyama, T.; Mori, T. *J. Mater. Chem*. 1993, 3, 861−865.
[162] Trimm, D.L. *Stud. Surf. Sci. Catal*. 1991, 68, 29–51.
[163] Ozawa, M.; Kimura, M.; Isogai, A. *J. Alloys Compd*. 1993, 193, 73−75.
[164] Rankin, G.A.; Merwin, H.E. *J. Am. Chem. Soc*. 1916, 38, 568–588.
[165] Stevels, A.L.N.; Schrama-de Pauw, A.D.M. *J. Electrochem. Soc*. 1976,123, 691–697.
[166] Iyi, N.; Takekawa, S.; Kimura, S. *J. Solid State Chem*. 1989, 83, 8–19.
[167] Machida, M.; Eguchi, K.; Arai, H. *Bull. Chem. Soc. Jpn*. 1988, 61, 3659–3665.
[168] Inoue, H.; Sekizawa, K.; Eguchi, K.; Arai, H. *J. Am. Ceram. Soc*.1997, 80, 584– 588.
[169] Machida, M.; Shiomitsu, T.; Eguchi, K.; Haneda, H.; Arai, H. *J. Mater. Chem*. 1992, 2, 455–458.
[170] Bratton. R.J. *J. Am. Ceram. Soc*. 1971, 54, 141–143.
[171] Busca, G.; Cristiani, C.; Forzatti, P.; Groppi, G. *Catal. Lett.* 1995, 31, 65–74.
[172] Machida, M.; Eguchi, K.; Arai, H. *J. Catal*. 1987, 103, 385−393.
[173] Machida, M.; Eguchi, K.; Arai, H. *J. Catal*. 1989, 120, 377–386.
[174] Groppi, G.; Cristiani, C.; Forzatti, P. *J. Mater. Sci*. 1994, 29, 3441–3450.
[175] Iyi, N.; Takekawa, S.; Bando, Y.; Kimura, S. *J. Solid State Chem*. 1983, 47, 34–40.
[176] Artizzu-Duart, P.; Brulle, Y.; Gaillard, F.; Garbowski, E.; Guilhaume, N.; Primet, M. *Catal. Today*, 1999, 54, 181–190.
[177] Groppi, G.; Cristiani, C.; Forzatti, P. *J. Catal*. 1997, 168, 95–103.
[178] Ersson, A.G.; Johansson, E.M.; Järås, S.G. *Stud. Surf. Sci. Catal*. 1998, 118, 601–608.
[179] Groppi, G.; Cristiani, C.; Forzatti, P. *Appl. Catal. B: Environ*. 2001, 35, 137–148.
[180] Machida, M.; Eguchi, K.; Arai, H. *J. Catal*. 1990, 123, 477–485.
[181] Gasperin, M.; Saine, M.C.; Kahn, A.; Laville, F.; Lejus, A.M. *J. Solid State Chem.* 1984, 54, 61–69.

[182] Sadamori, H. *Catal. Today*, 1999, 47, 325–338.
[183] Eguchi, K.; Inoue, H.; Sekizawa, K.; Arai, H. *Stud. Surf. Sci. Catal.* 1996, 101, 417–425.
[184] Li, T.; Li, Y. *Ind. Eng. Chem. Res*. 2008, 47, 1404–1408.

In: Catalytic Combustion
Editor: Sophie A. Cottilard, pp. 141-172
ISBN: 978-1-61324-279-7

Chapter 4

CATALYTIC COMBUSTION: KINETICS AND REACTOR DESIGN

Ilenia Rossetti* *and Lucio Forni*
Dipartimento di Chimica Fisica ed Elettrochimica,
Università degli Studi di Milano
v. C. Golgi 19, I-20133 Milano, Italy

ABSTRACT

Catalytic combustion may find application in the removal of pollutants from exhaust gases or in the energy conversion field. Proper reactor design is needed for optimised operation, *i.e.* to fully convert the fuel. When the catalytic combustion of methane is coupled with a turbogas plant, further attention should be paid to control the combustor temperature. This is needed to avoid the formation of NO_x and to preserve the catalyst from thermal deactivation. For all these reasons, a detailed knowledge of the kinetics of the process is welcome. Furthermore, some non trivial process layouts may be found for this application, such as those based on monolithic reactors. This contribution reviews some of the most typical applications of catalytic combustion, including noble metal or mixed oxide based catalysts. The discussion particularly focuses on kinetic aspects and reactor design.

1. INTRODUCTION

Recent reports from the Global Atmosphere Watch (GAW) Programme show that carbon dioxide (CO_2), methane (CH_4) and nitrous oxide (N_2O) reached in 2008 levels higher than those in pre-industrial age (before 1750) by 38%, 157% and 19%, respectively (CO_2 at 385.2 ppm, CH_4 at 1797 ppb and N_2O at 321.8 ppb). Furthermore, the emission rates of CO_2 were constantly increasing during recent years (Figure 1). As a consequence, from 1990 to 2008 the radiative forcing by all long-lived greenhouse gases has increased by 26.2% [1].

* E-mail: ilenia.rossetti@unimi.it

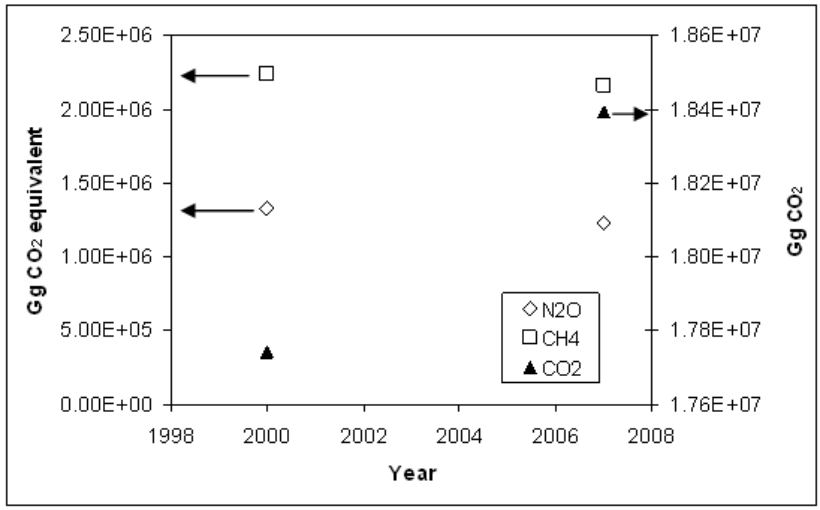

Figure 1. Emissions of some green house gases in years 2000 and 2007 [3].

CO_2 is the single most important human-emitted greenhouse gas in the atmosphere, contributing 63.5 % to the overall global radiative forcing. For about 10,000 years before the industrial revolution, the atmospheric abundance of CO_2 was nearly constant at ~ 280 ppm, balanced between the atmosphere, the oceans and the biosphere. Since the mid XVIII century, due to the industrial revolution, the atmospheric CO_2 concentration increased by 38%, primarily because of combustion of fossil fuels (8.62 Gt carbon in 2007), coupled to deforestation and modification of land use (0.5-2.5 Gt carbon per year over the 2000-2005 time period). These figures have been criticised because high-precision measurements of atmospheric CO_2 began in 1958 only. Nevertheless, even restricting the analysis to recent years only, one may find that the increase of CO_2 concentration in the atmosphere corresponds to ~ 55% of the CO_2 emitted by fossil fuels combustion.

Methane also contributes for a 18.2 % to the overall global radiative forcing. It is emitted by natural (~ 40%) or anthropogenic sources (~ 60%, *e.g.*, ruminants, rice agriculture, fossil fuel exploitation, landfills and biomass burning). It is also part of a natural removal cycle mainly based on its reaction with hydroxyl radical (OH). Before the industrial era, the atmospheric methane concentration was *ca*. 700 ppb. Increasing emissions from anthropogenic sources are responsible for the 157% increase in CH_4. Methane was increasing by up to 13 ppb per year during the late 1980s, while the growth rate decreased during the past decade due to efficient exhausts cleanup.

Nitrogen oxides (mainly N_2O) contribute for a 6.2% to the overall global radiative forcing. N_2O atmospheric abundance prior to industrialisation was 270 ppb. It can be emitted into the atmosphere from both natural and anthropogenic sources, the latter accounting for about 40%. It may be removed from the atmosphere by photochemical processes in the stratosphere. The mean growth rate of this pollutant has been equal to 0.78 ppb per year over the past 10 years. Summarising, CO_2 emissions are continuously growing, despite the worldwide attempts to establish regulations and limitations [2] (Figure 1). By contrast, NO_x and CH_4 emissions are moderately more stable and their growth rate is a bit less critical, mainly due to proper processes for exhausts cleanup.

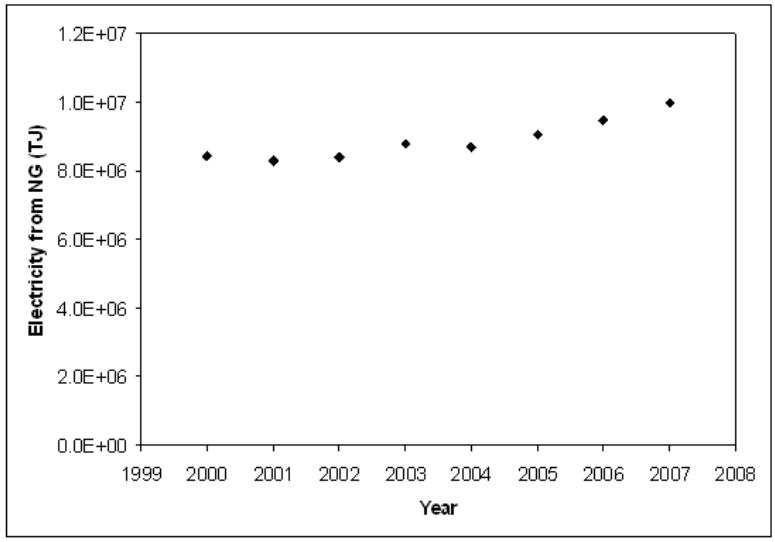

Figure 2. Electricity production (TJ) from natural gas since year 2000 [3].

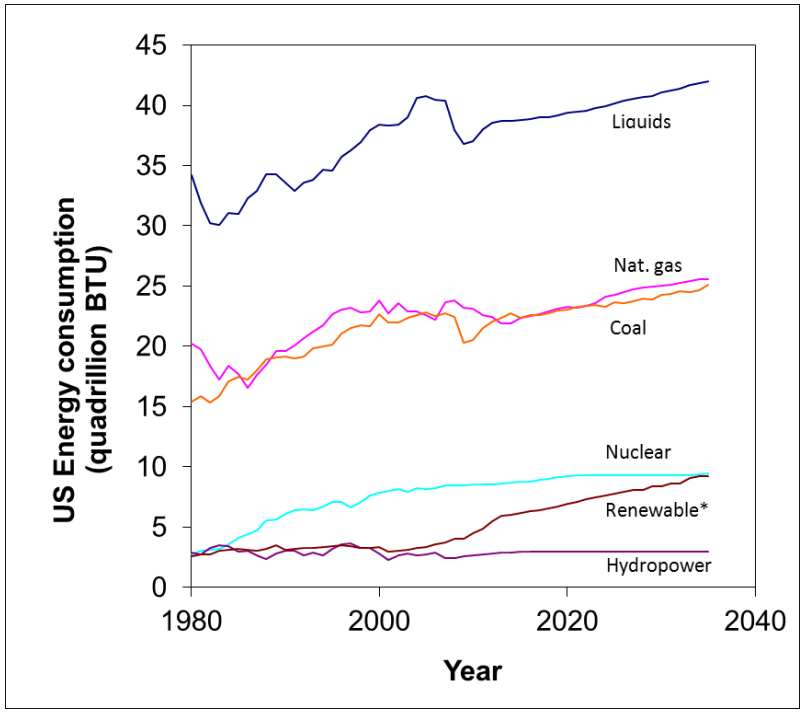

Figure 3. Energy consumption in the US by type of fuel.Data available 1980-2010; DOE forecasts 2011-2035 [4]. * Renewable energy excluding hydroelectric.

Data from the UN Statistics division reveal that in 2007 49 billions GJ of electrical energy have been produced worldwide through thermal plants. Among these, in the same year *ca*. 10 billions GJ were based on natural gas combustion [3] and the growing trend during the first decade of the millennium is reported in Figure 2.Thermal processes for energy

production are responsible of the emission of a huge amount of greenhouse gases, among which the above mentioned are particularly powerful. All these pollutants may indeed arise from combustion processes, carbon dioxide as main product, CH_4 due to incomplete combustion and nitrogen oxides in general due to a radical mechanism between N_2 and O_2 occurring at high temperature in the flame. The scenario is becoming even more critical since the energy consumption projections for developed and developing countries report an ever growing trend. An example is reported in Figure 3, according to the DOE forecasts relative to the United States [4].The US production of electrical power is based on many different sources, though natural gas (NG) combustion represents a growing portion. The contribution of NG combustion has indeed increased during the last 15 years (1996-2010) from *ca.* 13% to *ca.* 24%, with peaks around 30%. As a consequence, the number of generators with capacity higher than 100 MW in the US has grown from 1,300 in 1997 (nameplate capacity *ca*. 377 GW) to *ca.*1,570 in 2008 (nameplate capacity *ca*. 427 GW) [5].The R&D efforts should be then focused on the increase of energy conversion efficiency and on a further improvement of emissions control. Catalytic combustion is an efficient process aiming at both these goals.

Three different mechanisms are proposed for NO_x formation during combustion [6]. 1) "Thermal NO_x", forming from the reaction between oxygen and nitrogen through the Zeldovich mechanism [7]. The rate of thermal NO_x production mainly depends on flame temperature. 2) "Prompt NO_x", forming from the fast coupling of nitrogen with oxygen containing radicals in the flame front. This mechanism is preferentially active at moderate temperature and under fuel-rich conditions. 3) "Fuel NO_x", forming during the oxidation of nitrogen containing species in the fuel. This formation is less dependent on flame temperature and is usually favoured under fuel-lean conditions.Catalytic combustion is based on the oxidation of a gaseous fuel without flame. The reaction mechanism is mediated by a catalyst, which offers an alternative route with respect to the radical mechanism. An immediate advantage of this technology is its higher selectivity towards CO_2 and H_2O with respect to flame combustion. This is of course true if a proper catalyst is selected. An indirect advantage is related to the lower operating temperature, which makes thermodynamically unfavourable the formation of NO_x. Furthermore, less restrictive demands are required as for flammability limits and reactor design. This is especially important when dealing with gas turbines for power generation [8,9]. Indeed, the typical operating temperature of a traditional burner reaches *ca*. 2000°C, leading to the formation of a huge amount of NO_x (>200 ppm).This figure may be decreased down to 25 ppm in modern furnaces with a strict control of the operating conditions, but catalytic combustion may further decrease the emission level of these pollutants by *ca.* one order of magnitude. Though the design and operation of a catalytic burner for this application may be more expensive, the overall cost of the installation is cheaper, since additional units for the clean-up of the tail gas (such as SCR reactors) may be avoided. Total methane combustion under fuel lean conditions can be achieved at 550-800°C depending on catalyst formulation.

However, the adiabatic temperature increase would be unacceptable, leading to catalyst ignition and irreversible deactivation. Therefore, a hybrid combustor design has been proposed, based on one or two catalytic beds, converting only part of the fuel, and a further conventional burner zone, where the remaining fuel (and, when needed, additional air) are added and homogeneous flame combustion takes place. This improves temperature control, so reducing the formation of NO_x in the flame zone and decreasing down to 2-3 ppm their concentration. A review of the materials suitable for the catalytic combustion of hydrocarbons

is reported elsewhere [6,10-18]. In the present review the attention will be focused on the technologies available for the catalytic combustion of hydrocarbons for different applications, in particular for power generation and for the abatement of volatile organic compounds (VOCs).

2. CATALYTIC COMBUSTION TECHNOLOGIES

2.1. Power Generation Systems

One of the most interesting applications of catalytic combustion is its coupling with gas turbines (GT) for power generation. GT are available in different size from 500 kW to 250 MW and they may be efficiently used for the combined heat and power (CHP) generation (Figure 4) [19]. The most efficient commercial technology for stationary power generation is a gas turbine-steam turbine combined-cycle, which includes a Rankine and a Brayton thermodynamic cycle. The overall efficiency attains 60%, though simple-cycle gas turbines for power-only generation are in use with efficiency *ca*. 40% (size < 40 MW). A high-quality exhaust heat may be also recovered (tri-generation), which can be recovered in CHP configurations to reach overall system efficiencies (electricity and heat) up to 80%. Furthermore, GT are among the cleanest means of generating electricity, with lower NO_x emissions than related technologies, either with catalytic exhaust cleanup or lean pre-mixed combustion. In addition, due to their high efficiency and feeding with natural gas, GT emit substantially less CO_2 per kWh produced than any other commercial technology based on fossil fuels.GT systems operate on the basis of the Brayton thermodynamic cycle (Figure 5), where air is compressed, heated and subsequently expanded. Power is produced by the expander (turbine), by coupling it with a generator [20]. The power produced by the turbine and consumed by the compressor is dependent on the temperature of the gas passing through the machine. Therefore, it is convenient to operate the expansion turbine at the highest practical temperature (but of course taking into account materials resistance and cost) and to operate the compressor with inlet air at the lowest temperature. High temperature and pressure ratios increase efficiency. Some variations of the Brayton cycle help improving the net efficiency.

For instance, fuel consumption may be decreased by preheating the compressed air with heat recovered from the turbine exhausts (recuperator). In addition the compressor work may be reduced through intercooling or precooling of air and the exhausts may be used for steam generation for internal use in a plant or for expansion in a steam turbine (combined cycle).The so called AeroderivativeGT are adaptations from jet engines. They are very efficient and light, but much more expensive than those especially designed for stationary power production. 40 - 50 MW capacity machines are available, though larger size systems (> 40 MW) are approaching 45% efficiency for a simple-cycle. Industrialor frame gas turbines are designed for stationary power generation and are commercially available from 1 to 250 MW capacity. They are generally less expensive and are suitable for continuous operation with longer inspection and maintenance intervals than the previous versions, though less efficient and heavier. Industrial GT operate at lower compression ratio (up to 16:1, with respect to 30:1 for aeroderivative GT) and often do not require an external fuel gas compressor.

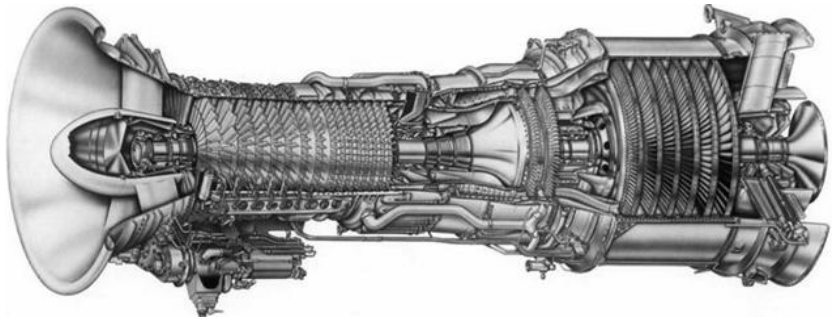

Figure 4. Sketch of a General Electric LM2500 GT. Readapted from [19].

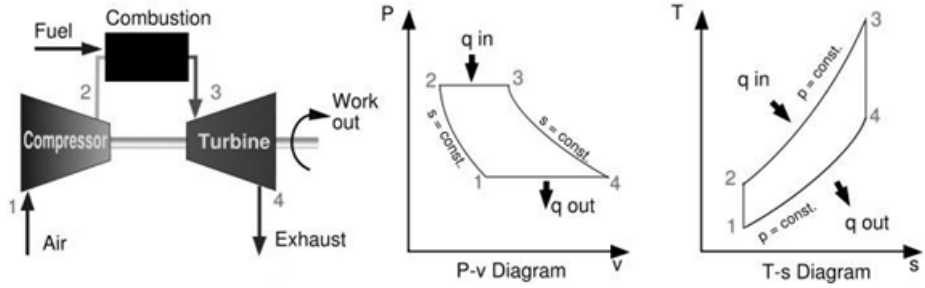

Figure 5. Ideal Brayton cycle. Readapted from [20].

Table 1. Installation costs, operating parameters and efficiency for single-cycle or CHP units of some commercial GT systems [21]

Cost and Performance Characteristics	System 1	System 2	System 3	System 4	System 5
Capacity (kW)	1,150	5,457	10,239	25,000	40,000
Basic Installed Cost (2007 $/kW)	3,324	1,314	1,298	1,097	972
Complex Installation wth SCR (2007 $/kW)	5,221	2,210	1,965	1,516	1,290
Electrical Efficiency (%), HHV *	21.27	27.72	28.44	34.30	37.00
Fuel Input (MMJ/hr)	19,518	70,900	129,666	262,287	389,105
Required Fuel Gas Pressure (bar)	5.7	14.9	21.9	23.4	30.0
CHP Characteristics					
Exhaust Flow (1,000 kg/hr)	23.3	77.4	148.9	259.0	432.7
GT Exhaust Temperature (°C)	510	516	491	510	457
Steam Output (kW equivalent)	2,435	8,279	14,385	26,469	37,876
Total CHP Efficiency (%), HHV*	66.3	69.8	68.4	70.7	72.1
Power/Heat Ratio	0.47	0.66	0.71	0.94	1.06

* Based on the higher heating value (HHV).

Some operating details, efficiency and installation costs for commercial GT systems are reported in Table 1 [21]. From such data one may conclude that increasing efficiency is expected with increasing plant size. The cost per kW of power produced decreases with incresing plant size. However, one may notice the impact of exhausts post treatment on the installation cost, especially for small installations, as better detailed in Table 2. An intrinsically cleaner combustion technology is therefore more than welcome.From this point of view, the primary pollutants from GT plants are NO_x, CO and VOCs. Other pollutants such as SO_x and particulate matter (PM) depend on the fuel used, though SO_x emissions from GT fed with desulphurated NG are negligible. The main parameter governing the emissions levels of the primary pollutants is the operating load. GT are designed to achieve maximum efficiency and optimal combustion conditions at high loads, where higher NO_x emission occur due to high flame temperature (thermal NO_x). By contrast, at lower load, lower thermal efficiencies and incomplete combustion take place, leading to higher emissions of CO and VOC_s. The control of peak flame temperature is commonly made by injecting a diluent (*e.g.* steam) or by maintaining a homogenous fuel-to-air ratio. In addition, new GT plants are based on lean pre-mixed combustion systems ("dry low NO_x" or "dry low emissions"), which operate in a tightly controlled lean (lower fuel-to-air ratio) premixed mode, that maintains modest peak flame temperatures.Nevertheless, the primary post-combustion NO_x control method in use is selective catalytic reduction (SCR). Ammonia is injected into the flue gas and reacts with NO_x in the presence of a catalyst to produce N_2 and H_2O. This significantly reduces NO_x concentration (down to *ca.* 5 ppm), but SCR systems are expensive (Table 2) and significantly impact the economic feasibility of small GT installations. For instance, for a 5 MW system electric generation costs increase approximately by half a cent per kWh including exhausts treatment. Furthermore, SCR requires on-site storage of ammonia, with the correlated safety risks. A different approach makes use of catalytic combustion, where the fuel is oxidised under lean conditions in the presence of a catalyst. The catalyst is commonly loaded on the combustor surfaces.

Table 2. Breakdown of installation costs and operation requirements for some commercial GT systems including special operations (*e.g.* tail gas clean-up by SCR) [21]

	System 1	System 2	System 3	System 4	System 5
Nominal Turbine Capacity (MW)	1	5	10	25	40
Installation Cost with no additional equipment (2007$ 1000)	489	864	1,551	2,987	5,280
Additional Equipment					
Building (2007$)	n.a.	311	414	576	759
Compressor Incremental Cost (2007$ 10^6)	0.416	0.937	1.182	1,223.5	1,797.9
Compressor Power Use (kW)	9	90	203	500	1,000
SCR Incremental Cost (2007$ 1000)	397	732	986	1,350	1,743
SCR Power Use (kW)	6	29	53	120	225

Additional advantages are low vibration and acoustic noise, only one-tenth to one-hundredth the levels measured in the same turbine equipped with common combustors. Past efforts to develop catalytic combustors for GT achieved promising results as for pollutants emission, but the operating durability was still unsatisfactory. This was typically due to cycling damage and to the brittle nature of the materials used for catalysts and catalyst support systems.

Catalytic combustor developers and GT manufacturers are currently testing durable catalytic and "partially catalytic" systems that are overcoming the problems of past designs. Catalytic combustors capable of achieving NO_x levels below 3 ppm are in full-scale demonstration and are entering early commercial development. For example, Kawasaki offers a version of its M1A 13X, 1.4 MW gas turbine with a catalytic combustor with guaranteed less than 3 ppm NOx emissions.

Similarly to flame combustion, optimised catalytic combustion requires an integrated approach to combustor and turbine design. One of the most known applications of catalytic combustion to GT is represented by the XONON process, developed by Catalytica Inc. [22]. The Xonon™ Cool Combustion system was tested on a Kawasaki M1A-13A gas-turbine-generator (1.5 MW) located in Santa Clara, California. It completely converted the fuel to produce a gaseous mixture at *ca.*1300 °C. Dilution air was added to shape the temperature profile required at the turbine inlet.

The Xonon™ Cool Combustion system consists of four sections: 1) A preburner, a lean, premixed combustor, used to preheat air to *ca*. 470°C before it enters the catalyst module and during the startup phase for acceleration of the turbine. 2) A fuel injection and fuel/air mixing system, allowing the injection of a homogeneous fuel/air mixture to the catalyst. 3) A catalyst module, where a portion of the fuel is flameless burnt,and 4) A homogeneous combustion region, located immediately downstream of the catalyst bed. NO_x in the turbine exhaust is usually formed in the preburner or in the homogeneous combustion section. The design of the Xonon™ combustor is customised to the particular turbine model and operating conditions of the application. The footprint may vary depending on the implementation, although the Xonon™ combustion system would likely be a bit larger than the combustor that is typically supplied as standard equipment by the turbine manufacturer.

The expected lifetime of the catalyst module is 8,000 h.Some examples of the performance of this system are reported in Table 3. A verification of the performance at 98-99% load allowed to conclude that at 15% O_2, on a dry basis, the average NO_x concentration was as low as 1.13 ± 0.03 ppmv, that of CO 1.36 ppmv and that of unburnt hydrocarbons *ca*. one order of magnitude lower (the latter on a wet basis).Finally, in the CATHLEAN project ("Catalytic Hybrid Lean Burner", an EU Framework 5 project performed between 2003 and 2006), a consortium of researchers investigated the development of an advanced, ultra-low NOx, hybrid burner for heavy-duty gas turbines [23].

The design combined catalytic and lean-premixed combustion components (Table 4). Catalytic elements were developed to preheat the incoming lean fuel/air mixture up to *ca.*870°C at the required high (20–30 m/s) operating velocity and inlet temperature (400–420°C). High-pressure aging of a Pd-based catalyst at 10 bars indicated that the catalyst activity decreases to *ca.* one third with respect to the fresh sample in the first 200 h of operation, then remaining constant, and that an optimal catalyst design should contain different regions (in the axial direction) to allow optimisation of catalyst activity and material

stability, *e.g.* higher activity at the flow entrance, greater thermal stability at the reactor outlet where temperatures are high.

Full-scale burner investigations demonstrated the feasibility of the CATHLEAN hybrid catalytic burner concept and provided an indication of performance enhancement due to catalytic conversion. Both NO_x emissions and lean stability limit were improved (25% reduction in NO_x emissions).

Table 3. Examples of XONON system test runs [22]

Run	Ambient Temp.	Turbine Load		Fuel Flow Rate	Compressor Inlet Temp.	Compressor Discharge Pressure	Compressor Discharge Temp.	Temp. at Catalyst Inlet	Temp. Out of Catalyst	Exhaust Gas Temp.
	°C	(MW)	(%)	kg/h	°C	kPa	°C	°C	°C	°C
1	15.2	1.39	97.9	428	17	910	356	480	847	524
2	16.3	1.38	98.1	425	17	903	356	480	847	527
3	17.4	1.37	97.9	423	19	896	357	480	848	529
4	25.2	1.25	98.9	406	26	869	364	484	850	535
5	24.1	1.27	98.6	405	25	869	364	484	851	534
6	21.3	1.29	98.4	411	22	876	361	481	849	532
7	14.6	1.36	98.2	428	16	910	355	480	846	526
8	16.3	1.35	98.3	425	17	910	356	480	847	527
9	17.4	1.33	98.2	423	19	896	357	480	847	529
10	20.7	1.29	98.4	412	22	882	361	481	846	531
11	21.9	1.25	99.0	408	25	876	362	481	847	533
12	23.5	1.23	98.4	407	25	869	362	482	849	533
Minimum	15.2	1.23	97.9	405	16	869	355	480	846	526
Maximum	25.2	1.39	99.0	425	26	910	364	484	851	535

Run	Ambient Temp. (°F)	NO_x (ppmv)	CO (ppmv)	UHC (as propane) (ppmv)
1	59	1.15	1.19	0.17
2	61	1.14	1.71	0.16
3	63	1.08	1.50	0.17
4	77	1.06	1.10	0.15
5	75	1.11	1.03	0.17
6	70	1.13	1.22	0.15
7	58	1.22	1.10	0.18
8	61	1.17	1.02	0.13
9	63	1.13	1.19	0.20
10	69	1.14	1.91	0.12
11	71	1.12	1.88	0.18
12	74	1.13	1.46	0.19

Table 4. Main parameters of the CATLEAN burner [23]

Parameter	Boundary condition
Burner dimensions	Cylindrical envelope: ≈450mm long, 200mmdiameter
Inlet velocity	20–30 m/s @ 400–450°C
Pressure	15–25 bar
Total pressure loss	<3% of engine operating pressure
Total heterogeneous fuel conversion	>40% of total fuel flow

2.2. Abatement of Volatile Organic Compounds (VOCs)

Volatile Organic Compounds (VOCs) originate from various processes, as vapour release and similar molecules and may appear as Products of Incomplete Combustion (PICs). Such effluents can be treated by means of different technologies, among which the most common are condensation, adsorption, biological treatment or thermal treatment.

Condensation applies to relatively high concentration of VOCs only, *e.g.* in the case of solvents in air. Its efficiency is severely restricted by residual vapor pressure, as well as by the possible formation of fog or aerosols. It is improved by operating under cryogenic conditions or by combining condensation with absorption.

Adsorption allows an almost unlimited reduction in VOCs concentration. Since it is capacity-limited, it may be used as an additive tool to condensation.

Biological treatment mostly proceeds on trickle bed filters. Its limitations are temperature dependence, slow conversion rates, presence of inert molecules and sensitivity to toxic molecules for organisms.

Combustion of VOCs and other combustible species is advantageous, since the main oxidation products are water and carbon dioxide and the process is very fast. Thermal combustion of VOCs proceeds at temperature $\geqslant 800^{o}C$. However, at these temperatures harmful by-products, such as NO_x and CO can form and care must be taken to attain high efficiency under variable input conditions.

Particular care should be put in the flame treatment of chlorine containing VOCs, since dioxins, or polychlorinated dibenzo-p-dioxins and dibenzofurans, occur invariably in incinerator effluents because of their presence, prior to combustion, in the original materials to be incinerated, their formation at high temperature, during post-combustion in a temperature window ranging from flame temperature to *ca*. 500°C and their formation at low temperature, below 500°C, during heat recovery and/or gas cleaning. Dioxins are almost always already present in materials to be incinerated, but they are deeply destroyed by the fire and reduced to levels close to present limit values. By contrast, active dioxin formation generally takes place between 300 and 350°C through several mechanisms, operating in parallel, descibed in detail elsewhere [24].

Catalysts can lower the required combustion temperature to 200 – 400°C, depending on the substrate, so that the additional fuel consumption is lower or even nil (auto-thermal operation) and the formation of secondary pollutants is negligible. Moreover, less $CO_2$is formed, since the auxiliary fuel consumption is lower, and less expensive construction materials can be used, such as standard carbon steel. The cleaning efficiency by catalytic combustion is very high [24].

Catalytic after-combustors are employed to treat flammable solvent vapors, control odors and eliminate toxic compounds. Catalytic post-combustion lowers both oxidation temperature and fuel input to the combustion process. The most commonly used catalysts are based on the platinum group metals, but some mixed-oxide types are gradually gaining importance. Catalysts are employed as pellets or as monolith honeycomb blocks, less commonly in form of fibers.

Catalytic postcombustion is applicable to off-gases free from dust and catalytic poisons, *e.g*. arsenic, phosphorus, sulfur or halogen compounds, so requiring special formulations for chlorinated VOCs. Nitrogen compounds are partly converted to NO_x, SO_2 to SO_3, HCl to Cl_2.

Over platinum-based catalysts the typical inlet temperature is between 200 and 350°C, approaching the adiabatic combustion temperature during conversion. The final temperature is limited by sintering risks, generally appearing above 500°C, and other undesirable thermal phenomena, such as volatilisation of active components. Catalytic processes are composed of a series of consecutive transport, mixing, mass transfer, adsorption, chemical reaction and desorption steps. The effect of the numerous transport phenomena are reduced by an adequate internal pore distribution and turbulent flow conditions, leading to thin boundary layers, so that the over-all rate can be easily chemicallycontrolled. As the operating temperature is raised, chemical reaction rates rise rapidly (the activation energy is often of the order 20 to 50 kcal mol^{-1}). The rate of diffusion increases slowly with temperature, so that chemical reaction gradually overtakes internal diffusion. It can be shown that the activation energy is halved, when a first order chemical reaction becomes controlled by internal diffusion.At even higher temperatures external diffusion becomes rate-determining and the sites located within catalyst pores become quite inactive. Mass transfer rates are commonly described by empirically established relationships between the relevant dimensionless groups, *i.e.* the Sherwood (*Sh*), Reynolds (*Re*) and Schmidt (*Sc*) numbers.Economic conditions imply relatively low operating temperature, low auxiliary fuel requirements, high space velocity, low pressure drop, long lifetime and easy recovery of precious metals if used. Other general rules prescribe that higher molecular weight hydrocarbons are more easily oxidised than lower ones, but have a higher tendency to coke, whereas oxygenated compounds are easier to convert and chlorinated ones are more difficult. The principal design parameters for catalytic postcombustion units are the volumetric flow of the off-gas to be treated and the minimum, maximum and average concentration of organics to be fired. A guard bed is often placed before the catalyst layer, in order to homogenise gas flow and possibly entrap poisons.

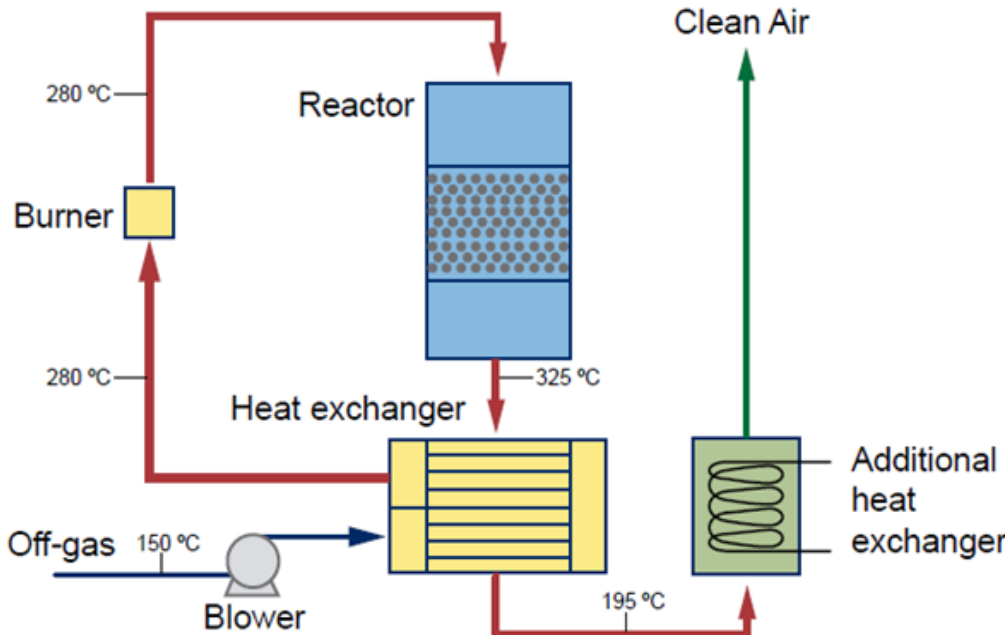

Figure 6. Scheme of the Topsøe CATOX process. It is suitable for air with medium or high (typically 2-10 g/Nm^3) concentrations of VOCs [25].

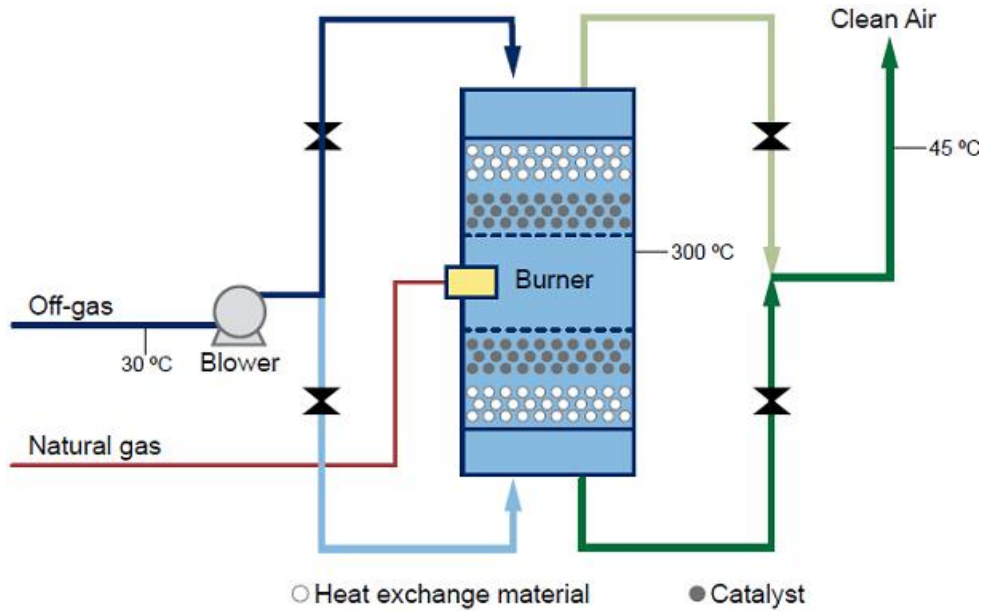

Figure 7. Scheme of the Topsøe REGENOX process. The air flow direction changes several times per hour in order to maintain the temperature level in the central zone where the catalyst is located. It is suitable for air streams with low or medium (typically 0.3-4 g/Nm^3) concentrations of VOCs and it is able to operate without support heating at concentrations as low as 0.7 g/Nm^3 [25].

Examples of commercial catalytic combustion units are the CATOX and REGENOX modules (HaldorTopsøe). Depending on the feed, the catalyst operates at 200 - 400ºC to light off the combustion reaction. In case the temperature of the gas to be treated is lower than required, heat generated by oxidation of the pollutants is used for preheating, so optimising the energy efficiency of the catalytic unit. CATOX (Figure 6) is selected for higher pollutant concentrations, while REGENOX (Figure 7) is suitable in the opposite case [25,26]. Both CATOX and REGENOX units are easily designed for a purification grade of 99% or higher, or for a maximum emission level of 20 mg per Nm^3 of organic matter in the cleaned gas [24].

The catalysts are based on porous alumina or silica supports, available as spheres or rings, or as honeycomb monolith structures. The most common Topsøe combustion catalysts are constituted by metal oxides on alumina (used for the most common solvents and tolerant to silicon), noble metals on alumina (for the abatement of CO and sulphur tolerant), metal oxides and noble metals on alumina (for chlorinated hydrocarbons and special applications) and metal oxides and noble metals on silica (especially for sulphur compounds and ammonia).

3. KINETIC ASPECTS OF CATALYTIC COMBUSTION

The kinetics for the catalytic combustion of CH_4 over palladium in its metal and oxide forms has been studied by Zhu *et al.* [27]. The results show that the reaction rate was not dependent on the structure of the catalyst, but it was strictly proportional to the total surface area. The catalytic combustion of methane/air mixtures was investigated experimentally and numerically on a Pd-based catalyst under GT realistic conditions (inlet temperatures up to

600°C, pressures up to 15 bar and spatial velocities up to $3*10^6$ h^{-1}) [28]. Simulations were carried out with a 2-D elliptic fluid mechanical code that incorporates detailed transport, heat loss mechanisms and a heterogeneous-homogeneous reaction network. The authors concluded that, under certain conditions, the absolute temperature rise across the catalyst became essentially independent of pressure, a feature highly desirable for many practical systems. Even though the computed catalyst surface temperatures remain well below the decomposition temperature of PdO, a significant section of the catalyst, *ca*. 30% of the total reactor length, contributed minimally to the total fuel conversion, suggesting design improvements mainly at the reactor inlet.

A more fundamental approach to methane catalytic combustion is presented in [29]. A Monte Carlo simulation has been carried out based on a pseudo-Langmuir-Hinshelwood (LH) mechanism, to alternatively interpret the behavior of this reaction, usually assumed to be of the Mars-van Krevelen (MvK) type. A sketch of the mechanism proposed is represented in Figure 8. The model represented reasonably some experimental results, leading to a sound estimation of activity and of the reaction orders with respect to H_2O and CH_4.

A kinetic study on CH_4 combustion over a 10wt% PdO/ZrO_2 catalyst is presented in [30,31] as an example of a demanding problem which requires both the development of appropriate experimental tools and a theoretical insight on surface chemistry. An annular catalytic reactor was used to collect kinetic data under unusually severe conditions (high temperature and CH_4 concentration) and compared with a conventional packed bed reactor. The annular reactor allowed to widen the temperature range of the kinetic investigation towards higher values, *i.e*. to approach the real operating conditions in GT units.

A careful evaluation of the effect of the thickness of the catalyst layer on diffusional limitations has been also provided. Mass, heat and momentum transfer were taken into account, addressing the effects of CH_4, O_2, H_2O and CO_2 concentration in a temperature range from 400 to 550°C. The inhibiting effect of water was also confirmed, observing a decrease of methane conversion at every temperature. CO_2 inhibition was a bit more controversial, since in this work it has been found comparable to that of water, but it was not even noticed in the case of a different acidic support (alumina). This suggested a role of the support itself on this point.

The data were analysed by means of a purely empirical power law model and of a formal kinetic model assuming methane dissociative adsorption as the rate controlling step (Figure 9). The power rate model represented fairly good the experimental data, estimating a reaction order of -0.32 for water, -0.25 for CO_2 and an apparent activation energy of 108 kJ/mol. However, attempts to improve the physical significance of the model led to the development of a LH rate equation (Figure 9).

It is worth noticing that such expression can be derived either via the classical LHHW approach or following the MvK mechanism, under the assumption of a slow catalyst reduction, controlled by the surface reaction between CH_4 and PdO, with competitive adsorption of CO_2 and H_2O on the oxidised sites, followed by fast re-oxidation of surface vacancies.

Evidences in favour of a MvK mechanism were reported by Baiker and co-workers [32,33] and more recently by Pfefferle and co-workers [34]. The LHHW approach led to a worse representation of the experimental data, mainly failing in prediction of catalyst inhibition by water and carbon dioxide.

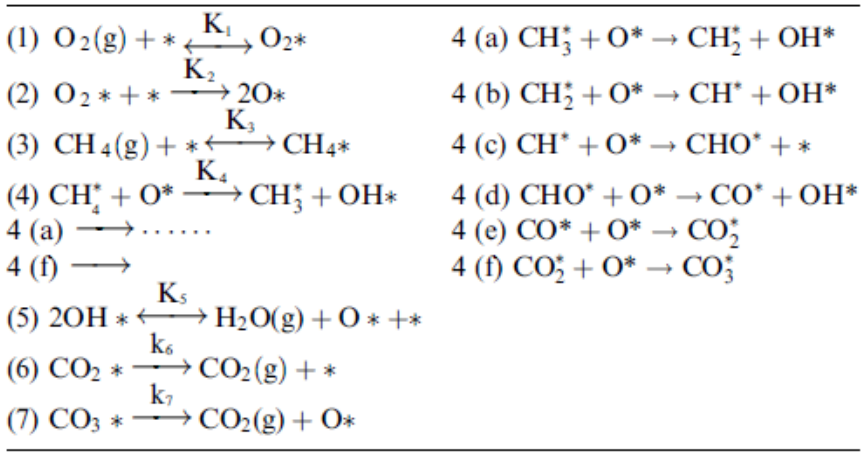

Figure 8. Detailed kinetic scheme for methane catalytic combustion. * represents an active site, free or occupied by the indicated molecule [29].

Material balance

$$F\frac{dY_{CH_4}}{dW_{cat}} = -r$$

$$Y_{CH_4} = Y^0_{CH_4} \text{ at } z = 0$$

Power law model:

$$r\ (cm^3/g_{cat}/s \text{ at STP}) = \frac{k_c P_{CH_4}}{P^a_{H_2O} P^b_{CO_2}}$$

Langmuir-Hinshelwood model:

$$r\ (cm^3/g_{cat}/s \text{ at STP}) = \frac{k_c P_{CH_4}}{1 + K_{H_2O} P_{H_2O} + K_{CO_2} P_{CO_2}}$$

Figure 9. Kinetic models describing methane combustion in the 400-550°C range in an annular reactor [30].

Steady state isotopic transient kinetic analysis (SSITKA) was used to elucidate the reaction mechanism of the flameless methane combustion over a PdO/Al_2O_3 catalyst [35]. Indeed, as introduced a few lines above, in many papers arguments are presented in favour of the Eley–Rideal (ER) mechanism [36], of the LHHW mechanism [37,38], or of the MvK redox mechanism [34,39].

The latter seems supported by the data collected by Machoki*et al.* [35], which also indicate that an increase of the reaction temperature leads to an increase in the number of active sites over the $Pd(PdO)/Al_2O_3$ catalyst surface. Therefore, a greater amount of oxygen from the lattice of the catalyst becomes accessible for the reaction.

Experimental conditions near to those relevant for GT application have been used by Mantzaras [40], coupled with spectroscopic devices able to detect high temperature intermediates (Raman and Laser Induced Fluorescence). Both homogeneous and heterogeneous kinetics have been reviewed and validated under high pressure operation regimes (Figure 10).

The hetero-homogeneous reaction network and its coupling to transport phenomena, as well as the advent of *in situ*, locally resolved measurements of major and minor gas-phase species concentration over the catalyst boundary layer has opened new directions for the study of catalytic combustion.

It was shown that the hetero-homogeneous radical coupling inhibits only mildly the onset of homogeneous ignition. The catalytic reactivity of fuel-lean methane/air mixtures over platinum increases with rising pressure, but the rate of increase is moderated by the corresponding decrease in surface free sites. Similar kinetic investigations are also reported for fuel-rich partial catalytic oxidation of methane over rhodium. In catalytic channels turbulent transport is controlled by flow laminarisation, induced by the hot catalytic walls. Near-wall turbulence models describe adequately the degree of relaminarisation only under intense wall heat transfer.

Such kind of investigation represents an intriguing problem for most applications, since complex computer fluid dynamics (CFD) models should be adapted to the specific case. A simplified formulation of the heat and mass balance for heterogeneous combustion has been proposed by Mellado*et al.* [41], who reduced the problem to the solution of a set of algebraic equations.

The resulting problem was particularly simple in computations where the catalytic rate was determined from an explicit expression in terms of conversion and temperature[42,43]. The catalytic combustion of propane was used as example, but the method may be also attractive for bifurcation analyses with detailed surface kinetics [44-48].

Since the solution procedure did not require integration of any differential equation, the set of nonlinear algebraic equations that emerged could be solved with a standard numerical routine, thereby reducing considerably the required computation time. However, this simplified formulation is only applicable when the temperature is sufficiently low, so that homogeneous reactions become negligible.

A catalyst is often used also for the self-ignition of fuel/air mixtures. For instance, a catalytic Pt-based microdevice has been evaluated by Norton *et al.* [49] for the combustion of hydrogen and/or propane. The objective is the design of a microburner for portable applications.

The latter are usually conceived by downscaling conventional burners, but homogeneous combustion is easily quenched by confinement in small devices. In confined ceramic microchannels hydrogen/air mixtures self-ignite over a wide range of compositions and may help to light on propane/air mixtures. Propane kinetically inhibits hydrogen catalytic combustion at low hydrogen concentration and a minimum hydrogen concentration of 3.6 mol% is needed, irrespective of the propane/air composition. A two-stage ignition can occur under certain conditions, where hydrogen first ignites, followed by the ignition of propane.

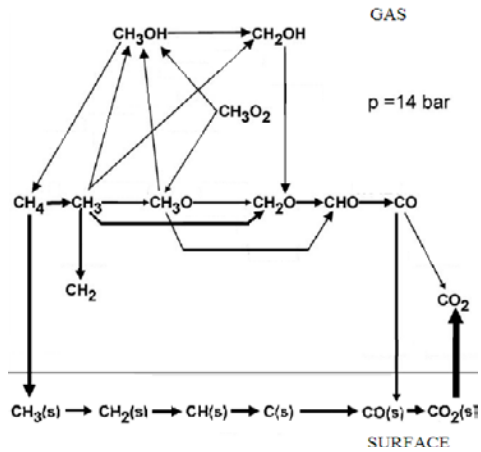

Figure 10. Reactions at the catalytic surface and in gas-phase in industrially relevant conditions [40].

The catalytic combustion of *n*-butane/air mixtures, in case diluted with N_2, on a platinum wire was studied by Oancea*et al.* [50]. The analyses can be carried out on an isothermally heated platinum wire in stagnant mixtures at various initial gas pressures and wire temperatures. The experimental setup allows the measurement of the heat flow rate during combustion, straightly related to the heterogeneous reaction rate. The heat flow rate, dQ_r/dt, of the surface reaction was measured under isothermal and isobaric conditions and the overall kinetic parameters were evaluated for both steady state and initial transient catalytic combustion. The catalytic combustion followed a first order kinetics with respect to *n*-butane, while the overall reaction order was around 0.37 within the pressure range investigated. To extend the analysis at higher temperatures, where the platinum wire melts during the ignition, the *n*-butane/air mixture was diluted with N_2. For diluted mixtures, at low total pressure, the temperature dependence of dQ_r/dt indicated an Arrhenius behavior in the 425-625°C temperature range. An anti-Arrhenius behavior was found at higher temperature, consistent with a diffusion-controlled process, accompanied by reactant depletion around the catalytic surface. A kinetic study of the catalytic combustion of stagnant *n*-butane/air mixtures on an isothermally heated platinum wire was undertaken to establish the effect of composition, total pressure and catalyst temperature [51]. The overall reaction order varied between 0.20 and 0.42 without an apparent dependence on fuel concentration or catalyst temperature. The reaction order with respect to *n*-butane was close to unit, while the reaction order with respect to oxygen was negative, around -0.16, indicating an inhibiting effect within this range of experimental conditions. The pressure dependence of the reaction rate was analysed using the empirical power law equation and two mechanistic kinetic models based on the LHHW approach, implying non-dissociative or dissociative oxygen adsorption. Both models were able to explain the quasi-hyperbolic reaction rate dependence on the total pressure. The overall activation energy obtained on the basis of Arrhenius equation was characteristic of a diffusion controlled process, while the pressure dependence of the reaction rate indicated a mixed control. A 2 wt% $Pd/Ce_xZr_{1-x}O_2$ catalyst was employed for a kinetic study [52]. The experiments were carried out in a continuous recycle reactor, operated under differential conditions. Twelve different possible rate equations, derived according to ER, LHHW and MvK approaches, were used to fit the experimental data (Table 5).

Table 5. Kinetic models used for the interpretation of methane combustion over Pd/ $Ce_xZr_{1-x}O_2$ catalyst [52]

model	equation
ER1	$R_{CH_4} = k_{sr}\frac{K_{O_2}p_{O_2}p_{CH_4}}{1 + K_{O_2}p_{O_2}}$
ER2	$R_{CH_4} = k_{sr}\frac{\sqrt{K_{O_2}p_{O_2}}p_{CH_4}}{1 + \sqrt{K_{O_2}p_{O_2}}}$
ER3	$R_{CH_4} = k_{sr}\frac{K_{O_2}^2p_{O_2}^2p_{CH_4}}{(1 + K_{O_2}p_{O_2})^2}$
ER4	$R_{CH_4} = k_{sr}\frac{K_{O_2}p_{O_2}p_{CH_4}}{(1 + \sqrt{K_{O_2}p_{O_2}})^2}$
LH1	$R_{CH_4} = k_{sr}\frac{K_{O_2}p_{O_2}K_{CH_4}p_{CH_4}}{(1 + K_{O_2}p_{O_2} + K_{CH_4}p_{CH_4})^2}$
LH2	$R_{CH_4} = k_{sr}\frac{\sqrt{K_{O_2}p_{O_2}}K_{CH_4}p_{CH_4}}{(1 + \sqrt{K_{O_2}p_{O_2}} + K_{CH_4}p_{CH_4})^2}$
LH3	$R_{CH_4} = k_{sr}\frac{K_{O_2}^2p_{O_2}^2K_{CH_4}p_{CH_4}}{(1 + K_{O_2}p_{O_2} + K_{CH_4}p_{CH_4})^3}$
LH4	$R_{CH_4} = k_{sr}\frac{K_{O_2}p_{O_2}K_{CH_4}p_{CH_4}}{(1 + \sqrt{K_{O_2}p_{O_2}} + K_{CH_4}p_{CH_4})^3}$
MvK1	$R_{CH_4} = \frac{k_1p_{O_2}k_2p_{CH_4}}{k_1p_{O_2} + 2k_2p_{CH_4}}$
MvK2	$R_{CH_4} = \frac{k_1\sqrt{p_{O_2}}k_2p_{CH_4}}{k_1\sqrt{p_{O_2}} + 2k_2p_{CH_4}}$
MvK3	$R_{CH_4} = \frac{k_1p_{O_2}k_2p_{CH_4}}{k_1p_{O_2} + 2k_2p_{CH_4}}\left(1 - \frac{k_1p_{O_2}}{k_1^*}\right)$
MvK4	$R_{CH_4} = \frac{k_1p_{O_2}k_2p_{CH_4}}{k_1p_{O_2} + 2k_2p_{CH_4} + \left(\frac{k_1k_2}{k_3}\right)p_{O_2}p_{CH_4}}$

Methane combustion over $Ce_{0.75}Zr_{0.25}O_2$ and $NiO/Ce_{0.75}Zr_{0.25}O_2$ catalysts was investigated also by Thaicharoensutcharitthame*t al.* [53] in the temperature range 300–800°C, using the initial rate method. The reaction order determined was in good agreement with a pseudo first order mechanism with respect to methane. The apparent activation energies for methane combustion were calculated as 63.10 ± 2.51 and 74.26 ± 2.40 kJ/mol, respectively.The catalytic combustion of methane has been studied over ceria, lanthana and their mixed oxides [54]. The combustion rate was approximately first order with respect to methane partial pressure, close to zeroth order for oxygen partial pressure and strongly inhibited by carbon dioxide. Lanthana in ceria seem to act synergistically since cerium is involved in a redox cycle responsible for methane oxidation, whereas lanthanum offers basic

sites for methane activation. By contrast, doping either ceria or lanthana with low amounts of the other oxide retards the reaction of CO oxidation [55]. The reaction was almost first-order with respect to CO over ceria, but over the lanthana-containing catalysts the order changed from positive to negative with increasing CO partial pressure. With all catalysts, the rate approached zeroth order with respect to oxygen. The catalytic combustion of methane/air mixtures over catalyst spheres was studied over specially designed burners, used as portable burners and IR emitters [56]. A study on the optimisation of the combustor geometry has been carried out, maximising combustion efficiency and optimising products distribution (*e.g.* minimum CO emission). The contribution of the surface reaction was found predominant in the chosen design and the surface temperature of the catalyst pellet could be enhanced by proper modulation of the fuel/air ratio. As an additional feature, the pellet can be used as emitter in the near infrared field.Experiments with a flat axisymmetric catalytic combustor operating with methane/air-mixtures at temperatures between 720 and 1020°C showed a spatio-temporal unstable behaviour of the surface temperature distribution [57]. Indeed, during combustion, transients may occur, during which at the catalytic surface spotwise dark zones appear. The position and the extent of the dark zones were not repeatable, indicating that their occurrence was not related with local deactivation of the catalyst. The appearance of the temperature inhomogeneity was also related with an unstable behaviour of the combustor itself. In the presence of dark spots, a small modification of the power or of the excess air ratio may lead to a sharp increase of the temperature, or also to a blowout of the burner. The possible thermal instability modes were analysed, so to determine the onset of such unstable combustion behaviour. This instability was supposed to exist, apart from the chemical kinetics instability effects.In addition to such instability phenomena, one should take into account the possible poisoning of the catalyst, in particular in the presence of sulphur containing compounds. The effect of the concentration of sulphur dioxide (15–65 ppm) and temperature (350–550°C) on the deactivation of a commercial Pd/Al_2O_3 catalyst used in the oxidation of methane has been studied by Ordóñez*et al.* [58]. It was observed that, although at a given temperature a common steady-state of constant methane conversion was attained at all sulphur dioxide concentrations, the deactivation rate increased as sulphur dioxide concentration in the feed increased. On the other hand, the deactivation rate decreased as temperature increased, the activity at steady state increasing as temperature increased. The behaviour of the system has been modelled on the basis of a pseudo-first-order mechanism with respect to methane. Catalyst deactivation was mainly caused by the formation of surface Pd sulphate, which is less active than Pd oxide. The rate of formation of Pd sulphate was considered to be first-order for both sulphur concentration and fraction of unsulphated Pd. A similar investigation on the effect of sulphur poisoning has been recently carried out on different catalytic systems, based on nanostructured mixed oxides of perovskitic structure. The selected poisoning agent was tetrahydrothiophene (THT), a common odoriser used in the natural gas grid, which quite immediately oxidised to CO_2, H_2O and SO_2. The latter remained more or less strongly adsorbed on the catalyst surface, depending on the reaction conditions and, most of all, on catalyst formulation. Among different compositions, the most resistant to poisoning showed $LaCoO_3$ and, mainly, $LaMnO_3$ samples [16]. The effect of partial substitution at the perovskite A site was also investigated, elucidating that Sr doping of manganite catalysts led to a very high catalyst stability even after prolonged poisoning. The possibility of doping with a very small amount of noble metals (0.5 wt% Pd or Pt) showed beneficial in some cases only, due to the possibility of regeneration of the catalyst by *in situ*

reduction. Silver doping was also tried on both cobaltites [17] and manganites [18], looking for a shielding action by Ag ions. This goal was not fully achieved, but the main advantage of Ag-doping was found in the strong improvement of the initial catalytic activity, leading to satisfactory conversion even after prolonged poisoning.The kinetics of methyl-ethyl-ketone oxidation (MEK) in air over bimetallic PdO_x(0–1 wt% Pd)–MnO_x(18 wt% Mn)/Al_2O_3 and the corresponding monometallic formulations was studied [59]. Monometallic Pd/Al_2O_3 was the most selective catalyst for complete oxidation, whereas the partial oxidation of MEK in the presence of manganese oxides was significant. The maximum yield for the partial oxidation products (acetaldehyde, methyl-vinyl-ketone and diacetyl) was always below 10%. Kinetic studies showed that the rates of CO_2 formation over PdO_x/Al_2O_3 were well fitted by a MvK kinetic expression and also by a LHHW model derived after considering the surface reaction between adsorbed MEK and oxygen as the rate-determining step. In the case of the Mn containing catalysts the MvK model provided the best fit. Irrespective of the model, the kinetic parameters for the bimetallic Pd–Mn catalysts lied between the values obtained for the monometallic samples, suggesting an additive rather than a cooperative effect between palladium and manganese active sites for MEK combustion.

The reaction kinetics of MEK catalytic combustion has been investigated also over Fe_2O_3 catalysts [60]. Data have been collected under quasi-differential conditions in a fixed bed reactor and a series–parallel reaction network (Figure 11) has been proposed. The LHHW mechanism with one type of active site over which adsorption of oxygen, MEK and carbon monoxide take place, fitted reasonably the experimental results, at the contrary of the MvK model. Moreover, the kinetic parameters so obtained were able to predict the performance of a Fe_2O_3 based catalytic membrane reactor.Au/γ-Al_2O_3 catalysts were tested for the catalytic combustion of light alcohols (methanol, ethanol, iso-propanol and *n*-propanol) [61]. The full conversion of a 2.0 g/m^3 methanol, ethanol, iso-propanol and *n*-propanol feed was achieved at 60, 155, 170 and 137°C, respectively, but they were completely mineralised into CO_2 and H_2O at *ca*. 70°C higher temperature in every case with the exception of methanol. In this latter case, the experimental data have been fitted with a *quasi*-first order reaction kinetics obtaining a value of apparent activation energy of 54.7 kJ/mol.The catalytic combustion of toluene, propylene and CO over Pt/Al_2O_3/Al catalyst was investigated by Shijie*et al*. [62]. Strong inhibition effects were observed when combusting the mixture. A reaction mechanism was proposed, with good agreement with the experimental data. The effects of VOC concentration and space velocity have been investigated, showing that lower inlet concentration and space velocity were beneficial to the efficiency of VOCs removal. The Langmuir adsorption model showed suitable in the investigation of catalytic combustion kinetics.

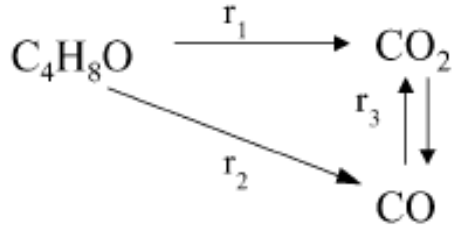

Figure 11. Generalised reaction scheme for MEK combustion [60].

The elementary steps required for catalytic combustion of dimethyl ether (DME) on Pt clusters supported on alumina or zirconia were determined by combining isotopic and kinetic analysis with density functional theory (DFT) estimates of activation energies and activation barriers to probe the lowest energy paths [63]. Reaction rates were limited by C-H bond activation in DME molecules adsorbed on oxygen atoms chemisorbed on Pt at near-saturation coverages. Reaction energies and activation barriers for C-H bond activation in DME to form methoxymethyl and hydroxyl surface intermediates showed that this step was more favorable than the activation of C-O bonds to form two methoxides. This kinetic preference was driven by the greater stability of the CH_3OCH_2* and OH* intermediates, with respect to chemisorbed methoxides. Experimental activation barriers on Pt clusters agreed with DFT-derived barriers on oxygen-covered Pt(111). Measured DME turnover rates increased with increasing DME pressure, but decreased as the O_2 pressure increased, because vacancies on Pt surfaces nearly saturated with chemisorbed oxygen were required for DME chemisorption. DFT calculations showed that, although these surface vacancies are required, higher oxygen coverages lead to lower C-H activation barriers, because the basicity of oxygen adatoms increases with coverage and they become more effective in hydrogen abstraction from DME. Water inhibited reaction rates via *quasi*-equilibrated adsorption on vacancies, consistent with DFT results indicating that water binds more strongly than DME on vacancies. Turnover rates also increased with Pt cluster size, because small clusters, with more coordinatively unsaturated surface atoms, bind oxygen atoms more strongly than larger ones and exhibit lower steady-state vacancies concentrations and a consequently smaller concentration of adsorbed DME intermediates involved in kinetically relevant steps.

Wave propagation fronts in the catalytic combustion of H_2 at low temperature were modeled with kinetic Monte Carlo simulations [64]. Such simulations constituted a direct validation of molecular models and of the proposed mechanisms using realistic parameters validated by means of experimental STM data. As the diffusion of water increased, both the front speed and width increased. While wave propagation was in qualitative agreement with experimental data for slow H_2O*diffusivities, fast Fickian diffusion of H_2O*led to sufficient mixing prior to reaction and lack of wave propagation. Intermolecular forces (attractive interactions) between adsorbates were critical for quantitative comparison with experiments at low temperature. Multiscale algorithms have been also extended to the catalytic combustion of H_2 in a CSTR. For this relatively complex reaction mechanism, in the absence of any adsorbate-adsorbate interactions, the continuum model based on a mean field approximation of surface processes yielded a good prediction of ignition conditions. However, under fuel-lean conditions and near extinction, where oxygen clusters form, significantly different predictions were observed depending on the surface model.

The effect of *intra*-phase diffusion for channel-flow oxidation reactors with washcoats has been investigated together with a detailed surface chemistry picture in the case of low-temperature (<200°C)H_2 oxidation over supported Pd/PdO_xcatalysts [65]. A numerical model of a porous catalyst washcoat was developed to assess how local conditions influence catalyst effectiveness when considering a detailed multi-step surface mechanism. This washcoat model has been integrated into a channel flow reactor model. The Pd–H_2–O_2 surface chemistry mechanism has been validated against experimental measurements in an annular flow reactor, implementing thermodynamically consistent interaction potentials of surface species and predicting non-linear behavior of conversion with respect to H_2 concentration. The catalytic washcoat model further indicated that conversion and catalyst effectiveness

were strongly dependent upon the site fractions of vacancies available for H_2 adsorption, which vary strongly in the porous washcoat with flow conditions and with depth at higher conversions. This leads to a hard development of simple models for catalyst washcoat effectiveness based upon any parameter such as a Thiele modulus.

Despite the success of adsorption and thermal incineration of chlorinated-VOC emissions, there is still a need for research on techniques which are both economically more sustainable and actually destroy these pollutants rather than merely remove them for recycling elsewhere in the biosphere. Their catalytic decomposition to CO_2, H_2O and HCl/Cl_2 appears very promising.

Transition metal oxide catalysts, in particular V_2O_5–WO_3/TiO_2 appear among the most active for the current application, available and studied with different reactor geometries (*e.g.* fixed pellet beds, honeycombs, coated metal fibers). The conversion of chlorinated-VOC by thermo-catalytic reactions is governed by both reaction kinetics and reaction equilibrium. A first-order rate equation is proposed for the Chlorinated-VOC oxidation reactions in a very extensive review on this topic [66]. The apparent rate constant was a combination of reaction kinetics and mass transfer effects, for which an estimation of the oxidation efficiencies has been also proposed. Mass transfer resistances were generally negligible for coated fibers reactors and fixed pellet beds, but can be of importance for honeycomb monoliths.

The experimental investigations demonstrate that: (*i*) conversion was independent of oxygen concentration, (*ii*) conversion was a first-order reaction with respect to the substrate, (*iii*) the oxidation proceeded to a higher extent with increasing temperature and (*iv*) multiple chlorine substitution enhanced the reactivity. The activation energy was related to the characteristics of the compound under examination and correlated in terms of its molecular weight. The Arrhenius pre-exponential factor *A* could be expressed in terms of the activation entropy.

The deep oxidation of tri-chloroethene in air, under dry or wet conditions, was studied over a 0.5 wt% Ru/Al_2O_3 catalyst [67] proposing a mechanism for the formation and removal of different intermediates (Figure 12). The authors suggest that the mechanism of the combustion reaction, involving a double-bond scission, was essentially specific for this catalyst and propose a pseudo-first order kinetic expression, providing fairly good fit of the experimental data.

A fundamental numerical method for simulating heat transfer and chemical reactions on surfaces was developed through a molecular dynamics simulation of the effects of adsorbates on surface reactions and energy transfer [68]. The simulation system chosen was the process of collision of oxygen molecules on a silver surface. The molecule–surface interaction was expressed, including the effects of surface temperature, by a London–Eyring–Polanyi–Sato potential energy surface. Ar, Kr, Xe and O_2 molecules constituted the typical adsorbates and their potential energies were modeled by Lennard–Jones functions.

Surface temperature and the characteristics of the adsorbates were taken into account with regard to the statistically averaged values of the surface reaction probability and energy transfer under varying initial conditions for an oxygen molecule and its target position on the surface. Even though the coverage of the adsorbates on the surface on a real molecular scale remained the same, the surface reaction probability and the average energy transfer changed, depending on the characteristics of the adherent molecules. When the adsorbates were highly mobile, absorbing much of the kinetic energy of a colliding oxygen molecule, their dynamic behavior enhanced the surface reaction probability and surface energy transfer in reflection.

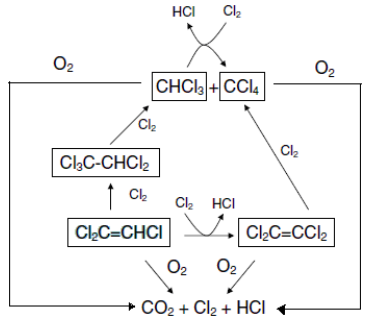

Figure 12. Proposed mechanism for trichloro-ethene combustion [67].

4. REACTOR DESIGN

The combustion of preheated lean homogeneous mixtures of hydrogen with methane in air in a Pt-based catalytic packed-bed reactor was modelled at atmospheric pressure [69]. A non-equilibrium 1-D model was developed employing multi-step surface and gas-phase reactions and accounting for the three modes of heat transfer within the bed, as well as for heat loss from the bed. The model could predict the effects of changes in operational conditions such as inlet mixture temperature, fuel composition and mixture equivalence ratio on methane and hydrogen conversions, as well as species concentrations and gas temperature profiles along the bed. Hydrogen was consumed completely in the early portion of the reactor length in all the cases considered, leading to an improving effect on methane conversion, especially at relatively low inlet temperature and for very lean mixtures. However, this effect diminished significantly with increasing inlet temperature and equivalence ratio.

The catalytic combustion of methane may be also coupled to endothermal reactions, such as the steam reforming of methane, in order to directly supply the reaction heat needed. This requires the design of an efficient heat exchange network, possible by proper reactor configuration.

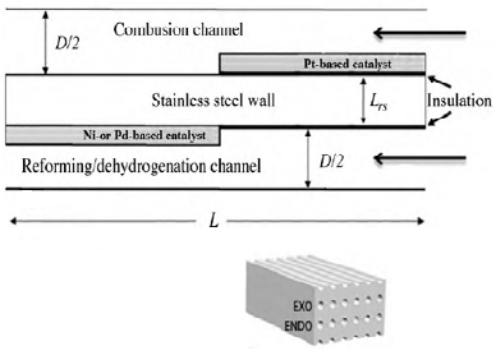

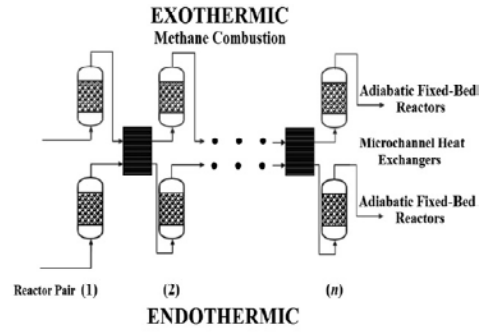

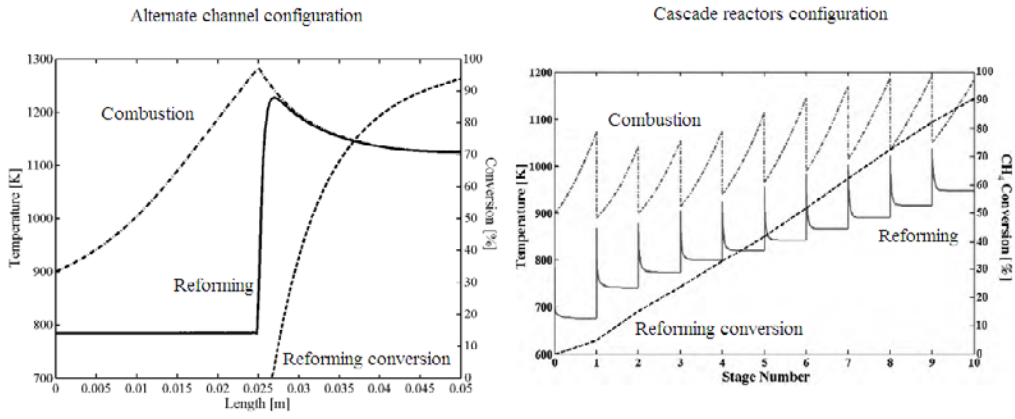

Figure 13. Steam reforming/catalytic combustion coupling in alternate channels reactor and in cascade reactors configuration. Readapted from [70,72].

Avci*et al*. [70] investigated methanol synthesis, with syngas produced in a microchannel reactor where both steam reforming and catalytic combustion of methane take place in alternate channels. Another example is the dehydrogenation of ethane to produce ethylene, whose reaction enthalpy is supplied by the catalytic combustion of CH_4 and a severe temperature control is required to avoid extensive coking. Reactor simulation was carried out for a parallel microchannel array and for a cascade reactor system in which the reaction occur in a series of beds and heat exchange in interconnecting microchannels is modelled through heat exchangers. Conversion was slightly higher in the microchannel system, but the advantages of better temperature control and easy replacement of deactivated catalyst favoured the cascade array (Figure 13). The enhancement of methane combustion in a microchannel reactor was attempted through catalyst segmentation and cavities [71]. The effects and combustion characteristics were evaluated using numerical simulation with detailed heterogeneous and homogeneous chemistry. Catalytic combustion represents a competition between heterogeneous and homogeneous reactions for fuel, oxygen and radicals. The pre-reaction of the heterogeneous step in an upstream catalyst segment can produce intermediate chemical radicals and catalytically induced exothermicity. The homogeneous reaction is subsequently induced in the cavity. Carbon monoxide was massively produced after the homogeneous reaction due to incomplete combustion. The downstream catalyst segments strongly deplete CO due to its high sticking coefficient on the platinum surface. Full methane conversion and complete combustion can thus be achieved in a short distance. Cavities can appreciably extend the stable operational range of a micro-reactor for a wide variety of inlet flows. Moreover, etching localised cavities in a small-scale system can further stabilise the flame and cavities could serve as the heat source for the reaction.

Table 6. Equations set and relative boundary conditions for 2-D modelling of microchannel reactors [72]

Fluid phase	
Equation of continuity	$\frac{\partial v_{xj}}{\partial x_j} + \frac{\partial v_{yj}}{\partial y_j} = 0$
Equation of motion	$\rho_{fj}\left(v_{xj}\frac{\partial v_{xj}}{\partial x_j} + v_{yj}\frac{\partial v_{xj}}{\partial y_j}\right) = -\frac{\partial p_j}{\partial x_j} + \mu_j\left[\frac{\partial^2 v_{xj}}{\partial x_j^2} + \frac{\partial^2 v_{xj}}{\partial y_j^2}\right]\rho_{fj}\left(v_{xj}\frac{\partial v_{yj}}{\partial x_j} + v_{yj}\frac{\partial v_{yj}}{\partial y_j}\right) = -\frac{\partial p_j}{\partial y_j} + \mu_j\left[\frac{\partial^2 v_{yj}}{\partial x_j^2} + \frac{\partial^2 v_{yj}}{\partial y_j^2}\right]$
Equation of species continuity	$v_{xj}\frac{\partial c_{ij}}{\partial x_j} + v_{yj}\frac{\partial c_{ij}}{\partial y_j} = D_{AB}\left[\frac{\partial^2 c_{ij}}{\partial x_j^2} + \frac{\partial^2 c_{ij}}{\partial y_j^2}\right]$
Equation of energy	$\rho_{fj}C_{pf,j}\left(v_{xj}\frac{\partial T_j}{\partial x_j} + v_{yj}\frac{\partial T_j}{\partial y_j}\right) = \lambda_{fj}\left[\frac{\partial^2 T_j}{\partial x_j^2} + \frac{\partial^2 T_j}{\partial y_j^2}\right]$
Washcoat phase	
Equation of continuity	$\frac{\partial v_{xj}}{\partial x_j} + \frac{\partial v_{yj}}{\partial y_j} = 0$
Equation of motion	$\left(\frac{\mu_j}{\kappa}\right)v_{xj} = -\frac{\partial p_j}{\partial x_j} + \left(\frac{\mu_j}{\varepsilon_p}\right)\left[\frac{\partial^2 v_{xj}}{\partial x_j^2} + \frac{\partial^2 v_{xj}}{\partial y_j^2}\right]\left(\frac{\mu_j}{\kappa}\right)v_{yj} = -\frac{\partial p_j}{\partial y_j} + \left(\frac{\mu_j}{\varepsilon_p}\right)\left[\frac{\partial^2 v_{yj}}{\partial x_j^2} + \frac{\partial^2 v_{yj}}{\partial y_j^2}\right]$
Equation of species continuity	$v_{xj}\frac{\partial c_{ij}}{\partial x_j} + v_{yj}\frac{\partial c_{ij}}{\partial y_j} = D_{AB,eff}\left[\frac{\partial^2 c_{ij}}{\partial x_j^2} + \frac{\partial^2 c_{ij}}{\partial y_j^2}\right] - \rho_s R_{ij}(c_{ij}, T_j)$
Equation of energy	$\rho_{sj}C_{ps,j}\left(v_{xj}\frac{\partial T_j}{\partial x_j} + v_{yj}\frac{\partial T_j}{\partial y_j}\right) = \lambda_{j,eff}\left[\frac{\partial^2 T_j}{\partial x_j^2} + \frac{\partial^2 T_j}{\partial y_j^2}\right] + \rho_{sj}\sum_{k=1}^{N}(-\Delta H_k)(-r_k(c_{ij}, T_j))$
Solid phase	
Equation of energy	$\lambda_w\left[\frac{\partial^2 T_w}{\partial x^2} + \frac{\partial^2 T_w}{\partial y_w^2}\right] = 0$

j – Channel or washcoat
1. Combustion
2. Steam reforming

i – Species
$i_{(j=1)}$: CH_4, O_2, H_2O, CO_2, N_2
$i_{(j=2)}$: C_7H_{16}, H_2O, CO, CO_2, H_2, CH_4

Boundary conditions

1. Channel entrance: $x_j = L$ (for COMB), $x_j = 0$ (for SR); $\forall y_j$

   $U_j = U_j^{in}$
   $c_{ij} = c_{ij}^{in}$
   $T_j = T_j^{in}$
2. Symmetry at the centerline:
   $\forall x_j$; $y_j = 0$ (for SR), $y_j = H + L_w$ (for COMB)

   $\mathbf{n}\cdot\mathbf{v}_j = 0$
   $\mathbf{n}\cdot(-D_{AB}\nabla c_{ij} + \mathbf{v}_j c_{ij}) = 0$
   $\mathbf{n}\cdot(-\lambda_f\nabla T_j + \mathbf{v}_j\rho_{fj}C_{pf,j}T_j) = 0$
3. Along the fluid–solid wall interface:
   $\forall x_j$; $y_j = H/2 + \delta_s$ (for SR), $y_j = H/2 + \delta_s + L_w$ (for COMB)

   $\mathbf{n}\cdot\mathbf{v}_j = 0$
   $\mathbf{n}\cdot(-D_{AB}\nabla c_{ij} + \mathbf{v}_j c_{ij}) = 0$
   $\mathbf{n}\cdot(-\lambda_w\nabla T_w) = \mathbf{n}\cdot(-\lambda_f\nabla T_j + \mathbf{v}_j\rho_{fj}C_{pf,j}T_j)$
4. Channel exit: $x_j = 0$ (for COMB), $x_j = L$ (for SR); $\forall y_j$

   $p_j = p_j^{out}$
   $\mathbf{n}\cdot(-D_{AB}\nabla c_{ij}) = 0$
   $\mathbf{n}\cdot(-\lambda_f\nabla T_j) = 0$
5. Solid boundaries: $x = 0$ and $x = L$; $\forall y_w$

   $\mathbf{n}\cdot(-\lambda_w\nabla T_w) = 0$

Two compact reformer configurations in the context of H_2 production in a fuel processing system for a Proton Exchange Membrane Fuel Cell (PEMFC) have been compared using computer-based modelling techniques [72]. H_2 was produced via catalytic steam reforming of *n*-heptane and the heat required was supplied by catalytic combustion of CH_4. The combination of both reactions was modelled for a microchannel reactor configuration (Table 6) in which reactions and heat transfer take place in parallel, micro-sized flow paths with wall-coated catalysts and for a cascade reactor configuration, in which reactions occur in a series of adiabatic packed-beds, heat exchange in interconnecting microchannel heat exchangers being used to maintain the desired temperature. Size and efficiency of the fuel processor consisting of the reformer, hydrogen clean-up units and heat exchange peripherals were estimated for either the use of a microchannel or a cascade configuration in the reforming step. The cascade system also offers advanced temperature control and ease of catalyst replacement.

The performance of a gasoline steam reformer with facing catalytic burner and reformer, both based on the microchannel concept was modeled and then compared with a reference catalytic SR reactor facing, as heat source, a microchannel heat exchanger, fed with the flue gases from an external burner [73].

Reactions in the catalytic reformer and the catalytic burner occurred heterogeneously on Pt-CeO_2 catalysts. Simulation results showed that the integrated burner-reformer microchannel reactor was able to transfer heat from the hot to the cold side very efficiently, thus enabling high compactness. However, the best design conceived (the catalytic burner facing the reformer microchannel) showed mass-transfer limitations inside the combustion catalyst layer, because of the low values of the effective diffusion inside the solid catalytic phase. As a consequence, there was not an "ignited" condition in the catalytic burner (confirmed by the lack of peaks in the temperature profile), but a diffuse heat generation along the microchannel length. This condition involved a longer reformer start-up, but at the same time allowed to limit the temperature increase in the catalyst solid layer, preserving its activity and stability.

The same concept was applied to methane steam reforming using fundamental chemical kinetics in a pseudo-2-D microreactor model coupled with methane catalytic combustion [74] and later extended to methanol [75]. The microreactor allowed millisecond or lower contact times and proper balancing of flow rates can give high conversions, reasonably high temperatures and high yield to syngas. Furthermore, tuning catalyst surface area and internal and external mass and heat transfer through reactor sizing can lead to further process intensification.

A $LaFe_{0.5}Mg_{0.5}O_3/Al_2O_3$/FeCrAl metallic monolith catalyst for the catalytic combustion of methane and an Ni/SBA-15/Al_2O_3/FeCrAl metallic monolith catalyst for the endothermic reforming of methane with CO_2 have been also studied [76].

A micro methanol reformer for portable fuel cell applications has been proposed by T. Kim [77]. Cu/ZnO was selected as steam reforming catalyst and Pt was used for the catalytic combustion of hydrogen with air. The performance of the reformer was analysed under various conditions and the results showed a good agreement with a 3-D model of the reacting flow. Considering the energy balance of the reformer/combustor model, the exhaust gas of the fuel cell could be recycled as a feed to the combustor. The conversion of methanol was 95.7%, producing a hydrogen flow of 53.7 ml/min (with 1.24% CO). The reformate flow was sufficient to operate a 4.5W PEMFC.

A packed bed and a micro-channel reactor for methanol catalytic combustion over Pt/Al_2O_3 catalysts were also compared [78]. The results showed better performance for the micro-channel system, though the sealed pad creating free space detrimentally affected the efficiency of methanol catalytic combustion. Temperature profiles by IR imaging on the micro-channel plate were also provided.

A monolithic reactor washcoated with 1 wt% Pt/γ-Al_2O_3 (catalyst loading 15 wt%) has been tested at high pressure (5-16 bar) for the catalytic combustion of synthetic gasified biomass [79]. A 2-D boundary layer model was applied successfully to a single channel of the monolith. At constant inlet velocity to the monolith the combustion efficiency decreased with increasing pressure. A multi-step surface mechanism predicted that the flow of CO_2 and H_2O from the surface increased with pressure. However, as the pressure increased, unreacted gas near the center of the channel penetrated significantly longer into the channel compared to lower pressures. Conversion of hydrogen and carbon monoxide were diffusion limited after ignition, while methane never ignited and was kinetically controlled. According to the kinetic model, surface coverage of major species changed from CO, H and CO_2 before ignition to O, OH, CO_2 and free surface sites after ignition. The model predicted further that combustion efficiency increases with increasing pressure at constant mass flow.

The combustion of liquid fuels in a catalytic micro-combustor is an attractive alternative to batteries. An evaporation model was developed to calculate the minimum distance required for complete droplet evaporation, in view of the miniaturisation of the combustion device [80]. By increasing the temperature from r.t. to 77°C, the distance required for complete evaporation of a 6.5 μm droplet decreased from 3.5 to 0.15 cm. A series of tests was carried out on a Pt mesh, leading to 75% conversion of ethanol. By contrast, 100% conversion of ethanol and 95% of 1-butanol under fuel lean conditions have been achieved on a Rh-coated alumina foam. An interesting feature is that, by tuning the equivalence ratio, the same device can combust completely the fuel for thermoelectric applications, operate as a fuel reformer to produce H_2 for fuel cells or perform as a bio-refinery for paraffin and olefin synthesis.

A pseudo-2-D model has been developed to analyse platinum-catalysed microburners for lean propane/air combustion [81]. Comparison with computational fluid dynamics (CFD) simulations revealed that the transverse heat and mass transfer was reasonably captured using constant values of Nusselt and Sherwood numbers. The transverse heat and mass transport strongly depended on the inlet flow rate and the thermal conductivity of the burner solid structure. The microburner was surface reaction limited at very low velocities and mass transfer limited at high velocities. At intermediate range of velocities, mass transfer strongly affected the microburner performance at low wall conductivities, whereas transverse heat transfer affected stability under most conditions and had a greater influence at high wall conductivities. At sufficiently low flow rates, complete fuel conversion occurred and reactor size had a slight effect on conversion and temperature. By contrast, for fast flows propane conversion strongly depended on residence time. Comparison to homogeneous burners was also presented.

CFD may be a useful tool for the development of 3-D models of monolith channels, able to predict different ignition behaviors with respect to 2-D models [82]. The sensitivity analysis of the importance of chemical kinetics relative to mass transport suggested the need of a better description of surface reaction mechanism, even if the simulated data are not under chemical control only. A parameter-fitting procedure for kinetic studies based on the detailed 3-D, segmented CFD model, was also developed and successfully tested for modelling

inhibition by water. However, CFD modelling of full-scale catalytic converters with realistic chemistry remained elusive, primarily due to the extreme computational requirements. A new low-memory coupled implicit solver, based on the conservative unstructured finite-volume method, was used to simulate lab-scale methane/air catalytic combustors with implicit coupling between fluid flow, heat transfer, mass transfer and heterogeneous chemical reactions. The complexity of the surface reaction mechanism dominated the overall CPU time requirements [83].

A monolithic adsorption reactor has been used for cyclic VOC abatement [84]. In the first step the pollutants were adsorbed and subsequently desorbed/reacted. After attaining the desired concentration of adsorbed VOC, air was fed to the reactor, leading to exothermal combustion, which increased the surface temperature, so causing the desorption of reaction products. The combination of the exothermal combustion and endothermal desorption offered a much better temperature control, preventing any thermal runaway even at high VOC concentration. A 2-D mathematical model has been proposed, accounting for both adsorption and reaction, taking into account mass trasfer limited adsorption kinetics and non linear adsorption equilibria.

Structured metallic short-channel reactors of various geometries may be used as an alternative to ceramic monoliths. Catalyst testing and reactor structure modelling are presented in [85], including mass transfer limitations and models for the quantification of the relevant dimensionless numbers. It was expected that mass transfer coefficients for laminar flow partially developing in short channels could be increased up to 10 times comparing to standard monoliths, but the increased transfer properties involved elevated pressure drop. Performance evaluation criteria have been developed to properly estimate the structure performance. The criteria derived covered both the general case for comparable mass transport and kinetics and the restricted case of diffusional limitations of the process. In comparison with monoliths, the best structures (sinusoidal and triangular) seem to be from 1.5 times up to 4 times more efficient. Chromium–aluminium (CrAl) steel was surveyed in terms of its applicability for carrier manufacturing and catalyst deposition. Catalytic tests were carried out for the combustion of diluted *n*-hexane, with 100% selectivity to CO_2.

Large amounts of methane are discharged into the atmosphere with mine ventilation air. A single ventilation shaft can emit over 500,000 m^3(STP)/h of ventilation air in which methane content can be as high as 1 vol%. The abatement of this huge emission is therefore important from both the economic and the environmental points of view, also allowing energy recovery. Due to very low CH_4 concentration, the most promising solution seems to be autothermal combustion in reverse-flow reactors. A comparison between a thermal flow-reversal reactor (TFRR) and a catalytic flow-reversal reactor (CFRR), equipped with a monolithic or pellettised catalyst, has been carried out by Gosiewski*et al.* [86]. Complete combustion was expected above 750°C, but heat accumulation in the reverse-flow reactor led to a much higher maximum temperature. However, for optimised process parameters the maximum temperature for the thermal combustion of coalmine ventilation air did not exceed 1200°C, *ca.*400 °C higher than for the CFRR with a Pd catalyst. Such a temperature is poorly acceptable from the standpoint of the formation of NO_x. It is important to equip both types of reactor with a control system able to protect them either against extinguishing when CH_4 concentration is very low, or against too high temperature when the concentration is high. The basic question is whether the cost of more expensive materials of construction for the TFRR does not exceed the cost of the expensive catalyst in the CFRR. On the other hand, the

analysis should take into account the fact that, due to the higher temperature of the hot gas withdrawn from the TFRR, the efficiency of heat recovery should also be higher.

Reverse flow reactors were applied also to the combustion of lean mixtures of aliphatic and aromatic hydrocarbons (hexane and toluene) in air over a commercial Pt/Al_2O_3 catalyst [87]. The investigation has been carried out both experimentally, in a bench-scale unit, and by simulations, using a heterogeneous 1-D dynamic model. The reactor performance was mainly determined by the combustion enthalpy and reactivity of the reactants: increasing total concentration and increasing the fraction of toluene (the most reactive compound) led to more stable operation. The model was later generalised to different substrates [88].

Fluidised-bed combustion of premixed lean methane/air and propane/air mixtures over a copper-based catalyst has been studied [89,90]. Combustion experiments have been performed in a 0.10 m fluidised-bed reactor with unexpanded bed heights of 0.10 and 0.20 m. The influence of temperature, gas velocity and catalyst loading on fuel conversion have been assessed. A model of the fluidised-bed combustor has been also developed, based on the two-phase fluidisation theory. The cooperative role of intrinsic kinetics and of intraparticle and interphase (bubble-to-emulsion phase, emulsion phase–to–catalyst particle) diffusional resistances was taken into account.

Catalytic combustion of methane was also studied over Pd and $Pt/SiO_2/\alpha\text{-}Al_2O_3$ membranes [91] with reactants fed at opposite membrane sides. In order to improve reactor controllability, the Al_2O_3 membranes were impregnated with a SiO_2 sol, to decrease pore size. Methane conversion up to 100% for the palladium membrane and only up to 42% for the platinum membrane were achieved. A transition from kinetic to mass transfer control within the temperature range investigated was also shown.

The performance of a perovskite hollow fibre membrane reactor for the catalytic combustion of methane was studied by Tan *et al*. [92]. The ionic–electronic $La_{0.6}Sr_{0.4}Co_{0.2}Fe_{0.8}O_{3-\delta}$ mixed conductor, in the form of an oxygen-permeable hollow fibre membrane, has been prepared by means of a phase-inversion spinning/sintering technique. A mathematical model combining the local oxygen permeation rate with approximate catalytic reaction kinetics has been developed. The effects of operating temperature and methane and air feed flow rates on the performance of the membrane have been investigated both experimentally and theoretically. Both methane conversion and oxygen permeation rate can be improved by coating platinum on the air side of the hollow fibre membranes.

A counterdiffusive radiant heater was used for the combustion of methane and VOCs [93]. When increasing natural gas feed rate the conversion dropped, due to a lack of oxygen for combustion. It was found that the presence of water did not significantly impact catalytic activity when added as a vapour and when other hydrocarbons were present in the feed stream. Complete hydrocarbon conversion could be achieved by satisfying the oxygen demand.

Finally, in order to abate diesel soot particles, many catalysts have been studied. However, the comparison of kinetic data is not straightforward, due to the different experimental conditions used in the activity measurement of the various research groups. Temperature-programmed analysis is the most common technique used to determine catalytic activity for soot oxidation. For a given catalyst, the temperature-programmed oxidation profile depends on variables such as heating rate, oxygen partial pressure, gas flow rate, catalyst/soot weight ratio, contact mode between catalyst and soot and existence of energy and/or mass transfer limitations during the analysis. A systematic study of the influence of all

these testing variables on the TPO profile and the optimum testing conditions to obtain good reproducibility during the kinetic study was presented by Peralta *et al*. [94].

CONCLUSIONS

The catalytic combustion of organic substrates finds application in many fields. Some commercial or semi-commercial processes are yet available for VOCs abatement or for energy conversion in GT plants. Different catalyst formulations may be used, based on noble or transition metals. The assessment of a detailed mechanism for the interpretation of kinetic data is still controversial, mainly depending on catalyst formulation and on the operating conditions. Different reactor configurations may be adopted, among which the annular one seems suitable for the collection of kinetic data under commercially relevant conditions. By contrast, monolith supported systems seem the most used and CFD modelling in catalyst channels is in an advanced development stage. Nevertheless, due to non standard reactor configuration, its design should be developed together with the progressive catalyst refining.

REFERENCES

[1] WMO Greenhouse Gas Bullettin, World Meteorological Organization, no. 5 (2009), available online at http://www.wmo.int/gaw/
[2] "Climate Change 2007: Synthesis Report", IPCC Plenary XXVII,Valencia, Spain, 12-17 November 2007.
[3] UNStatisticsDivision, http://data.un.org
[4] http://www.eia.doe.gov/oiaf/forecasting.html
[5] http://www.eia.doe.gov/
[6] D. Ciuparu, M. R. Lyubovsky, E. Altman, L. D. Pfefferle, A. Datye, *Catal. Rev*., 44(4) (2002) 593.
[7] Y. Zeldovich, *J. Phys*. (U.S.S.R.), 10 (1946) 321.
[8] http://www.energy.ca.gov/pier/energy_update/2002-08_FACTSHEET_CATALYTIC.PDF
[9] S. Cocchi, R. Modi, G. Nutini, M.J. Spencer, G.N. Sarento, in "*CatalyticCombustion*", P. Forzatti, G. Groppi, P. Ciambelli, D. Sannino, Eds., Polipress, Milano, Vol.1, 2005, p. 27.
[10] "Oxide nanomaterials for the catalytic combustion of hydrocarbons ", I. Rossetti and L. Forni, in "*Synthesis, Properties and Applications of Oxide Nanomaterials*", J.A. Rodrìguez and M. Fernàndez-Garcìa, Eds., Wiley, 2007, p.563-602.
[11] P. Gélin, M. Primet, *Appl. Catal. B: Environmental*, 39 (2002) 1.
[12] G. Centi, *J.Molec. Catal. A: Chemical*, 173 (2001) 287.
[13] M. Machida, K.Eguchi, H. Arai, *J. Catal*., 123 (1990) 477.
[14] G. Groppi, M. Bellotto, C. Cristiani, P. Forzatti, P.L. Villa, *Appl. Catal. A: General*, 104 (1993) 101.
[15] J. Wang, Z. Tian, J. Xu, Y. Xu, Z. Xu, L. Lin, *Catal. Today*, 83 (2003) 213.

[16] I.Rossetti, O. Buchneva, C. Biffi and R. Rizza, *Appl. Catal. B: Environmental*, 89 (2009) 383.
[17] O.Buchneva, I.Rossetti, C. Biffi, M. Allieta, A. Kryukov, N. Lebedeva, *Appl. Catal. A: General,* 370 (2009) 24.
[18] O.Buchneva, I. Rossetti, C. Oliva, M. Scavini, S. Cappelli, B. Sironi, M. Allieta, A. Kryukov, L. Forni, *J. Mater. Chem*., 20 (2010) 10021.
[19] http://media.defenseindustrydaily.com
[20] http://www.utpb.edu
[21] "*Technology characterization: gas turbines*", EPA document, December 2008.
[22] "NOx Control Technologies. Catalytica Combustion Systems, Inc. XononTM Flameless Combustion System", Environemtal Technology Verification Report, MRI, RTI, December 2000.
[23] R. Carroni, T.Griffin, *Catal. Today*, 105 (2010) 2.
[24] A. Buekens, "Thermal and Catalytic Combustion", in Pollution Control Technologies, B. Nath and G.St. Cholakov, Eds.], in *Encyclopedia of Life Support Systems* (EOLSS), 2005.
[25] www.topsoe.com
[26] K. Herbst, G. Mogensen, F. Huber, M. Østberg, M. S. Skjøth-Rasmussen, *Catal. Today*, 157 (2010) 297.
[27] G. Zhu, J. Han, D.Y. Zemlyanov, F.H. Ribeiro, *J. Amer. Chem. Soc*., 126 (2004) 9896.
[28] R. Carroni, T. Griffin, J. Mantzaras, M. Reinke, *Catal. Today*, 83 (2003) 157.
[29] J. Cortés, E. Valencia, P. Araya, *Catal. Lett*., 112 (2006) 121.
[30] G. Groppi, *Catal. Today*, 77 (2003) 335.
[31] W. Ibashi, G. Groppi, P. Forzatti, *Catal. Today*, 83 (2003) 115.
[32] C. Muller, M. Maciejewski, R. Koeppel, R. Tschan, A. Baiker, *J. Phys. Chem*., 100 (1996) 20006.
[33] C. Muller, M. Maciejewski, R. Koeppel, A. Baiker, *Catal. Today*, 47 (1999) 245.
[34] D. Ciuparu, E. Altman, L. Pfefferle, *J. Catal*., 203 (2001) 64.
[35] A.Machocki, M. Rotko, B. Stasinska, *Catal. Today*, 137 (2008) 312.
[36] S. Seimanides, M. Stoukides, *J. Catal*., 98 (1986) 540.
[37] C.F. Cullis, B.M. Willatt, *J. Catal*., 83 (1983) 267.
[38] J.H. Lee, D.L. Trimm, *Fuel Process. Technol*., 42 (1995) 339.
[39] E. Kanezaki, S. Tanaka, K.I. Murai, T. Moriga, J. Motonaka, M. Katoh, I. Nakabayashi, *Anal. Sci*., 20 (2004) 1069.
[40] J. Mantzaras, *Catal. Today*,117 (2006) 394.
[41] J.D. Mellado, M. Kindelàn, A.L. Sànchez, Combust. *Flame*, 132 (2003) 596.
[42] X. Song, W.R. Williams, L.D. Schmidt, R. Aris, Combust. *Flame*, 84 (1991) 292.
[43] H. Ikeda, P.A. Libby, F.A. Williams, Combust. *Flame*, 93 (1993) 138.
[44] D.G. Vlachos, P.-A. *Bui, Surf. Sci*., 364 (1996) L625.
[45] O. Deutschmann, R. Schmidt, F. Behrendt, J. Warnatz, *Proc. Comb. Inst*., 26 (1996) 1747.
[46] Y.K. Park, P.-A. Bui, D.G. Vlachos, *A.I.Ch.E. J*., 44 (1998) 2035.
[47] N.E. Fernandes, Y.K. Park, D.G. Vlachos, Combust. *Flame*,118 (1999) 164.
[48] C. Treviño, J.C. Prince, *Surf. Sci*., 449 (2000) 61.
[49] D.G. Norton, D.G. Vlachos, *Proc. Comb. Inst*., 30 (2005) 2473.
[50] D. Oancea, O. Staicu, V. Munteanu, D. Razus, *Catal. Lett*. 121 (2008) 247.

[51] O. Staicu, V. Munteanu, D. Oancea, *Catal. Lett*., 129 (2009) 124.
[52] S. Specchia, F. Conti, V. Specchia, *Ind. Eng. Chem. Res*.,49 (2010) 11101.
[53] S. Thaicharoensutcharittham, V. Meeyoo, B. Kitiyanan, P. Rangsunvigit, T. Rirksomboon, *Catal. Commun*., 10 (2009) 673.
[54] M.F. Wilkes, P. Hayden, A.K. Bhattacharya, *J. Catal*., 219 (2003) 286.
[55] M.F. Wilkes, P. Hayden, A.K. Bhattacharya, *J. Catal*., 219 (2003) 295.
[56] G. Ohmura, T. Keida, T. Seo, C. Ahn, F. Akamatsu, M. Shibahara, *J. Themal Sci. Technol*., 4 (2009) 453.
[57] G. Capitaine, *Inter. J. Heat and Mass Transfer*, 46 (2003) 3927.
[58] S. Ordóñez, P. Hurtado, H. Sastre, F.V. Dìez, *Appl. Catal. A: General*, 259 (2004) 41.
[59] G. Arzamendi, V.A. de la Peña O'Shea, M.C. Álvarez-Galván, J.L.G. Fierro, P.L. Arias, L.M. Gandía, *J. Catal*., 261 (2009) 50.
[60] G. Picasso Escobar, A. Quintilla Beroy, M.P. Pina Iritia, J. Herguido Huerta, *Chem. Eng. J*., 102 (2004) 107.
[61] Q. Deng, X.-m. Li, Z.-s. Peng, Y.-f. Long, L.-m. Xiang, T.-j. Cai, *Trans. Nonferrous Met. Soc. China*, 20 (2010) 437.
[62] L. Shijie, Y. Weiyong, F. Dingye, K. Hideo, *React.Kinet.Catal.Lett*. 85 (2005) 205.
[63] A. Ishikawa, M. Neurock, E.Iglesia, *J. Amer. Chem. Soc*., 129 (2007) 13201.
[64] S. Raimondeau, D. G. Vlachos, *Chem. Eng. Sci.,* 58 (2003) 657.
[65] S.-A. Seyed-Reihani, G.S. Jackson, *Chem. Eng. Sci*., 59 (2004) 5937.
[66] K. Everaert, J. Baeyens, *J. of Hazardous Materials*, B109 (2004) 113.
[67] B. Miranda, E. Dìaz, S. Ordòñez, F.V. Dìez, *Catal. Commun*., 7 (2006) 945.
[68] M. Shibahara, M. Katsuki, *Combust.Flame*, 144 (2006) 17.
[69] S.A. Shahamiri, I. Wierzba, *Int. J. Hydrogen Energy*, 34 (2009) 5785.
[70] A.K. Avci, D.L. Trimm, M. Karakaya, *Catal. Today*, 155 (2010) 66.
[71] Y.-H. Li, G.-B. Chen, H.-W. Hsu, Y.-C. Chao, *Chem. Eng. J*., 160 (2010) 715.
[72] M. Karakaya, A.K. Avci, *Int. J. Hydrogen Energy*, 35 (2010) 2305.
[73] G.A.Petrachi, G. Negro, S. Specchia, G. Saracco, P.L. Maffettone, V. Specchia, *Ind. Eng. Chem. Res*., 44 (2005) 9422.
[74] G.D. Stefanidis, D.G. Vlachos, *Chem. Eng. Technol*.,31 (2008) 1201.
[75] G.D.Stefanidis, D.G. Vlachos, *Chem. Eng. Sci*., 64 (2009) 4856.
[76] F. Yin, S. Ji, H. Mei, Z. Zhou, C. Li, *Chem. Eng. J*., 155 (2009) 285.
[77] T. Kim, *Int. J. Hydrogen Energy*, 34 (2009) 6790.
[78] C.-H. Leu, S.-C. King, C.-C. Chen, J.-M. Huang, S.-S. Tzeng, I-H. Liu, W.-C. Chang, *Appl. Catal. A: General*, 382 (2010) 43.
[79] J.C.G. Andrae, D. Johansson, M. Bursell, R. Fakhrai, J. Jayasuriya, A. Manrique Carrera, *Appl. Catal. A: General*, 293 (2005) 129.
[80] D.A. Behrens, I.C. Lee, C.M. Waits, *Journal of Power Sources*, 195 (2010) 2008.
[81] N.S. Kaisare, S.R. Deshmukh, D.G. Vlachos, *Chem. Eng. Sci*., 63 (2008) 1098.
[82] P. Canu, S. Vecchi, *A.I.Ch.E. J*., 48 (2002) 2921.
[83] A. Kumar, S. Mazumder, *Computers and Chemical Engineering*, 34 (2010) 135.
[84] M.A. Kolade, A. Kogelbauer, E. Alpay, *Chem. Eng. Sci*., 64 (2009) 1167.
[85] A. Kołodziej, J. Łojewska, *Chemical Engineering and Processing*, 46 (2007) 637.
[86] K. Gosiewski, Y.Sh. Matros, K. Warmuzinski, M. Jaschik, M. Tanczyk, *Chem. Eng. Sci*., 63 (2008) 5010.
[87] P. Marín, S. Ordóñez, F.V. Díez, *Chem. Eng. Sci*., 63 (2008) 5003.

[88] P. Marín, S. Ordóñez, F.V. Díez, *J. Chem. Technol. Biotechnol*., 84 (2009) 1292.
[89] M. Iamarino, P. Salatino, R. Chirone, R. Pirone, G. Russo, *Proc. Comb. Inst*., .29 (2002) 827.
[90] M. Iamarino, P. Ammendola, R. Chirone, R. Pirone, G. Ruoppolo, G. Russo, *Ind. Eng. Chem. Re*s., 45 (2006)1009.
[91] M. Murru, A. Gavriilidis, *Chem. Eng. J*., 100 (2004) 23.
[92] X. Tan, K. Li, A. Thursfield, I.S. Metcalfe, *Catal. Today*, 131 (2008) 292.
[93] N. Jodeiri, L. Wu, J. Mmbaga, R.E. Hayes, S.E. Wanke, *Catal. Today*, 155 (2010) 147.
[94] M.A.Peralta, M.S. Gross, B.S. Sánchez, C.A. Querini, *Chem. Eng. J*., 152 (2009) 234.

In: Catalytic Combustion
Editor: Sophie A. Cottilard, pp. 173-188
ISBN: 978-1-61324-279-7

Chapter 5

CATALYTIC COMBUSTION OF METHANE OVER CERIA-ZIRCONIA CATALYSTS

S. A. Larrondo[1,*] and M. G. Zimicz[2]

[1]Departamento de Ingeniería Química, Facultad de Ingeniería Universidad de Buenos Aires, Pabellón de Industrias, Ciudad Universitaria, (1428) Buenos Aires, Argentina
[2]CINSO (Centro de Investigaciones en Sólidos) CONICET-CITEFA J.B. de La Salle 4397, (1603) Villa Martelli, Pcia. de Buenos Aires, Argentina

ABSTRACT

The energy production by combustion of methane or natural gas in gas turbines and burners constitutes a well-developed technology. However, due to the fact that methane is a hydrocarbon molecule difficult to oxidize, the homogeneous combustion with air occurs in flames with very high temperatures. These high temperatures thermodynamically favor the formation of nitrogen oxides (NO_x), which constitutes the "photochemical smog", harmful to aquatic and terrestrial ecosystems and to human health.

In recent years, global concern about the rapid increase in emissions of gaseous pollutants and greenhouse gases caused by the growth in energy demand has been growing. Under the Kyoto protocol, the reductions of hydrocarbons, carbon dioxide (CO_2) and NO_x emissions, and the increase of combustion efficiency, especially in the case of methane and natural gas, have become a central research topic.

The catalytic combustion of methane emerges as a possible solution due to its advantages over the homogeneous combustion. The presence of a catalyst facilitates the total oxidation of methane and, moreover, a suitable catalyst will promote the total combustion at lower temperatures than the homogeneous reaction, leading to a reduction of NO_x emissions. The goal in this area is to develop a catalyst that promotes the total oxidation of methane at low temperatures, reducing the emission of greenhouse and harmful gases.

In this review, the important aspects of the catalytic combustion of methane using ceria-zirconia catalysts are addressed. The major findings in recent years are presented.

* E-mail: susana@di.fcen.uba.ar

1. INTRODUCTION

The combustion of methane (CH_4) has attracted great attention in the last years due to the increment in the use of Natural Gas (NG) in the energy production area, not only in electric power plants but also in thermal power production and transportation (Natural Gas Vehicles: NGVs). The following represents the chemical equation of the global reaction:

$$CH_4\,(g) + 2O_2\,(g) \rightarrow CO_2\,(g) + 2H_2O\,(l) \Delta H^0 = -889.5\ kJ/mol\ ^{(*)}$$

Methane is the most inert hydrocarbon molecule. Its homogeneous combustion, a typical process in power production, proceeds within the flammability limits and usually takes place in flames with very high temperatures (adiabatic flame temperature at constant pressure: 2223K) following a mechanism of formation of free radicals. At those temperatures, when nitrogen and oxygen are present as a consequence of using air as the oxidizing agent, the formation of nitrogen oxides (NO_x) is thermodynamically favored, producing high levels of NO_x, which is harmful to human beings and ecosystems [1,2].

In the last years, the replacement of traditional fuels (diesel oil, gasoline) by methane in vehicles (cars, buses, trucks) has rapidly increased in order to reduce NO_x and particulate emissions in urban areas. However, these advantages are balanced by the emission of unburned methane in the exhausted gases, which constitutes an important source of emission of gas with high greenhouse effects.

The catalytic combustion emerges as an alternative to the homogeneous combustion process for energy production, and as a way to reduce the emissions of unburned methane in NGVs exhaust gases. In the first case, it offers the possibility to work in controlled conditions and outside the flammability limits. In the latter case, it makes it possible under lean conditions to achieve complete methane combustion. In order to develop appropriate catalysts for these methane combustion applications, it is necessary to design materials exhibiting high activity at low temperatures and high resistance to sulfur poisoning.

The catalytic combustion of methane proceeds on the surface of a solid catalyst, which has two essential functions: the activation of the oxygen molecule (O_2) and its dissociation into more oxidized species, and the dissociation of methane C-H bonds. Noble metals, and oxides of transition-metals or rare-earths, are capable to perform these dissociations at temperatures much lower than 2223K, reducing the production of nitrogen oxides [3-6].

Noble metals have the ability to dissociate the O_2 molecule and the C-H bond even at room temperature. We can cite in this group metals such as Pt, Pd or Rh supported on alumina or silica. The advantage of noble metals over metal oxides are their better activity per active site, the high dispersion grade that is possible to achieve when dispersed over conventional supports like silica and alumina, and their higher resistance to sulfur poisoning when NG is combusted. The main disadvantage is their cost. The complete oxidation of methane over noble metal-based catalysts was reviewed by Géllin and Primet [6].

Transition and rare-earths metal oxides are cheaper than noble metals. The cations in those oxides exhibit various possible oxidation states, with a reversible redox process of interconversion among them. In the group of the rare-earths oxides, ceria (CeO_2) has been thoroughly studied as a catalyst for oxidation reactions [4, 5]. Cerium is the only member of the rare-earths family with a stable oxide of composition CeO_2 (“ceria”) in atmospheric

conditions, due to the easy loss of the last valence electron to form the Ce^{4+} ion. Ceria has a Face-Centered-Cubic phase of fluorite- type (CaF_2), where each cerium cation is in the center of a cube formed by eight oxygen anions (Figure 1). It is one of the better hydrocarbon oxidation catalysts and is one of the key components in the Three-Way Catalyst (TWC) formulation [7]. It has attracted great attention in heterogeneous catalysis, not only in hydrocarbon combustion but also in other redox reactions [8]. Among its different uses, its participation in catalysts formulation for the removal of particulate matter from exhaust gases of diesel engines, the removal of organic substances in wastewater (catalytic wet oxidation), and the combustion of hydrocarbonsare the most studied applications [7]. Cerium cation has two possible oxidation states; Ce^{4+} and Ce^{3+}. These oxidation states constitute a redox couple Ce^{4+}/Ce^{3+} with a normal electrochemical potential of 1.61V, which indicates that Ce^{4+} is a strong oxidant [9]. Due to the ability of cerium cations to easily change between their oxidized and reduced states (Ce^{4+}/Ce^{3+}), ceria exhibits a great capacity to store or release oxygen in the presence of an oxidizing or reducing atmosphere, respectively. When the oxide is immersed in a reducing atmosphere or with low oxygen partial pressure, it suffers the reduction of some of their cerium cations, releasing the oxygen of its cell to compensate for the lack of O_2. A strong oxygen-deficient non-stoichiometric in the composition structure is formed, which could be described as$CeO_{2-\alpha}$ (with $0<\alpha<0.5$). However, the oxide still conserves the fluorite-type crystal structure which facilitates the re-incorporation of oxygen inside the crystal structure as soon as an oxidizing atmosphere is established, resulting in a total solid recovery [10]. The ability of this oxide to be reduced and reversibly oxidized gives a unique behavior which is called "Oxygen Storage Capacity" (OSC) [11], that is directly related with the generation of the oxygen vacancies in the oxide structure. As a consequence of the oxygen vacancy formation, O^{2-} ions are transported in the structure mainly by the “jumping” mechanism of O^{2-} ions on vacancies, conferring ionic conductivity to the material [7]. The main disadvantage of this oxide relies on its textural properties. Although we can say that the pure cerium oxide can be synthesized with a specific surface area and pore volume values appropriated to its use as catalyst or support in heterogeneous catalysis, these textural properties are of limited stability. Thus, the specific surface area usually falls to a few square meters per gram when the oxide is treated at temperatures above 973K [4].

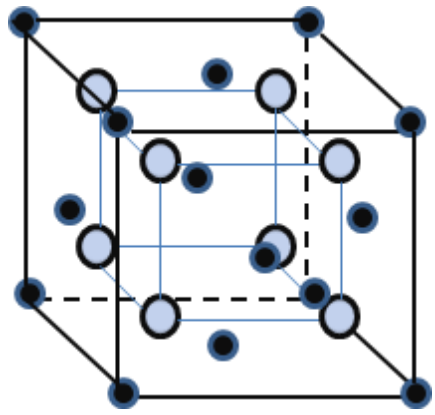

Figure 1. CeO_2 fluorite-type structure.

As an alternative to enhance the morphological stability of ceria, doping with different metal cations was tried. The incorporation of a metal cation in the ceria crystal structure introduces structural defects (structural vacancies) which drastically changes the oxygen mobility, the OSC, the ionic conductivity and, as a consequence, the catalytic activity. Then, the characteristics of these solid solutions are strongly influenced by the kind and the amount of the metal cation incorporated to the structure. The ability of one metal cation to be incorporated in ceria structure is strongly related with various factors like cation dimension, synthesis conditions and the resultant structure of the solid solution.

2. THE CeO_2-ZrO_2 SYSTEM

CeO_2-ZrO_2 solid solutions are well known for their higher Oxygen Storage Capacity (OSC), oxygen mobility and thermal stability, which exceed those of pure ceria. These characteristics became crucial for the development of a new generation of Three-Way Catalysts (TWC), capable to achieve the more severe regulations in exhaust gases emissions [7]. Since the beginning of 1990, an increasing number of publications related to synthesis, redox properties and OSC have appeared. Besides, their use in other catalytic processes was also reported [8]. In coming sub-sections, the main conclusions related with synthesis, morphological characteristics, structure, OSC and redox properties are summarized. In section 3, the application of this system as a catalyst in methane total combustion is presented.

2.1. Synthesis, Morphological Aspects and Structural Characterization

The formation of CeO_2-ZrO_2 solid solutions has been thoroughly studied [3-5, 7, 10-26]. Even though the ionic radius of Zr^{4+} (0.84 Å) is smaller than that of Ce^{4+} (0.97 Å), the CeO_2 and the ZrO_2 easily form a solid solution in a wide range of compositions. The ZrO_2 is a refractory oxide that has the same Fluorite-type structure, causing the Zirconium ions to enter the CeO_2 network without generating stress in the structure [7].

The phase diagram of the CeO_2-ZrO_2 system has been investigated, finding thermodynamically stable phases and several metastable phases dependent on the synthesis conditions [14-17]. In Figure 2, the CeO_2 - ZrO_2 phase diagram published by Kasparet. al. [13] is reproduced. This figure shows that at temperatures lower than 1273K, there is a monophasic region of monoclinic structure (m) for CeO_2 contents smaller than 10 molar%, while for contents larger than 80 molar%, a cubic phase (c) is observed. In the intermediate region, the actual nature of the diagram is uncertain. In this region, a large number of stable and metastable phases of tetragonal symmetry were reported [14-17].

According to Yashima and collaborators [17], three different regions are distinguished, corresponding to phases *t, t'* y *t"*. The *t* structure is stable, while the *t'* and *t"* phases are metastable. The above mentioned regions have fuzzy borders. These borders are depicted in Figure 2 to indicate the zones where these metastable phases could likely be found. These metastable phases are stabilized at nanometric crystallite sizes, giving rise to an important

area of study: the synthesis of CeO_2-ZrO_2nanopowders that could exhibit extraordinary properties [15-17].

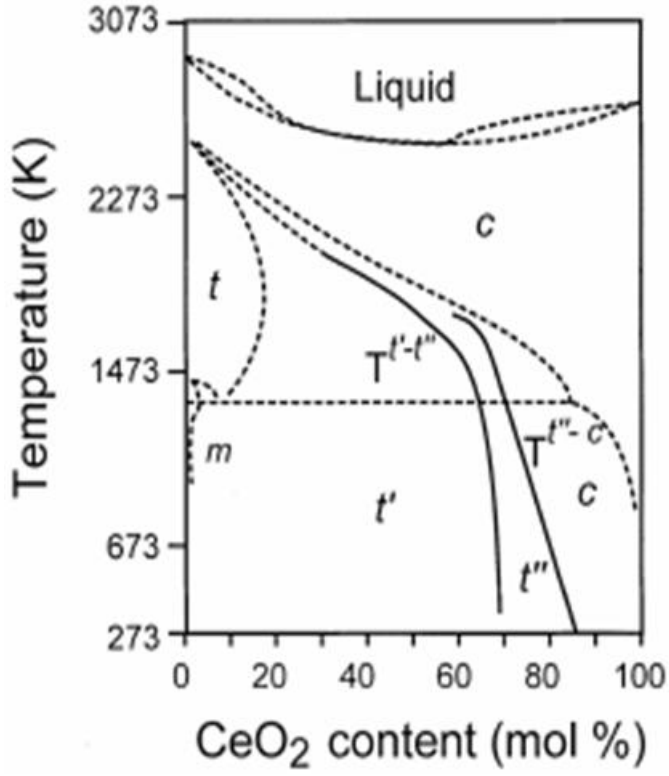

Figure 2. CeO_2 - ZrO_2 Phase Diagram (Ref. [13])

Despite the intensive research work done through the present day, the fine structural details of CeO_2–ZrO_2 mixed oxides were not fully explained. The structural characteristics are influenced by the thermal treatment, the textural properties and the crystallite sizes. Therefore, there are many relations with the synthesis process and the textural and structural characteristics of the solid solutions obtained.CeO_2-ZrO_2 solid solutions have been synthesized in different compositions by different methods like co-precipitation [18-21], sol-gel [3, 21-23], solution combustion [14, 15, 21, 24-26], Pechini-based methods [27-30], microemulsion [31-32], solvothermal [33] and many others [34, 35]. Co-precipitation process [18-21] is an easy traditional way to synthesize these mixed oxides. It consists of the preparation of a homogeneous solution of soluble cation salts and the further precipitation by adding a chemical precipitation agent or changing some conditions, like temperature, pH, etc. The advantage of this method is the possibility to control the particle size by controlling the nucleation and nucleus-growing rates. The main disadvantage of this synthesis process is that it produces inhomogeneities that affect the final textural and chemical properties of the mixed oxide [16]. The sol–gel synthesis process [3, 21-24] starts with the formation of a solution with the desired proportion of the metal alcoxides, which evolves towards the formation of a gel by adding an external agent (i.e. urea). Further drying and calcination processes are applied. The microstructure homogeneity and porosity strongly depend on the unstabilization

and drying steps. Then, the synthesis conditions should be controlled in order to get homogeneous composition. Rossignol et al. [36] clearly showed that Ce/Zr mixed oxides synthesized by co-precipitation or sol-gel methods are not compositionally homogeneous, even for similar compositions and thermal treatments to those studied by other authors [20].However, homogeneous Ce-Zr mixed oxides were obtained by different researchers [14, 15, 21, 24-26] following the solution combustion method. This synthesis process produces very homogeneous solids, even in micro and nano-domains, as it was confirmed in many works [14, 15]. This synthesis process is comprised of two steps. The first one involves the formation of a solution of cation metal nitrate salts in the desired Ce/Zr molar ration, the adding of an organic fuel in stoichiometric or non-stoichiometric quantity, and the evaporation of water until the formation of a gel. The second step involves a deeper drying process resulting in a self-sustained combustion, which is produced by the exothermic redox reaction between nitrate ions and fuel molecules. The main characteristics of this technique are high combustion temperatures, high temperature gradients and rapid expulsion of gases (short reaction times), which lead to final products with smaller particle size, higher surface areas, lower agglomeration and higher purity and homogeneity [37]. Zhang et al. [21] synthesized $Ce_{0.6}Zr_{0.4}O_2$ solid solutions by co-precipitation, sol–gel, solution combustion and surfactant-assistant methods. The solid solution synthesized by solution combustion maintained the surface area and the particle size. Besides, it showed the highest activity for lube combustion. Therefore, the stability of morphology obtained by this synthesis method is better than that obtained by the others.Terribile et al. [31] synthesized $Ce_{0.68}Zr_{0.32}O_2$ and $Ce_{0.80}Zr_{0.20}O_2$ solid solutions by the microemulsion method. CeO_2–ZrO_2 solid solutions characterized by high surface areas (~230 m^2/g) were obtained after calcination a 723K. This value dropped to 40 m^2/g after heating at 1173 K. Besides, only fairly homogeneous solid solutions were obtained.It is worth mentioning the great relevance of the synthesis and characterization of nanosized systems, not only in order to determine structural nanodomains but also to determine surface nanodomains, which would strongly affect the catalytic properties of these intriguing CeO_2–ZrO_2 mixed oxides. A multi-technique characterization is needed with a careful correlation of all of the results. The combination of these techniques with *"in situ"* catalytic characterization will provide a more detailed picture of the solid chemical properties in nanoscale domains.

2.2. Oxygen Storage Capacity and Redox Properties

The study of the reduction properties of ceria-zirconia mixed oxides has gained great attention. Many research groups investigated the reduction properties of the Ce-Zr solid solutions and their strong relation with the Oxygen-Storage Capacity (OSC) (7, 19, 32, 36, 38-41). Several factors affecting the reducibility and the OSC were studied. One of these factors is associated to the crystalline structure which, in turn, is related with the Ce/Zr molar ratio. The incorporation of Zr in the ceria structure strongly modifies the redox behavior of cerium cations, improving the OSC. Results presented by different researchers [7, 38-41] indicate that the fluorite-type cubic structure has better reducibility and OSC than the other metastable phases. The cubic-structure can accommodate oxygen vacancies in an easier way than tetragonal structure. The highest OSC values were reported for compositions close to

$Ce_{0.5}Zr_{0.2}O_2$, showing a pseudo cubic phase t" [7, 38-41] which, as it was explained in the previous sub-section, corresponds to a cubic fluorite-type structure with oxygen-anions displaced from the original fluorite position to that corresponding to an internal tetragonal symmetry. Other important factors considered to affect the redox properties of CeO_2-ZrO_2 mixed oxides are the textural characteristics. These characteristics are strongly related with the synthesis conditions, crystallite sizes and particles agglomeration grade. Di Monte and Kaspar [16] introduced a novel analysis of these solids, pointing out that the synthesis routes modify the microstructures, creating inhomogeneities that affect the textural and chemical properties of the oxide. It is worth mentioning, at this point, that also the crystallite size plays an important role because, as it was mentioned before, nanosizes allow stabilizing structures that are thermodynamically unstable in higher sizes [14]. It was mentioned in the previous sub-section that the synthesis process also affects the homogeneity at a nanoscale analysis. But, in a general way, it is important to say that combustion synthesis leads to solids with lower crystallite sizes and high surface areas, with a better stabilization of the structure with temperature treatments [26]. In recent years, Yang et al. [42] presented a detailed computational study of the effect of Zr-doping on the reduction of cerium cations corresponding to plane (110) for the solid solution with $Ce_{0.75}Zr_{0.25}O_2$ composition. Their results are very important because they clearly showed the decrease in the formation energy of O^{2-} vacancies and the improvement of the redox properties of the (110) surface of ceria when doping with zirconium. The formation of an oxygen vacancy produces two electrons that seem to localize on the two Cecations neighboring the oxygen vacancy. As soon as the reduction of the two Cecations proceeds, a large structural relaxation occurred on O vacancy formation, lowering the reduction energy. Therefore, it is still necessary to conduct studies of these mixed phases to analyze the relationship of the chosen synthesis route with particle sizes and their agglomeration, the stability with redox cycles and temperature treatment, the development of bulk and surface microdomains, which altogether will play an important role in the redox and catalytic properties of CeO_2-ZrO_2-mixed oxides.

3. METHANE COMBUSTION OVER CeO_2-ZrO_2 CATALYSTS

As it was mentioned in previous sections, the catalytic combustion of methane has gained great interest because methane is the main component in Natural Gas (NG) composition. The development of active catalysts for its catalytic combustion in fuel-rich and fuel-lean conditions is very important in the area of the energy production and emissions abatement [2, 6]. Although in recent years and as a consequence of the general concern about global warming, a driving-force toward the development of a "hydrogen economy" in the area of energy production and transportation has gained more attention in the research and development area, the situation is still far from the massive incorporation of hydrogen as fuel. In the meantime, methane has increased its uses due to an increment in the global reserves. Besides, potential reserves in the deep ocean and the generation of methane-rich biogas from anaerobic fermentation of organic waste, position methane with a promising future in the area of energy generation [43, 44]. The critical aspects of the use of CeO_2-ZrO_2-mixed oxides in the complete oxidation of methane are structure, morphology stability, and redox properties. All of these characteristics are strongly related to the synthesis process and the composition

selected. Many compositions and synthesis processes have been reported, leading to a wide scope of catalytic behaviors. Besides, in the last years, the synthesis of nanomaterials remarked the influence of the particle size over the properties of metal oxides. From a thermodynamic point of view, in nanozised materials, the surface-free energy and the surface tension gained importance due to the reduction of the particle sizes, which produce, in turn, changes in the thermodynamical stability of the phase. In this way, some phases that are not thermodynamically stable at high particle sizes (μm) are stable at the nanometric level [14]. Besides, at nanometric size, the electronic properties of the oxides change, and the increment of the ionic character of the metal-oxygen bond is observed. In the catalytic combustion of methane, the chemical processes are confined to the solid surface. When talking of nanoparticles, this surface could present extraordinary chemical characteristics because of the ease of vacancy accommodation and the presence of atoms with a much lower coordination than in the bulk [45]. Bozo et al. [20] studied the total oxidation of methane over CeO_2–ZrO_2 solid solutions prepared by co-precipitation. They tested $Ce_{0.83}Zr_{0.17}O_2$, $Ce_{0.67}Zr_{0.33}O_2$ and $Ce_{0.47}Zr_{0.53}O_2$ compositions as active phase in methane combustion. The samples were calcined during 6 hrs at 873, 973 and 1173K. An aging treatment in a flowing mixture of oxygen (5 mol%), water (10 mol%) and nitrogen (balance) at 1273K, was also performed in order to simulate the effect of reaction conditions on the catalytic performance. X-ray diffraction patterns are not presented in the paper but authors claimed that the samples calcined at 873, 973 and 1173K were monophasic. No values of crystal sizes are reported. Bozo et al. indicated that when the samples were calcined at 1273K, the diffraction peaks became asymmetrical. New phases clearly appear for samples $Ce_{0.67}Zr_{0.33}O_2$ and $Ce_{0.47}Zr_{0.53}O_2$ when calcined at 1473K.The formation of these new phases and the asymmetry in the diffraction peaks of sample $Ce_{0.83}Zr_{0.17}O_2$ observed by Bozo et al. [20], are indicative of the presence of inohomogeneities in the synthesized solid. This analysis is in accordance with the findings of Egami et al. [46], who proved, using pulsed neutron scattering, that localized inhomogeneities may be present in CeO_2–ZrO_2-mixed oxides. These inhomogeneities are Ce-rich and Zr-rich microdomains, segregated at a nanometer scale that cannot be detected by the conventional diffraction methods. They also suggested that the microdomain interfaces may destabilize oxygen and facilitates oxygen releasing and diffusion. The microdomains with different compositions arise as new phases when the solids are calcined at 1273K. The catalytic performances of the synthesized solids reported by Bozo et al. [20] were studied in a fixed bed reactor fed with a CH_4 (1 mol%), O_2 (4 mol%), N_2 (balance) mixture. No strong effect of solid solution composition on catalytic activity was found. Half conversion temperatures were in the 843-863K range. Aged catalysts calcined at 1273K experienced a methane conversion drop of more than 50%. Also, a drastic reduction in the specific surface area was observed.Therefore, it is possible to conclude that the mixed oxides synthesized by co-precipitation are not homogeneous in their composition, and textural properties and catalytic activity are strongly affected by heating treatments.Pengpanich et al. [3] reported the preparation of CeO_2-ZrO_2 solid solutions, with nominal compositions $Ce_{1-x}Zr_xO_2$ in which x = 0, 0.25, 0.50, 0.75 and 1.0, via the urea hydrolysis method. The samples were calcined at 773K and 1173K during 4 hrs prior to testing their activities in the total oxidation of methane. Besides, kinetics studies with the best catalysts were performed. The specific surface areas of the catalysts were reasonably high (80 to 120 m^2/g), being the values for CeO_2-ZrO_2 solid solutions higher than that of pure ceria.It was observed that increasing Zr contents increases the specific surface areas. Samples calcined at 1173K showed a drastic loss of surface areas

(4.6-21.3 m^2/g). Nevertheless, the reduction was lower as Zr content increases, suggesting some sintering inhibition effects of Zr incorporation in the cell. From X-ray diffraction patterns it is evident that all CeO_2-ZrO_2 samples are biphasic. Crystallite sizes were not reported.The authors claimed that only samples with $x \geq 0.5$ were biphasic, with a mixture of cubic and tetragonal structures. Nevertheless, due to the fact that no calcinations at high temperatures (1273K) were performed, the presence of another phase or nanosizedinhomogenoeusmicrodomains could not be discarded. These results make the interpretation of the CO-Temperature Programmed Reduction (CO-TPR) and catalytic activity results difficult. It is not easy to know the effect of the presence of these minoritary phases in oxygen mobility and releasing. Nevertheless, the authors observed that reduction temperatures of cerium cations in the solid solutions shifted to higher temperatures when ZrO_2 is above 50 mol%. The authors ascribed the change in the reducibility behavior to the presence of a tetragonal phase much more difficult to reduce than the cubic one. This is in agreement with the findings reported by Fornasiero et al. [38].Pengpanich et al. [3] reported that the CO-TPR profiles for samples calcined at 1173K show peaks more sharp than those corresponding to pure ceria, suggesting that zirconium promotes redox properties. A positive effect of zirconium incorporation in catalytic performances and a tiny dependence of catalytic performances with specific surface area were reported. Kinetic studies showed a strong dependence of reaction rate with methane partial pressure and a minor effect of the oxygen partial pressure. Three mechanisms were adjusted, being the more appropriate Langmuir-Hinshelwood mechanism, with methane chemisorption being the rate-limiting step. Apparent activation energy of 100.0 kJ/mol was found. This value is much lower than the value reported byother authors for homogeneous combustion [47].Larrondo et al [26] prepared nanocrystalline CeO_2-ZrO_2-mixed oxides synthesized by a pH-controlled nitrate-glycine combustion method following a non-stoichiometric route. Different solids containing 10, 30 and 50 mol% of ZrO_2, were prepared. Samples were calcined at 873K an 1073K in order to see the effect of calcination temperature on textural and structural properties. The specific surface areas for all compositions and calcination temperatures were almost the same (~ $30m^2/g$), pointing out the stabilization effect of zirconium incorporation on the textural properties. Only the sample containing 30mol% of ZrO_2 has a specific surface area that doubles the others when calcined at 873K, but this value is not stable with temperature and drops down to $30m^2/g$. Synchrotron radiation X-ray diffraction experiments with a wavelength set as 1.50006 Å were presented.

In Figure 3, the diffractograms of samples calcined at 873K are plotted for the 2θ region 20-100°, in logarithmic scale. In Figures 4 and 5, the (4 0 0) and (0 0 4) reflections, and (1 1 2) peak are presented, respectively. The small splitting of peaks (4 0 0) and (0 0 4) observed for the sample containing 50 mol% of ZrO_2 showed in Figure 4 and the absence of a (1 1 2) reflection for sample 10 mol% of ZrO_2 observed in Figure 5 indicate that the sample containing 50 mol% of ZrO_2 exhibits the t'-form of the tetragonal phase, the sample containing 30 mol% of ZrO_2 exhibits the t''-form of the tetragonal phase and the sample containing 10 mol% of ZrO_2 exhibits the cubic phase. Likewise, no inhomogeneities, even in nanosized domains, were observed for all samples.The crystallite sizes determined by the Scherrer equation were in the 13-16nm range for all of the powders calcined at 873K, and in the 25-30 nm range for samples calcined at 1073K. This is another confirmation of the Zr sintering inhibition role when it is incorporated in ceria structure. The stabilization effect is

more evident in these solids with nanometric sizes, than in those reported by other authors [20, 3]. The same result was obtained by Zhang et al. [21]. They also observed that the solid solutions of the same composition synthesized by the solution combustion method showed lower sintering of the particles when compared with solid synthesized by other techniques (co-precipitation, sol-gel, etc.).

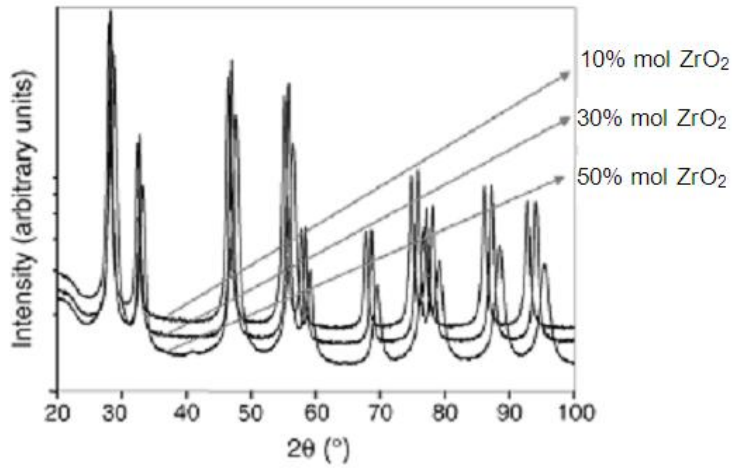

Figure 3. SR-XRD data of powder calcined at 873K (Ref. [26]).

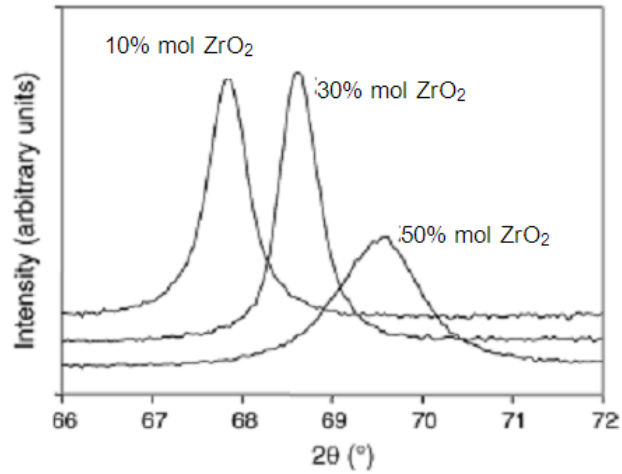

Figure 4. SR-XRD data of powder calcined at 873K for the 2θ region corresponding to (0 0 4) and (4 0 0) reflections (Ref. [26]).

TPR results are presented in Table 1. A strong effect of Zr content is observed. The presence of Zr not only enhances the reduction of surface sites but also the reduction of bulk sites. These results differed from those previously reported by Bozo et al. [20] and Pengpanich et al. [3]. These authors observed a shifting of the TPR peaks to higher temperatures as Zr is incorporated in the structure Another important result found by Larrondo et al. is the presence of centers of intermediate reducibility that could release

oxygen more easily for sample containing 10 mol% of zirconia. Catalytic results are reproduced in Figure 6. The sample containing 10 mol% of ZrO_2 showed higher values of methane conversion in all of the temperature ranges.

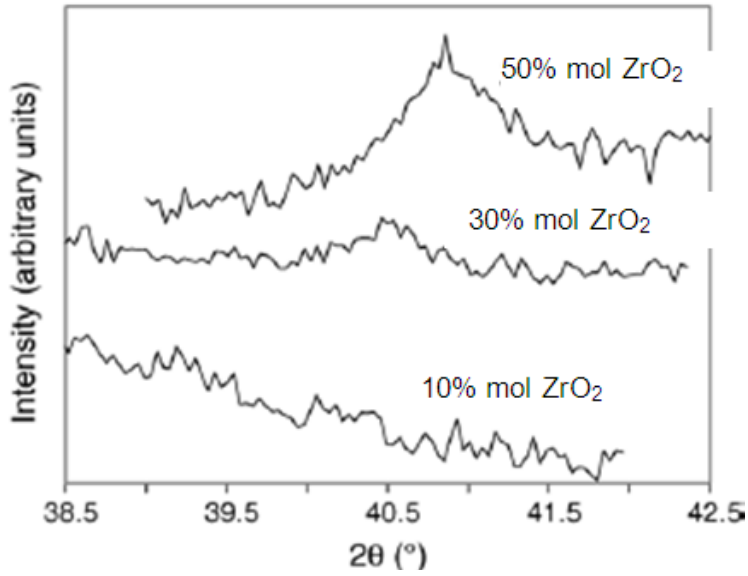

Figure 5. SR-XRD data of powder calcined at 873K for the 2θ region corresponding to (112) reflection (Ref. [26]).

The different behavior is related to redox properties and not to the specific area because, as indicated above, all samples have similar values of this parameter. The more labile oxygen ions present in this sample would oxidize methane more easily. At 873K, the best methane conversion was 20%. This conversion is low when compared with that reported by previous authors [3, 20]. Nevertheless, it is important to remark that the solids were tested at a space-time (catalyst mass/feed flow) 3 times lower than that used by Pengpanich et al. [3] and 12.5 times lower than that used by Bozo et al. [20].

The results presented in [26] reveal that the solids synthesized following a gel-combustion process have high homogeneity, sintering resistance and reducibility. Zimicz et al. [48] studied the influence of synthesis conditions in the catalytic performance of these solids. The authors assessed the influence of the α-aminoacid/nitrate process conditions on nanosized $Ce_{0.9}Zr_{0.1}O_2$-mixed oxide, following either stoichiometric or non-stoichiometric routes. The analysis of the influence of synthesis conditions on the reducibility and catalytic behavior of synthesized solids was reported.

All samples exhibited fluorite-type crystalline structures. Inhomogeneities or segregation of secondary phases was not detected. It was concluded that the α-amino acid selected as fuel and the α-aminoacid/nitrate molar ratio strongly influences not only morphology and textural properties but also the reducibility and catalytic activity of the solid obtained. The authors concluded that the $Ce_{0.9}Zr_{0.1}O_2$ catalyst synthesized by the sotoichiometric route with glycine shows a higher surface area (~ 40 m^2/g) and pore volume, smaller particle size (~9nm) and lower agglomeration grade.

Temperature Programmed reduction experiments with hydrogen on this solid, showed a lower reduction temperature and a higher surface / bulk Ce^{4+} sites ratio, indicating more availability of oxygen to oxidize the methane molecule.

Table 1. Peak temperatures of TPR profiles (Ref. [26])

	$T_{calcination}$ = 873K			$T_{calcination}$ = 1073K		
	50 mol% ZrO_2	30 mol% ZrO_2	10 mol% ZrO_2	50 mol% ZrO_2	30 mol% ZrO_2	10 mol% ZrO_2
T1	187	181	108	194	247	197
T2	-	-	472	-	-	494
T3	569	530	719	582	597	747

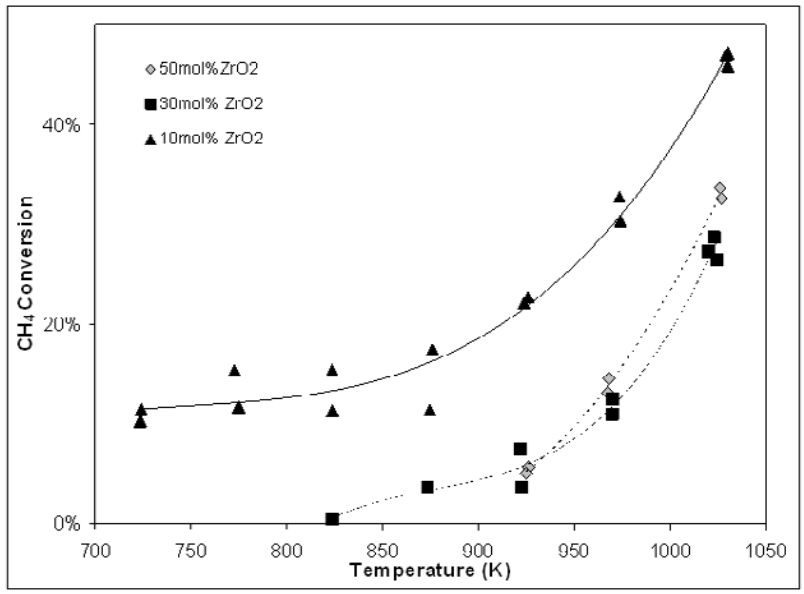

Figure 6. Methane conversion vs Reaction Temperature for powders calcined at 1073K (Ref. [26]).

Therefore, the solid behaves as a total oxidation catalyst producing only carbon dioxide and water as products. The easy reducibility of this catalyst is in accordance with its higher catalytic activity (conversion of methane ~ 80% at 973K).

Kuznetsova et al. [49] studied the effect of the real structure and chemical composition on the mobility and reactivity of surface and bulk oxygen sites in ceria-zirconia-based catalysts. In order to control the lattice oxygen mobility and reactivity, the systems were doped with transition metal cations. The authors studied two fluorite-like systems named CeZr (I) and CeZr (II). The solid solution with 50 mol% CeO_2 – 50 mol% ZrO_2 composition was used as the base component. In system CeZr (I), Ce substitution by Mn or Nb was performed, while for system CeZr(II),Zr substitution by Ca, Mn, Co and Bi was done. For system II, surface modification by Mn supporting was also studied. Samples were synthesized by polymeric precursor route based on the Pechini process [27-30]. The structural features of the samples were studied by XRD, IR, EXAFS, UV-Vis spectroscopy techniques. Beside, their oxygen mobility, reactivity and catalytic activity in methane combustion, were studied

by O_2-Temperature Programmed Desorption, H_2-Temperature Programmed Reduction, CH_4-Temperature Programmed Reduction and catalytic combustion of methane experiments.

The authors observed an anion-deficient fluorite-type structure with disordered anion vacancies when doping up to 20 mol% of Ca, Mn, Co, Bi or Nbcations. Doping with transition metal cations increased the mobility and reactivity of the surface/bulk oxygen sites. A relationship was found between the structure and the specific rates of methane combustion. When Nb or Bi replaces Zr, a negative effect on methane conversion was observed indicating that these cations would interfere with the ability of Zr^{4+} to activate the methane molecule. In general, no straightforward relationships between the activity of methane combustion and the characteristics of the surface and lattice-oxygen (bonding strength, surface coverage, lattice-oxygen mobility) were revealed.

CONCLUSIONS

In previous sections, a short review of the main characteristics of CeO_2-ZrO_2 solid solutions and their performances as catalysts for the combustion of methane at low temperature (~1000K) were presented. A clear evidence of the effect of synthesis conditions in homogeneity and textural properties was presented. CeO_2-ZrO_2 mixed oxide powders with nanometric crystallite sizes can be synthesized with structures not thermodynamically stable at room temperature. The synthesis of these nanopowders promotes new chemical properties like higher reducibility, sintering resistance and catalytic activity. The use of CeO_2–ZrO_2-mixed oxides prepared by gel combustion as catalysts for low temperature combustion of methane and other hydrocarbons is promising.

The synthesis and characterization of nano-sized systems will have great relevance to determine not only structural nanodomains but also surface nanodomains that would strongly affect the catalytic properties of these intriguing CeO_2–ZrO_2 mixed oxides. A multi-technique characterization with a careful correlation of all of the results will be needed. The combination of these techniques with *"in situ"* catalytic characterization will provide a more detailed picture of the solid chemical properties at nanoscale level. The combination of DFT studies with experimental characterization will clarify the influence of concentration of surface cations Ce^{3+}, Ce^{4+} and Zr^{4+} and the surface / bulk oxygen anions ratio, on the mechanism of methane activation and methane combustion.

REFERENCES

[1] M. Primet and E. Garbowski, *"Fundamentals and applications of ceria in combustion reactions"*, *in"Catalysis by CeO_2 and related materials"*, Chap. 13, A. Trovarelli (Editor), Imperial College Press (2002), London, United Kingdom.

[2] T. V. Choudhary, S. Banerjee and V. R. Choudhary, "Catalysts for combustion of methane and lower alkanes", *Appl. Catal. A: General* 234 (2002) 1-23.

[3] S. Pengpanich, V. Meeyoo, T. Rirksomboon, K. Bunyakiat, "Catalytic oxidation of methane over CeO_2-ZrO_2 mixed oxide solid solution catalysts prepared via urea hydrolysis", *Appl. Catal. A: Gen* 234 (2002) 221.

[4] A. Trovarelli, M. Boaro, E. Rocchini, C. de Leitenburg, G. Dolcetti, "*Some recent developments in the characterization of CeO_2-based catalysts"*, *J. Alloys Compd*. 323 – 324 (2001) 584.

[5] A. Trovarelli, *"Catalytic properties of Ceria and CeO_2 – containing Materials"*, *Cat. Rev. Sci. Eng*. 38 (4) (1996) 439.

[6] P. Géllin and M. Primet, *"Complete oxidation of methane at low temperature over noble metal-based catalysts: a review"*, *Appl. Catalysis B: Environ*. 39 (2002) 1.

[7] P. Fornasiero, G. Balducci, R. Di Monte, J. Kaspar, V. Sergo, G. Gubitosa, A. Ferraro, M. Graziani, "Modification of the redox behavior of CeO_2 induced by structural doping with ZrO2"; *J.Catal*. 164 (1996) 173.

[8] L. Vivier and D. Duprez, *"*Ceria-based solid catalysts for organic chemistry*"*, *ChemSusChem*.3 (2010) 654.

[9] A. Bielanski and J. Haber, "Mechanism of the Catlytic Oxidation", in "*Oxygen in Catalysis*", Chap. 4, Marcel Dekker (1991), New York, USA.

[10] A. Trovarelli, "Catalytic properties of Ceria and CeO_2–containing Materials", *Cat. Rev. Sci. Eng.* 38 (4) (1996) 439.

[11] M. Shelef, G. W. Graham and R. W. McCabe, "Ceria and other oxygen storage components in automotive catalysts", in "Catalysis by CeO_2 and related materials" Chap. 10, A. Trovarelli (Editor), Imperial College Press (2002), London, United Kingdom.

[12] G. R. Rao and B. G. Mishra, "Structural, redox and catalytic chemistry of ceria-based materials", *Bull. Catal. Soc.of India,* 2 (2003)122.

[13] J. Kaspar, P. Fornasiero, M. Graziani; "Use of CeO_2-based oxides in the three way catalysis"; *Catal. Today,* 50 (1999) 285-298.

[14] D.G. Lamas, G.E. Lascalea, R.E.J. Juárez, E. Djurado, L. Pérez, N.E. Walsöe de Reca, "Metastable forms of the tetragonal phase in compositionally homogeneous, nanocrystalline zirconia–ceria powders synthesized by gel-combustion", *J. Mater. Chem.* 4 (2003) 904.

[15] D.G. Lamas, G.E. Lascalea, M.D. Cabezas, R.O. Fuentes, I.O. Fábregas, M.E. Fernández de Rapp, N.E. Walsöe de Reca, S. Larrondo, R. Tejeda, y N. Amadeo, "Ánodos basados en ZrO2-CeO2 para celdas de combustible de óxido sólido de una cámara", Jornadas SAM / CONAMET / Simposio Materia 2003, 1030.

[16] R. Di Monte and J. Kaspar; "Nanostructured CeO2-ZrO2 mixed oxides"; *J. Mater. Chem*. 15 (2005) 633.

[17] M. Yashima, H. Arashi, M. Kakihana, M. Yoshimura; "Raman Scattering Study of CubicTetragonal Phase Transition in $Zr_{1-x}Ce_xO_2$ Solid Solution"; *J. Am. Ceram. Soc*. 77 (4) (1994) 1067.

[18] S. Letichevsky, C.A. Tellez, R.R. de Avillez, M. I. P. da Silva, M. A. Fraga, L. G. Appel, *"Obtaining CeO_2–ZrO_2 mixed oxides by co-precipitation: role of preparation condition*"*,Appl. Catal. B* 58 (2005) 203.

[19] C. E. Hori, H. Permana, K. Y. Simon Ng, A. Brenner, K. More, K. M. Rahmoeller, D. Belton, "Thermal stability of oxygen storage properties in a mixed CeO_2-ZrO_2 system"*,Appl. Catal. B: Environ*. 16 (1998) 105.

[20] C. Bozo, N. Guilheume, E. Garbowski, M. Primet, *"Combustion of methane on CeO_2-*ZrO2 based catalysts", *Catal. Today* 50 (2000) 33.

[21] Z. Zhang, Y. Zhang, Z. Mu, P. Yu, Z. Ni, A. Wang, L. Zheng "Synthesis and catalytic properties of $Ce_{0.6}Zr_{0.4}O_2$ solid solutions in the oxidation of soluble organic fraction from diesel engines",*Appl. Catal. B: Environ*. 76 (2007) 335.

[22] M. Thammachart, V. Meeyoo, T. Risksomboon, S. Osuwan, "Catalytic activity of CeO2–ZrO2 mixed oxide catalysts prepared via sol–gel technique: CO oxidation", *Catal. Today,* 68 (2001) 53.

[23] E. V. Frolova, "Nanocrystallization of amorphous ZrO_2-GeO_2 mixed oxides prepared by sol-gel techniques", *Mater. Sci. Eng*., C 23 (6-8) (2003) 1093.

[24] S.T. Aruna, K.C. Patil, "Combustion synthesis and properties of nanostructured ceria-zirconia solid solutions", *NanoStruct. Mater*. 10 (1998) 955.

[25] H.S. Potdar, S.B. Deshpande, Y.B. Khollam, A.S. Deshpande, S.K. Date, *"Synthesis of nano-sized $Ce_{0.75}Zr_{0.25}O_2$ porous powders via an autoignition: glycine nitrate process", Mater. Lett*. 57 (2003) 1066.

[26] S. Larrondo, M. A. Vidal, B. Irigoyen, A. F. Craievich, D. G. Lamas, I. O. Fabregas, G. E. Lascalea, N. E. Walsöe de Reca, N. Amadeo, "Preparation and characterization of Ce/Zr mixed oxides and their use as catalysts for the direct oxidation of dry CH4", *Catal. Today,* 107–108 (2005) 53.

[27] V.A. Sadykov, T.G. Kuznetsova, S.A. Veniaminov, V.V. Lunin, E. Kemnitz, A. Aboukais, "Cation/anion modified ceria-zirconia solid solutions promoted by pt as catalysts of methane oxidation into syngas by water in reversible redox cycles", *React. Kinet. Catal. Lett*. 76 (2002) 83.

[28] T.G. Kuznetsova, V.A. Sadykov, S.A. Veniaminov, G.M. Alikina, Moroz E.M., V.A. Rogov, O.N. Martyanov, V.F. Yudanov, I.S. Abornev, S. Neophytide, *"Methane transformation into syngas over Ce–Zr–O systems: role of the surface/bulk promoters and oxygen mobility", Catal. Today* 91-92 (2004) 161.

[29] T.G. Kuznetsova, V.A. Sadykov, E.M. Moroz, S.N. Trukhan, E.A. Paukshtis, V.N. Kolomiichuk, E.B. Burgina, V.I. Zaikovskii, M.A. Fedotov, V.V. Lunin, E. Kemnitz, *"Preparation of Ce-Zr-O composites by a polymerized complex method", Stud Surf SciCatal.* 143 (2000) 659.

[30] L, Quinelato, E. Longo, L. Perazolli, L A. Varela, "Effect of ceria content on sintering of ZrO_2-based ceramics synthesized using polymeric precursor", *J. Eur. Ceram. Soc*. 20-8 (2000) 1077.

[31] D. Terribile, A. Trovarelli, J. Llorca, C. de Leitenburg, G. Dolcetti, "The preparation of high surface area CeO2–ZrO2 mixed oxides by a surfactant-assisted approach", *Catal. Today* 43 (1998) 79.

[32] A. Martínez-Arias, M. Fernández-García, V. Ballesteros, L. N. Salamanca, J. C. Conesa, C. Otero, *J. Soria, "Characterization of High Surface Area Zr-Ce (1:1) Mixed Oxide Prepared by a Microemulsion Method"*, Langmuir 15 (1999) 4796.

[33] M.K. Devaraju, X. Liu, K. Usuke, S. Yin, T. Sato, *"Solvothermal synthesis and characterization of ceria-zirconia mixed oxides for catalytic applications" ,Nanotechnology*,20 (2009) 405606 (6pp).

[34] W.J. Stark, L. Ma¨dler, M. Maciejewski, S.E. Pratsinis, A. Baiker, *"Flame synthesis of nanocrystalline ceria–zirconia: effect of carrier liquid"*, Chem.Commun. 5 (2003) 588.

[35] A. Cabanas, J.A. Darr, E. Lester, M. Poliakoff, "A continuous and clean one-step synthesis of nano-particulate $Ce_{1-x}Zr_xO_2$ solid solutions in near-critical water*"*, *Chem. Commun.* 11 (2000) 901.

[36] S. Rossignol, F. Gérard and D. Duprez, "Effect of the preparation method on the properties of zirconia-ceria materials", *J. Mater. Chem*. 9 (1999) 1615.

[37] L.A. Chick, L.R. Pederson, G.D. Maupin, J.L. Bates, L.E. Thomas, G.J. Exarhos, "Glycine-nitrate combustion synthesis of oxide ceramic powders", *Mater. Lett*. 10 (1-2) (1990) 6.

[38] P. Fornasiero, R. Di Monte, G. RangaRao, J. Kaspar, S. Meriani, A. Trovarelli, M. Graziani, "Rh-Loaded CeO_2-ZrO_2 Solid-Solutions as Highly Efficient Oxygen Exchangers: Dependence of the Reduction Behavior and the Oxygen Storage Capacity on the Structural-Properties", *J. Catal*. 151 (1995) 168.

[39] C. de Leitenburg, A. Trovarelli, J. Llorca, F. Cavani, G. Bini, "The effect of doping CeO_2 with zirconium in the oxidation of isobutane", *Appl. Catal. A Gen*. 139, 161 (1996).

[40] A. Trovarelli, F. Zamar, J. Llorca, C. De Leitemburg, G. Dolcetti, J. T. Kiss, "Nanophase Fluorite-Structured CeO2–ZrO2Catalysts Prepared by High-Energy Mechanical Milling", *J. Catal.* 169 (1997) 490.

[41] G. Balducci, J. Kaspar, P. Fornasiero, M. Graziani, M. Saiful Islam, J.D. Gale, "Computer Simulation Studies of Bulk Reduction and Oxygen Migration in CeO2−ZrO2 Solid Solutions", *J. Phys Chem*. B 101(10) (1997) 1750.

[42] A. Yang, A. Fu, Y. Wei, K. Hermansson, "The electronic and reduction properties of $Ce_{0.75}Zr_{0.25}O_2$ (110)", *Chem Phys. Lett*. 450 (2008) 286.

[43] S. Specchia, G. Toniato, "Natural Gas combustion catalysts for environmental-friendly domestic burners", *Catal. Today* 147 (2009) 99.

[44] British Petroleum (BP), *"Statistical review of world energy 2008"*, available in website: www.bp.com/worldenerg.

[45] M. Fernández-García, A. Martínez-Arias, J. C. Hanson and J. A. Rodriguez, "Nanostructured Oxides in Chemistry: Characterization and Properties", *Chem. Rev.* 104 (2004) 4063.

[46] T. Egami, W. Dmowski and R. Brezny, "Characterization of the Local Structure of CeO2/ZrO2 by Pulsed Neutron Scattering", *SAEInternational Technical Papers* (1997) Paper Number 970461.

[47] H. Arai, T. Yamada, K. Eguchi, and T. Seiyama, "Catalytic combustion of methane over various perovskite-type oxides", *Appl. Catal. A: Gen*.26 (1986) 265.

[48] [XX] M.G. Zimicz, D.G. Lamas, S.A. Larrondo, "*Influencia de las condiciones de síntesis en la reducibilidad y actividad catalítica del óxido mixto* $Ce_{0,9}Zr_{0,1}O_2$*"*, Actas del XXII Congreso Iberoamericano de Catálisis (2010) CEO40 (CD, 6 pp.).

[49] T. Kuznetsova, V. Sadykov, L. Batuev, E. Moroz, E. Burgina, V. Rogov, V. Kriventsov, D. Kochubey,"Modified Ceria- Zirconia Fluorite-Like Catalysts for the Combustion of Methane", *J. Nat. Gas Chem*. 15 (2006)149.

INDEX

C

D

E

F

G

H

I

J

K

L

M

N

O

P

Q

R

S

T

U

V

W

X

Y

Z